Novel Quantum Dot and Fluorescent Protein Based Liquid Light-emitting Diodes and Luminescent Solar Concentrators

by

Sadra Sadeghi

A Dissertation Submitted to the
Graduate School of Sciences and Engineering
in Partial Fulfillment of the Requirements for
the Degree of
Doctor of Philosophy
in

Materials Science and Engineering

KOÇ ÜNİVERSİTESİ

July, 2020

Novel Quantum Dot and Fluorescent Protein Based Liquid Light-emitting Diodes and Luminescent Solar Concentrators

Koç University

Graduate School of Sciences and Engineering

This is to certify that I have examined this copy of a doctoral dissertation by

Sadra Sadeghi

and have found that it is complete and satisfactory in all respects, and that any and all revisions required by the final examining committee have been made.

Committee Members:

____

Assoc. Prof. Sedat Nizamoğlu (Advisor)

____

Assoc. Prof. Uğur Ünal

____

Prof. Erdem Alaca

____

Prof. Şenol Mutlu

____

Assoc. Prof. Onur Ferhanoğlu

Date: ______________________________

To My Wonderful Wife …

For having such a beautiful spirit that kept me warm for the last eight years

ABSTRACT

Novel Quantum Dot and Fluorescent Protein Based Liquid Light-emitting Diodes and Luminescent Solar Concentrators

PhD thesis

Sadra Sadeghi
Ph.D. in Material Science and Engineering
Supervisor: Assoc. Prof. Dr. Sedat Nizamoğlu
July 2020

Fluorescent nanomaterials have attracted significant attention in the last three decades due to their exceptional size-dependent optical properties such as high photoluminescence quantum yield (PLQY) and tunable electronic properties via quantum confinement effect and material composition. Among them, colloidal quantum dots (QDs) and fluorescent proteins (FP) have been widely used in lighting, display and energy harvesting applications such as light-emitting diodes (LEDs), luminescent solar concentrators (LSCs) and solar cells.

In this thesis, high-performance and biocompatible light-emitting diodes and luminescent solar concentrators based on QDs and fluorescent proteins have been demonstrated.

So far, the main approach for efficient lighting in color conversion nanomaterial-based LEDs is to increase the PLQY of the nanomaterials. However, even with near-unity emitting fluorophores, their utilization for efficient solid-state lighting sources has remained a challenge due to the decrease of PLQY from synthesis batch in liquid-state to host matrix in solid-state, which is also known as the host material effect. In the first part of this thesis, we design, develop and demonstrate a novel liquid-integration architecture, which improves the optical performance of QD- and FP-LEDs. In the first section, we synthesized green-emitting CdSe//ZnS/CdSZnS QDs with PLQY up to 84% and integrated the as-synthesized QDs in liquid-state directly onto the blue LED die using a novel architecture, which can hold the QD solutions on top of the blue LED. The liquid-state integration and the optimization of the PLQY led to a luminous efficiency of 64 lm/W for RGB (Red, Green, Blue)/ and 105 lm/W for GB-based white light generation, which are the most efficient QD-based LEDs reported to date. In the second section, we determined red-emitting mScarlet and green-emitting eGFP fluorescent proteins for high-

performance white LEDs, expressed them in living Escherichia coli and integrated the purified proteins in their natural aqueous environment onto blue LED chips. The aqueous integration preserved PLQY levels of the proteins above 70% in the device architecture and facilitated a high luminous efficiency of 81 lm/W with a color rendering index (CRI) of 83, which is the most efficient eco-friendly white LED reported to date. Moreover, we also optimized the concentration ratio of red- and green-emitting proteins and demonstrated white protein-based LEDs with a maximum CRI of 92. In the third section, we optimized the PLQY of magic-sized CdSe QDs up to 22% via controlling the synthesis parameters without any shelling or post-treatment process and integrated them in liquid-state on blue LED. The fabricated white LEDs showed CRI and luminous efficiency up to 89 and 11.7 lm/W, respectively. In the fourth section, we demonstrated QD-LEDs that operate at a luminous efficiency level of 95 lumens lm/W, luminous efficacy of optical radiation (LER) of 395 lm/W, and external quantum efficiency (EQE) of 23.3% in the green spectral region. For that, we synthesized 1-octanethiol-capped CdSe@ZnS QDs with the PLQY of 91% and integrated them in liquid matrix that allows conservation of the QD efficiency in device architecture. Finally in the last section, we synthesized red- and green-emitting cadmium-based QDs with PLQY of 52% and 74%, respectively and incorporated the synthesized QDs into the polydimethylsiloxane (PDMS) polymer matrix by using doctor blade technique, which led to the polymeric films with 123 mm×68 mm dimensions for smart phone displays. By using the large-area QD-polymeric films on blue-emitting backlight unit, the NTSC and sRGB color gamut ratio was measured as 91% and 127%, respectively.

In the second part of this thesis, we design and fabricate LSCs based on novel InP-based QDs and developed an innovative architecture, which enabled the liquid-integration of fluorescent protein in sunlight harvesting. In the first section, we demonstrate the copper-doping of zinc carboxylate-passivated InP core and nano-engineering of ZnSe shell, which facilitated the high in-device quantum efficiency of QDs over 80%, having well-matched spectral emission profile with the photo-response of silicon solar cells. The optimized QD-LSCs showed an optical quantum efficiency of 37% and an internal concentration factor of 4.7 for a 10×10 cm^2 device area under solar illumination, which is comparable with the state-of-the-art LSCs based on cadmium-containing QDs and lead-containing perovskites. Synthesis of the copper-doped InP/ZnSe QDs in gram-scale and large-area deposition (3000 cm^2) onto commercial window glasses via doctor-blade technique showed their scalability for mass production. In the second section, we report LSCs based on cadmium-free InP/ZnO core/shell QDs with type-II band alignment that allow for the suppression of reabsorption by Stokes-shift engineering. The spectral emission and absorption overlap was controlled by the growth of a ZnO shell on an InP core. At the same time, the ZnO layer also facilitates the photostability of the QDs within the host matrix. We analyzed the optical performance of indium-based LSCs and identified the optical efficiency as 1.45%. In the third section, we synthesized mScarlet fluorescent proteins, which is the brightest protein with the PLQY of 61% in red spectral region that matches well with the spectral response of silicon solar cells and integrated fluorescent proteins in an aqueous medium into solar concentrators, which preserved their quantum efficiency in LSCs and separated luminescence and wave-guiding regions due to refractive index contrast for efficient energy harvesting. Solar concentrators based on mScarlet fluorescent proteins achieved an optical efficiency of 2.64%, and the integration at high concentrations increased their efficiency approaching to 5%. In the last section of this part, alloyed green-emitting CdSe@ZnS QDs, which were incorporated into a PDMS waveguide, were synthetically engineered to match their photoluminescence spectra with the photo-response of P3HT:$PC_{61}BM$ solar cells. QDs maintained high in-film PLQY of 64% that led to an optical quantum efficiency of 44.7%. The fabricated LSCs can generate sufficient power for the active radio frequency identification (RFID) tags to send signals in the communication distance of 35 meters at low power levels of 0.1-sun and ~0.1 km under 1-sun conditions, respectively.

This research work led to the successful demonstration of highly efficient QD- and FP-LEDs, which can pave the way towards efficient and zero-waste lighting. Moreover, the demonstrated QD- and FP-based LSCs in this thesis can be directly integrated inside the buildings and cars as the ecofriendly and efficient sunlight energy harvesting solutions.

ÖZETÇE

Yeni Kuantum Nokta ve Floresan Protein Tabanlı Sıvı Işık Yayan Diyotlar ve Lüminesans Güneş Konsantratörleri

Doktora tezi

Sadra Sadeghi
Malzeme Bilimi ve Mühendisliği Doktora
Tez Yöneticisi: Doç. Dr. Sedat Nizamoğlu
Temmuz 2020

Son otuz yılda floresan nanomalzemeler, boyuta bağlı optik özellikleri ve buna bağlı olan yüksek fotolüminesans kuantum verimi (PLQY), kuantum hapsetme etkisi ve malzeme kompozisyonu yoluyla ayarlanabilir elektronik özellikler gibi nedenlerle önemli ilgi görmüştür. Bunlar arasında, kolloidal kuantum noktaları (QD) ve floresan proteinleri (FP), ışık yayan diyotlar (LED), ışıklı güneş konsantratör (LSC) ve güneş pilleri gibi aydınlatma, ggörüntü ve enerji depolama uygulamalarında yaygın olarak kullanılmaktadır.

Bu tezde, QD'lere ve floresan proteinlerine dayanan yüksek performanslı ve biyouyumlu ışık yayan diyotlar ve ışıklı güneş konsantratörgösterilmiştir.

Şimdiye kadar, nanomateryal tabanlı renk dönüşüm LED'lerde verimli aydınlatma için ana yaklaşım nanomalzemelerin PLQY'sini arttırmaktır. Bununla birlikte, yüzdeyüz PLQY’e sahip floroforlarla bile, ana malzeme etkisi diye bilinen nedenden (katı halindeki PLQY’ın sıvı halindekinden daha düşük olması) dolayı, verimli katı hal aydınlatma kaynakları için kullanımları bir sorun olmaya devam etmektedir. Bu tezin ilk bölümünde, QD ve FP-LED'lerin optik performansını artıran yeni bir sıvı entegrasyon mimarisi tasarlıyor, geliştiriyor ve sergiliyoruz. İlk bölümde, yeşil yayan % 84 PLQY’e sahip CdSe // ZnS / CdSZnS QD'leri sentezledik, sonrasında QD'leri sıvı halde doğrudan QD’ye uygun olan yeni bir mimari kullanarak mavi LED kalıbına entegre edip mavi LED’ın üstüne ettik. Sıvı hal entegrasyonu ve PLQY'nin optimizasyonu ile bugüne kadar raporlanmış en verimli QD tabanlı LED'leri ürettik (RGB (Kırmızı, Yeşil, Mavi) için 64 lm/W ve Yeşil-Mavi tabanlı beyaz ışıyan için 105 lm/W for GB-based white light.) İkinci bölümde, yüksek performanslı beyaz LED'ler için kırmızı yayan mScarlet ve yeşil yayan eGFP floresan proteinleri kullandık. Bu proteinler canlı Escherichia coli'den yapılmak da olup ve saflaştırılmış proteinleri doğal sulu ortamlarında mavi LED çiplerine entegre

ettik. Sulu entegrasyon, cihaz mimarisinde proteinlerin PLQY seviyelerini% 70'in üzerinde korudu ve rapor edilen en verimli çevre dostu beyaz LED olan 83 renk işleme indeksi (CRI) ile 81 lm / W'lık yüksek bir ışık verimliliği sağladı. Dahası, kırmızı ve yeşil yayan proteinlerin konsantrasyon oranını optimize ettik ve maksimum 92 CRI değerine sahip beyaz protein bazlı LED'ler ürettik. Üçüncü bölümde, sihirli boyutlu (Magic-sized) CdSe QD'lerin PLQY'sini% 22'ye kadar optimize ettik. Bu esnada, sentez parametrelerini optimize ettik ve hiçbir kabuklama işlemi veya sentez sonrası işlem uygulamadan mavi LED üzerinde sıvı halde entegre ettik. Üretilen beyaz LED'ler sırasıyla 89 ve 11,7 lm/W'a kadar CRI ve ışık verimliliği gösterdi. Dördüncü bölümde, 95 lümen lm/W ışık verimliliği seviyesinde, 395 lm/W optik radyasyonun (LER) ışık etkinliği ve % 23.3 harici kuantum verimliliği (EQE) ile çalışan yeşil spektral bölgede ışıyan QD-LED'leri gösterdik. Bunun için, 1-oktanetiol başlıklı CdSe@ZnS QD'leri% 91 PLQY ile sentezledik ve bunları cihaz mimarisinde QD verimliliğinin korunmasına izin veren sıvı matrise entegre ettik. Son olarak, sırasıyla% 52 ve% 74 PLQY ile kırmızı ve yeşil yayan kadmiyum bazlı QD'leri sentezledik ve sentezlenen QD'leri doctor-blade tekniğini kullanarak polidimetilsiloksan (PDMS) polimer matrisine dahil ettik ve akıllı telefon ekranları için 123 mm × 68 mm boyutlarında polimerik filmler. Mavi yayan arka ışık ünitesinde geniş alan QD-polimerik filmler kullanılarak NTSC ve sRGB renk gamı oranı sırasıyla% 91 ve% 127 olarak ölçülmüştür.

Bu tezin ikinci bölümünde, yeni InP tabanlı QD'lere dayanan LSC'ler tasarlıyor, üretiyor, ve güneş ışığında enerji depolayan floresan proteinin sıvı entegrasyonunu sağlayan yenilikçi bir mimari geliştirdik. İlk bölümde, çinko karboksilat ile pasifleştirilmiş InP çekirdeğinin bakır ile doplanmasını ve ZnSe ile kabuklanmasını gösterdik, bu nanomühendislik işlemi QD'lerin% 80'in üzerinde yüksek cihaz-içi kuantum verimliliğini sağladı. Optimize edilmiş QD-LSC'ler, güneş aydınlatması altında 10 × 10 cm^2'lik bir cihaz alanı için% 37'lik bir optik kuantum verimi ve 4.7'lik bir iç konsantrasyon faktörü gösterdi; bu sonuçlar, en verimli kadmiyum içeren veya kurşun içeren perovskitler LSC'lerle karşılaştırılabilir. Bakır katkılı InP/ZnSe QD'lerin gram ölçekli sentezi ve doctor-blade tekniği ile geniş alanlı (3000 cm2) ticari pencere camları üzerine kaplanması, seri üretim için ölçeklenebilirlik göstermiştir. İkinci bölümde, Stokes-shift mühendisliği ile yeniden emilimin (reabsorption) bastırılmasına imkan sağlayan tip-II bant hizalamalı kadmiyumsuz InP/ZnO çekirdek/kabuk QD'lerine dayanan LSC'leri rapor ediyoruz. Spektral emisyon ve emilim çakışması, ZnO kabuğunun InP çekirdeği üzerinde büyümesi ile kontrol edildi. Aynı zamanda ZnO katmanı, ana matris içindeki QD'lerin fotostabilitesini de kolaylaştırır. İndiyum bazlı LSC'lerin optik performansını analiz ettik ve optik verimliliği % 1.45 olarak belirledik. Üçüncü bölümde, silikon güneş pillerinin ve entegre flüoresan proteinlerin sulu bir ortamdaki spektral tepkisi ile iyi eşleşen kırmızı spektral bölgede % 61 PLQY ile en parlak protein olan mScarlet floresan proteinlerini sentezledik. MScarlet floresan proteinlerine dayanan güneş konsantratörleri, % 2.64'lük bir optik verimlilik elde etti ve yüksek konsantrasyonlardaki entegrasyon, verimliliklerini% 5'e kadar yaklaştırarak arttırdı. Son bölümde, bir PDMS dalga kılavuzuna dahil edilen alaşımlı yeşil yayan CdSe@ZnS QD'leri, fotolüminesans spektrumlarını P3HT: PC61BM güneş pillerinin foto-yanıtıyla eşleştirmek için sentetik olarak tasarlanmıştır. QD'ler %64'lük yüksek film-içi PLQY'yi korudu, bu da %44.7'lik bir optik kuantum verimliliğine yol açtı. Üretilen LSC'ler, aktif radyo frekansı tanımlama (RFID) etiketlerinin, 1-güneş koşulları altında sırasıyla 0.1-güneş ve ~ 0.1 km'lik düşük güç seviyelerinde 35 metre iletişim mesafesinde sinyal göndermesi için yeterli güç üretebilir.

Bu araştırma çalışması, verimli aydınlatmasına yol açabilecek yüksek verimli QD- ve FP-LED'lerin başarılı bir şekilde gösterilmesine yol açtı. Ayrıca, bu tezde gösterilen QD ve FP tabanlı LSC'ler, çevre dostu ve verimli güneş ışığı enerji depolama çözümleri olarak doğrudan binaların ve araçların içine entegre edilebilir.

ACKNOWLEDGMENTS

My PhD studies in Koç University was accompanied with many stories both beautiful and sad. I had the opportunity to obtain the knowledge from the elite scientists around the world and I was lucky enough to work with many talented and intelligent people in a productive and fun environment. My family members, advisors, professors, colleagues and friends each had their unique and undeniable impact on the thesis in your hand.

At first, my sincere gratitude goes to Prof. Sedat Nizamoğlu for being not only my advisor and mentor but at the same time a great and caring elder brother. It was and always will be my great honor to be one of his first PhD students. His superior knowledge, great patience and understanding, positive and friendly character, invaluable guidance, limitless motivation and encouragement, and endless support always pushed me towards more success and recognition. I will never forget our scientific discussions and his endless efforts to improve our academic levels and also to strengthen our personalities. I learnt so much from him and I owe him many thanks.

I would like to sincerely thank my brilliant wife Saeedeh, who made these five years of PhD look so much easier with her endless kindness, tolerance, trust, consideration and love. She has stood by me through all my travails, my absences, my fits of pique and impatience. She gave me support and help, discussed ideas and prevented several wrong turns. Her strong character and dedication has enabled us both to pursue our dreams as PhD students and has enlighten our path towards a bright future. I would never be able to completely thank her and this story could not be finished without her.

My appreciation also extends to my beloved parents, who sadly passed away during my PhD studies. I am always inspired by them and I will miss their endless support through my whole life forever. This thesis is dedicated to their souls and I hope they will be happy together forever.

I would like to thank Prof. Erdem Alaca and Prof. Uğur Ünal for helpful scientific discussions as my thesis committee members and also for the invaluable knowledge, which I obtained from the courses that I had with them. I would like to also thank Prof. Şenol Mutlu and Prof. Onur Ferhanoğlu for giving me the honor to be my thesis committee members and helpful suggestions and useful comments for improving the thesis.

I would like to sincerely thank Prof. Aplhan Sennaroğlu and Dr. Işınsu Baylam for their scientific contributions and helpful discussions, which led to the publication of one my best studies in PhD. My appreciation also goes to Prof. Elif Nur Firat-Karalar and Dr. Deniz Conkar for their great and tireless efforts to synthesize the fluorescent proteins. I would like to thank Prof. Cleva W. Ow-Yang and her PhD student Sirous Khabbaz Abkenar for their endless efforts to characterize our nanomaterials and their great patience and meticulous vision for improving our manuscripts. I sincerely thank Prof. Funda Acar Yağcı, Prof. İsmail Lazoğlu, Prof. Erkan Şenses, Prof. Hakan Ürey, Prof. Umut Aydemir, Prof. İskender Yılgör, Prof. Emel Yılgör and Mr. Muzaffer Bütün for their kind support and collaborations. My appreciation also goes to Dr. Barış Yağcı, Dr. Cansu Yıldırım, Dr. Ceren Yılmaz Akkaya, Dr. Mahsa Barzgar Vishlaghi, Dr. Amir Motallebzadeh and all of the members in Koç University Surface Science and Technology Center (KUYTAM) and Koç University TÜPRAŞ Energy Research Center (KUTEM), who significantly helped us for our measurements and characterizations.

I would like to appreciate my former lab-mate and mentor Dr. Bakaran Ganesh Kumar, who made me interested in chemistry and taught me invaluable knowledge about the materials and synthesis. My appreciation also extends to my current lab-mates and colleagues Houman Bahmani Jalali and Rustamzhon Melikov, who collaborated with me for publishing many high quality papers. I would like to thank all of the former and current colleagues specially, Dr. Shashi Bhushan Srivastava, Mr. Onuralp Karatüm, Mr. Mertcan Han, Mr. Guncem Ozgun Eren and Mr. Asım Onal for their efforts and contributions during these five years. I would like to thank Mr. Efdal Mutcu, Dr. Güneş Aydındoğan and their great R&D team in VESTEL Company for their tireless efforts and collaborating on an exciting project about cellphones. I owe many thanks to the professors, researchers, students and staff in the Graduate school of Materials Science and Engineering, Department of Biomedical Engineering, Department of Electrical and Electronics Engineering and Department of Mechanical Engineering in Koç University.

Finally, I would like to acknowledge the generous support from the Scientific and Technological Research Council of Turkey (TUBITAK) (115E115, 115E242, 114F317, 115F451, 114E194, 117E177, 118E357, and 3160189), European Research Council (ERC) under the European Union's Horizon 2020 Research and Innovation Programme (Grant agreement no. 639846), Marie Curie Career Integration Grant (PROTEINLED, 631679), and Turkish Academy of Sciences (GEBIP).

TABLE OF CONTENTS

LIST OF TABLES

LIST OF FIGURES

ABBREVIATIONS

QD	Quantum dots
QY	Quantum yield
LED	Light-emitting diode
LE	Luminous efficiency
LER	Luminous efficacy of radiation
EQE	External quantum efficiency
PDMS	Polydimethylsiloxane
PCE	Power conversion efficiency
SSL	Solid-state lighting
RGB	Red, Green, Blue
GB	Green, Blue
QE	Quantum efficiency
PL	Photoluminescence
EL	Electroluminescence
LQD-LED	Liquid light-emitting diode
FWHM	Full width at half maximum
CRI	Color rendering index
LCD	Liquid crystal display
FP	Fluorescent protein
PLED	Protein-based light-emitting diode
CIE	Commission on illumination
CCT	Correlated color temperature
CQS	Color quality scale
TEM	Transmission electron microscopy
HRTEM	High resolution transmission electron microscopy
SEM-EDAX	Scanning electron microscopy-Energy dispersive x-ray
XRD	X-ray diffraction
InGaN	Indium Gallium Nitride

CRT	Cathode ray tube
TFT	Thin film transistor
BLU	Backlight unit
PET	Polyethylene terephthalate
NTSC	National Television Standards Committee
LSC	Luminescent solar concentrator
OQE	Optical quantum efficiency
ML	Monolayer
SILAR	Successive ionic layer adsorption and reaction
TRPL	Time-resolved photoluminescence
Si-PV	Silicon-based photovoltaic
FTIR	Fourier transform infrared spectroscopy
TCSPC	Time-correlated single-photon counting
IoT	Internet of things
RFID	Radio frequency identification
WSN	Wireless sensor networks
FF	Fill factor
XPS	X-ray photoelectron spectroscopy

Chapter 1

INTRODUCTION

Efficient solid-state lighting (SSL) offers significant potential to save the energy and to protect the environment [1]. If light-emitting diodes (LEDs) at the targeted efficiency levels are replaced with conventional lighting sources, the global electricity that is consumed for lighting would be decreased by more than 50%, which is equal to the reduction of either 230 typical 500-MW coal plants or 200 million tons of greenhouse gas emission [1, 2]. During the last two decades, LEDs have revolutionized the lighting industry by exposing themselves as a fitting alternative to old-fashion light sources such as incandescent light bulbs and fluorescent lamps due to their high efficiency, long lifetime and small size [3-6]. In addition to the improvement of the external quantum efficiency of blue LEDs, the studies were mainly concentrated on the performance improvement of the white LEDs for outdoor, indoor and display applications [7, 8]. For that, different types of doped phosphorous were investigated as the wavelength converters to obtain efficient white light generation [9, 10]. Despite the efficiency of the phosphorous, there are concerns on their ecology risks, sustainability and toxic effects [11]. Moreover, the color quality of the generated light from phosphor-based down converters remained low due to the lack of tunability and large emission bandwidth, which decreases the efficiency at near infrared wavelength range. As a result, the quest for finding nanomaterials, which simultaneously satisfy efficiency, color quality and the biocompatibility of the color conversion LEDs is still continuing.

Semi-transparent luminescent solar concentrators (LSCs) are novel class of nanomaterial based optoelectronic devices, which offer simple and cost-effective solar energy harvesting solutions to boost the solar energy contribution to global electricity production. LSCs are made of fluorescent materials embedded inside transparent optical waveguides. Fluorescent materials absorb the incoming solar radiation impinging on a large area, convert it to longer-wavelength radiation and the down-converted light is then guided to the small-area solar cells placed at the edges of the waveguide. The concentration of light by luminescence leads to a significant increase of energy production for the same area of solar cells [12-15]. Therefore, this approach provides a practical energy harvesting solution that can be broadly used as ‘solar windows’ in buildings, vehicles and roofs. For its wide-spread use, LSC technology needs to be transformed such that it can simultaneously satisfy efficiency, biocompatibility, and feasibility for large-volume production. So far, different types of nanomaterials have been used inside the LSC architectures for efficient solar energy harvesting such as organic dyes [16], fluorescent proteins [17], lanthanide-based materials [18] and perovskites [19].

Colloidal quantum dots (QDs) have attracted significant attention for numerous optoelectronic applications due to high photoluminescence quantum yield, narrow emission bandwidth and tunable emission [20-26]. Since the first QD synthesis by Brus and co-workers in 1983 [27], they have been extensively used in different applications such as biology, photovoltaic devices, LEDs, displays, photodetectors, photo-catalysis, neural photo-stimulation, lasers, energy harvesting devices, imaging, sensing, bio-labeling, field-effect transistors and energy transfer. Even though QDs have many advantageous features for LEDs and LSCs, the efficiencies that have been achieved so far were not at desired levels mainly due to host material effect and reabsorption [13, 28, 29]. In order to address the low efficiency of the QD-LEDs, one possible solution is the design and implementation of an architecture, in which the as-synthesized QDs can be directly integrated as efficient down-converters in QD-based LEDs. Moreover, to overcome the efficiency barrier in QD-LSCs, the optical properties of the QDs needs to be carefully tailored for increasing the Stokes-shift and decreasing the efficiency loss upon integration in the waveguide matrix.

Alternatively, fluorescent proteins offer excellent optical properties for optoelectronic applications including high photo-stability, narrow emission and high photoluminescence quantum yield in the visible range (, i.e. 400-700 nm). Different from the other color-conversion materials, they can be produced in a wide variety of living organisms such as bacteria, mammalian cells and vertebrates [30, 31]. These advantageous properties in terms of biocompatibility, edibility and optical properties make them a unique alternative for waste-less down-conversion material in LEDs and LSCs [32, 33].

This thesis demonstrates the application of QDs and fluorescent proteins in two different optoelectronic devices: i) light-emitting devices (LEDs), ii) luminescent solar concentrators (LSCs). The organization of the thesis is as follows:

In the first chapter, we make a general introduction about light-emitting diodes, luminescent solar concentrators, colloidal QDs, fluorescent proteins and their applications in nanomaterial-based LEDs and LSCs.

In the second chapter, we provide the basic background knowledge about QDs, their synthesis procedures, optical and structural properties, QD-based light-emitting diodes, fluorescent proteins and FP-based light-emitting diodes, QD-based luminescent solar concentrators and the corresponding working mechanisms, optical analysis and measurement techniques for each of the nanomaterial-based LEDs and LSCs.

In the third chapter, we focus on our studies about nanomaterial-based LEDs including the highly efficient liquid white QD-based LEDs based on red- and green-emitting cadmium-based QDs, the most efficient ecofriendly white LEDs based on fluorescent proteins, the efficient liquid white QD-LEDs based on magic-size cadmium-based QDs, the highly efficient green QD-LEDs based on liquid-integration of cadmium-based QDs and high quality QD polymeric films based on red- and green-emitting cadmium-based QDs for smart phone applications.

In the fourth chapter, we discuss our studies about novel nanomaterial-based LSCs including the demonstration of highly efficient QD-LSCs based on copper-doped InP QDs, the first time synthesis and demonstration of efficient QD-LSCs based on InP/ZnO QDs, the demonstration of liquid LSCs based on fluorescent proteins and the integration of organic solar cells and LSCs for 'Internet of Things' applications.

In the fifth chapter, we conclude our thesis by describing and remarking our achievements.

Chapter 2

SCIENTIFIC BACKGROUND

2.1 Quantum dots

Colloidal semiconductor quantum dots (QDs) are nanomaterials in the range of 1-10 nanometers, which possess the crystal structure similar to the bulk semiconductor crystals. Nanocrystals can be composed of periodic groups of II-VI, III-V, or IV-VI materials. An exciton Bohr radius is the distance in an electron-hole pair. A QD is so small that the size of the crystal is on the same order as the size of the exciton Bohr radius (e.g., the exciton Bohr radius of InP QDs ~ 10 nm). This unique size property causes the "band" of energies to turn into discrete energy levels, which is called as 'quantum confinement' (Figure 2.1a). 'Quantum confinement' is the main reason for the size-dependent optical properties of QDs.

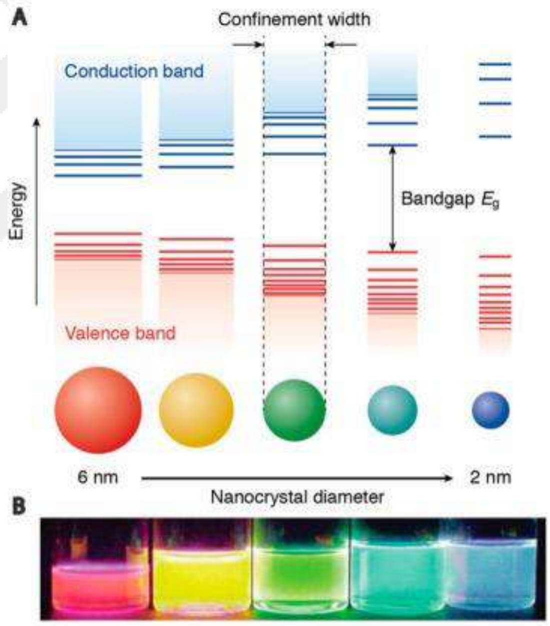

Figure 2.1: (a) The schematic representation of quantum confinement effect in semiconductor nanocrystals. (b) The size-dependent emission of the nanocrystals under UV illumination [34].

The size-dependent optical properties of QDs have motivated the increasingly active research in different areas of next-generation optoelectronic and biomedical applications. Since the first QD synthesis by Brus and co-workers in 1983 [27], they have been extensively used in different applications such as biology, photovoltaic devices, light-emitting diodes (LEDs), displays, photodetectors, photo-catalysis, neural photo-stimulation, lasers, energy harvesting devices, imaging, sensing, bio-labeling, field-effect transistors and energy transfer.

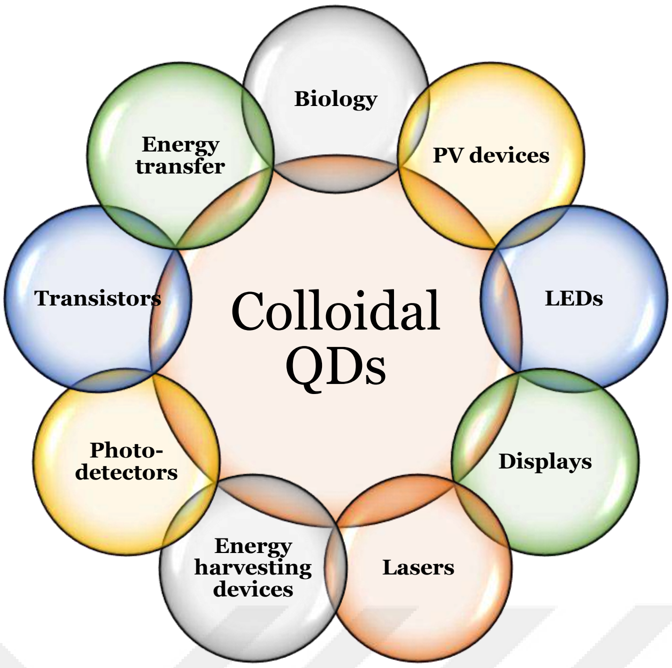

Figure 2.2: Different applications of colloidal QDs.

2.1.1 Synthesis of colloidal QDs

Different synthesis procedures have been developed in order to synthesize QDs with various size, shape and chemical compositions. In recent decades, wet chemistry methods have been investigated to synthesize mono-disperse QDs in large-scale, which is preferable comparing to the high-cost physical techniques. The major solution-processing techniques in order to synthesize QDs include hot-injection method, heat-up method, co-precipitation approach, over-coating by SILAR method and cation exchange.

Hot-injection method

Hot injection is a well-studied and most commonly used approach to synthesize high quality QDs with narrow emission bandwidth. Typically, one of the precursors is heated up to a certain temperature. At this temperature, the other precursor was injected inside the reaction flask, upon which the nucleation of seeds will start and be followed by the growth to QDs. The obtained QDs in this approach usually exhibit monodispersity, narrow size distribution, relatively high QY and chemical/photo-stability (Figure 2.3). This method is extensively used for the synthesis of cadmium- and indium-based QDs.

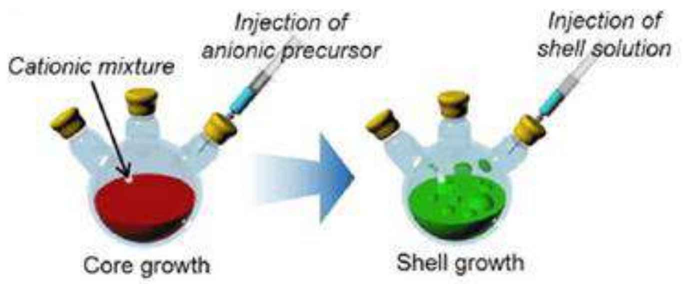

Figure 2.3: The schematic representation of the hot-injection method for the synthesis of core/shell QDs [35].

Heat-up method

Heat-up technique is another method to produce nanocrystals. Comparing to hot-injection method, in heat-up technique precursors are prepared and mixed in a flask before the solution is increased to controllably high temperature where eventually the nanocrystal formation takes place. The heat up method is specifically useful for large-scale production of QDs. The size of the QDs can be increased by increasing the reaction time, thus providing an easy control on the size and dispersity (Figure 2.4).

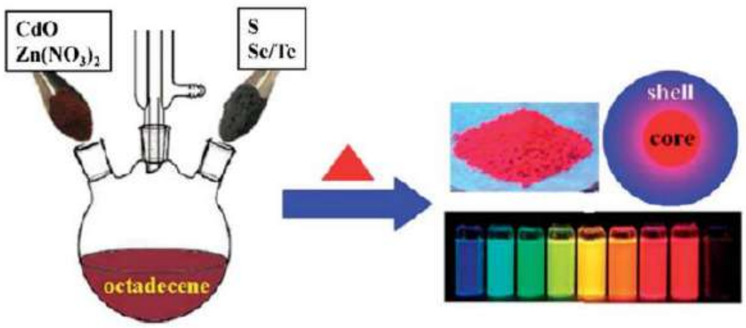

Figure 2.4: The schematic representation of the heat-up method for the synthesis of Cd-based core/shell QDs. The large-scale synthesis and the size-tunability is achieved by this method [36].

Co-precipitation approach

The co-precipitation approach has been used to synthesize ternary I–III–VI_2 semiconductors. For example, CuInSeS QDs were synthesized using Cu and In ionic precursors. In comparison with hot-injection method, the size distribution of the QDs synthesized by co-precipitation is much wider due to the continuous nucleation and growth.

SILAR method

Core/shell QDs have most commonly been synthesized either through a successive ionic layer adsorption reaction (SILAR) approach or a cation exchange approach (Figure 2.5). In this process, cation and anion precursors are cyclically added into the core mixture in sequence for the layer by layer shell growth. The shell thickness can be precisely controlled by varying the amounts of precursors. The most important advantage of the core-thick shell QDs synthesized by this method is their excellent chemical/photo-stability. However, their QY is typically lower than core-thin shell structures.

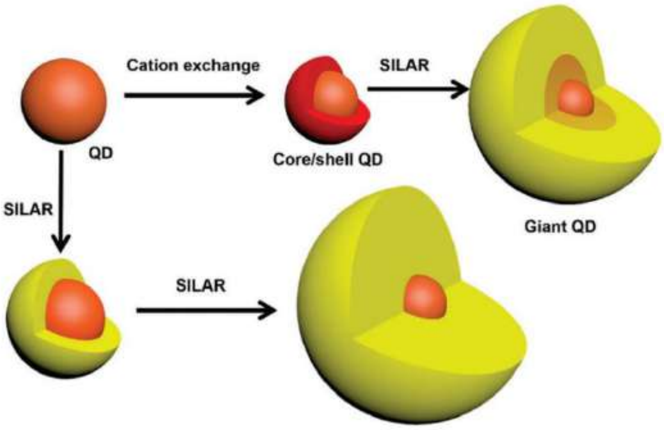

Figure 2.5: The schematic representation of the cation exchange and SILAR method to synthesize core/shell QDs [37].

Cation exchange

Cation exchange method is especially useful when the core and shell compounds crystal structures have rather large lattice mismatch, which induces the defects in the core/shell structure and significantly deteriorates the optical properties of the QDs. In contrast with the SILAR method, the size of the core varies in different steps of the cation exchange procedure. This method has been used for different core/shell structures such as PbS/CdS, CISeS/ZnS and CISeS/CdS QDs.

2.1.2 The structural properties of QDs

As mentioned in the last section, QDs are semiconductor nanocrystals typically with a core/shell structure and a diameter that typically ranges from 1 to 10 nm. The core of QDs is usually composed of elements from groups II–VI such as CdSe, CdS or CdTe, groups III–V such as InP or InAs, or groups IV–VI such as PbSe. Based on the synthesis conditions, precursors and reaction kinetics, QDs can nucleate and grow in different types of crystal structures such as zinc blende (InP, CdSe and most of III–V group), wurtzite (ZnS and CdS), and perovskite crystal structures (Figure 2.6).

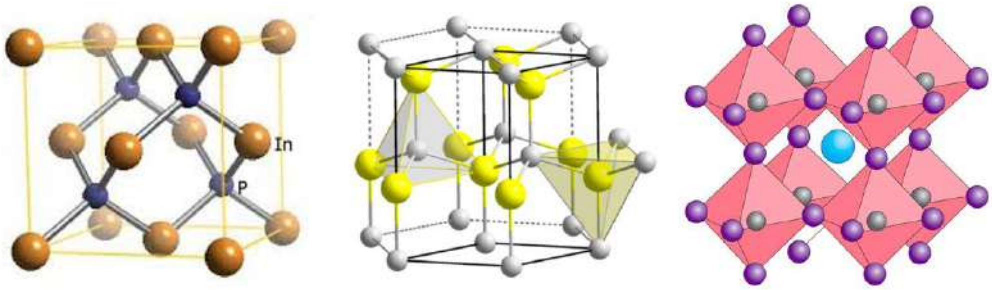

Figure 2.6: Different crystal structures of QDs. (Left) zinc blende crystal structure of InP QDs, (middle) wurtzite crystal structure of CdSe QDs, and (right) perovskite crystal structure [38].

Based on the crystalline nature of the QDs, different techniques can be used in order to structurally characterize the synthesized QDs such as transmission electron microscopy (TEM), High-resolution transmission electron microscopy (HRTEM), X-ray diffraction (XRD), scanning electron microscopy-energy dispersive X-ray (SEM-EDAX), X-ray photoelectron spectroscopy (XPS), Atomic force microscopy (AFM), inductively coupled plasma-atomic emission spectroscopy (ICP-AES), Scanning transmission electron microscopy (STEM), Nuclear magnetic resonance (NMR), and High-angle annular dark-field scanning transmission electron microscopy (HAADF-STEM). A typical HRTEM image and electron diffraction mapping of InP/ZnSe/ZnS are shown in Figures 2.7 and 2.8.

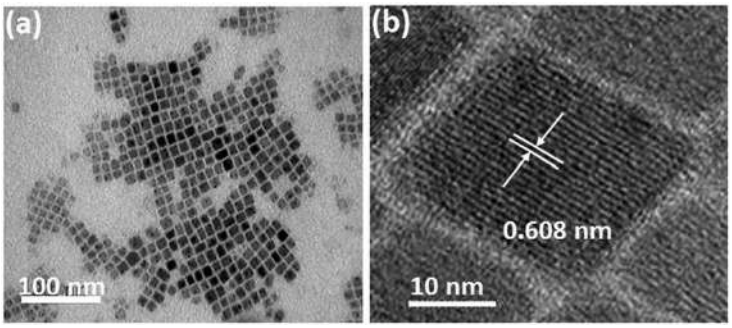

Figure 2.7: (a) The TEM image and (b) The high-resolution TEM image of perovskite QDs [39]. The lattice constant has been calculated and shown in (b).

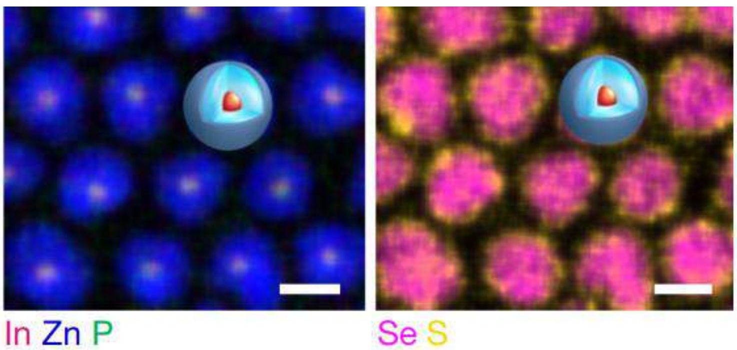

Figure 2.8: Electron diffraction spectroscopy mapping of In, Zn, P, Se and S for InP/ZnSe/ZnS QDs (scale bar, 10 nm) [40].

2.1.3 The optical properties of QDs

Absorbance and photoluminescence (PL)

Numerous factors can determine the optical properties of QDs such as size distribution, shape, structure and material composition. Once QDs are being illuminated with a high-energy photon, the electron will be excited from ground state to excited state. Upon relaxation, the electron will lose its energy in the form of photon. Due to the specific width of the bandgap in QDs, the wavelength of this photon can be positioned in the visible portion of the light spectrum (Figure 2.9). In other words, the energy needed to overcome the bandgap is inversely proportional to wavelength of the fluorescence emitted (the color of light). This means that the larger the QD, the smaller is the bandgap energy, and therefore its fluorescence emission is shifted toward the red region of the visible spectrum. In general, their optical properties in terms of fluorescence are strongly dependent upon their size and therefore, can be tailored for specific applications.

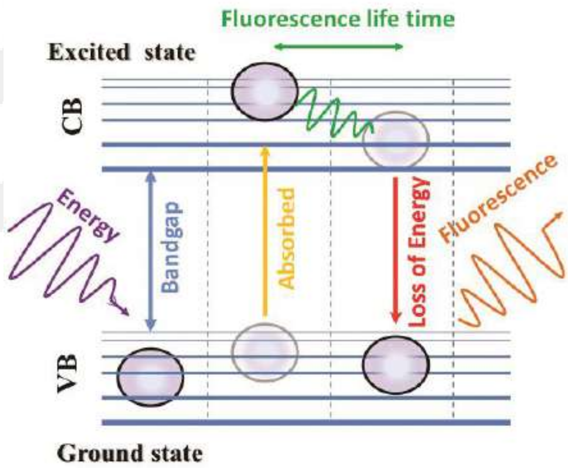

Figure 2.9: The electronic structure of QDs and the absorption and emission of light mechanism. CB stands for conduction band, VB for valence band [41].

The main important optical properties of the QDs are absorbance, photoluminescence (PL) and photoluminescence quantum yield (PLQY). In order to further realize the QDs and their optical properties, other optical features such as reabsorption (i.e., Stokes-shift), fluorescence lifetime decay, quantum efficiency (QE) of QDs inside the matrix and ultrafast decay times can be employed. Due to the size-dependent optical properties, the band gap of the QDs can also be measured and used for accurate prediction of emission behavior. In absorption measurements, photons are absorbed inside the QD by electron-hole pair “exciton” excitation. In PL measurements, an exciton created by laser excitation from and external light source recombines inside the QD, whereby a photon is emitted, which is measured [42]. A typical absorbance and emission profile of the QDs have been demonstrated in Figure 2.10.

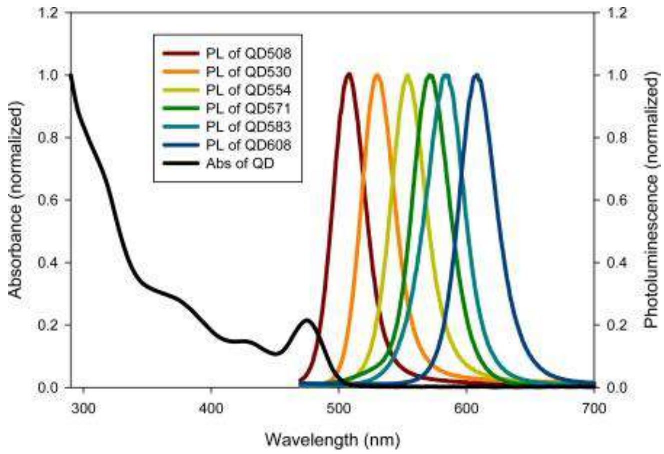

Figure 2.10: The normalized absorbance and PL spectra of typical CdTe QDs synthesized with different reaction times [43]. .

The photoluminescence quantum yield (PLQY)

An essential performance metric is the photoluminescence quantum yield (PLQY), which is determined by the competition between radiative relaxation of the excited material and nonradiative losses, typically due to defects. The PLQY is directly related to the electronic and structural quality of QDs, with the highest values recorded to date of 99.5 and 99.7%, respectively, in rare earth– doped high-bandgap single crystals and epitaxially deposited thin films [44]. PLQY can be measured by non-direct method, in which the PLQY of the QDs will be measured by comparison of emission intensity with a standard dye (such as Rhodamine B or Rhodamine 6G) or direct method, in which the absolute PLQY will be measured.

The Stokes-shift

The Stokes-shift of the QDs is measured by the difference between the peak of the absorption shoulder and the PL (Figure 2.11). The Stokes-shift is an important optical parameter for optoelectronic devices, which defines the optical losses in the fluorescent material. The higher the Stokes-shift (lower the reabsorption), the lower optical losses in the device, which leads to the improved optical performances. The Stokes-shift can be calculated based on the wavelength difference between the peak of absorption and emission spectra as $\Delta\lambda = \lambda_f^{max} - \lambda_a^{max}$ (Figure 2.11) and the Stokes-shift energy is calculated based on Equation (2.1).

$$\Delta E = h\Delta\nu = hc\,\left(\frac{1}{\lambda_f^{max}} - \frac{1}{\lambda_a^{max}}\right) \tag{2.1}$$

In the case of QDs, the absorption peak is considered as the first excitonic peak (absorption shoulder).

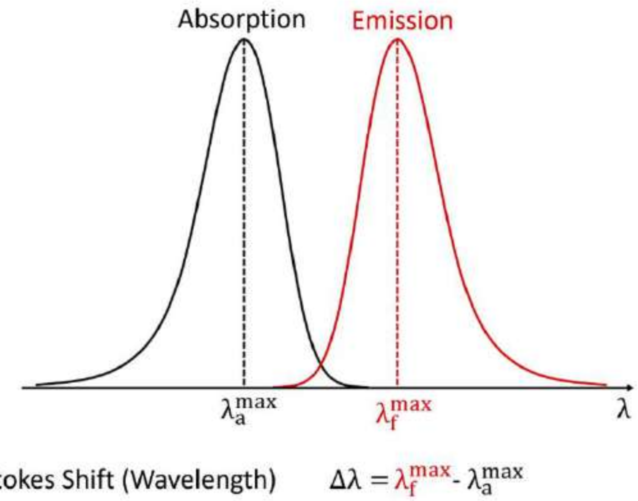

Figure 2.11: The representation of Stokes-shift and its calculation method.

The band alignment in core/shell QDs

It is believed that QDs are more stable than organic semiconductors in terms of photo-bleaching and oxidation [45]. Inorganic shell compounds improve the stability of QDs considerably owing to passivation of surface defects and also prevention of oxygen diffusion into the core [46].

Based on the type of the materials being used in core/shell structures, there are three main type of band-alignments in QDs:

i) Type-I: In this type of QDs, core is surrounded with a larger band gap shell. Both electron and hole wave-functions reside in the core as electron and hole energy is lower there. Type-I QDs are the most used QDs in LED applications mainly due to their high PLQY, strong confinement of electron and hole, and narrow emission spectra.

ii) Quasi-Type-II: Similar to type-I structure, both electron and hole are confined in the core because of larger band gap shell, however, one of the charge carriers tends to delocalize to the shells due to the similar energy levels between core and shell conduction band or valence band. In quasi-type-II structures, radiative lifetimes are longer compared to type-I structures as the electron-hole wave-function overlap is lower, which means they can be separated more easily. This feature will be observed as large Stokes-shift in quasi-Type II band alignments.

iii) Type-II: In this configuration, one charge carrier is confined in the core, while the other one is confined in the shell. Electron and hole wave-functions slightly overlap. As in Figure 2.12, electrons have lower energy states in the conduction band of the shell, thus, the absorption occurs via core-shell transition of electrons. Similarly, since electrons reside in the shell, emission occurs via core-shell transition as well. That means absorption and emission energy get lower when core is covered with type-II aligned shell. Hence, type-II configuration causes a considerable red-shift in absorption and emission compared to core absorption/emission. As electron-hole wave-function overlap is very small in type-II configuration, it is easier to separate electron and hole, which makes them convenient for solar cell and photodetector applications.

The energy alignment of core/shell structure for type-I, quasi type-II and type-II QDs together with the electron and hole wave-functions are shown in Figure 2.12.

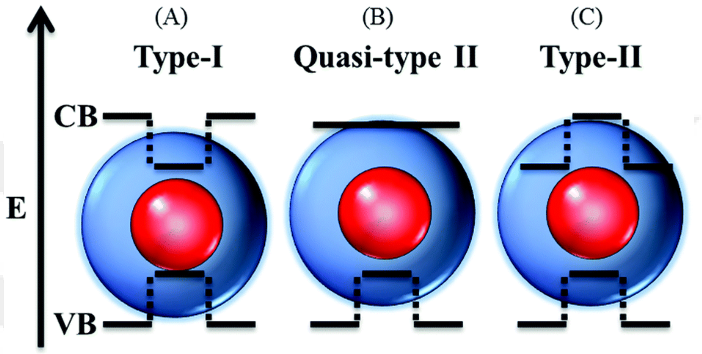

Figure 2.12: The different types of (a) Type I, (b) quasi-Type II and (c) Type II band-alignment in core/shell QDs [47].

2.2 *Light-emitting diodes (LEDs)*

Since the development of incandescent light bulbs in the late 1800s, various methods of producing white light more efficiently have been investigated. Of these, white-light sources based on light-emitting diodes (LEDs) look set to have a considerable impact on issues such as energy consumption, environment and even the health of individuals. A light-emitting diode is an electronic device integrating electrical access to the bandgap structure and allowing for efficient light generation [48]. The first generations of white light-emitting diodes were introduced by coating of YAG (Yttrium Aluminum Garnet) on the GaN (Gallium Nitride) blue LED chips (Figure 2.13). In 2014, Nakamura, Akasaki and Amano were awarded the Nobel Prize in Physics for the invention of blue light-emitting diodes, which provide bright and energy-efficient white light sources [49].

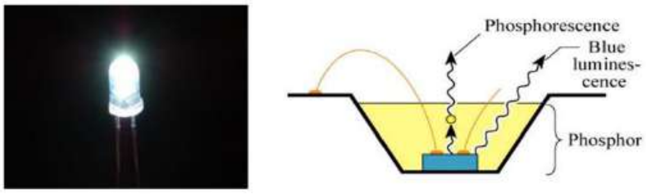

Figure 2.13: The white LED illumination when the forward current is applied. **(b)** The structure of the white LED, in which the blue LED chip is coated with YAG phosphor [50].

There are two main approaches for the light generation in nanocrystal based-LEDs in the literature. The first one is by electronically exciting the nanocrystals (i.e., electroluminescent LEDs), and the second is the light generation as a result of photoluminescence by optically exciting the nanocrystals (i.e., photoluminescent or color conversion LEDs) (Figure 2.14). The electroluminescent LEDs have limited lifetimes [51, 52]. Hence, the commercially available lighting and backlight technologies uses the photoluminescent LEDs. For this reason, we aim to solve the current technological and scientific efficiency problem of nanocrystal-based color conversion LEDs that use the second approach in our studies.

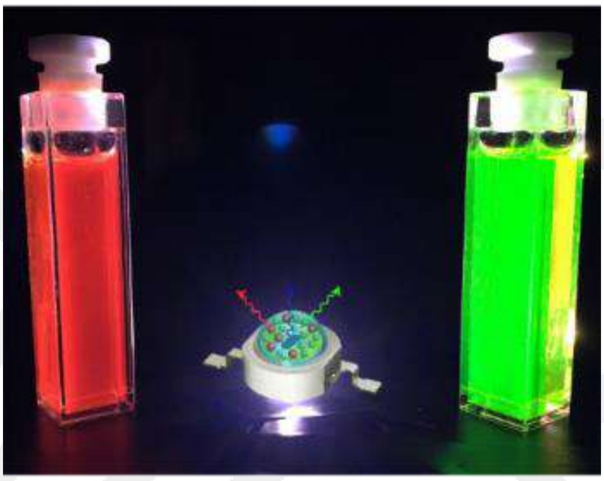

Figure 2.14: Cover image of our article on nanocrystal-based white LEDs published in Optica journal in 2018 [53], which demonstrates the QD-based color conversion LEDs based on the optical excitation of the green- and red-emitting QDs. The combination of red and green photoluminescence and blue electroluminescence will lead to the white light generation.

2.2.1 Quantum dot-based light-emitting diodes (QD-LEDs)

Since the fabrication of first QD-LEDs by Alivisatos and co-workers in 1994 based on CdSe QDs [54], colloidal QDs have attracted significant attention for efficient lighting due to high PL quantum yield, narrow emission bandwidth and tunable luminescence [20-26]. Conventional white LEDs, which comprise a blue inorganic LED backlight coated with a yellow phosphor as a down-conversion layer, typically exhibit a cool bluish emission that is characteristic of high CCTs (>5000 K) and low CRIs (mostly in the range of 80–85). For lower-CCT lights (for example, 2700 K) it is particularly difficult to maintain high luminous efficiency and high color quality simultaneously because the required red fluorophores must have relatively narrow emission to avoid photon loss as infrared emission [55]. The emission spectra of conventional red phosphors is unfortunately so wide (>60 nm FWHM) to avoid this loss (see Figure 2.15).

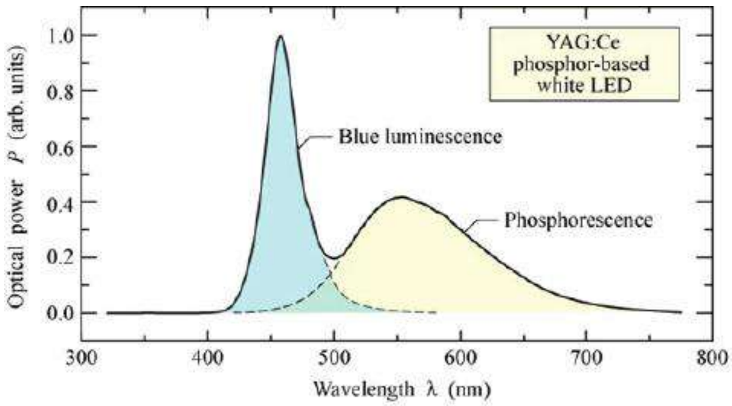

Figure 2.15: The intensity spectra of a typical phosphor-based white LED [56].

On the other hand, the narrow spectral emission (~30 nm FWHM) of the QDs (Figure 2.16) leads to a CRI of more than 90 and a superior CCT of 2700 K while maintaining a high luminous efficiency of more than 65 lm W^{-1} [55]. QDs therefore enable higher color quality and, accordingly, lower power consumption in solid-state lighting sources. Analogous approaches can also be utilized as backlights in high color quality LCDs.

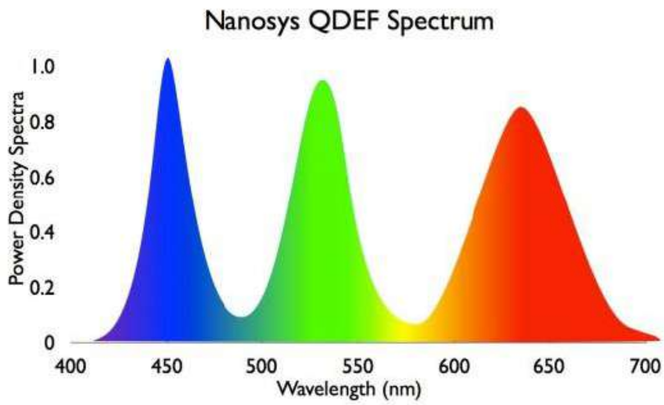

Figure 2.16: The intensity spectra of a QD-LED fabricated by Nanosys used in backlight displays. .

Even though QDs have many advantageous features for LEDs, the efficiencies that have been achieved so far were not at the same level of phosphor-based LEDs (with typical LE of more than 100 lm.W^{-1}) due to host material effect and reabsorption [13, 28, 29]. The report by Tsao has predicted that by 2020, the efficiency of the QD-LEDs needs to reach the level of 200 lumens per electrical watt [57]. To overcome the efficiency limitation, numerous approaches has been used such as giant shell growth on a core, recycling of trapped excitons via energy transfer and synthesizing near-unity emitting QDs [44]. However, the fabrication of these types of QD-LEDs is accompanied with the transformation of QDs from liquid- to solid-state, which drastically decrease the PLQY and color conversion ability and generates undesirable inhomogeneity due to coffee ring effect [58]. Therefore, design and implementation of an architecture, which facilitates the liquid-state integration of highly efficient QDs can generate a solution for the above-mentioned problems, leading to the high luminous efficiency of the light sources. In this regard, we used the liquid-state integration of synthesized QDs in order to achieve high efficiency light with different emission colors in our studies.

2.2.2 Fluorescent proteins

Fluorescent proteins are members of a structurally homologous class of proteins that share the unique property of being self-sufficient to form a visible wavelength chromophore from a sequence of amino acids within their own polypeptide sequence. Different kinds of fluorescent proteins with the emission inside the visible wavelength region have been synthetically produced during recent years (Figure 2.17).

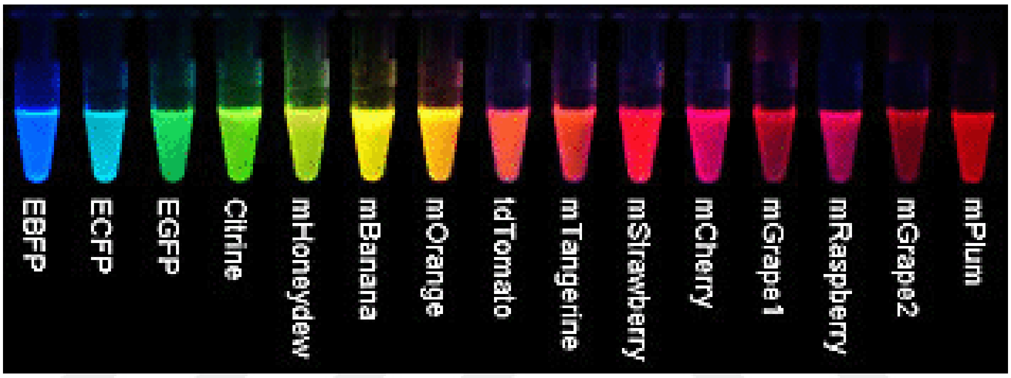

Figure 2.17: The different types of fluorescent proteins [59].

The main nanostructure of fluorescent proteins were designed and perfected by nature to efficiently operate in aqueous environments. Their structure consist of an central chromophore surrounded by a helix structure composed of β-sheets [60, 61]. The helix structure acts as a "bumper" and effectively protects the chromophore from the close contact between the neighboring molecules in aqueous environments, which can prevent the coupling of excitons to non-radiative centers and can decrease their QE (Figure 2.18). Based on the PLQY and emission wavelength, these proteins can be used in different optoelectronic applications. The major advantages of the fluorescent proteins is their fully biocompatible nature in comparison with QDs and other fluorescent materials.

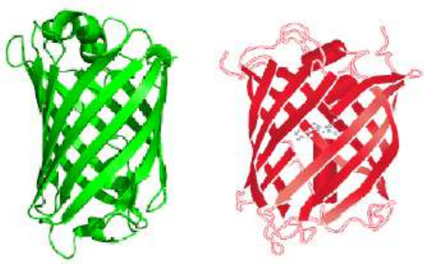

Figure 2.18: The schematic representation of green-emitting eGFP and red-emitting mScarlet fluorescent proteins.

Fluorescent protein-based LEDs (FP-LEDs)

Fluorescent proteins offer excellent optical properties for LEDs due to their biocompatibility and high PLQY in the visible range (, i.e. 400-700 nm). Moreover, they can be produced in a wide variety of living organisms [30, 31]. However, the efficiency and color-rendering performance of fluorescent protein-based white LEDs (FP-LEDs) are still low due to the fact that the fabrication process generally include the liquid- to solid-state transition, which significantly quenches the PLQY of the fluorescent material due to the introduction of non-radiative channels [13]. For example, blue-, green- and red-emitting protein coatings as color conversion layers led to the maximum LE of 15 lm/W [62]. Instead, the interaction between proteins and the polymer blend matrix can be controlled. By this way, a maximum LE of 55 lm/W was reported by using fluorescent proteins on UV LED chips [32]. One alternative to maintain the improved optical performance of the FP-LEDs is the direct liquid-state integration of proteins inside the LED structure, which we used in our studies.

2.3 The optical analysis of the generated light

In order to investigate the optical properties of the generated light in our studies, we used the optical parameters of LEDs such as luminous efficiency (LE), luminous efficacy of radiation (LER), correlated color temperature (CCT), color rendering index (CRI), color gamut coverage and ratio, (x, y) coordinates of light in the tristimulus color coordinates, external quantum efficiency (EQE) and power consumption efficiency (PCE).

2.3.1 Luminous efficiency (LE)

Luminous flux is a measure of light power of a source perceived by the human eye and its unit is lumen (lm). Based on the Schubert book, 1 luminous flux is equal to a monochromatic light source emitting an optical power of (1/683) watt at 555 nm [7]. Hence, the luminous flux can be calculated by using Equation (2.2) as follows:

$$\phi_{\mathbf{lum}} = 683\ \frac{\mathrm{lm}}{\mathrm{W}} \int \mathrm{V}(\lambda)\ \mathrm{P}(\lambda)\ \mathrm{d}\lambda \tag{2.2}$$

, where $\mathrm{P}(\lambda)$ is the power spectral density, i.e. the light power emitted per unit wavelength, and the pre-factor 683 lm/W is a normalization factor. $\mathrm{V}(\lambda)$ is the eye-sensitivity function (Figure 2.19). As a result, the luminous efficiency in units of lumens per electrical watt will be calculated by using Equation (2.3) as follows:

$$\text{Luminous efficiency (LE)} = \frac{\phi_{lum}}{\mathrm{IV}} \tag{2.3}$$

, where I and V is the forward injection current and voltage of the LED.

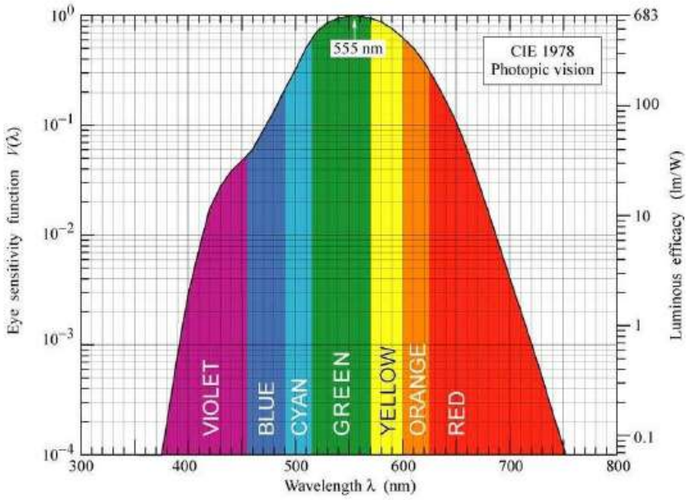

Figure 2.19: The eye sensitivity function [7].

2.3.2 *Luminous efficacy of radiation (LER)*

The luminous efficacy of optical radiation (also called the luminosity function), measured in units of lumens per watt of optical power, is the conversion efficiency from optical power to luminous flux. The luminous efficacy is defined as Equation (2.4) [7]:

$$\text{Luminous efficiency of optical radiation (LER)} = \frac{\phi_{\text{lum}}}{\text{P}} \tag{2.4}$$

, where P is the optical power from the light source.

2.3.3 *Color rendering index (CRI)*

Another important characteristic of a white light source is its ability to show (i.e. render) the true colors of physical objects that are being illuminated by the source. The ability to render the colors of an object is measured in terms of the color-rendering index or CRI. For CRI calculation, color-rendering ability of the lighting device is characterized by eight international agreed-upon test samples (from R1 to R8) having distinct reflection profiles in the visible spectrum. These test samples correspond to different colors in the visible spectrum such as light greyish red (R1), dark greyish yellow (R2), strong yellow green (R3), moderate yellowish green (R4), light bluish green (R5), light blue (R6), light violet (R7) and light reddish purple (R8) [7].

2.3.4 *Correlated color temperature (CCT)*

If the color of a white light source does not fall on the planckian locus (Figure 2.20), the correlated color temperature (CCT), also given in units of kelvin, is used. The correlated color temperature of a white light source is defined as the temperature of a planckian black-body radiator whose color is closest to the color of the white light source [7].

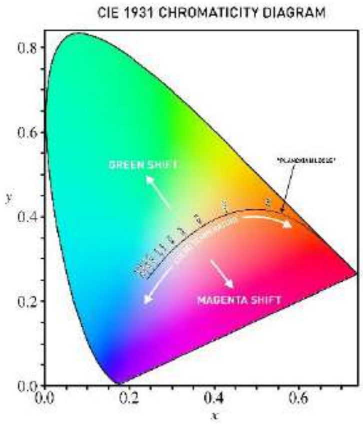

Figure 2.20: The representation of planckian locus in CIE 1931 color tristimulus.

2.3.5 Color gamut

Color gamut represents all colors that can be created by mixing the three primary colors red, green, and blue. The ability to create a great variety of colors is an important quality for displays. It is desirable that the color gamut provided by the three light sources is as large as possible to create displays able to show brilliant, saturated colors (Figure 2.21). For the calculation of color gamut coverage and ratio, the power intensity spectra of the generated light needs to be multiplied with the standard color filters.

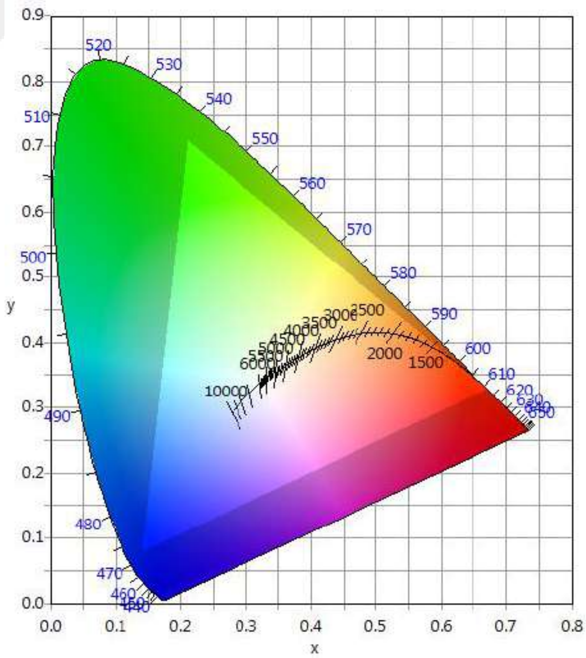

Figure 2.21: The representation of NTSC color gamut (bright triangle) in CIE 1931 color tristimulus.

2.3.6 External quantum efficiency (EQE)

The EQE of the LEDs in our studies was calculated based on Equation (2.5) [7], which is the ratio of the number of emitted photons to the number of injected charges.

$$\eta_{ext} = \frac{\text{Number of photons emitted into free space per second}}{\text{Number of electrons injected into LED per second}} = \frac{P/h\nu}{I/e} \tag{2.5}$$

2.3.7 Power conversion efficiency (PCE)

The power conversion efficiency of the LEDs was calculated based on Equation (2.6) as follows [7]:

$$\text{PCE}\ (\%) = \eta_{ext}\frac{\lambda_1}{\lambda_2} \tag{2.6}$$

, where λ_1 and λ_2 are the wavelength of the photons absorbed and emitted by the LED, respectively.

2.4 Measurement techniques (Nanomaterial-based LEDs)

2.4.1 The structural properties of QDs

Powder X-ray diffraction measurements of QDs were performed by Bruker D2 PHASER X-ray Diffractometer [$\lambda_{Cu\text{-}K\alpha}$ = 1.54 Å] with 1° min^{-1} scan rate. Powder samples were prepared by drying QD solution dissolved in hexane. The drying process was carried out by heating the solution to 200 °C for 1 hr. Powder samples were supported by PMMA holder, and the studies were carried out at room temperature. SEM-EDAX measurements were obtained by a Zeiss Ultra Plus field emission scanning electron microscope by using Bruker XFlash 5010 EDX detector. The accelerating voltage was set to 20 kV. The samples were prepared by drying the QDs dissolved in hexane solution to 200 °C for 1 hr. Transmission electron microscope (TEM) imaging was performed using a 200 keV accelerating voltage in a spherical aberration-corrected scanning TEM (JEOL JEM200ARMCF). Diffraction contrast images, for estimating the particle size distribution, were recorded using a 60 μm objective aperture. Phase-contrast, high resolution TEM imaging was performed for investigating crystallinity in the specimen.

2.4.2 The optical properties of QDs

UV/Visible absorption and photoluminescence spectra of QDs were carried out by Edinburgh Instruments Spectroflourometer FS5. The system included 150 W Xenon lamp combined with an excitation monochromator. The excitation source was set to 375 nm with a band pass filter that has a FWHM of 2 nm. QDs in hexane are poured into standard quartz cuvettes for absorbance and photoluminescence. The emission detector was a single photon counting photomultiplier tube (R928P) and the detection spectral width was 2 nm. Absolute fluorescence quantum efficiency values were measured by using an integrating sphere. The measurement module that contained an integrating sphere with an inner diameter of 150 mm was placed into FS5 system for the determination of QE. Time-resolved microscopy was carried out by Picoquant MicroTime 100 Time-resolved Fluorescence Microscope. A PDL 800-D diode laser driver for picosecond pulses combined with a 375 nm laser head was used as the excitation source with a repetition rate of 8 MHz. A single photon sensitive detector (PMA Hybrid 50) based on a photomultiplier tube (R10467 from Hamamatsu) was used. The time-correlated single photon counting electronics of HydraHarp 400 was adjusted to a resolution of 4 ps. The samples were measured at room temperature.

2.4.3 The photometric analysis of LEDs

In order to measure the optical properties of the fabricated nanomaterial-based LEDs in our studies, after the fabrication process was finished, we turned on the LEDs by connecting to the voltage supply. The voltage supply was used in order to adjust the forward injection current and turn-on voltage. Then, the LEDs were integrated inside an integrating sphere in order to collect all of the generated photons (Figure 2.22a). The integrated sphere was connected to an optical detector via an optical fiber. LED measurements were performed with multi-port Ocean Optics integrating sphere. The detector was Ocean Optics Torus with optical resolution of 1.6 nm FWHM over the spectra range, the integration time from 1 ms to 65 s and the wavelength range was from 360-825 nm. The signal to noise ratio was 250:1 (2.22b).

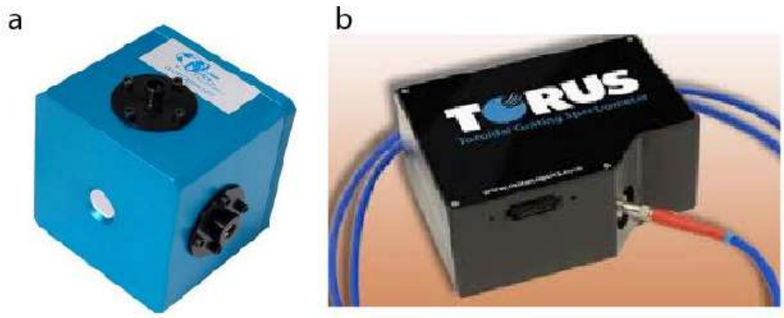

Figure 2.22: (a) The integrating sphere and (b) the optical detector, which was used for the LED measurements in our studies.

In order to calculate the optical parameters, the intensity spectra was input inside the OSRAM Calculator software.

2.5 Luminescent solar concentrators

Luminescent solar concentrators (LSCs) offer simple and cost-effective solar energy harvesting solutions to boost the solar energy contribution to global electricity production. LSCs are made of fluorescent materials embedded inside transparent optical waveguides.

Fluorescent materials absorb the incoming solar radiation impinging on a large area, convert it to longer-wavelength radiation and the down-converted light is then guided to the small-area solar cells placed at the edges of the waveguide. The concentration of light by luminescence leads to a significant increase of energy production for the same area of solar cells [12-15]. Therefore, this approach provides a practical energy harvesting solution that can be broadly used as 'solar windows' in buildings (Figure 2.23).

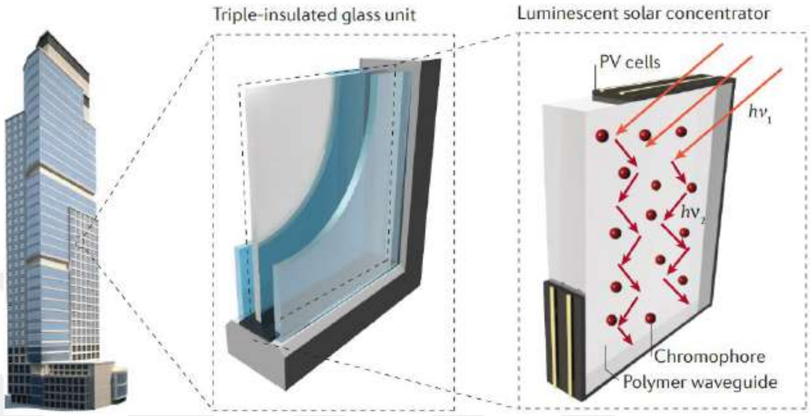

Figure 2.23: The representation of luminescent solar concentrators as solar windows in building for sunlight energy harvesting [12].

2.5.1 Fluorophores inside LSC architectures

For its wide-spread use, LSC technology needs to be transformed such that it can simultaneously satisfy efficiency, biocompatibility, and feasibility for large-volume production. More specifically, the following challenges need to be simultaneously addressed:

(1) High PLQY of fluorescent material in its synthesis batch

(2) High quantum efficiency (QE) of them in host matrix

(3) Low overlap between the absorbance and photoluminescence (i.e., reabsorption) of the fluorophore (large Stokes-shift)

(4) Well-matched spectral profile between the photoluminescence of the fluorescent material with the photo-response of the solar cells

(5) Being free of toxic elements

(6) Scalable production for wide-spread use.

Optical quantum efficiency of a LSC is a key efficiency-related figure of merit [19] defining the ratio of the output photons, which are extracted from the edges of the LSC to the total number of absorbed photons by the LSC. In order to reach a high optical quantum efficiency level, simultaneous satisfaction of (1)-(3) are required. In addition, (4) allows for efficient conversion of luminescence to electricity, (5) ensures minimum adverse effects of LSCs on environmental sustainability, and (6) shows their ability for large-scale production. Therefore, fulfilling the requirements (1)-(6) can lead to an efficient, ecofriendly and practical LSC technology for safe and effective solar energy harvesting.

Fluorophores inside the transparent medium are the key building-block of the LSCs. To date, different types of fluorophores have been employed in LSC structures such as organic dyes [16], fluorescent proteins [17], lanthanide-based materials [18] and perovskites [19]. However, the use of each type of these fluorophores is accompanied with major challenges. Organic dyes have low stability and PLQY when integrated into host materials [37]. Fluorescent proteins, despite their unique bio-compatibility and even edibility, similarly suffer from the low PLQY in solid-state, which leads to high optical losses [17, 63]. Lanthanides show low absorption coefficient and their compounds are expensive, which are not appropriate for their wide-spread use [18, 64]. Perovskites show limited operational lifetime for LSCs [19, 65].

Colloidal QDs offer exceptional optoelectronic properties for LSCs. They allow the control of the optical properties by tuning their size, shape and chemical composition [66-69]. By using different inorganic core/shell structures, high PLQY can be reached to decrease the optical losses [70]. The ability of precisely tailoring the absorbance and emission of the QDs can enable low reabsorption losses, which is important to efficiently deliver the down-converted light to solar cells [13]. Moreover, the photo/chemical stability of the QDs can be optimized for long-term use [71-74]. Therefore, QDs are highly promising candidates for LSC applications.

One compelling material design of QDs is Stokes-shift engineering that can suppress reabsorption losses, which is important to minimize the propagation losses of the down-converted luminescence inside the waveguide. Different synthetic procedures have been performed to enlarge the Stokes-shift of the QDs such as using indirect band-gap materials [75], varying the semiconductor compositions [76], growing giant shells [13] and synthesis of quasi-Type II QDs [13, 77]. However, QDs produced by these approaches have either toxic heavy-metal content (such as cadmium or lead) or low in-device PLQY. An alternative strategy to engineer the Stokes-shift of QDs and enhancing the in-device PLQY can be doping with transition-metal ions [78-80]. Incorporation of small amount of metal impurities (0.1-10 atomic %) as dopants into the host semiconductor QDs introduces new electronic states within the bandgap [80, 81]. The emission from these states are due to the exchange-mediated energy transfer from the photo-excited host semiconductor [82]. Based on the energy level of the metal activator ion, the reabsorption can be effectively suppressed in doped QDs and leads to the Stokes-shift up to hundreds of meV [83, 84]. However, the QE of the doped QDs is typically low due to the slow radiative recombinations, which can be easily outcompeted with the non-radiative processes [13]. The optical properties of the previously-reported fluorophores inside the LSC architectures are shown in Figure 2.24. In our studies, we aimed to increase the optical efficiency of the nanomaterial-based LSCs by using novel architecture and nanomaterials.

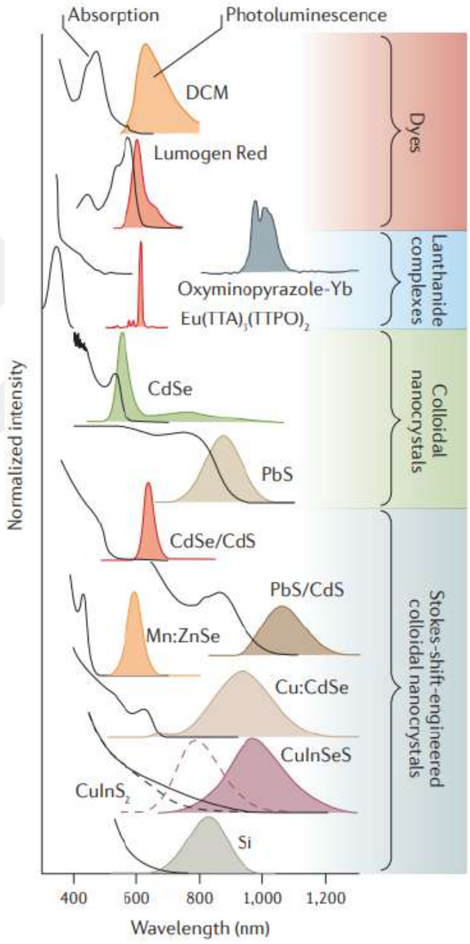

Figure 2.24: Optical absorption and photoluminescence spectra of some organic dyes, lanthanide complexes and colloidal nanocrystals used in LSCs. The combination of a large solar coverage and small spectral overlap between the absorption and photoluminescence spectrum is obtained only in nanocrystals with a carefully engineered Stokes-shift [12].

2.6 The optical characteristics of the LSCs

2.6.1 The optical efficiency

When calibrated PV cells are used to investigate the optical performance of LSCs, generally, the optical efficiency of the LSC is defined based on Equation (2.7) as follows:

$$\eta_{opt} = \frac{I_{LSC} \times A_{PV}}{I_{PV} \times A_{LSC}} \tag{2.7}$$

2.6.2 The internal quantum efficiency

The internal quantum efficiency or optical quantum efficiency (defined as the ratio of number of photons emitted from the edges of the LSC and the number of photons absorbed by the LSC) can be estimated based on Equation (2.8) as follows [85]:

$$\eta_{int} = \frac{\eta_{ext}}{\eta_{abs}} \tag{2.8}$$

, where the external quantum efficiency (η_{ext}) is defined as the ratio of number of photons collected from the edges of the LSC and the number of incident photons, η_{abs} is the absorption efficiency, corresponding to the ratio of the number of photons absorbed by the LSC and number of incident photons.

2.6.3 The absorption efficiency

Absorption efficiency, which quantifies the number of the absorbed photons over solar spectrum was calculated based on Equation (2.9) [86] as follows:

$$\eta_{abs} = \frac{\int \phi_{sol}(1-R)\left(1-e^{-\alpha(\lambda)d}\right)d\lambda}{\int \phi_{sol}(\lambda)d\lambda} \tag{2.9}$$

$\phi_{sol}(\lambda)$ is the spectral profile of the solar spectrum. R is reflectivity, d was considered as the LSC thickness and $\alpha(\lambda)$ is the absorption coefficient of the fluorophore calculated from absorbance spectrum.

2.6.4 Reflectivity (R)

Reflectivity of the LSC is calculated by considering the refractive index of the medium and the substrate depending on the architecture based on Equation (2.10).

$$R = \frac{(n_2 - n_1)^2}{(n_2 + n_1)^2} \tag{2.10}$$

2.6.5 Reshaping factor (q_{LSC})

q_{LSC} is the reshaping factor, which was calculated based on Equation (2.11) [15].

$$q_{LSC} = \frac{<Q_{PL}>}{<Q_s>} = \frac{\int \phi_{PL}(\lambda)EQE(\lambda)d\lambda}{\int \phi_{sol}(\lambda)EQE(\lambda)d\lambda} \tag{2.11}$$

In Equation (2.11), $\phi_{PL}(\lambda)$, $EQE(\lambda)$, and $\phi_{sol}(\lambda)$ are the photoluminescence spectral profile of the fluorophore, external quantum efficiency of the silicon solar cell and the spectral profile of the solar spectrum that obtained from the solar simulator, respectively.

2.6.6 The optical gain factor (G)

The optical gain factor was measured based on G = L / (4D), in which the L is the side length of LSC and D is the thickness of the LSC.

2.6.7 Power conversion efficiency (PCE)

Another commonly used parameter to determine the optical performance of an LSC is the PCE, which can be calculated according to Equation (2.12) as follows:

$$\mathrm{PCE}\ (\%) = (\eta_{\mathrm{ext-LSC}})(\eta_{\mathrm{ext-PV}}) \tag{2.12}$$

2.7 Measurement techniques (Nanomaterial-based LSCs)

The photoluminescence and UV/Visible absorbance spectra of synthesized QDs and the transmission measurement of the fabricated QD-based LSCs were performed by Edinburgh Instruments spectroflourometer FLS1000 with 325 mm focal length monochromator. The excitation source was 450 W ozone free xenon arc lamp that covers a range of 230 nm to >1000 nm for steady state measurements. The QD solutions were excited with 275 nm and 400 nm wavelengths for PL intensity and PLQY measurements, respectively. The integrating sphere was used to measure absolute PLQY of the synthesized QDs. Standard quartz cuvettes with the cross dimensions of 1 × 1 cm^2 was used for photoluminescence, UV/Visible and PLQY measurements. For the optical properties of the solid-state samples, another sample holder was used. The scatter and emission ranges were adjusted between 370-440 nm and 560-975 nm for the copper-doped samples, respectively. The absolute PLQY measurement method, which was used for the calculation of the PLQY in the FLS1000 integrating sphere module, has an estimated error of ±5%. The repeatability has an error of ±3%. For the calibration of the integrating sphere, Rhodamine 6G dye with the emission peak wavelength of 548 nm and a mean PLQY of 95% was obtained, as expected. The number of recorded signal photons (i.e., detector linearity) was adjusted as 1 million photons per second to eliminate the instrumental factors affecting the measured PLQY of the QDs. The non-linear absorption properties and ultrafast decay dynamics of the QDs were investigated by using a femtosecond pump-probe spectrometer (Helios, Ultrafast Systems). The QD solution was excited at 400 nm by using the fourth-harmonic output of a tunable, femtosecond optical parametric amplifier (OPA, TOPAS Prime, Spectra-Physics), which was pumped with a 2-mJ, 800-nm Ti^{3+}: sapphire regenerative amplifier (pulse duration: 120 fs, pulse repetition rate: 1 kHz, Spitfire Ace, Spectra-Physics). A portion of the 800-nm output of the regenerative amplifier was further focused inside a sapphire plate to generate the femtosecond white light continuum probe pulses in the 450-800 nm wavelength range. The white light continuum probe was split into two before passing through the sample. One of them was directly sent to the sample and the other beam was used as a reference to monitor the fluctuations in the generated white light continuum intensity during the measurements. In the pump-probe spectroscopy experiments, the pump and probe beams were overlapped and focused inside a 0.5-mm-long spectrosil cuvette containing QD solution with the optical density of 1 at the band-edge absorption. The average number of electron-hole pairs (N_{e-h}) generated during the pumping process was calculated from $N_{e-h}=J/J_{sat}$, where J is the photon fluence and the saturation fluence J_{sat} is given by $h\nu_{pump}/\sigma_a$ [87]. During the pump-probe experiments, the 400-nm fluence (J) incident on the QDs was sufficiently low (135 μJ/cm^2), giving N_{e-h}=0.5. For reabsorption measurement, a picosecond pulsed diode laser (EPL) from Edinburgh Instruments with operation wavelength of 365 nm and pulse width of 65 ps, repetition rate of 20 MHz, average output power of 5 mW and horizontal polarization was used for the excitation of the QD-LSCs at different optical distances. For scattering measurements, a continuous-wave Ti:sapphire laser operating at 780 nm with the power of 900 mW and horizontal polarization was used.

For electro-optical measurement, a calibrated Newport Oriel LCS-100 solar simulator AM 1.5G was used (Figure 2.25) according to the ref [88]. The output power of the Xe lamp was 100 mW.cm^{-2}.

Figure 2.25: The solar simulator, which was used for illumination of LSCs in our studies.

Two different silicon solar cells with dimensions of 11 × 7 cm^2 and 24 × 24 cm^2 were used for the efficiency measurements of QD-LSCs with different dimensions. Since the surface area of solar cells were greater than LSC edge area, a black tape was used to mask the excessive area. During the measurement, the uncoupled edges of the LSCs were covered with black paint and only one edge was coupled to the solar cell in order to eliminate any incident light from outside and PL reflection back to the waveguide. Depending on the size of the fabricated QD-LSCs, a mate black paper was placed at the back of the LSC in order to block any direct illumination from the solar simulator (Figure 2.26).

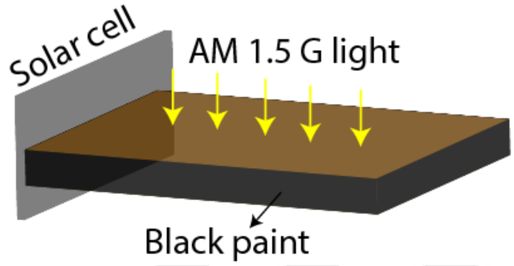

Figure 2.26: The schematic representation of the optical efficiency measurements in our studies for the fabricated LSCs.

Chapter 3

NANOMATERIAL-BASED LIGHT-EMITTING DIODES WITH IMPROVED OPTICAL PERFORMACE

3.1 Quantum Dot White LEDs with High Luminous Efficiency

This section is based on the publication "*Quantum Dot White LEDs with High Luminous Efficiency*" S. Sadeghi, B. G. Kumar, R. Melikov, M. M. Aria, H. B. Jalali, and S. Nizamoglu, Optica 5. 7 (2018) 793-802. Reproduced (or "Reproduced in part") with permission from Optical Society of America Copyright 2018.

Colloidal quantum dots (QDs) have attracted significant attention in the last three decades due to high quantum yield (QY) and tunable electronic properties via quantum confinement effect and material composition. However, their utilization for efficient solid-state lighting sources has remained a challenge due to the decrease of QY from synthesis batch in liquid-state to host matrix in solid-state, which is also known as the host material effect. In this section, we demonstrate a novel architecture in order to suppress the host material effect by simple liquid-state integration in light-emitting diodes (LEDs) that led to a luminous efficiency (LE) of 64 lm/W for RGB (Red, Green, Blue) and 105 lm/W for GB-based (Green, Blue) white light generation. For that, we maximized the QY of red- and green-emitting QDs by optimizing synthesis parameters, and integrated efficient QDs with QY up to 84% on blue LED dies in liquid form at appropriate injection amounts for high-efficiency white lighting. Liquid-state integration showed 2-fold and 6-fold enhancement of efficiency in comparison with incorporation of QDs in PDMS film and close-packed formation, respectively. Our theoretical calculations predicted that luminous efficiency of liquid QD-LEDs can reach over 200 lm/W.

3.1.1 Introduction

Efficient solid-state lighting (SSL) offers high potential to save the energy and to protect the environment [1]. If light-emitting diodes (LEDs) at the targeted efficiency levels are replaced with conventional lighting sources, the global electricity that is consumed for lighting would be decreased by more than 50%, which is equal to the reduction of either 230 typical 500-MW coal plants or 200 million tons of greenhouse gas emission [1, 2]. According to the SSL road map, white LEDs were targeted to reach a luminous efficiency

(LE) level over 200 lumen per electrical watt until 2020 [57]. To this end, there is a significant world-wide effort to boost the efficiency levels of white LEDs.

Today, white LEDs generally use a down-conversion material that is integrated on a blue LED die in a solid-state matrix [1, 89]; instead, the synergetic combination of fluids and optics, which is also known as opto-fluidics, may open up new horizons due to its ability to reveal novel and advanced functionalities [90-94]. Photonic materials in liquid-state advantageously enable simple integration. In addition, the optical properties of the fluid medium can be changed by replacing with another one, and the spectra can be adjusted by controlling the blend ratio of the fluids. Hence, photonic materials in liquid-state facilitated significant progress in displays, lasers, energy storage and wave- guiding [95-98]. Furthermore, there have been previous reports that use liquid-state photonic materials on LEDs for spatial radiation control [99], color-mixing [100], and flexible electronics [101], and it has recently started to be explored as an alternative for efficient lighting [102, 103].

Colloidal quantum dots (QDs) have attracted significant attention for efficient lighting due to high quantum yield (QY>80%), narrow emission bandwidth and tunable luminescence [20-26]. Even though QDs have many advantageous features for LEDs, the efficiencies that have been achieved so far were not at desired levels mainly due to host material effect and reabsorption [13, 28, 29]. To overcome this limitation, giant shell growth on a core facilitated the preservation of QY from solution to polymer matrix in addition to suppressing the self-absorption [104-106]. However, the QY of these structures was less than 50% and the emission could only cover the red spectral region. Alternatively, recycling of trapped excitons via energy transfer is another effective way to increase the in-film quantum efficiencies (QEs). It was demonstrated that by using this approach, the in-film QE can be increased [107], which can be also used for LEDs as well [108]. But, since QE in closed-packed formation drastically decreases, it cannot be recovered close to its original levels. Moreover, dispersion of the colloidal QDs while transferring from liquid to solid (e.g., inkjet printing [109]) generates undesirable inhomogeneity due to coffee ring effect [58]. Therefore, liquid-state integration can generate a solution for the above-mentioned problems.

Here, in this section, we explain the integration of synthesized QDs in liquid-state on blue LED chips for efficient lighting (Figure 3.1a). The electroluminescence of blue LED chip excites the QDs in liquid, which generate photoluminescence (PL), and the joint electroluminescence of blue LED and PL of QDs form the white light (Figure 3.1b). For that, we optimized the QY of red- and green-emitting Cd-based QDs by varying the synthesis parameters. The integration of QDs in liquid-state enables the preservation of QY. We integrated as-synthesized liquid QDs without any chemical or interfacial modification and injected at appropriate injection amounts, which led to the most-efficient QD-based white LED reported to date, according to our best of knowledge.

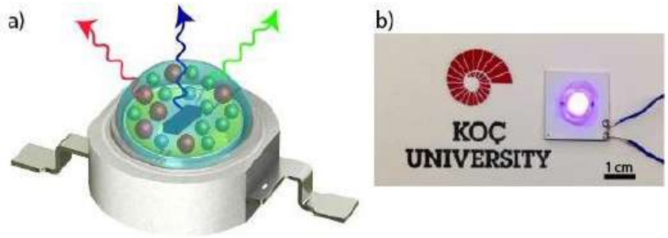

Figure 3.1: (a) Schematic of the LQD-LED. The red and green spheres represent red- and green-emitting QDs in a liquid, respectively. QDs absorb the blue electroluminescence and emit red and green light. The combination of red and green emission by QDs and blue emission by blue LED die generates white light. (b) The photograph of an exemplary white LQD-LED, while it is turned on.

3.1.2 Synthesis of red- and green-emitting QDs

Synthesis of red-emitting CdSe/CdS/ZnS core/shell/shell QDs

CdSe/CdS/ZnS QDs were synthesized based on the method by Jang *et al.* [110]. In a typical synthesis, 0.4 mmol cadmium oxide (0.0515 g, >99.99% Aldrich), 1.6 mmol oleic acid (0.5 ml, 99% Alfa), and 5 ml tri-n-octylamine (>97% TCI) were mixed together in a 100 ml three-neck round bottom flask. The solution was heated to 150 °C under nitrogen inert atmosphere using the Schlenk line (Figure 3.2a). At this temperature, the solution was evacuated by vacuum and placed under inert atmosphere repeatedly (Figure 3.2b). After degassing process, the solution was heated to 300 °C. Once the temperature was stable, 0.05 ml of 0.792 g selenium (>99.5% Aldrich) in trioctylphosphine (90% Acros) precursor (2M TOPSe) was injected into the solution. After 2 minutes, 1.5 ml of 210 µl 1- octanethiol (>98.5% Aldrich) in 6 ml TOA precursor was injected into the solution in 90 seconds. The heating continued for 40 minutes until the reaction was complete. Then, 4 ml of 0.92 g zinc acetate (>99.0% Sigma-Aldrich) in 3.15 ml OA (100 °C, transparent) precursor (0.25 M Zn-OA) was injected into the solution in 2 minutes. Quickly after this injection, 1.75 ml of 1.12 ml 1-octanethiol (6.4 mmol) in 6 ml TOA precursor was injected into the solution in 105 seconds. Finally, the solution was cooled down to room temperature. The final red solution consisted of red-emitting CdSe/CdS/ZnS QDs, which was purified with ethanol and re-dispersed in toluene. For the preparation of the precursor solutions, the glove-box filled with the nitrogen inert atmosphere was used (Figure 3.2c). The oxygen and water level was adjusted at below 1 ppm.

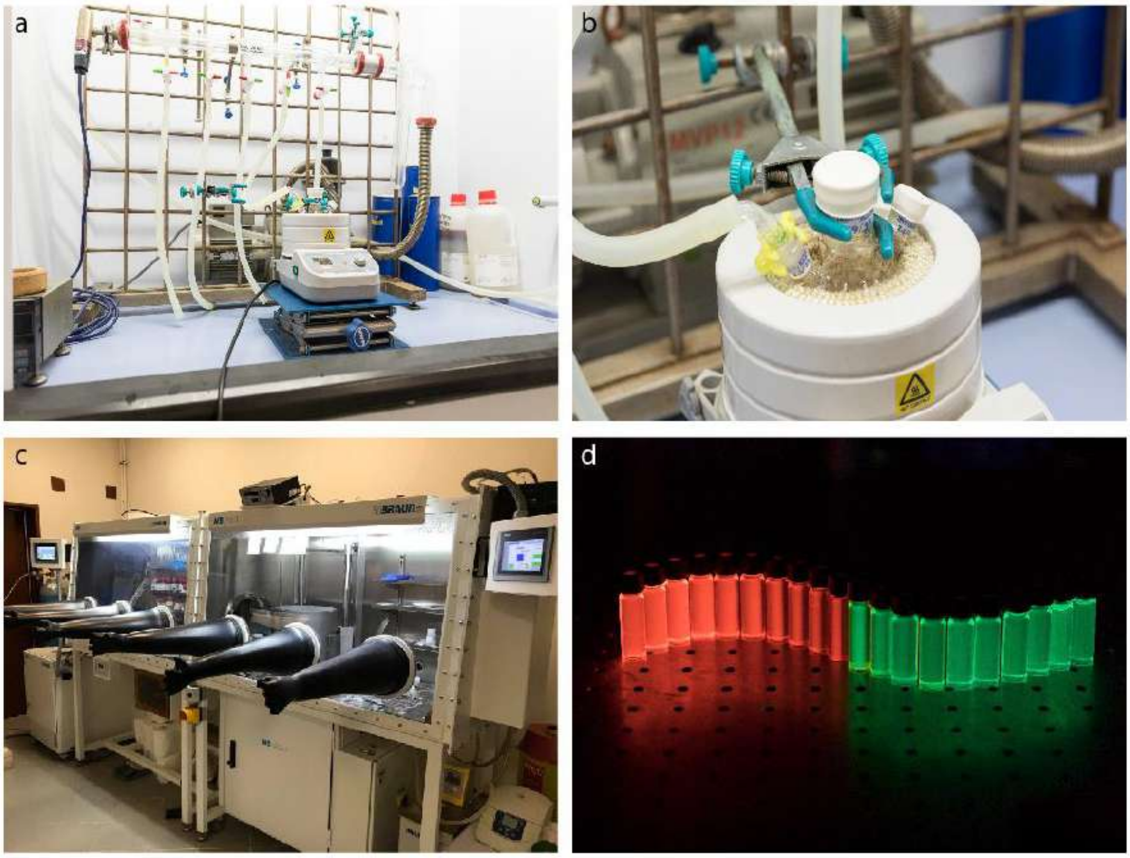

Figure 3.2: (a) The Schlenk line, (b) the reaction flask inside the heating mantle, and (c) the glove-box for the synthesis of quantum dots in our laboratory. The synthesized red- and green-emitting Cd-based QDs in this study under 365 nm UV illumination.

Synthesis of green-emitting CdSe//ZnS/CdSZnS core/shell QDs

CdSe//ZnS/CdSZnS quantum dots were synthesized based on the method by Jang *et al.* [25, 111]. In a typical synthesis, 0.4 mmol CdO (0.0515 g), 0.8 mmol of octadecylphosphonic acid (0.268 g, >98% TCI) and 16 ml of TOA were mixed together in a 100 ml three-neck flask. The solution was heated to 150 °C under nitrogen inert atmosphere. At this temperature, the solution was evacuated by vacuum and placed under inert atmosphere repeatedly. After degassing process, the solution was heated to 320 °C under nitrogen atmosphere. Once the temperature was stable, 1 ml of 0.792 g Se in TOP precursor (2M TOPSe) was injected into the solution. After 2 minutes of the reaction time, the heating was stopped and the mantle was removed. The synthesized core CdSe quantum dots were purified, centrifuged and re-dispersed in toluene. The optical density of the ×100 times diluted core solution was adjusted at 0.1 at the first absorption maximum. Then, 0.4 mmol of zinc acetate dihydrate (0.088 g) was mixed with 0.8 mmol of OA (252 µl) and 16 ml TOA in a three-neck round bottom flask. The mixture was heated to 150 °C under nitrogen inert atmosphere. At this temperature, the solution was evacuated by vacuum and placed under inert atmosphere repeatedly. After degassing process, the solution was heated to 320 °C under nitrogen atmosphere. Once the temperature was stable, 1 ml of core solution was injected into zinc-containing solution. Right after injection, 1.6 mmol of 1- octanethiol (278 µl) in 2 ml TOA was injected into the solution incrementally. The heating was continued for 40 minutes. The synthesized CdSe//ZnS interfused quantum dots were purified and re-dispersed in toluene. CdSZnS shell was formed according to the procedure in reference [25]. 0.05 mmol cadmium acetate (0.0115 g, ≥99.995% Aldrich), 0.04 mmol zinc acetate (0.0088 g) and 1.5 mol OA (480 µl) was dissolved in 20 ml TOA in a round-bottom flask. The mixture was heated to 150 °C under nitrogen inert atmosphere. At this temperature, the solution was evacuated by vacuum and placed under inert atmosphere repeatedly. After degassing process, the solution was heated to 320 °C under nitrogen atmosphere. Once the temperature was stable, 0.6 ml of the core CdSe//ZnS solution with optical density of 0.15 was injected into the Cd and Zn containing solution. Right after the injection, 2 ml of 0.4 M sulfur (Reagent grade 100 mesh particle size, Sigma-Aldrich) in TOP was injected into the solution incrementally. The heating continued for 45 minutes. The synthesized CdSe//ZnS/CdSZnS quantum dots were purified with ethanol and re-dispersed in toluene. Each synthesis for optimization of the QY for both red- and green-emitting QDs was performed three times to assure the reproducibility of the results.

3.1.3 Device fabrication

Polymeric lens making procedure

For making semi-spherical lens, 1 g of Polydimethylsiloxane (PDMS) SYLGARD 184 Elastomer was mixed with 0.1 g of SYLGARD 184 curing agent and stirred for 3 minutes until bubbles appeared in the mixture. Then, the mixture was degassed in the vacuum desiccator for 20 minutes until the bubbles were disappeared completely. The mixture was poured into the pre-fabricated aluminum mold, and heated at 70 °C for 6 hours for completion of PDMS curing process (Figure 3.3). After heating was finished, the aluminum mold was opened and the lens was brought out. The product was a semi-spherical lens with outer diameter of 9 mm and inner diameter of 7 mm and lens thickness of 1 mm.

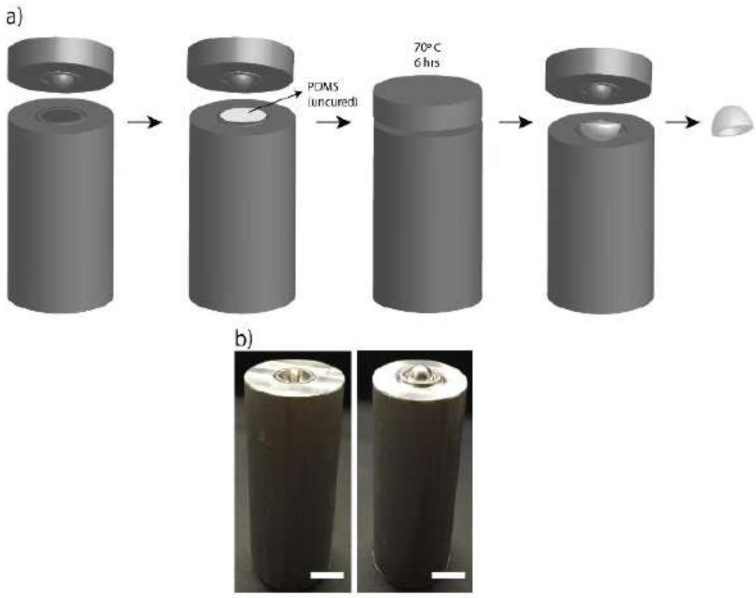

Figure 3.3: (a) The schematic of lens fabrication procedure using the designed aluminum mold and PDMS. (b) (Left) the lower and (right) the upper part of the mold, which was placed on top of each other to fabricate the polymeric lens with hollow hemispherical shape. The scale bar is 1 cm.

LED device making procedure

For making LED device, the blue chip was mounted on board and two electrical wires were soldered to the board for connection to the voltage supply. As a step-wise curing process, the PDMS lens was attached to the LED PCB board with using NOA 68 UV curable polymer. UV curable polymer was dripped on the sides of the lens, and it was cured for 20 minutes in front of UV irradiation at 365 nm. This process was repeated two times to assure that the structure was leakage proof.

Fabrication of close-packed and solid-state LEDs

As close-packed state LED, UV curable polymer was mounted around the blue chip to prevent the liquid from moving to the board edge. 10 µl of red-emitting QDs solution with optical density of 0.033 and 120 µl of green-emitting QDs solution with optical density of 0.048 (the same amounts used for RGB LQD-LED) was mixed and poured on top of blue chip to dry. For solid-state LED, 10 µl of red-emitting QDs solution with optical density of 0.033 and 120 µl of green-emitting QDs solution with optical density of 0.048 was mixed with 250 µl SYLGARD 184 Elastomer and 50 µl SYLGARD 184 curing agent. The mixture was degassed and cured at 70 °C for 6 hours. Each structure were fabricated and measured 3 times to assure the reproducibility of the results.

3.1.4 Quantum yield optimization of red- and green-emitting QDs

Since the QY of the synthesized QDs directly affect the overall performance of the LEDs, it is critical to synthesize QDs with high QY. In this study, we used "/" for separation between core/shell structures, and "//" to indicate the interfused structure. For red-emitting QDs, the synthesis starts with CdSe core. Since the core QY directly affects the QY of the core/shell structures, different selenium precursor injection temperatures have been investigated to observe the effect of temperature on QY of the synthesized CdSe core QDs. For this purpose, selenium was injected into the Cd-containing solution (1:1 molar ratio) at reaction temperatures of 220 °C, 240 °C, 260 °C, 280 °C, 300 °C and 320 °C (see Figure 3.4a). As the temperature increased, the QY increased and CdSe core showed the highest value of 38% at 300 °C after 2 minutes reaction time (Figure 3.4a). In principle, there were also other alternative QD reaction times and temperatures that have high efficiency (e.g., QY of 35% at 260 °C in 7 minutes or QY of 37% at 240 °C in 60 minutes). But, we selected CdSe core at 300 °C with 2 minutes of reaction time due to the position of PL peak wavelength, which will experience wavelength-shift after shell growth and could reach an appropriate final wavelength for efficient white light generation. On CdSe core, CdS shell with a low lattice mismatch of 4.3% was grown, which facilitates the reduction of trapped states [112]. To find the optimum point, the reaction proceeded up to 60 minutes and aliquots were taken at different CdS growth time (Figure 3.4b). The highest QY was observed 56% after 40 minutes of CdS shell growth on CdSe core. After the growth of CdS shell, the full width at half maximum (FWHM) did not change considerably (i.e., 28 nm for CdSe and 31 nm for CdSe/CdS), which indicated the homogenous size distribution of the synthesized QDs after shelling. Finally, ZnS shell was grown for strong confinement of both electron and hole inside the QDs. We optimized the final heterostructure by varying CdS and ZnS shells, and the structure with only one shelling of CdS and ZnS showed the highest QY of 77% (Figure 3.4c). The progress in absorbance and PL spectra of CdSe core, CdSe/CdS and CdSe/CdS/ZnS QDs were shown in Figure 3.4d. The PL peak wavelength of the synthesized red-emitting QDs were 640 nm, 659 nm and 609 nm for CdSe, CdSe/CdS and CdSe/CdS/ZnS, respectively (Figure 3.4d).

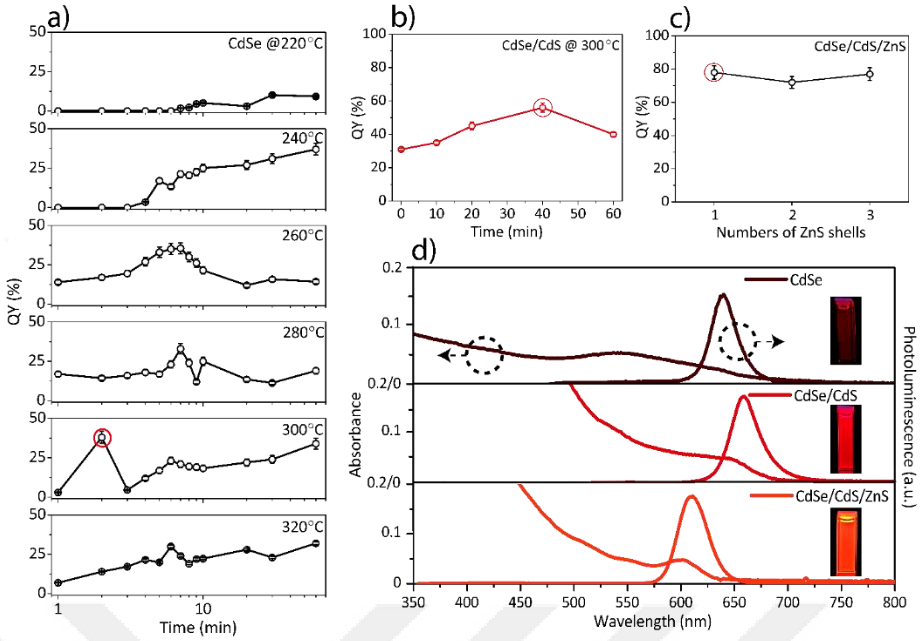

Figure 3.4: (a) Optimization of QY of CdSe core by modifying the temperature and time. (b) The optimization of QY of CdSe/CdS core/shell QDs by varying the reaction time at 300 °C. (c) The effect of multiple ZnS shelling on the QY of CdSe/CdS/ZnS core/shell/shell QDs. (d) The absorbance and photoluminescence spectra of CdSe (upper panel), CdSe/CdS (middle panel) and CdSe/CdS/ZnS (lower panel) QDs at the optimized reaction time and temperatures. Inset: Photograph of the QD solutions at each step under 365 nm UV radiation. The optimized operating points were placed in solid red circles (n=3).

Similarly, we investigated the synthesis procedure of green- emitting CdSe//ZnS/CdSZnS core/shell QDs to maximize the QY. CdSe core investigation was re-performed because of using a different surfactant, which is a mixture of octadecylphosphonic acid (ODPA) and oleic acid (OA), and the synthesis showed the highest QY of 17% at 320 °C (Figure 3.5a). Afterward, an interfused CdSe//ZnS core formation was generated, which showed a significant blue shift from CdSe QDs PL peak wavelength from 526 nm to 501 nm (Figure 3.5b) due to the larger bandgap of CdSe//ZnS in comparison with CdSe. After 40 minutes, the interfused core showed the maximum QY of 51% (Figure 3.5c). CdSZnS shell synthesis on the core for 45 minutes caused a significant boost of QY from 51% to 84% (Figure 3.5d). At the same time, favorably the CdSZnS shell resulted in a significant red-shift in PL peak wavelength from 501 nm to 550 nm with a FWHM of 35 nm (Figure 3.5b), which is in the close proximity of the peak of eye-sensitivity function (at 555 nm) to achieve efficient white LEDs.

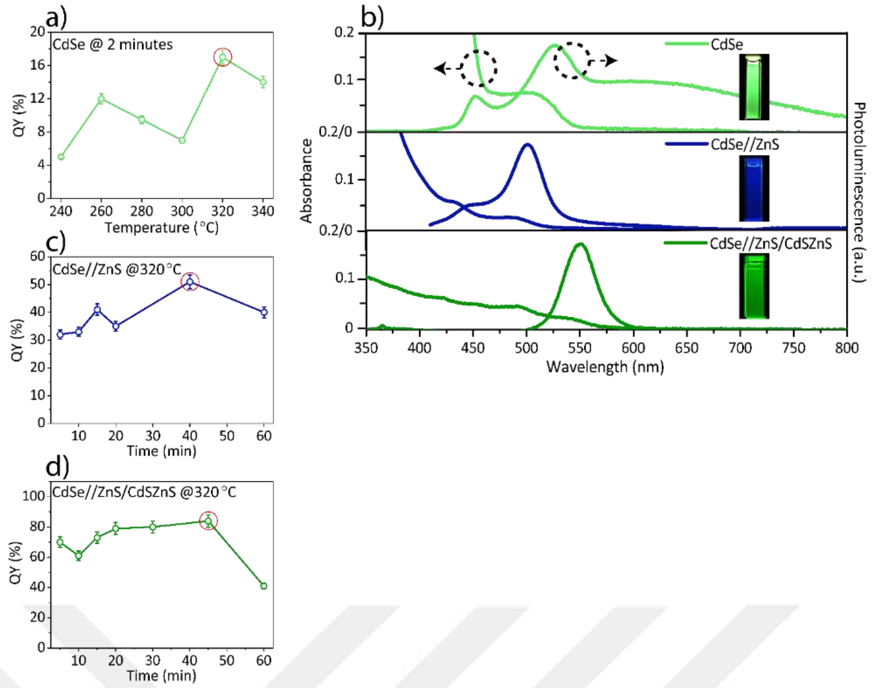

Figure 3.5: (a) Optimization of QY of green-emitting CdSe core QDs by changing the temperature at 2-minutes reaction time. (b) The absorbance and photoluminescence spectra of optimized CdSe core (upper panel), CdSe//ZnS core (middle panel) and CdSe//ZnS/CdSZnS core/shell (lower panel) QDs. Inset: Photograph of the QD solutions at each step under 365 nm UV radiation. (c) The optimization of QY of CdSe//ZnS interfused core QDs by varying the reaction time at 320 °C. (d) The optimization of QY of CdSe//ZnS/CdSZnS QDs by modifying CdSZnS shelling reaction time at 320 °C. The optimized operating points were placed in solid red circles (n=3).

The structural analysis of the synthesized QDs was investigated by using TEM (Figure 3.6). The synthesized red- and green-emitting QDs showed a size distribution of 6.23 ± 0.77 nm and 5.89 ± 0.93 nm, respectively. Moreover, the SEM-EDAX measurement confirmed the presence of cadmium, selenium, zinc and sulfur in red- and green-emitting QDs. The cubic structures of the synthesized red- and green- emitting QDs were identified by XRD. The peaks at 25°, 28°, 42°, and 57° confirmed the CdSe, CdS and ZnS structures. At the same time, XPS measurement showed the core/shell structures of the red- and green-emitting QDs (see Appendix A for XRD, XPS and SEM-EDAX results).

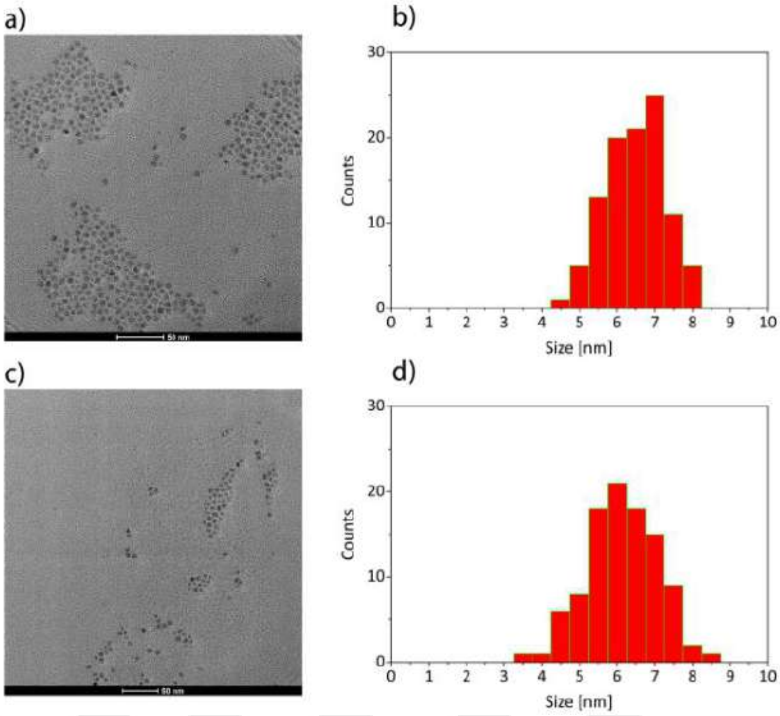

Figure 3.6: (a) TEM images of red-emitting CdSe/CdS/ZnS QDs. (b) The size distribution of the red-emitting QDs. (c) TEM images of green-emitting CdSe//ZnS/CdSZnS QDs. (d) The size distribution of the green-emitting QDs (Scale bar =50 nm). The size distribution was performed for 100 particles in each image.

3.1.5 *The simulation of the optical properties of the generated white light*

To achieve the highest level of efficiency in color conversion, it is necessary to optimize the injection ratio (concentration) of red- and green-emitting QDs. For this purpose, we initially simulated external quantum efficiency (EQE) of single-type red- and green-emitting QDs at different optical densities. The solid lines in Figure 3.7a and 3.7b showed the theoretical EQE of the QDs in liquids, and according to the simulation, they need to drop due to the reabsorption losses. Experimentally, we also confirmed this behavior as well; as the optical density of red-emitting QDs increased from 0.0033 to 0.2, the EQE decreased from 76.7% to 61.2%, respectively. The same behavior was also observed for green-emitting QDs in which by increasing the optical density from 0.0026 to 0.2, the EQE of the QDs decreased from 83.9% to 77.6%, respectively. Furthermore, the spectrum of the liquid- state QDs also shifted, while the optical density varied. As the optical density increased toward 0.2, the FWHM of the red- emitting QDs increased from 32 nm to 36 nm in Figure 3.7c. Moreover, the PL peak wavelength of the red-emitting QDs was red-shifted 8 nm (from 610 nm to 618 nm) (Figure 3.7c). Similarly, the FWHM of green emission increased from 36 to 37 nm accompanied by peak wavelength change from 550 to 553 nm, which were also in agreement with the simulations. According to these analyses, it is necessary to take the reabsorption-originated spectral and efficiency shift into account to achieve efficient lighting. Therefore, the injection optical density of red- and green-emitting QDs needs to be optimized. To explore the possible injection ratios that may lead to high-efficiency LEDs, we investigated the single and double combinations of red- and green-emitting QDs on a blue LED die (see Figure 3.7c & Appendix A for detailed explanation about the simulation). First, our simulation showed that the injection amounts need to be carefully adjusted that could lead to (x, y) tristimulus coordinates in the white region. By considering an optical density range [0, 0.1] and [0, 1] for red- and green- emitting QDs, respectively, white light region covered only ~5% of the total possible combinations. Second, we calculated that liquid-state integration with 77% and 84% QY of red- and green-emitting QDs could reach a maximum LE of 112 lm/W for white light generation on a blue die with an EQE of 50% (Figure 3.7f), while the device originating losses such as the refractive index mismatch, total internal reflection, waveguiding effect, and other possible optical loss mechanisms were considered in our simulation by an approximate factor ($\eta = 0.77$) [113]. If red- and green-emitting QDs were synthesized with QY of 100%, the maximum achievable LE would reach 140 lm/W by using a blue LED die with EQE of 50% (Figure 3.7f). At the same time, the simulation results showed that if the state-of-the-art blue LED die with EQE of 85% was used [114] with the red- and green-emitting QDs that have QY of 100%, the LE would reach over 200 lm/W (Figure 3.7f).

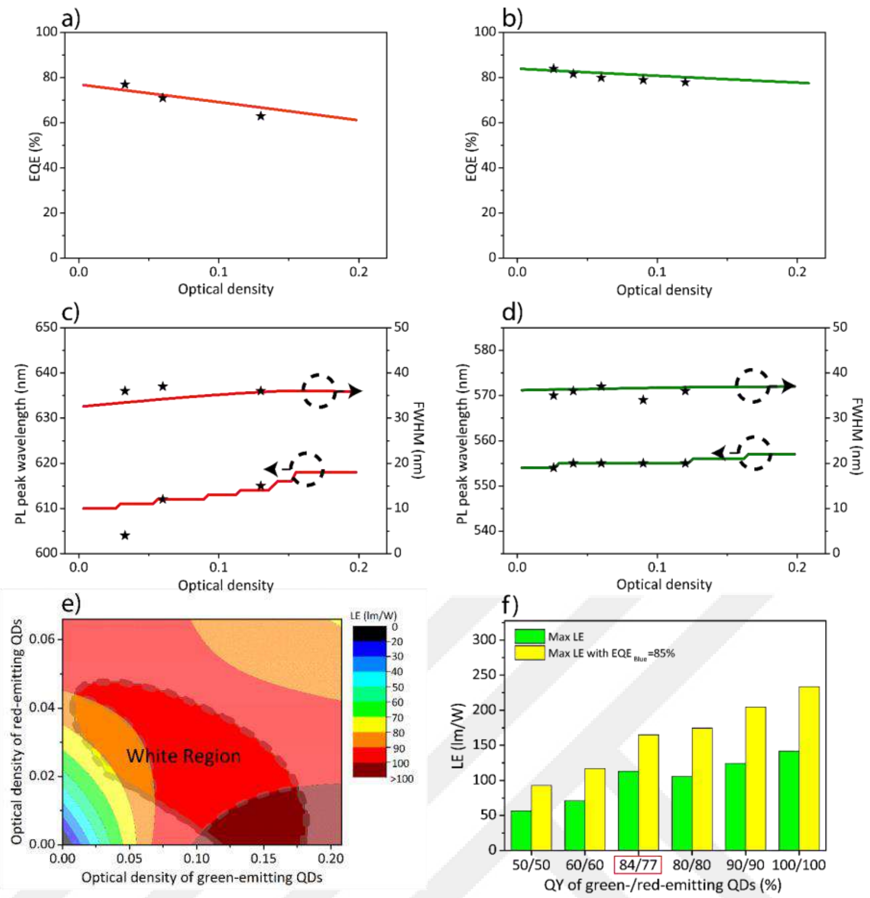

Figure 3.7: The EQE of (a) red-emitting CdSe/CdS/ZnS and (b) green-emitting CdSe//ZnS/CdSZnS QDs at different optical density levels. The photoluminescence peak position and FWHM of (c) red-emitting CdSe/CdS/ZnS and (d) green-emitting CdSe//ZnS/CdSZnS QDs at different optical density levels. The star symbols showed the experimentally measured data points and the solid lines showed the theoretically simulated data points. (e) Counter plot of luminous efficiency with the combinations of red- and green-emitting QDs at different optical density levels (η = 0.77). White color coordinates were shown as dashed bright region (white region). (f) Luminous efficiency simulation results for different QY of red- and green-emitting QDs illuminated with blue LED pump with EQE=50% (i.e., max LE) and 85% (i.e., max LE with EQE=85%) while η = 0.77.

3.1.6 The liquid-state integration of the quantum dots onto the blue LED die

For liquid-state integration, we fabricated a LED structure that held QD solution on top of the blue LED die. We prepared a transparent PDMS polymeric lens (Figure 3.8a) that was mechanically stable and that could recover its surface against the needle holes after the injection. The main advantage of PDMS lens is its scalability for mass production due to its quick production time and low cost [115]. In addition, the light extraction can be sensitively controlled by changing the lens design form a semi-sphere to flat lens geometry. We placed the lens on top of the blue LED chip (in Figure 3.8b and Figure 3.8c- left), and the polymeric lens and the LED chip board were adhered together by a commercial UV curable polymer and cured for stabilization of the lens on top of the board (Figure 3.8c-middle). Afterward, QD solution was injected into the PDMS polymer lens by using a typical micro-syringe (Figure 3.8c-right and 3.8d). To check the functionality of the hybrid LED device, red-emitting CdSe/CdS/ZnS and green-emitting CdSe//ZnS/CdSZnS QD solutions were injected into the device, respectively, and white light generation was observed while the LED was turned on (Figure 3.8e).

For display application, we injected red- and green-emitting QDs with optical densities of 0.033 and 0.048 on a blue LED die at 455 nm, respectively (see Appendix A for the detailed characterization of the blue LED die). The total emission spectrum that was generated by the QDs and LED die was shown in Figure 3.8f. The generated white light corresponded to (x, y) tristimulus coordinates of (0.31, 0.32) in CIE 1931 color gamut with luminous efficacy of optical radiation (LER) of 368 lm/W and color correlated temperature (CCT) of 6298 K. The LE of the white LED was measured 64 lm/W (see Figure 3.8j [25, 116-130]). By mixing the synthesized QDs with phosphorous, it is also possible to achieve high LE [131]. The intensity spectra of white LED at different injection currents from 10 mA to 150 mA were shown in Figure 3.8g, and the (x, y) tristimulus coordinates remained with small changes (Δx=0.002, Δy=0.003) in the white region due to non-photoluminescence-saturation of the QDs at higher injection currents. Furthermore, the functionality of the RGB LQD-LED was tested in the display panel in Figure 3.8h. Two manufactured white LQD-LEDs were used as a backlight in a LCD TV, and the LQD-LEDs led to bright and vivid images. Moreover, the EQE of the LQD-LEDs was measured during time to assess the photostability up to 100 hours (Figure 3.8j). The measured effective EQE at different time intervals, which was calculated by dividing luminous efficiency to luminous efficacy of optical radiation (LE/LER) [132], confirmed the stability of LQD-LEDs, which showed its potential for long-term applications. In addition to its high efficiency, liquid-state integration of QDs can be advantageous in terms of stability. It can prevent the elevation of LED temperature especially at higher injection currents [100]. According to the theoretical analysis, the use of green-emitting QDs on blue LED could generate efficiency level above 100 lm/W, if they were injected at an optical density range in-between 0.1 and 0.2. To further boost the LE, we injected green-emitting QDs at a concentration of 0.13 on blue LED die, which led to a GB-based white LED with a record performance of 105 lm/W (green star symbol in Figure 3.8j & see Appendix A for properties of GB white LED).

Since QDs have narrow emission linewidths (~35 nm) in comparison with inorganic phosphors (~100 nm), they can be spectrally-optimized to match the color filter spectra in LCDs by using the combination of the narrow emitters for display application, which can simultaneously result in both high color gamut and LE. According to our simulation, while sweeping the peak wavelengths by 5 nm steps and using the parameters of the optimized QDs, a maximum possible color gamut of 104% or a maximum LE of 120 lm/W are achievable. Moreover, for lighting application, our simulations showed that the highest CRI value of 84 with LE of 80 lm/W is achievable by using the optimized green- and red-emitting QDs (see Appendix A).

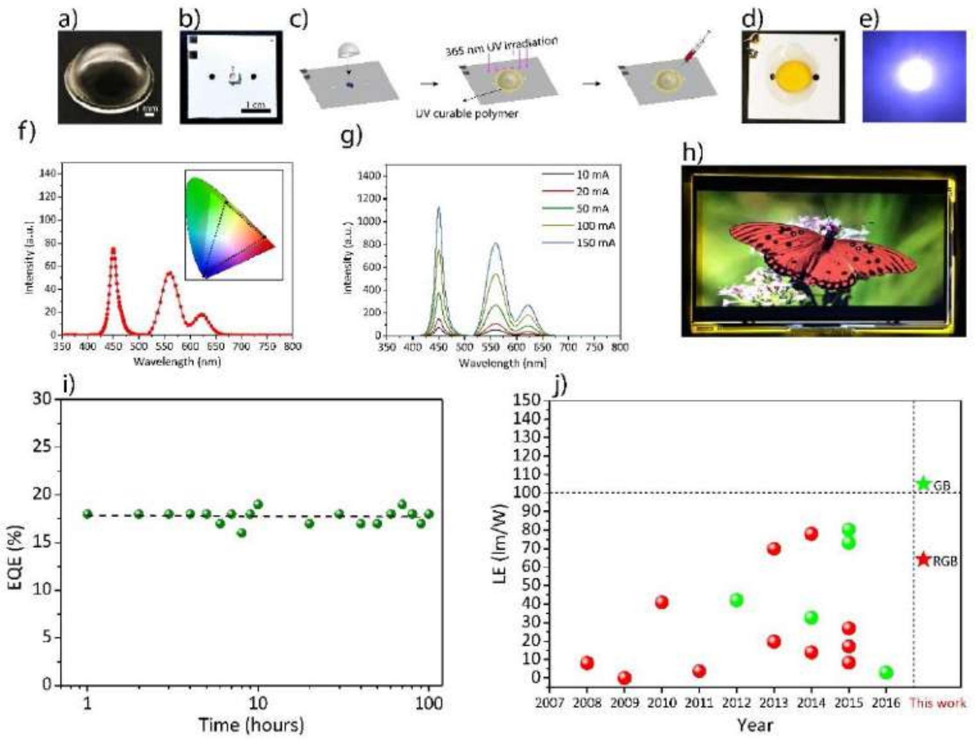

Figure 3.8: (a) PDMS polymeric lens. (b) The blue LED die on board. (c) The schematic of the fabrication process. The PDMS lens was placed on top of the chip and adhered via UV curable polymer with 365 nm UV irradiation. Afterward, red- and green-emitting QDs were injected into the lens. (d) Photograph of LQD-LED under ambient light. (e) Photograph of LQD-LED when it was turned on. (f) The spectrum of the white LQD-LED. Inset: The black dashed triangle showed the color gamut in CIE 1931 color coordinates. (g) The white LED spectra at different injection currents from 10 to 150 mA. (h) The photograph taken from a display illuminated by two white LQD- LEDs that were used as backlights in a 7-inch LCD TV. (i) Optical stability of the LQD-LEDs after 100 hours illumination. (j) The LE of the previous reports that use QDs as the only color converter. The red and green colors refer to dual- and single-type of quantum dot combinations for white LEDs, respectively. The red and green stars correspond to our dual-(RGB) and single-type (GB) of quantum dot combinations for white LEDs, respectively.

3.1.7 The comparison of liquid-state, solid-state and close-packed quantum dot-based LEDs

The performance of the LQD-LED was compared with close- packed QD-LED and solid-state QD-LED that was made of QDs in PDMS polymer matrix (see Appendix A for detailed explanation of preparation). In all the device architectures, the total amount of QDs was kept fixed, and Figures 3.9a and 3.9b showed OFF and ON states of the close-packed and solid-state QD-LEDs, respectively. For close-packed QD-LED, QDs were dried on top of the blue chip, and they showed aggregation and cracks in the film, which resulted in less green and red color conversion (Figure 3.9c). This led to an undesirable (x, y) tristimulus point of (0.19, 0.07) outside the white region (Figure 3.9c) and aggregation also induced significant reduction of the efficiency with a LE of only 11 lm/W (as shown in Figure 3.9e). While the QDs were in polymer matrix, this resulted in an effective color conversion (Figure 3.9d), which had an (x, y) point of (0.35, 0.37) in the white region with a CCT of 4812 K (Figure 3.9d). However, solid-state QD-LED showed an LE of 31 lm/W (as shown in Figure 3.9e) due to host material effect. Comparatively, the LQD-LED showed the highest LE of 64 lm/W due to keeping their high efficiency in liquid form (see Figure 3.9e).

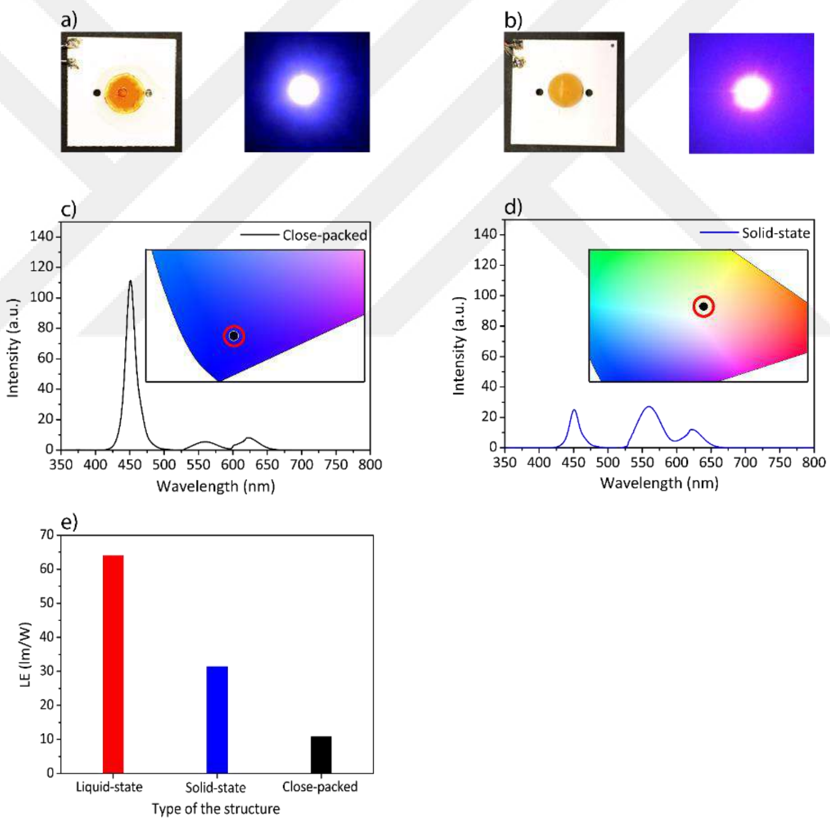

Figure 3.9: (a) The photograph of close-packed QD-LED when it was turned OFF under ambient light (left) and turned ON (right). In the close-packed QD-LED configuration, QDs were directly dried on top of the blue LED die. (b) The photograph of solid-state QD-LED when it was turned OFF under ambient light (left) and turned ON (right). In the solid-state QD-LED configuration, QDs were dispersed and cured in a PDMS polymeric matrix on top of a blue LED die. (c) The spectrum of the close-packed QD-LED at a current injection level of 10 mA. Inset: (x, y) tristimulus coordinates of the close-packed QD-LED. (d) The spectrum of the solid-state QD-LED at a current injection level of 10 mA. Inset: (x, y) tristimulus coordinates of the close-packed QD-LED. (e) The LE of all the QD-LEDs at a current injection level of 10 mA.

3.1.8 Conclusion

In conclusion, there were critical factors that were satisfied to achieve high-performance QD integrated white LEDs. First, high- efficiency LEDs were achieved by the liquid-state integration which significantly increased the luminous efficiency even more than 50% due to suppressed host material effect. Second, as the QY of the QDs increased, the number of emitted photons to the absorbed photons enhanced significantly, which resulted in a more efficient color conversion and consequently higher efficiency of the white LEDs. Third, the color converted spectra were fine-tuned to keep the peaks close to the peak of the eye sensitivity function, which led to high luminous efficacy of the optical radiation and simultaneously luminous efficiency as well. Moreover, minimization of the other losses such as using blue LED chips with higher EQE, refractive index matching, and using a back reflector can directly boost the performance levels reported within this study. In addition, our theoretical calculations showed that the combination of state-of-the-art blue LED die with an EQE of 85% and red- and green-emitting QDs with QY of unity has the potential to exceed the level of 200 lm/W, which was targeted by SSL road map until 2020. Therefore, we believe that liquid-state integration of QDs hold great promise for efficient white LEDs, and after quantum dot TVs in the market we may see them in the near future in lighting as well.

3.2 Ultra-efficient and High-quality White Light-emitting Devices Using Fluorescent Proteins in Aqueous Medium

This section is based on the publication "*Ultra-efficient and High-quality White Light-emitting Devices Using Fluorescent Proteins in Aqueous Medium*" S. Sadeghi, R. Melikov, D. Conkar, E. N. Firat-Karalar, and S. Nizamoglu, Advanced Materials Technologies (2020) 2000061. Reproduced (or "Reproduced in part") with permission from Wiley Online Library Copyright 2020.

Transformation of electronics towards "green" and efficient devices is critical for environmental sustainability and energy future. So far, majority of efficient lighting devices have been realized by artificial optical materials such as rare-earth-elements-doped phosphors, colloidal QDs and dyes. In this section, we determined red-emitting mScarlet and green-emitting eGFP fluorescent proteins for high-performance white LEDs, expressed them in living Escherichia coli and integrated the purified proteins in their natural aqueous environment onto blue LED chips. The aqueous integration preserved quantum yield levels of the proteins above 70% in the device architecture and facilitated a high LE of 81 lm/W with a color rendering index (CRI) of 83, which is the most efficient eco-friendly white LED reported to date. Moreover, we also optimized the concentration ratio of red- and green-emitting proteins and demonstrated white protein-based LEDs with a maximum CRI of 92.

3.2.1 Introduction

Eco-friendly electronic devices combined with high-efficiency are urgently required for environmental sustainability. Today, conventional devices consume high level of energy during their usage that is mostly produced by the fossil fuels. To meet the energy need, massive amount of carbon dioxide is globally released, which leads to negative side effects such as air pollution and climate change [133]. According to the recent report by World Bank, the climate change will force the migration of tens of millions of people around the world in the next decades [134]. Consequently, the transition toward efficient technologies is important. Furthermore, before the lifetime of devices finishes, significant amount of electronics and their components are disposed. Although there is strong effort to recycle electronic waste (e-waste), 60% of the discarded electronics (i.e., 12 million tons) still remain in the nature [135]. This constitutes serious problems for environmental sustainability, variety of species and public health. Therefore, one possible solution to further decrease the e-waste problem is incorporation of biomaterials into devices. However, since the biomaterials are primarily designed for their ecological compatibility, their in-device performance for the targeted electronic applications may not be optimal. Hence, simultaneous satisfaction of eco-friendly-material content and high performance is critical for the transformation of electronic devices toward waste-free and efficient technologies.

During the last two decades, LEDs have revolutionized the lighting industry by exposing themselves as a fitting alternative to old-fashion light sources such as incandescent light bulbs and fluorescent lamps due to their high efficiency, long lifetime and small size [3-6]. In addition to the improvement of the EQE of blue LEDs, the studies were mainly concentrated on the performance improvement of the white LEDs for outdoor, indoor and display applications [7, 8]. For that, different types of doped phosphorous were investigated as the wavelength converters to obtain efficient white light generation [9, 10]. For example, a typical InGaN blue LED chip is covered with the mixture of red-emitting Eu-doped nitride phosphorous and green-emitting Eu-doped silicate phosphorous [4]. Other than that, blue LED chip was directly coated with a yellow-emitting YAG:Ce phosphorous [136, 137]. Despite the efficiency of the phosphorous, there are concerns on their ecology risks, sustainability and toxic effects [11].

Instead of phosphorous, colloidal QDs are strong substitutes as color-conversion material for white LEDs [138-140]. They are synthetic nanomaterials in the range of 1-10 nm, which show unique size-dependent optical properties due to the “quantum confinement” effect [55, 141, 142]. Recently, QD-LEDs have been extensively studied to increase their efficiency levels and LEDs operating above 100 lm/W were demonstrated [53] (as shown in the previous section). However, the cadmium content of these QDs can have negative ecological effects. Recently, there are significant efforts to synthesize toxic-heavy-metal-free QDs and integrate them in LEDs [128, 143, 144]. According to the European Union research report [145], the toxicity of the QDs due to their vast number of substances, sizes, shapes, and crystallinity structures, chemical compositions of core and shell and also purity need to be carefully investigated to assure the safe usage of the QDs. Other than QDs, white LEDs can also be fabricated by using organic dyes [146]. However, the major limitation of organic dyes is their low photo-bleaching thresholds, which lead to short operational lifetime [7]. Another type of down-conversion white light sources, which has been investigated extensively during recent years, is organic-inorganic hybrid or all-inorganic perovskite-based LEDs. Although perovskite nanomaterials advantageously possess tunable narrow emission and high PLQY [147, 148] for LED applications, improvement of their stability [149] is currently under investigation.

Alternatively, fluorescent proteins offer excellent optical properties for LEDs including high photo-stability, narrow emission linewidth and high photoluminescence quantum yield (PLQY) in the visible range (, i.e. 400-700 nm). Different from the other color-conversion materials, they can be produced in a wide variety of living organisms such as bacteria, mammalian cells and vertebrates [30, 31]. Furthermore, these proteins can be also digested in the mammalian stomach [150]. These advantageous properties in terms of biocompatibility, edibility and optical properties make them a unique alternative for waste-less down-conversion material in LEDs [32, 33].

The efficiency and color-rendering performance of fluorescent protein-based white LEDs (PLEDs) remain low. The fabrication of PLEDs generally include the liquid- to solid-state transition, which reduces the quantum efficiency (QE) of the fluorescent material due to the introduction of non-radiative channels [13]. For example, blue-, green- and red-emitting protein coatings as color conversion layers led to the maximum LE of 15 lm/W [62]. Instead, the interaction between proteins and the polymer blend matrix can be controlled. By this way, a maximum LE of 55 lm/W was reported by using fluorescent proteins on UV LED chips [32]. To realize an eco-friendly and efficient lighting technology that has a comparable performance with the other color-conversion materials, the optical performance of the protein-based LEDs (PLEDs) needs to be further improved. In this section, we demonstrate fluorescent protein LEDs with ultra-high efficiency over 80 lm/W and excellent color rendering index (CRI) over 90, which are free of toxic elements and can be used for both illumination and display applications.

3.2.2 Simulation of the different combinations of green- and red-emitting fluorescent proteins

To understand the achievable LED performance levels by fluorescent proteins, we performed optical simulations that consider all the photonic processes including absorption, reabsorption, inter-absorption and their infinitely-many possible interactions [113]. For white light generation, one strategy is the combination of green- and red-emitting down conversion fluorescent materials with blue LEDs. We simulated the efficiency and the color quality of the generated white light with the combinations of the most efficient green-emitting fluorescent proteins including Citrine, Sapphire, mHoneydew, eGFP and red-emitting fluorescent proteins including mScarlet, mCherry, mPlum and dTomato. The selected green-emitting proteins show the PL peak wavelengths of 530 nm, 509 nm, 560 nm and 510 nm with the liquid-state PLQY of 76%, 78%, 12% and 64% for Citrine, eGFP, mHoneydew and Sapphire, respectively. The red-emitting proteins have the PL peak positions of 580 nm, 610 nm, 650 nm and 595 nm with the liquid-state PLQY of 69%, 22%, 10% and 71%, respectively (Figure 3.10a and 3.10b). The absorbance, PL spectra, and PLQY of the different proteins in liquid-state, electroluminescence (EL) spectrum and EQE of the blue LED (42.5% without polymeric lens) and the dimensions of the polymeric lens were input parameters in the simulation. The simulation was repeated for the combinations of green- and red-emitting fluorescent proteins for a wide variety of optical densities on blue LED, and more than 7 million spectra were produced. CIE 1931 color space, tristimulus functions, and eight standard reflectance spectra for color rendering analysis were utilized to analyze the generated spectra (see Appendix B for the detailed explanation of the simulation process). If their tristimulus color coordinates were inside the white region [151], the photometric properties of the generated white LEDs such as luminous efficiency and color-rendering index were calculated. According to the solid-state lighting roadmap [57], CRI more than 80 is desirable and based on the simulations, the protein combinations of Citrine + mScarlet, eGFP + mScarlet, eGFP + dTomato, mHoneydew + mScarlet and mHoneydew + mCherry lead to the maximum achievable CRI of 81,93,91,80 and 86, respectively. However, not all of the combinations result in high efficiency. For example, the combination of Citrine + mScarlet only leads to the LE of 61 lm/W. Similarly, the combinations of mHoneydew + mScarlet and mHoneydew + mCherry only yielded to the LE of 15.2 lm/W and 11 lm/W, respectively. In comparison, eGFP + dTomato and eGFP + mScarlet are the most efficient combinations with LE over 80 lm/W (Figure 3.10c). Between these two combinations, we selected eGFP and mScarlet, which can lead to the highest CRI among the combinations concurrently leading to a maximum LE of 83 lm/W.

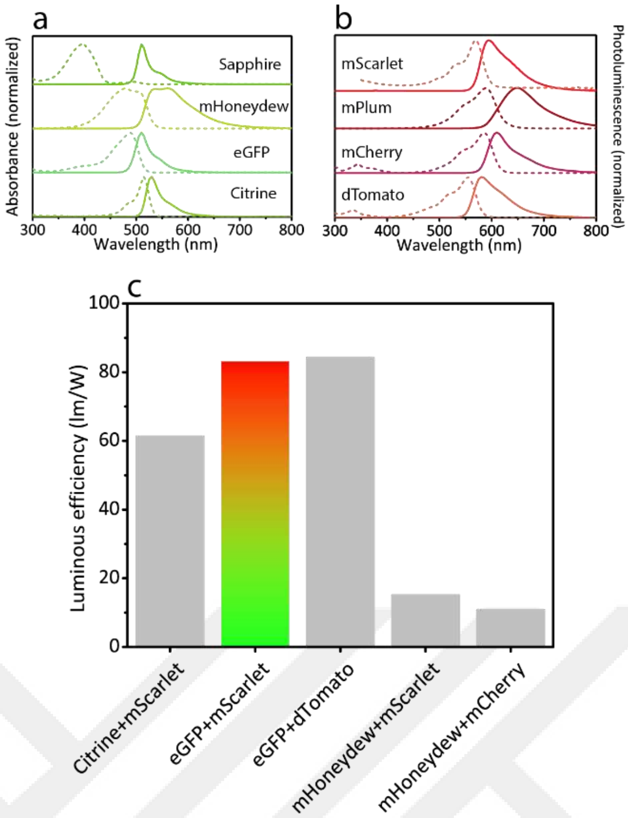

Figure 3.10: The absorbance and photoluminescence spectra of the investigated (a) green- and (b) red-emitting fluorescent proteins in the simulations. (c) The luminous efficiency of the generated white LEDs using different combinations of green- and red-emitting fluorescent proteins having CRI higher than 80.

3.2.3 Synthesis and optical properties of fluorescent proteins

For the synthesis of the determined fluorescent proteins (FPs), eGFP and mScarlet coding sequences were cloned into pDONR221 and then to GST bacterial expression vector pDEST-GST by Gateway cloning (Thermo-Fisher) as stated previously (Figure 3.11a) [17, 33]. *E.coli* BL21 (DE3.1) expressing GST-eGFP and GST-mScarlet was grown in lysogeny broth (LB) supplemented with 50 µg/ml ampicillin to OD_{600}=0.6. Expression of FPs was induced by 1 mM isopropyl-1-thio-beta-D-galactopyronoside (IPGT) for 3 days at 30 °C. For purification, cells were centrifuged at 4000 rpm for 20 minutes at 4 °C. Pellet was re-suspended in GST-binding lysis buffer (137 mM NaCl, 2.7 mM KCl, 10 mM Na_2HPO_4, 1.8 mM KH_2PO_4, 0.25 M KCl, protease inhibitors (10 µg/ml each of aprotinin, leupeptin, pepstatin, and 1 mM phenylmethylsulfonyl fluoride)). Cells were incubated with 1 mg/ml lysozyme on ice for lysis of cell wall and sonicated 7X for 20 seconds. The lysate was centrifuged, and the resulting supernatant containing GST-eGFP and GST-mScarlet were affinity purified by glutathione-Sepharose (GE Healthcare). After concentrating the purified proteins using 10.000 NMWL centrifugal filters (Amicon® Ultra-4), proteins were dialyzed into PBS and then ddH_2O using Slide-A-

Lyzer^{TM} dialysis cassettes (Thermo-Fisher). Concentrations of GST-eGFP and GST-mScarlet were estimated as 5 mg/ml by Bradford assay (Figure 3.11a) [152]. The purified eGFP and mScarlet show PL peak emission wavelengths at 509 nm and 595 nm with FWHMs of 33 nm and 65 nm, respectively (Figure 3.11b and 3.11c).

Since in general, fluorescent materials are incorporated as solid films for LED applications, we formed a close-packed film of red- and green-emitting proteins and tested their in-film efficiencies by using an integrating sphere. The QE in solid-state corresponded to 10.2% and 6.5% for eGFP and mScarlet, respectively (Figure 3.11d and 3.11e). However, these levels are not suitable to realize efficient light sources. Instead, the main nanostructure of fluorescent proteins were designed and perfected by nature to efficiently operate in aqueous environments. Their structure consist of an central chromophore surrounded by a helix structure composed of β-sheets [60, 61]. The helix structure acts as a "bumper" and effectively protects the chromophore from the close contact between the neighboring molecules in aqueous environments, which can prevent the coupling of excitons to non-radiative centers and can decrease their QE (Figure 3.11a) [153]. We measured PLQY of eGFP and mScarlet in aqueous medium as 70.8% and 77.8% (Figure 3.11d and 3.11e). Hence, incorporation of fluorescent proteins in liquid state appears as a viable strategy for efficient white LEDs.

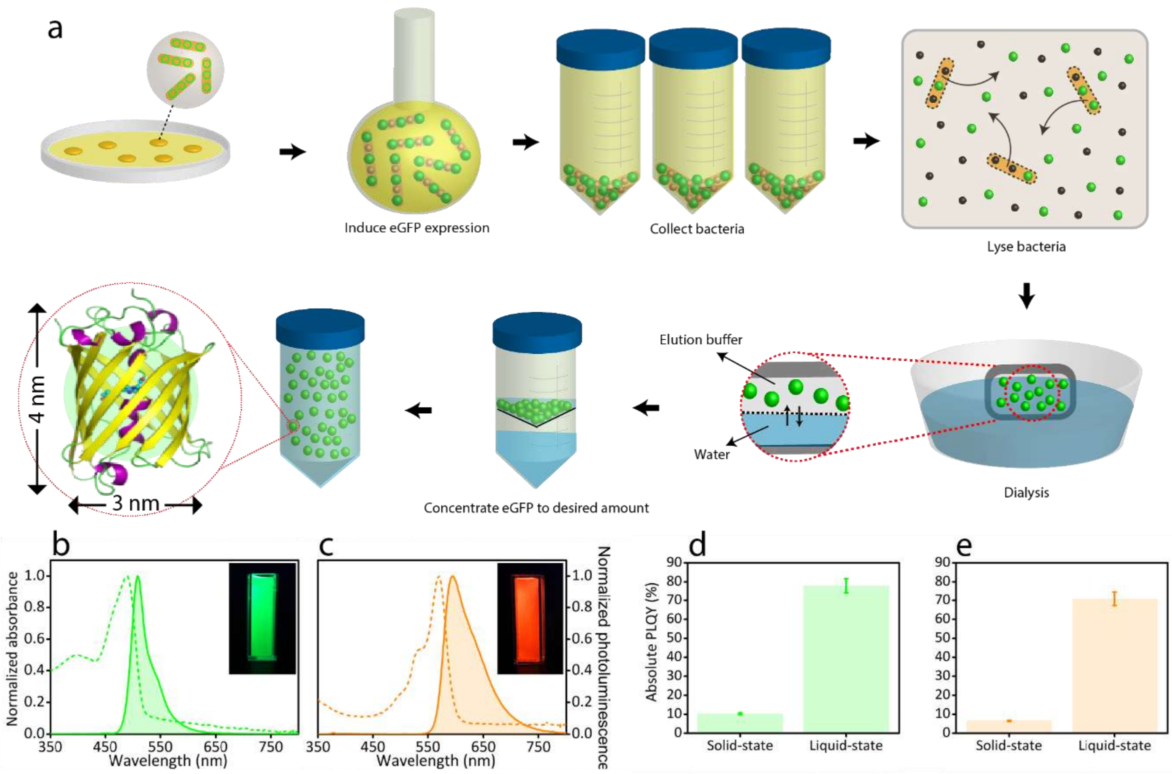

Figure 3.11: (a) The step-wise synthesis procedure of the eGFP and mScarlet fluorescent proteins. The normalized absorbance (dashed line) and PL (solid line) spectra of (b) eGFP and (c) mScarlet fluorescent proteins dispersed in aqueous medium. Inset: Photos of eGFP and mScarlet fluorescent proteins aqueous solutions under UV irradiation. The PLQY of the (d) green-emitting eGFP and (e) red-emitting mScarlet proteins in solid-state and aqueous medium (n=3).

3.2.4 Optimization of PLQY and LED fabrication

For highly efficient white LEDs, the optical efficiency of the liquid color-conversion layer of fluorescent proteins is critical. As shown in the simulation of the optical performance of the green- and red-emitting proteins, by increasing the optical density of eGFP from 0.0006 to 2.13 and the optical density of mScarlet from 0.0002 to 0.74, the PLQY was decreased from 78% to 12% and from 71% to 17%, respectively (Figure 3.12a and 3.12b). This behavior was also in agreement with experimental results, in which by increasing the optical density of the protein solution from 0.008 to 0.17, 0.18 and 2.13, the PLQY of the proteins decreased significantly from 77% to 72%, 72% and 10%, respectively (Figure 3.12a). Similar behavior was also realized in the optical performance of the mScarlet proteins, in which by increasing the optical density from 0.004 to 0.07, 0.12 and 0.74, the PLQY decreased from 71% to 59%, 52% and 18%, respectively (Figure 3.12b).

In order to realize the optical parameters of the generated photoluminescence form the combination of green- and red-emitting proteins at different optical densities, which consequently yields to the points with maximum LE and CRI, we performed the optical simulation of the generated light by changing the concentrations of the protein solutions (Figure 3.12c and 3.12d). The maximum achievable LE of the combination of eGFP and mScarlet was 83 lm/W at the optical density of 0.17 and 0.07 for eGFP and mScarlet proteins, respectively (Figure 3.12c). The simulation also showed that at the optical density of 0.18 and 0.12 of eGFP and mScarlet, the maximum CRI was achievable, which corresponded to 93 (Figure 3.12d).

To fabricate LEDs capable of incorporating proteins in liquid-state, we used an encapsulation method, which holds the proteins solution on top of the blue LED chips similar to section 3.1 [53, 154]. For that, we designed and cured a hemispherical PDMS polymeric lens with the inner and outer diameters of 7 mm and 9 mm (Figure 3.12e). At the next stage, the cured PDMS lens was placed on top of the LED (Figure 3.12e), and was fixed by using the UV curable resin and subsequent UV illumination (Figure 3.12f). The red-emitting mScarlet and green-emitting eGFP solutions were mixed together and injected inside the polymeric lens by using a typical micro-syringe (Figure 3.12g). After the injection, the polymeric lens has the ability to close the penetration hole, which assures the leakage proof ability of the liquid LED system. When the injection current was applied to the LED, the blue LED effectively excited the protein solutions. The combination of the green emission from eGFP proteins, red emission from mScarlet proteins and blue electroluminescence resulted in the white light generation (Figure 3.12h).

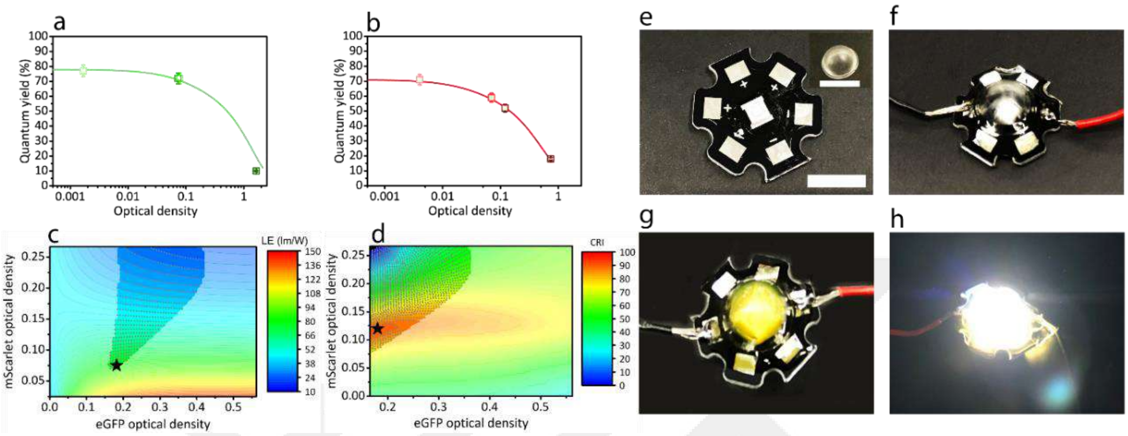

Figure 3.12: The simulation (line) and experimentally measured (squares) of the PLQY of (a) eGFP and (b) mScarlet at different optical densities. The simulation of (c) LE and (d) CRI of the generated light from the combination of green- and red-emitting proteins with different optical densities. The specified dark area represents the white region in tristimulus color coordinates. Star symbols in (c) and (d) represent the points with the highest achievable LE and CRI. (e) The blue LED chip, which was used for the fabrication of liquid PLED. Inset: PDMS polymeric lens. Scale bar = 1 cm (f) The polymeric lens was fixed on top of the blue LED by using UV curable resin. (g) The mixture of red-emitting mScarlet and green-emitting eGFP solutions was injected into the device by using a typical micro-syringe. (h) The white liquid PLED is turned on at a current injection level of 10 mA.

3.2.5 White LEDs with improved optical performance

The white LED with high CRI

High CRI of a light source ensures appearance of the good saturated and true natural colors [7] of the illuminated objects, which is important for indoor lighting applications such as offices and homes. To mimic the simulated spectrum having CRI of 93, we injected 11 µl of green-emitting eGFP with the optical density of 0.18 at 488 nm and 8 µl of red-emitting mScarlet with the optical density of 0.12 at 595 nm into the polymeric lens, respectively. The resulting device showed a spectral output profile similar with the simulation (Figure 3.13a). For CRI calculation, color-rendering ability of the lighting device is characterized by eight international agreed-upon test samples (from R1 to R8) having distinct reflection profiles in the visible spectrum. These test samples correspond to different colors in the visible spectrum such as light greyish red (R1), dark greyish yellow (R2), strong yellow green (R3), moderate yellowish green (R4), light bluish green (R5), light blue (R6), light violet (R7) and light reddish purple (R8) [7]. As a result, the lighting device showed CRI from R1 to R8 as 88, 97, 88, 82, 94, 95, 96 and 96, respectively (Figure 3.13b). These CRI levels show that the lighting device has the lowest color rendering ability at moderate yellowish green color and best color-rendering ability at light violet and light reddish purple colors. Moreover, the generated white light has the high color rendering ability to reproduce strong red colors with the R9 value of 95, which makes the PLEDs ideal for high quality lightning and display applications (see Appendix B for further R9-R15 values). The average CRI corresponds to 92 meaning that white LED has the ability to render the true color of the illuminated object. To qualify it, objects having different colors were lightened with the device (Figure 3.13c), and the device facilitates observation of true and vivid colors of the lightened objects. Moreover, the spectral stability of the device was investigated at different current injection levels (Figure 3.13d). By increasing the current from 10 mA to 90 mA, (x, y) color coordinates showed a minor change of 0.02 in the x-direction and 0.05 in the y-direction (equal to the Duv change from 0.0119 to 0.0016) of the CIE 1931 color space (Figure 3.13e). At the same time, the CRI also showed a stable profile and the fabricated white PLED showed CRI of 91, 90, 91 and 92 at the current injection levels of 30 mA, 50 mA, 70 mA and 90 mA, respectively.

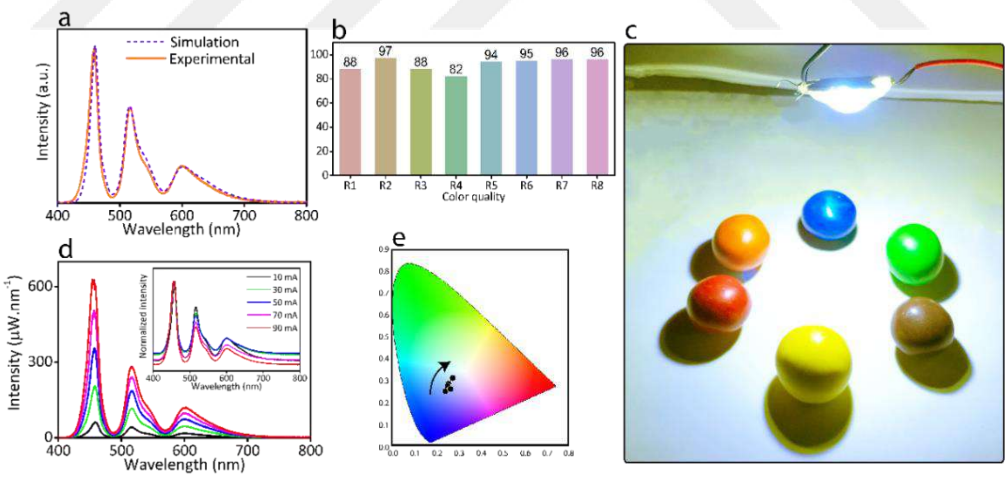

Figure 3.13: (a) The simulation and experimental intensity spectra of white PLED with the highest CRI point in Figure 3.12d. (b) The color rendering index from R1 to R8 of the PLED. (c) Photograph showing when PLED illuminates objects having different colors. (d) The intensity spectra of the PLED with highest CRI in different injection currents ranging from 10 mA to 90 mA. Inset: The normalized intensity spectra. (e) The (x, y) coordinates for the generated white light at different current levels from 10 mA to 90 mA in CIE chromaticity color space.

The white LED with high LE

Based on our simulations in section 3.2.2, eGFP and mScarlet fluorescent protein-based lighting devices has the potential to reach efficiency levels above 80 lumen per electrical Watt (Figure 3.10c). For that, we injected 8 µl of green-emitting eGFP with the optical density of 0.17 at 488 nm and 6 µl of red-emitting mScarlet with the optical density of 0.07 at 595 nm onto the blue LED. The lighting device showed the highest LE of 81 lm/W with CRI of 83 at the injection current of 10 mA (Figure 3.14a). The simultaneous realization of high LE and CRI offers the opportunity of its use both for illumination and display purposes (Figure 3.14a). The optical performance of the PLED was also investigated at higher injection currents (Figure 3.14b). By increasing the current from 10 mA to 90 mA, the intensity of the liquid LED did not experience a significant spectral change (Figure 3.14b). The spectral photo-stability of the device was also observed that the (x, y) coordinates of the generated white light only change as $\Delta x = 0.03$ and $\Delta y = 0.03$ (equal to the Duv change from 0.0022 to -0.0014) in the color tristimulus (Figure 3.14c). Moreover, the LE of the device at 10 mA, 30 mA, 50 mA, 70 mA and 90 mA was measured as 81 lm/W, 78 lm/W, 76 lm/W, 74 lm/W and 71 lm/W, respectively. Here, the decrease of the efficiency stems from the EQE drop of the blue LED. At the same time, the photo-stability of the liquid PLED was also measured when it was constantly turned on during 100 hours (Figure 3.14d). The EQE of the PLED was constant as 26.4% (dashed line in Figure 3.14d) during 100 hours at the current injection level of 10 mA. Moreover, since liquid type QD-LEDs can significantly lower the surface temperature [155], for high current injection levels two compartmentalization of liquid can be used to save the proteins against thermal quenching (see Appendix B). The liquid just above the blue LED (i.e., first compartment) can be used for proper thermal management and above it (i.e., second compartment) the proteins can stably operate at low temperatures.

The achieved luminous efficiency level in this study (81 lm/W) is higher than the previous RGB lighting devices using colloidal QDs (Figure 3.14e).[25, 32, 53, 62, 116-119, 121-125, 129, 130, 156-162] The red-points in Figure 3.14e showed the LE levels of QDs having toxic heavy metals such as cadmium, lead, etc. However, there are environmental and health concerns on the use of toxic-heavy-metal containing devices [163]. On the other side, the maximum efficiency levels reported for the “green” LEDs utilizing toxic-heavy-metal-free quantum dots such as $CuInS_2$, InP, Cu-doped ZnInS, etc. reached to the maximum efficiency level of 78 lm/W [130]. These QDs also need to be ensured before the industrialization due to the potential risks involved with the vast span of crystal structure, sizes, shapes, chemical compositions and purity, as declared by European Union [145]. Comparatively, fluorescent proteins offer a material class that is biocompatible and even edible, which can lead to efficient and zero-waste products.

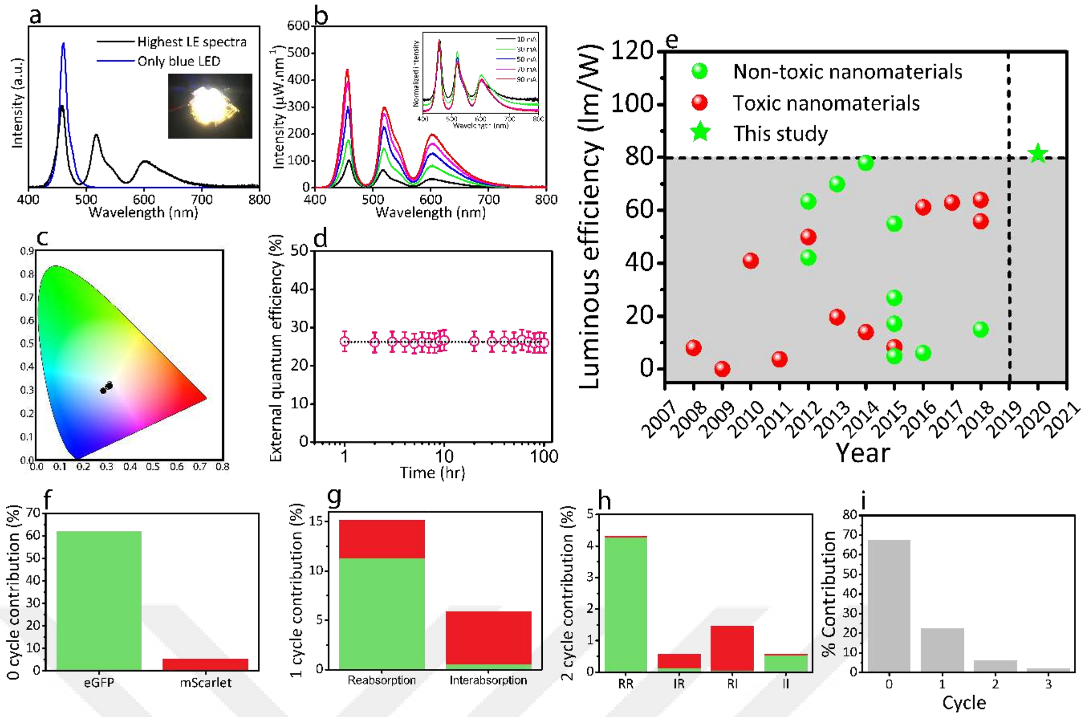

Figure 3.14: (a) The intensity spectra of the white PLED with the highest luminous efficiency. Inset: The illuminated PLED spectrum at 10 mA. (b) The intensity spectra of the liquid PLED at higher injection current levels ranging from 10 mA to 90 mA. Inset: The normalized intensity spectra. (c) The (x, y) coordinates of the generated white light at different injection currents in CIE chromaticity color space. (d) The photo-stability of the PLED during 100 hours at 10 mA (n=3). (e) The luminous efficiency summary of the previously reported colloidal nanomaterial-based white LEDs [25, 32, 53, 62, 116-119, 121-125, 129, 130, 156-162]. (f)-(h) The contribution of generated photoluminescence from each fluorophore in the total output spectrum after each photonic process. Green and red colors represent the portion of the photoluminescence contribution from green- and red-emitting proteins in the generated white light in each graph, respectively. RR, IR, RI and II represent two consecutive photonic processes of reabsorption-reabsorption, interabsorption-reabsorption, reabsorption-interabsorption and interabsorption-interabsorption, respectively. (i) The contribution of the generated photoluminescence from the double fluorophore mixture after each cycle of photonic process.

3.2.6 The optical analysis of the photonic processes

We simulated and analyzed the responsible photonic processes of radiative energy transfer for the efficient white light generation (having LE of 81 lm/W). Initially, the green- and red-emitting proteins were excited by the blue LED and the down converted photoluminescence was generated, denoted as the zeroth cycle (Figure 3.14f and Appendix B). Due to the higher absorbance of the eGFP in the blue LED spectral region, the zeroth cycle contribution of the eGFP protein to the output spectrum was above 60%, while it was only 5% for mScarlet protein (Figure 3.14f). After this initial process, the photoluminescence can be generated as a result of interabsorption between red- and green-emitting proteins or reabsorption, denoted as the first cycle (Figure 3.14g). According to our simulation the contribution of eGFP emission to the output photoluminescence spectrum due to reabsorption was 11.3% in comparison with the mScarlet having 3.8% (Figure 3.14g). In addition, there is also significant contribution to the total photoluminescence via interabsorption. Due to the strong overlap between the absorption of mScarlet and photoluminescence of eGFP proteins, the portion of the interabsorption from green to red is 5.4%, while the reverse interabsorption process contributes only 0.5% (Figure 3.14g). Moreover, the total contribution of two consecutive cycles (Figure 3.14h) of either reabsorption and/or interabsorption is 6.1% to the observed photoluminescence. Thus, while the total number of cycles increases, the contribution of the generated photons to the output was decreased from 67% for the zeroth cycle to only 2% for the third cycle (Figure 3.14i).

The engineering of the LED lights for different applications beyond the basic illumination such as human health, wireless communication and optical imaging demands high spectral control and engineering of the light sources [164]. To this end, fabrication of the white LEDs with high tuning ability of the generated light spectrum can be useful. In liquid LEDs, the feasibility of the liquid injection or ejection of fluorescent materials introduces a high-level tuning ability of the optical processes. The optical parameters of the generated white light can also be tuned by changing the optical density of eGFP and mScarlet proteins, as shown in our simulations as well. The tunability of the LED light can be also achieved by using active polarizers [165] and multi-package architectures [148]. Hence, the spectral content of the fabricated white PLEDs can be tailored for the targeted application.

3.2.7 Conclusion

In this section, we demonstrated eco-friendly, efficient and high-quality fluorescent protein-based white LEDs. For that, we produced red-emitting mScarlet with the absolute PLQY of 70.8% and green-emitting eGFP with the PLQY of 77.8%. Instead of incorporating the fluorescent proteins into a polymeric matrix that dramatically lowers efficiency of LEDs, since the helix structure of the proteins are optimized to operate efficiently in aqueous environments, we integrated them directly onto a blue LED in their natural aqueous environment. PLEDs, which are free of toxic elements, showed record-breaking performance levels, which were also predicted and supported by our simulations.

Significant improvements were made towards increasing the efficiency of the nanomaterials-based color conversion white LEDs during recent years, and there is still a huge gap between the reported efficiency levels and the targeted efficiency level of 200 lm/W for the white LEDs according to the solid-state lighting (SSL) road map [57]. To this end, this work constitutes a step toward eco-friendly, efficient and high-quality white LEDs, which can be used in both illumination and display applications. We believe that the liquid-state integration of the biocompatible nanomaterials (such as fluorescent proteins) can pave the way reaching toward this goal in the near future. Furthermore, ultra-efficient and eco-friendly lighting devices can be obtained by a multidisciplinary approach combining genetic engineering that can design and express proteins matching with the spectral requirements for efficient white light generation, optoelectronics further pushing the efficiency of the blue LEDs and optical engineering facilitating better device designs. Therefore, fluorescent protein-based LEDs may appear as an alternative in the near future for lighting and display applications. The study related to this section was highlighted as the frontispiece in the June 2020 issue of the Advanced Materials Technologies journal (Figure 3.15).

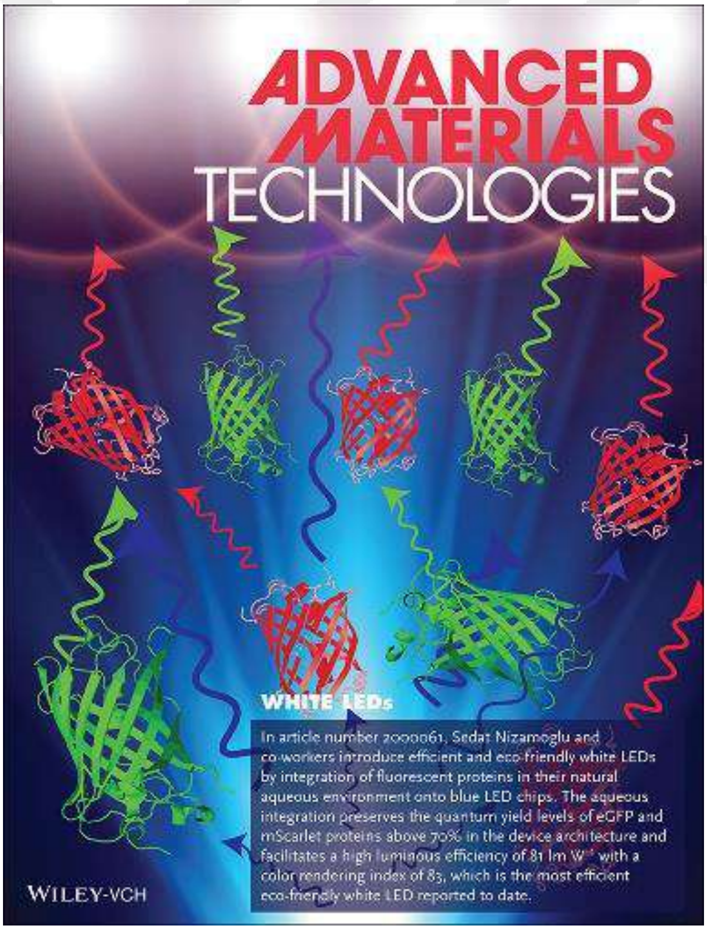

Figure 3.15: The frontispiece of the Advanced Materials Technologies (June 2020), which highlights the fluorescent protein-based liquid LEDs.

3.3 Efficient White LEDs Using Liquid-state Magic-sized CdSe Quantum Dots

This section is based on the publication "*Efficient White LEDs Using Liquid-state Magic-sized CdSe Quantum Dots*" S. Sadeghi, S. K. Abkenar, C. W. Ow-Yang, and S. Nizamoglu, Scientific Reports 9.1 (2019) 1-9. Reproduced (or "Reproduced in part") with permission from Nature Publishing Group Copyright 2019.

Magic clusters have attracted significant interest to explore the dynamics of quantum dot nucleation and growth. At the same time, CdSe magic-sized QDs reveal broadband emission in the visible wavelength region, which advantageously offer simple integration of a single-type of nanomaterial and high color rendering ability for white LEDs. In this section, we optimized the quantum yield of magic-sized CdSe QDs up to 22% via controlling the synthesis parameters without any shelling or post-treatment process and integrated them in liquid-state on blue LED to prevent the efficiency drop due to host-material effect. The fabricated white LEDs showed color-rendering index and luminous efficiency up to 89 and 11.7 lm/W, respectively.

3.3.1 Introduction

QDs are formed with an evolution from molecules to crystalline nanosolids [166, 167]. Among these nanosolids, magic clusters or magic-sized nanoparticles have attracted significant attention to understand the non-classical nucleation and growth of inorganic nanoparticles due to their controllable synthesis [166]. Depending on the geometry of the close-packed nanoclusters, they consist of specific number of atoms due to high thermodynamic stability [168], and they show heterogeneous growth, which indicates a discrete jump from one structure with a specific number of atoms to another one [169]. Hence, these magic-sized QDs were applied as a seed to grow exotic structures such as nanorods, tetrapods, belts, nanoplatelets, sheets and ribbons [25, 111, 170-175]. The white emission from the magic-sized QDs is due to their surface trap-states. At the surface of the CdSe QDs, there are some discoordinated Se atoms, which would provide the electrons and holes trap states inside the band gap region, and can be considered as dangling bonds [176]. The range of radiative recombinations in trap-sates will collectively lead to the white emission (Figure 3.16). Beside the structural properties, magic-sized QDs exhibit high surface to volume ratio, which leads to a high density of trap-states on the surface. In general, trap-states in QDs are not desirable due to the inefficiency that they lead for optoelectronic device applications [177]. Because of that, trap-states were passivated by binding a suitable ligand on the surface [178] or by the growth of a shell [179]. Differently, the trap-states of the magic-sized show broadband surface-state emission, which covers the entire visible region and can be used for LEDs [55, 180, 181]. Advantageously, they have benefitted a simple core structure with the integration of only one type of QDs comparing to the other traditional QD-based white LEDs, which use two or more types of QD layers [182, 183]. In addition to integration, simple synthesis of these nanomaterials can enhance its use for LED application [184]. For that, magic-sized CdSe QDs are the appropriate nanomaterials that can have both simple integration and synthesis at the same time.

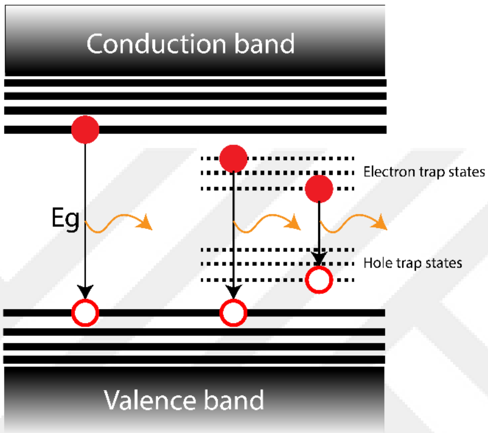

Figure 3.16: The schematic representation of surface trap-states in colloidal QD band energy diagram. The electron and hole recombinations from the trap states lead to the range of visible wavelengths emission, which by combination result in white color.

However, the quantum yield of magic-sized CdSe QDs are poor and white LEDs made of them have low efficiency. Schreuder and co-workers synthesized ultra-small white-emitting CdSe QDs with quantum yield of ~4% [185]. Later, they increased the quantum yield of ultra-small CdSe QDs to 45% by using formic acid for approximately two days post-treatment; even with this treatment, the predicted luminous efficiency levels of the white LEDs remained only 3.8 lm/W [186]. Other than CdSe QDs, Sapra and co-workers synthesized white-emitting CdS QDs with quantum yield of 17% [187]. Organic-capped ZnSe QDs [188, 189], and white-emitting layered perovskite with quantum yield of 9% have also been investigated [190]. Moreover, magic-sized $Zn_xCd_{13-x}Se_{13}$ alloyed structures with maximum quantum yield of 6% were achieved by Mn doping [191]. Recently, efficient white-emitting core/shell QDs were reported, which were prepared with a synthesis procedure that requires Mn doping on copper gallium sulfide QDs and extra step of zinc sulfide shell growth on core QDs [192]. Although there are worries about the industrial use of cadmium-based nanomaterials in devices due to their toxic material content [193], they continue attract significant scientific attention on LEDs due to their advantageous optical properties [194-198].

Different from the previous studies, we maximized the quantum yield of white-emitting CdSe QDs by controlling the synthesis parameters of reaction time and temperature, and their quantum yields reached up to 22% without shell formation or post treatment process for white LEDs. To prevent a possible decay of the QD efficiency in device architecture due to host material effect, we hybridized QDs in liquid-state on blue LED die that led to a white LED with a color rendering index up to 89 and a luminous efficiency of ~10 lm/W at a high current injection level of 0.1 A, which was higher than the previous studies.

3.3.2 Synthesis of trap-assisted white-emitting CdSe QDs

CdSe QDs were synthesized based on the previous method [25, 111]. In a typical synthesis, 0.4 mmol CdO (0.0515 g, >99.99% Aldrich), 0.8 mmol of octadecylphosphonic acid (0.268 g, >98% TCI) and 16 ml of tri-n-octylamine (>97% TCI) were mixed together in a 100 ml three-neck flask. The solution was heated to 150 °C under nitrogen inert atmosphere. At this temperature, the solution was evacuated by vacuum and placed under inert atmosphere repeatedly. After degassing process, the solution was heated to 310 °C under nitrogen atmosphere. Once the temperature was stable, 1 ml of 0.792 g selenium (>99.5% Aldrich) in trioctylphosphine (90% Acros) precursor (2M TOPSe) was injected into the solution. After 180 seconds of the reaction time, the heating was stopped and the mantle was removed. The synthesized core CdSe QDs were purified, centrifuged and re-dispersed in toluene. To ensure the reproducibility and scalability of the CdSe QDs synthesis, each synthesis was performed three times.

3.3.3 The optimization of the quantum yield

To achieve efficient and broad photoluminescence spectrum, which covers the entire visible region, we optimized radiative surface trap-states of CdSe QDs to find the point with highest quantum yield (known as photoluminescence bright point [199]). The photoluminescence bright point, which shows the highest quantum yield was demonstrated by Peng and co-workers by investigation of CdSe QDs in different reaction times, temperatures and precursor ratios. They observed that regardless of the system, solvent and the semiconductor nanocrystal size or shape, there always exist a point with highest quantum yield, which could be found by optimization of synthesis parameters [199]. To find the photoluminescence bright point in our synthesis method, we adjusted the synthesis parameters of hot injection method including reaction time and temperature. After the injection of selenium precursor into the cadmium-containing solution, the CdSe QDs started to nucleate and grow larger until the designated time. Initially, we determined a suitable reaction time for efficient broadband photoluminescence. For that, we selected a reaction temperature of 310 °C and aliquots were taken for different times after the injection of selenium precursor (Figure 3.17a). During the initial times of the reaction (until 120 seconds), the formed QDs were ultra-small, which had an absorbance without any distinct narrow peak in the deep blue and UV region (Figure 3.17a). In addition, these ultra-small QDs only had emission covering the deep blue and UV region, which is not suitable for white LED application. At 120 seconds, a broad tail of photoluminescence spectrum up to 800 nm was observable in the visible region. At 180 seconds, there exist two photoluminescence peaks one at 520 nm, which was possibly originated from the recombination between conduction and valence band and another one at 678 nm, which was due to the surface-states emission. In comparison with 120 seconds, the photoluminescence spectrum at 180 seconds experienced a red-shift due to size increase of the QDs. After 180 seconds, the effective trap-states emission lost its strength and the emission of the inter-band transitions became more dominant, which could be also clearly observed by their emission color detected by naked eye (Figure 3.17b). At the same time, the absorption spectrum also started to reveal clear excitonic transitions. Hence, while the size of the QDs increased, the emission strength of the surface trap-states significantly decreased, which was due to the reduced surface to volume ratio and lower probability of carrier coupling to trap-states due to the larger core size [180]. To further prove the structure of the magic-sized QDs, we investigated the synthesized QDs using HRTEM, which shows the particle size and lattice fringes (Figure 3.17c). The size distribution in TEM image showed the nanoparticles with the averaged diameter of 1.86 nm, which was in agreement with other magic-sized QDs studies [185, 186] (Figure 3.17c and 3.17d).

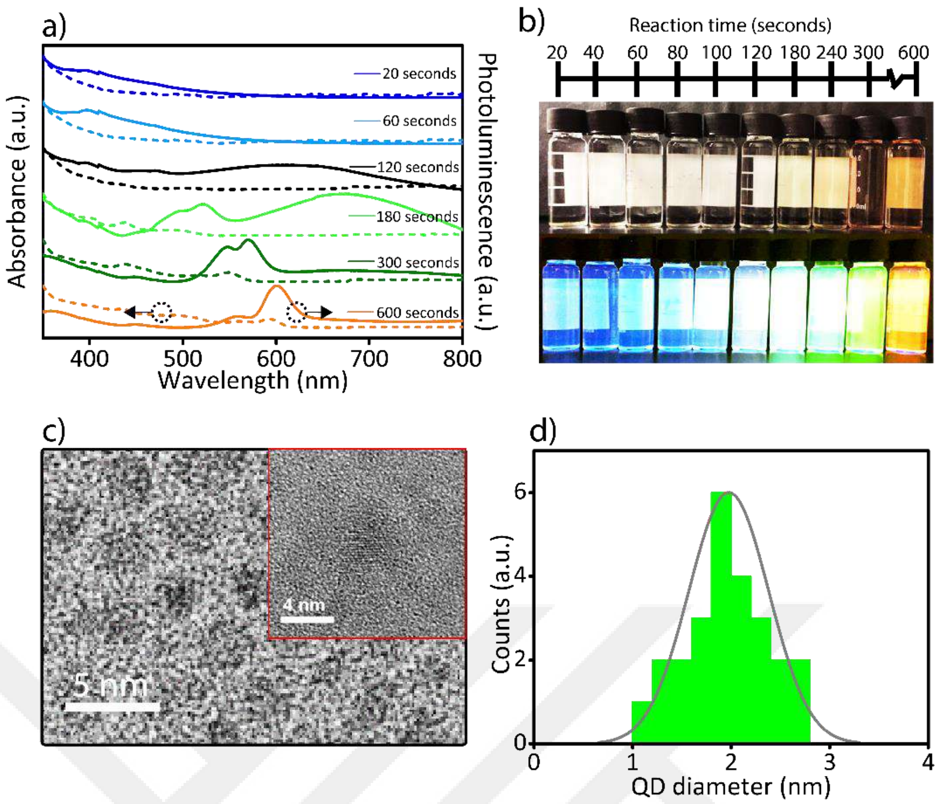

Figure 3.17: (a) The absorbance (dashed line) and photoluminescence (solid line) spectra of the synthesized CdSe QDs at different reaction times ranging from 20 to 600 seconds at 310 °C. (b) The photograph of synthesized CdSe QDs at different reaction times at 310 °C under (upper panel) ambient light and (lower panel) 365 nm UV irradiation. (c) TEM images of synthesized CdSe QDs at 310 °C and 180 seconds. Inset: the HRTEM image of the synthesized QDs. (d) The size distribution of the synthesized magic-sized CdSe QDs.

To optimize the efficiency of QDs, we investigated the quantum yield of the reaction temperatures between 280 °C and 320 °C at the reaction time of 180 seconds, which already showed strong trap-states emission at 310 °C (Figure 3.18a). Similarly, in this reaction time interval (180 seconds), CdSe QDs were emitting white color under 365 nm UV irradiation (Figure 3.18b) due to the broad photoluminescence spectra. We measured the quantum yield of the QDs (in toluene) in an integrating sphere at an excitation wavelength of 375 nm (FS5, Edinburgh Instruments). The quantum yield increased from 10.3% to 22.1%, as the reaction temperature increased from 280 °C to 310 °C and decreased to 8.9% at 320 °C (Figure 3.18c). Therefore, in the following LED studies, we will use QDs with the maximum efficiency, which were synthesized at 310 °C for 180 seconds.

To investigate the dynamics of radiative recombination mechanisms related to inter-band and surface-states transitions, the time-resolved photoluminescence measurement was performed for white-emitting CdSe QDs synthesized at 310 °C at the reaction time of 180 seconds (Figure 3.18d). The peak at 520 nm was attributed to inter-band recombination and the peak at 678 nm was attributed to surface state recombination (see Figure 3.17a). We used two band-pass filters at the photoluminescence peak wavelengths, excited the QDs in toluene at 375 nm and PL decays were fitted by two exponential decays [200, 201]. While the inter-band transition revealed considerably shorter fluorescent decay time (τ= 15 ns), the surface state emission showed longer lifetime (τ= 129 ns) due to trapped charge carriers (Figure 3.18d) [202].

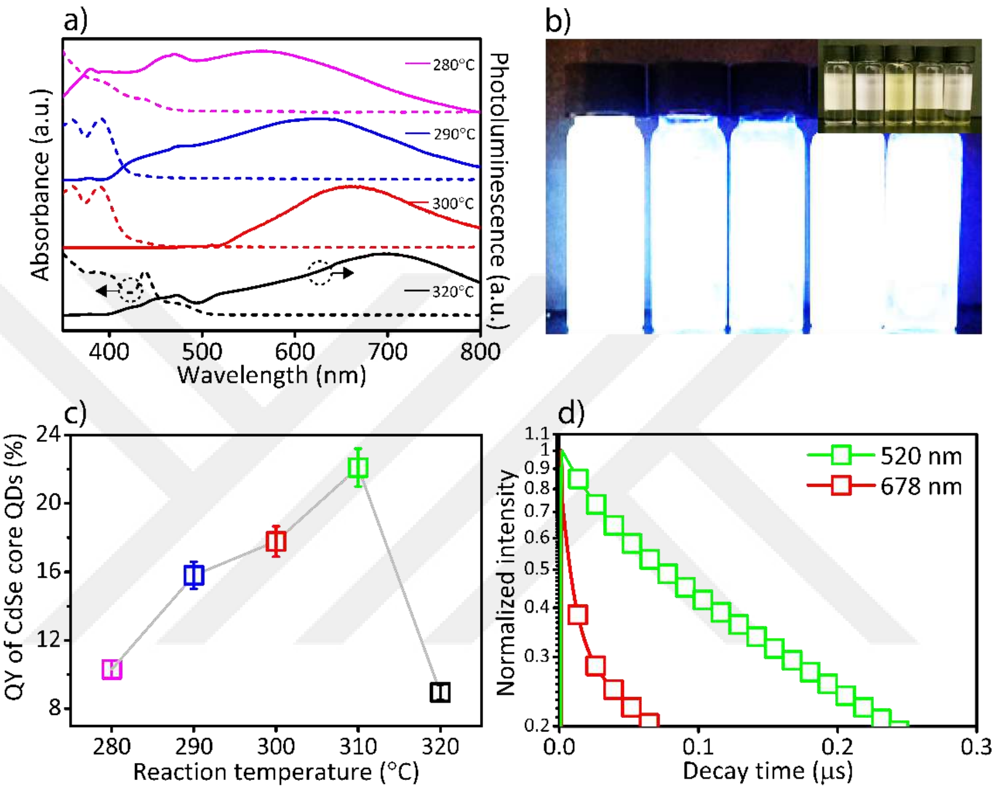

Figure 3.18: (a) The absorbance (dashed line) and photoluminescence (solid line) spectra of synthesized CdSe QDs at different reaction temperatures ranging from 280 °C to 320 °C. (b) The photograph of synthesized CdSe QDs at different reaction temperatures under 365 nm UV irradiation. Inset: the photograph of the as-synthesized QDs under ambient light. (c) The quantum yield of white-emitting CdSe QDs at different reaction temperatures ranging from 280 °C to 320 °C (the averaged quantum yield was measured from total three syntheses at each reaction temperature). (d) The time-resolved spectra of white-emitting CdSe QDs at 520 nm (i.e., inter-band transition), and at 678 nm (i.e., surface states transition).

3.3.4 Liquid white LED based on trap-assisted QDs

The trap-states emission can couple to the host polymeric material in a conventional LED configuration, which can lead to additional non-radiative recombination. As a solution for surface-state emitting QDs, we integrated white-emitting CdSe QDs in liquid-state on blue LED die. For that, we fabricated a polymer lens made of PDMS and positioned it on top of the blue chip by fixing it with a UV curable resin (Figure 3.19a-schematic). Then, the QD solution in toluene was injected onto the die by using a typical syringe (Figure 3.19b). To remove the air bubble inside the lens after the injection, another micro-syringe was used for evacuation (see Appendix C). To generate high efficiency and high quality white light, it is important to integrate appropriate amounts of QDs on blue LED die. For that, we investigated the white-emitting QDs solution with optical densities of 0.017, 0.026, 0.034, 0.041, 0.051, 0.068 and 0.172, and measured the optical properties, respectively (Figure 3.19c). The (x, y) tristimulus coordinates of the generated white light at different optical densities showed a wide range of color temperatures from 2428 K to 5219 K (Figure 3.19d). At optical density of 0.068, the (x, y) tristimulus coordinates corresponded to (0.43, 0.42) in CIE 1931 chromaticity diagram (Figure 3.19d). While the optical density rises, the contribution by the QDs increased until the point with maximum luminous efficiency reached [113] and this boosted the color rendering index level up to 89 at the optical density of 0.068 (Figure 3.19e). At the same time, LED with the QD optical density of 0.068 also showed a luminous efficiency level of 11.7 lm/W, which is the most efficient CdSe magic-sized QD-based white LED, according to our best of knowledge (Figure 3.19f).

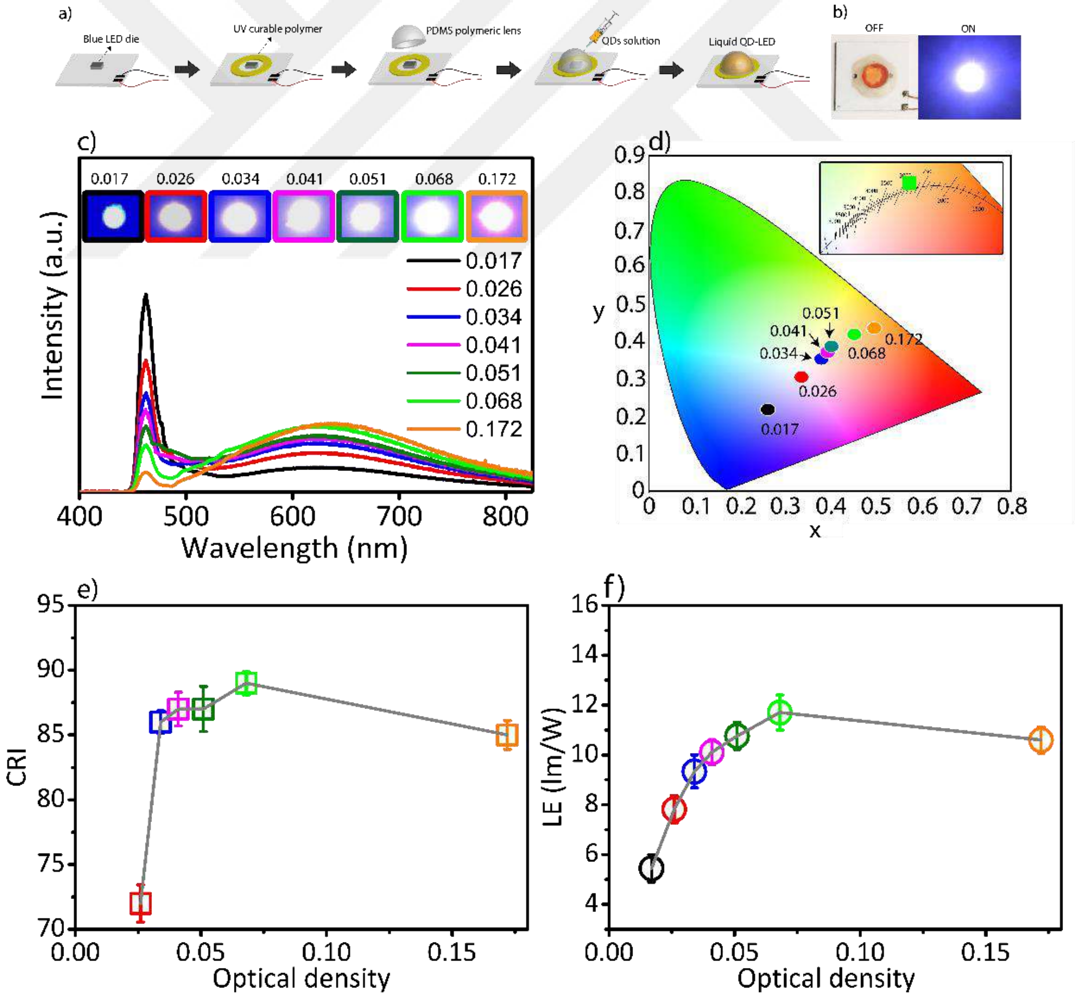

Figure 3.19: (a) The schematic of LED device fabrication. (From left to right) UV curable polymer was used to adhere the blue chip board to the PDMS polymeric lens. After curing, QDs solution was injected into the polymeric lens by using a typical micro-syringe. (b) The photograph of liquid QDs-LED (left) under the ambient light and (right) when it was illuminating with 10 mA injection current. (c) The LED

spectra at different optical densities of white-emitting CdSe QDs ranging from 0.017 to 0.172. The blue LED die was used as pump. (d) (x, y) tristimulus coordinates of the white-emitting QDs at different optical densities. Inset: The zoomed area in which the green square (with optical density of 0.068) showed the highest color rendering index (89) and highest luminous efficiency (11.7 lm/W). (e) The color rendering index and (f) the luminous efficiency of the white QD-LEDs at different optical densities ranging from 0.017 to 0.172 (The averaged CRI and LE data was measured from three LEDs).

3.3.5 The comparison between QD-LEDs with different architectures

To compare the optical performance of the solid- and liquid-state LEDs, we fabricated another LED with the synthesized QDs in close-packed state, in which the same volume of the synthesized CdSe QDs (130 μL) was dried on top of the blue LED chip and the optical properties of the close-packed QD-LED was investigated. For the close-packed QD-LED, the dried QDs on top of the blue LED chip showed aggregation and cracks in the film, which resulted in less color conversion (see Appendix C). This led to an undesirable (x, y) tristimulus point of (0.2, 0.13) outside the white region, and aggregation also induced a significant reduction of the efficiency with a LE of only 3.1 lm/W.

At higher injection currents, the LED spectra do not show a significant change (Figure 3.20a) and the change in the tristimulus coordinates corresponded to $\Delta x= 0.01$ and $\Delta y= 0.02$ from 10 mA to 100 mA. As the injection current increased from 10 mA to 100 mA, color rendering index remained almost constant (varying in-between 86-89), which showed the high stability in the color rendering ability of the generated white light (Figure 3.20b). Moreover, by increasing the current from 10 mA to 100 mA, the luminous efficiency of the white LEDs decreased from 11.7 lm/W to 9.6 lm/W (Figure 3.20c). Furthermore, we placed two QD-based white LEDs as backlight in a 7-inch LCD display (as shown in Figure 3.20d), and the produced image showed that objects and colors were easily and clearly distinguishable by using trap-state emitting QDs (Figure 3.20e). Moreover, the optical stability of the fabricated QDs-based white LEDs was investigated (Figure 3.20f) by constant illumination of the fabricated QD-LED up to 100 hours and the luminous efficiency showed a 20.5% decrease from 11.7 lm/W to 9.3 lm/W, respectively (Figure 3.20f).

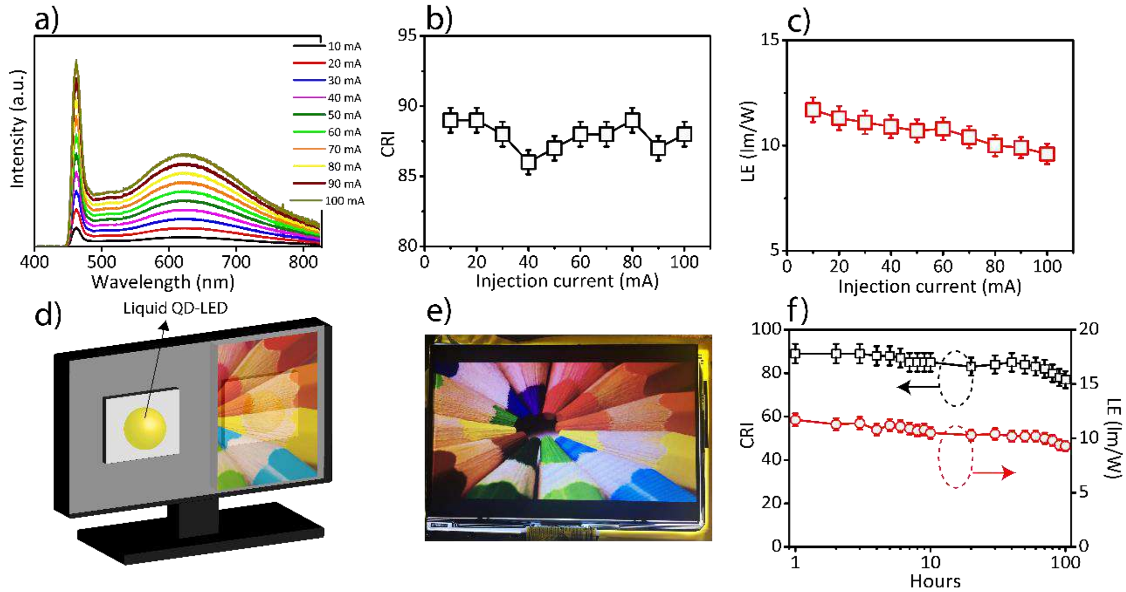

Figure 3.20: (a) The generated white light spectrum at different current levels ranging from 10 mA to 100 mA. (b) Color rendering index and (c) the luminous efficiency at different current levels. (d) The schematic of 7-inch LCD display being illuminated with two magic-sized QD based white LEDs. (e) The photograph of an image generated by the 7-inch LCD display. (f) The optical stability of a magic-sized CdSe QD based white LED during 100 hours.

3.3.6 *The optical stability of the liquid LEDs*

The stability of the fabricated white-emitting QD-based LEDs mainly depends on the optical stability of the blue LED chip and the synthesized QDs. To understand the origin of the efficiency drop, we initially characterized the luminous efficiency of the blue LED. For that, we fabricated LED by injecting only the solvent (toluene) inside the polymeric lens and measured the intensity of the blue LED and luminous efficiency at the same time interval (see Appendix C). We observed that the luminous efficiency of the blue LED chip only decreased 2% (from 15.2 lm/W to 14.9 lm/W) as the illumination time was continued until 100 hours. This proves that the majority of the 25% decrease in the luminous efficiency of the fabricated QD-LED originated from the poor stability of the QDs possibly due to accelerated photo-bleaching and irreversible photo-oxidation of trap-state assisted QDs under constant illumination in the air [203].

3.3.7 *Color gamut calculations*

The color gamut of the fabricated liquid QD-based white LEDs with different optical densities of white-emitting CdSe QDs ranging from 0.017, 0.026, 0.034, 0.041, 0.051, 0.068 and 0.172 were calculated as shown in Figure 3.21a and compared with sRGB standard color gamut by using blue, green and red color filters [142] (see Appendix C). The calculations showed that by increasing the optical density from 0.017 to 0.034, the gamut coverage increased from 82% to 84% and gamut ratio also improved from 90% to

93%, respectively. At the same time, by further increasing the optical density to 0.172, the gamut coverage decreased to 60% and gamut ratio also dropped to 70%, respectively (Figure 3.21b), which limits the applicability of the QD-LEDs with high optical densities of the white-emitting QDs for LCD displays.

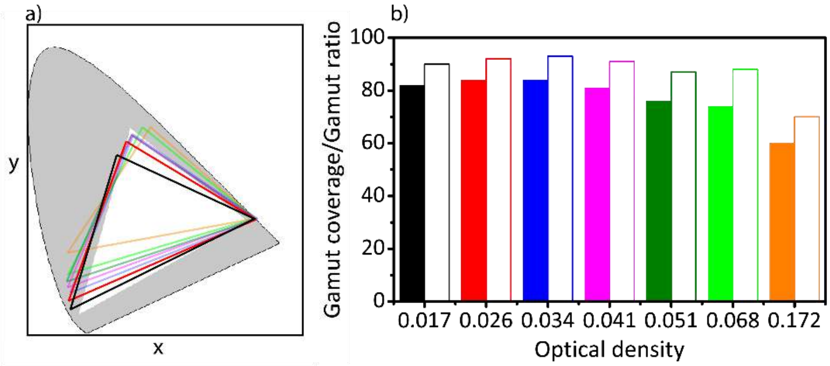

Figure 3.21: (a) The calculated color gamut of the liquid white-emitting QD-based LEDs with different optical densities ranging from (black) 0.017, (red) 0.026, (blue) 0.034, (magenta) 0.041, (dark green) 0.051, (green) 0.068 and (orange) 0.172 in comparison with the (white filled triangle) sRGB standard color gamut in tristimulus color coordinates. (b) The calculated (filled bar) gamut coverage and (unfilled bar) gamut ratio based on (a).

3.3.8 Conclusion

In this section, we synthesized white-emitting CdSe QDs with a quantum yield of 22.1% via the optimization of reaction time and temperature. The synthesis of only core QDs was performed without further shelling, doping or post-processing. We simply embedded the as-synthesized QDs in liquid-state at an optimized optical density onto a blue LED die, which simultaneously achieved a luminous efficiency of 11.7 lm/W and a color rendering index of 89 by using a single-type QDs. The integration of liquid-state magic-sized QDs suppressed the host material effect, and the broad emission spectrum of magic-sized combined with high quantum yield led to high-performance white LEDs. The liquid-state integration of white-emitting QDs with Cd-free materials can pave the way towards efficient and eco-friendly LEDs.

3.4 Ultra-Efficient Green LEDs Using Quantum Dots in Liquid Matrix

This section is based on the publication "*Ultra-Efficient Green LEDs Using Quantum Dots in Liquid Matrix*" S. Sadeghi, R. Melikov, H. B. Jalali, and S. Nizamoglu, IEEE Transactions on Electron Devices 66. 11 (2019) 4784-4789. Reproduced (or "Reproduced in part") with permission from IEEE Xplore Copyright 2019.

Green spectral range, which has the highest human eye sensitivity, is one of the most fundamental colors in lighting and display. QDs offer exceptional optical properties including high QY, strong absorption and narrow emission linewidths for efficient green-emitting diodes. In this section, we demonstrated QD-based LEDs that operate at a luminous efficiency level of 95 lumens per electrical watt, luminous efficacy of optical radiation of 409 lumens per optical watt, and external quantum efficiency of 23.3% in the green spectral region. For that, we synthesized 1-octanethiol-capped CdSe@ZnS QDs with an absolute quantum yield of 91% and integrated them in liquid matrix that allows conservation of the QD efficiency in device architecture. Our simulations were in agreement with the performance of the fabricated QD-LEDs, and they showed that the QD-LEDs can be further improved to reach luminous efficiency levels over 250 lm/W.

3.4.1 Introduction

Colloidal QDs have been identified as a promising class of materials for high-performance light-emitting devices. The nanoscale size of the QDs provides the 'quantum confinement' effect, which enables the effective tuning of band gap and the photonic transitions [204]. The optoelectronic tunability combined with structural adaptability offers them to be incorporated into unconventional and efficient device designs. To tailor their properties, various nano-chemistry routes have been developed that allowed for band alignment engineering, ligand-engineering and wave-function engineering of QDs. These strategies led to exceptional optical features such as high QY, strong absorption and photo/chemical stability [66, 205-212]. Moreover, narrow emission linewidths of QDs allow for the generation of monochromatic colors from violet to red in the visible range for LEDs. Among variety of colors, since monochromatic green color is one of the most fundamental spectral components in RGB (Red-Green-Blue) multi-chip LEDs and it has the strongest contribution to the vision due to the high sensitivity of the eye at that spectral range, QDs are favorable materials to be used for green LEDs.

Today, color-conversion is the most widely used approach for solid-state lighting [48, 213]. In these devices InGaN LED chips excite the fluorescent materials, and the layer generates Stokes-shifted photoluminescence in the targeted wavelengths [25, 104]. For the realization of color-conversion QD-LEDs, different QD incorporation methods were designed and implemented such as the formation of the close-packed QD layers [214, 215] and polymer-QD blends on LED chips [25, 110]. So far, the highest luminous efficiency and EQE of the green color-conversion QD-LEDs was reported as 32 lm/W [215] and 18% [216], respectively. Hence, despite the high-promise of QDs, the reported efficiency levels for green-light generation have so far remained below their high potential due to the low efficiency of QDs inside the color-conversion layer.

The efficiency of the QD-LEDs is directly dependent on the quantum efficiency of the synthesized QDs in device architectures. Incorporation of QDs inside a polymeric matrix or formation of closed-packed films leads to the increase of non-radiative recombinations due to coupling of the inter-band excitons to the defect or non-emitting states, which dramatically reduce the quantum efficiency of the devices [155]. To avoid emission quenching during LED integration, liquid-state incorporation have started to attract significant attention. The liquid-state integration of QDs inside the LED architecture has also been employed for different types of QDs such as graphene [217], CdSe/ZnS [218, 219] and inorganic halide perovskite [220], which led to the improved optical quality and efficiency of the generated photoluminescence. Hence, it has also high potential to obtain efficient green QD-LEDs

Different from the previous studies, we synthesized green-emitting CdSe@ZnS QDs with a QY of 91% by using 1-octanethiol as the ligand and directly integrated them in liquid-state. By this approach, QDs did not experience any efficiency drop due to host material effect. Our QD-LEDs showed a luminous efficiency of 95 lm/W, luminous efficiency of radiation (i.e., luminous efficacy) of 409 lm/W and EQE of 23.3% inside the green spectral region, which has the highest luminous efficiency among the green QD-LEDs reported to date. The fabricated green QD-LEDs showed stable optical performance during 100 hours with a constant EQE of 23%. Advantageously, our green QD-LEDs also showed remarkable optical performance of luminous efficiency and EQE of 83.7 lm/W and 19.6% at the current injection level of 50 mA, respectively.

3.4.2 The synthesis of the highly-efficient green-emitting QDs

We synthesized CdSe@ZnS QDs based on the previous method [221] with some modifications. To achieve the green-emitting QDs with photoluminescence peak wavelength at 503 nm, 0.2 mmol CdO (0.026 g), 16 mmol OA (5 ml), and 4 mmol $Zn(ac)_2$. $2H_2O$ (0.878 g) were combined with each other in a 50 ml flask. The flask was heated to 120 °C in Schlenk line under constant purge of nitrogen gas. At 120 °C, the solution was purged by vacuum and nitrogen repeatedly. After the completion of evacuation process, the temperature was increased to 300 °C. After 1 hour, 0.2 mmol Se (0.016 g) and 3 mmol S (0.128 g) in 2 ml TOP was quickly introduced into the flask. After 10 minutes, 0.5 ml of 1-octanethiol was injected. After the injection, the heating mantle was removed to cool down the reaction. The obtained QDs were washed several times and re-dispersed in toluene solvent.

3.4.3 The structural and optical properties of the synthesized QDs

We synthesized green-emitting CdSe@ZnS QDs by using a one-pot synthesis method, which was performed via an organometallic route. The surfactants with a phosphorous carboxylic acids or amine functional groups generally form weak bonding with the QDs surface, which leads to deterioration of the optical properties due to the detachment of ligands after purification. Instead, we used the ligand of 1-octanethiol with strong binding ability [221]. In a typical synthesis, cadmium oxide, oleic acid and zinc acetate dehydrate were mixed together and heated up to form $Cd(OA)_2$ and $Zn(OA)_2$, respectively (Figure 3.22a). By the simultaneous injection of selenium and sulfur dissolved in trioctylphosphine, CdSe QDs start to nucleate and grow. At the same time, ZnS shell forms gradually on CdSe core in the radial direction, which leads to the formation of CdSe@ZnS QDs (Figure 3.22a). During the synthesis, the non-coordinating solvent of 1-octadecene and long chain fatty acid of oleic acid enabled the control of the nucleation and growth of nanocrystals (Figure 3.22a). In addition, oleic acid simultaneously acted as stabilizer and surfactant, and it also yielded highly-crystalline QDs. As a result, the strong attachment of the ligand to the QD surface and ZnS shell passivation of surface defects yielded to an absolute QY of 91%.

The absorbance and photoluminescence spectra of the green-emitting QDs were demonstrated in Figure 3.22b. The first excitonic peak corresponded to 484 nm and photoluminescence peak wavelength was 503 nm. The XRD measurement was also performed to analyze the crystal structure of the synthesized CdSe@ZnS QDs (Figure

3.22c). The XRD pattern of the synthesized QDs showed the formation of the QDs with the zinc blende crystal structure. The peak positions were well-matched with the bulk CdSe crystal structure peak positions at 25°, 42° and 49° (red lines in Figure 3.22c). The shift of the bulk ZnS peak positions (with the similar zinc blende crystal structure) is possibly due to the phase change in the synthesized alloyed QDs [76]. At the same time, broadening of the XRD pattern peaks is due to the Debye-Scherer broadening [222]. The transmission electron microscopy (TEM) of the QDs was also carried out to measure the size of the QDs (Figure 3.22d). The average size of the QDs was measured as 8.6 nm ± 0.97 nm (Figure 3.22e).

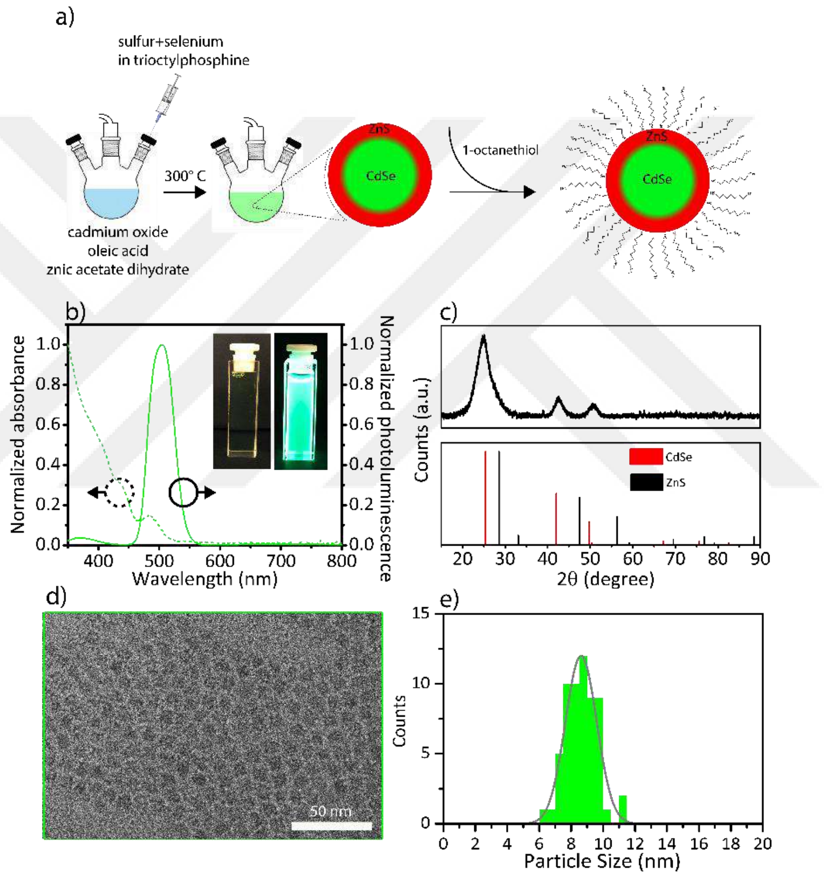

Figure 3.22: (a) The synthesis schematic of green-emitting CdSe@ZnS QDs and the consequent attachment of the 1-octanethiol ligand on top of the QDs. (not drawn in scale) (b) The absorbance (dashed line) and photoluminescence (solid line) of the synthesized green-emitting CdSe@ZnS QDs. (inset-left) The QD solution under ambient light and (inset-right) under 365 nm UV irradiation. (c) The XRD pattern of the synthesized QDs and CdSe and ZnS diffraction peaks with JCPDS card numbers of 18-0191 and 05-0566, respectively.(d) TEM image and (e) size distribution of the synthesized green-emitting CdSe@ZnS QDs, which was calculated from 60 particles.

3.4.4 The fabrication of liquid green QD-LED

To fabricate LEDs incorporating liquid-phase QDs, we prepared a polydimethylsiloxane (PDMS) polymeric lens by curing it in a hemispherical mold with the inner and outer diameters of 7 mm and 9 mm, respectively. A typical blue LED chip with the emission peak wavelength at 460 nm was used to pump the green-emitting QDs (Figure 3.23a). The blue LED chip was soldered on top of the printed circuit board (PCB) (Figure 3.23b). Then, the cured polymeric lens was positioned on the chip (Figure 3.23c), and UV-curable optical resin was applied at the edges of the polymeric lens to render liquid proof. PDMS enables facile design and fabrication of the lens that can allow for low-cost and high-scale production [53, 154]. The final LED architecture with polymeric lens was shown in Figure 3.23d. A micro-syringe was used to inject the synthesized green-emitting liquid QDs inside the polymeric lens (Figure 3.23e). After the injection, PDMS polymeric lens had the ability to close the penetration hole and prevent the QD leakage (Figure 3.23f). CdSe@ZnS QD solution are confined inside the lens (Figure 3.23g), and as a result of the pumping by the blue LED chip, their photoluminescence generated a bright green emission (Figure 3.23h).

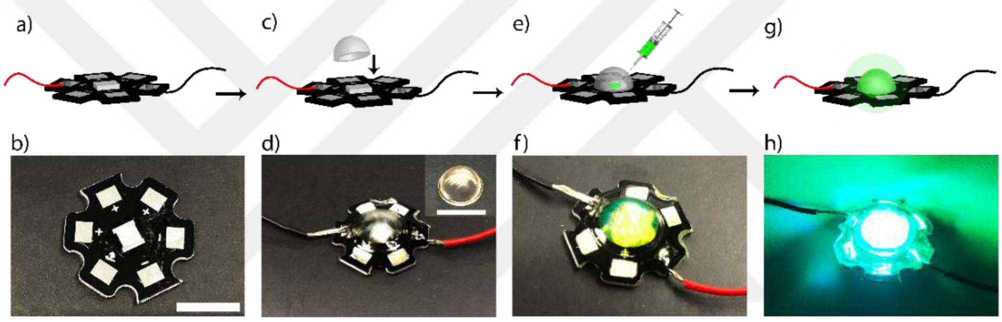

Figure 3.23: (a) The schematic and (b) the photo of blue LED chip soldered on the PCB used to fabricate the liquid QD-LED. (c) The schematic of the process, in which the PDMS polymeric lens was positioned on the chip and cured using the UV-curable optical resin. (d) The photo of the fabricated LED with polymeric lens adhered to the PCB (inset: the photo of the PDMS polymeric lens). (e) The injection schematic of green-emitting QDs solution onto the LED architecture using a typical micro-syringe. (f) The photo of liquid green QD-LED under ambient light. (g) The schematic and (h) the photo of QD-LED when it is turned on, which resulted in green emission (scale bar=1 cm).

3.4.5 The optical analysis of the generated green light

CdSe@ZnS QDs with a QY of 91% have high potential to achieve efficient green QD-LEDs. To understand the observable efficiency levels, we simulated QD-LEDs by using our previous theoretical approach [113] and their contributions to the final liquid QD-LED spectrum (see Figure 3.24c and 3.24d). The input parameters are quantum yield, absorbance and photoluminescence spectrum of the QDs, external quantum efficiency (measured as 42.5% without polymeric lens), electroluminescence spectrum of the blue LED chip and the dimensions of the liquid QD-LED. The EQE of the QD-LEDs was calculated based on Equation (3.1) [7], which is the ratio of the number of emitted photons to the number of injected charges. Our simulation predicted that optical density levels above 1 are required to obtain efficient green LEDs (Figure 3.24d).

$$\eta_{ext} = \frac{\text{Number of photons emitted into free space per second}}{\text{Number of electrons injected into LED per second}} = \frac{P/h\nu}{I/e} \tag{3.1}$$

To investigate the optical performance of QD-LEDs, we injected the as-synthesized CdSe@ZnS QD solutions with different optical densities and measured their optical properties by using an integrating sphere (Figure 3.24a). As the optical density of the QD solution inside the LED elevated from 1.1 to 6.6, green emission increased in comparison with blue due to the stronger absorbance and spontaneous emission by the QD solution. At the same time, the peak position of green photoluminescence shifted from 513 nm to 520 nm due to the reabsorption (Figure 3.24a). The (x, y) color coordinates of the generated light by QD-LEDs approached toward pure green region, while optical density increased (Figure 3.24a and Table 3.1). The intensity spectra of the QD-LED with optical density of 6.6 had a dominant green emission and showed stable spectral response under different current injection levels. A slight change in FWHM was observed from 22 nm to 23 nm and photoluminescence peak position also shifted from 520 nm to 521 nm while the current injection level increased from 10 mA to 50 mA (Figure 3.24b). The EQE of the fabricated QD-LEDs at optical densities of 1.1, 3.3, 4.4, 5.5 and 6.6 are also measured as 31%, 26.4%, 24.6%, 23.5% and 23.3%, respectively, which were in agreement with our simulation results (Figure 3.24c). The EQE of the green QD-LED with the optical density of 6.6 (23.3%) is higher than the state-of-the-art green color-conversion QD-LED with the highest EQE of 20% inside the green spectral region [216].

Table 3.1: The optical properties of green liquid QD-LEDs with different optical densities.

Optical density	Peak position (nm)	LE (lm/W)	EQE (%)	(x, y) coordinates	QY (%)
1.1	513	50	31	(0.13,0.16)	87.1
3.3	519	87	26.4	(0.13,0.54)	79.2
4.4	520	90	24.6	(0.13,0.62)	73.4
5.5	520	93	23.5	(0.13,0.67)	68.5
6.6	520	95	23.3	(0.13,0.69)	63.2

The luminous efficiency is the critical parameter showing the effectiveness of a light source for the transduction of electrical power to optical power sensed by human eye. The luminous efficiency of a light source is obtained by dividing the luminous flux over electrical input power based on Equation (3.2) [7]:

$$\text{Luminous efficiency (LE)} = \frac{\phi_{lum}}{\text{IV}} \tag{3.2}$$

At the same time, luminous efficiency of optical radiation (LER) of a light source is calculated based on Equation (3.3) [7] as follows:

$$\text{Luminous efficiency of optical radiation (LER)} = \frac{\phi_{lum}}{\text{P}} \tag{3.3}$$

, where P is the optical power from the light source. Based on Equations (2) and (3), it is revealed that the luminous efficiency of a light source is dependent on the LER and power conversion efficiency, which can be obtained by the EQE (η_{ext}) of a LED based on Equation (3.4) [7], where λ_1 and λ_2 are the wavelength of the photons absorbed and emitted by the green-emitting QDs, respectively.

$$\text{Power conversion efficiency (PCE)} = \eta_{ext}\frac{\lambda_1}{\lambda_2} \tag{3.4}$$

Based on our simulations, as the optical density of the QD solution rises, since the green emission starts to be more dominant in comparison with blue electroluminescence, LER increases. It was shown that by using the blue LED chip and the QDs with QY of 91%, LER could reach over 400 lm/W at an optical density above 7 for efficient green light generation (Figure 3.24d). To investigate the highest achievable LE, the simulation was performed at different optical densities of QD solution in liquid green QD-LED architecture (Figure 3.24d). Our simulations predicted that while the optical density increased from 1.1 to 6.6, the LE of the QD-LED boosted from 63 lm/W to 94 lm/W, respectively. Although by increasing the optical density of the QD solution from 1.1 to 6.6, the EQE of the green LED decreases from 30.5% to 21.2% (Figure 3.24c), the LER increment from 174 lm/W to 403 lm/W surpasses the decrease in EQE, which results in higher LE of green LED (Figure 3.24d). Experimentally, the LE of the liquid green QD-LEDs at optical densities of 1.1, 3.3, 4.4 and 5.5 were measured as 50 lm/W, 87 lm/W, 90 lm/W and 93 lm/W, respectively (Figure 3.24d), which were in close proximity with our simulations. For the optical density of 6.6, the green LED reached 95 lm/W, which is the highest reported LE of green QD-based LED up to date.

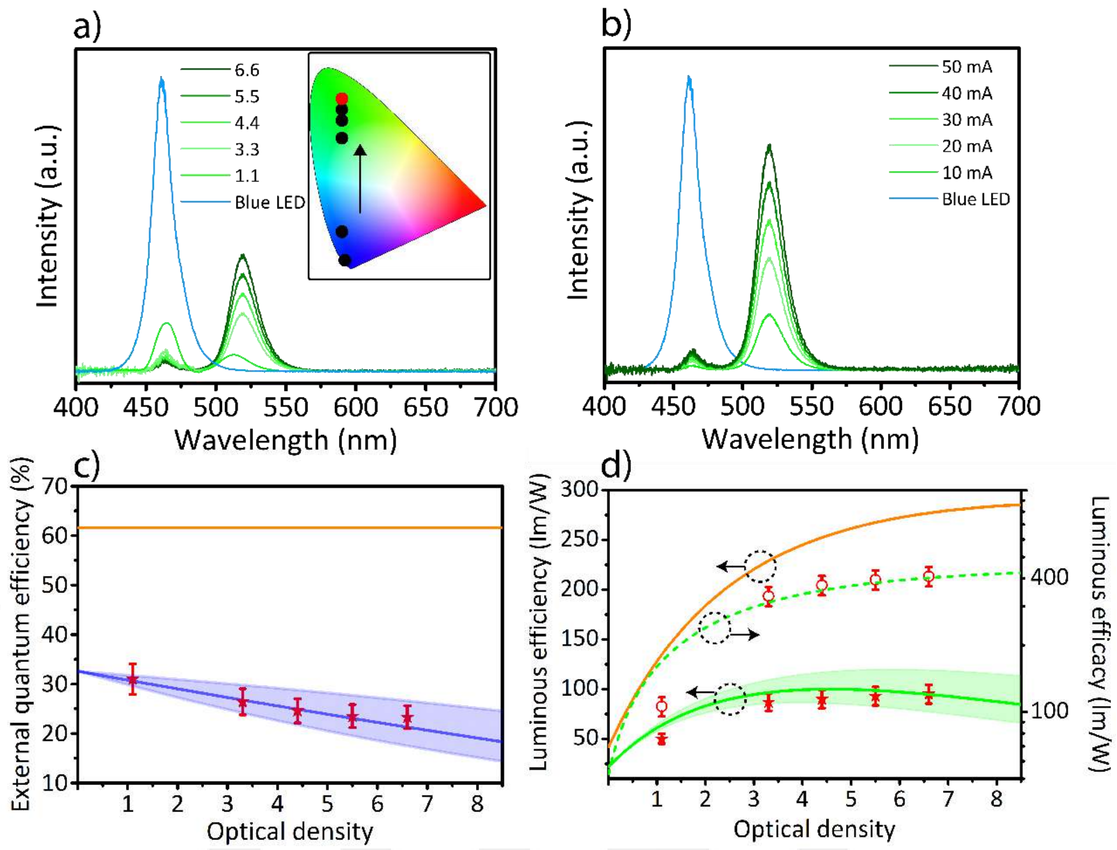

Figure 3.24: (a) The intensity spectra of green QD-based LEDs at different optical densities ranging from 1.1 to 6.6. Inset: the (x, y) color coordinates of the generated green light from the QD-LEDs at different optical densities. (b) The intensity spectra of the QD-LEDs with optical density of 6.6 at different current injection levels ranging from 10 to 50 mA. (c) The simulation considering the reabsorption originated losses (lines and shaded areas) and experimental results (red star and sphere symbols) of EQE, (d) LE and LER of green QD-LED at different optical densities ranging from 0 to 8.5. The solid line represents the simulation results when the EQE of the blue LED was considered as 42.5% (without lens) and the QY of the green-emitting QDs as 91%. The blue and green shaded area are the simulation results with QY of 91% ± 5%. The orange line represents the EQE and LE of green LED with the blue pump with EQE of 80% and green-emitting QDs with unity QY.

3.4.6 The optical stability of the fabricated green QD-LEDs

The stability of the liquid green QD-LEDs (with an optical density of 6.6) was investigated at different current injection levels (Figure 3.25a). It was shown that by increasing the forward current of liquid QD-LED from 10 mA to 50 mA, the LE and the EQE of the green QD-LED dropped from 95 to 83.7 lm/W and 23.3% to 19.6%, respectively. To further evaluate the photo-stability of the fabricated green QD-LEDs, the EQE of the QD-LED was also measured for 100 hours under constant illumination (Figure 3.25b). The EQE remained nearly constant as ~23% (dashed line in Figure 3.25b). The angle-dependent optical density for bare blue LED and QD-LEDs is shown in Figure 3.25b.

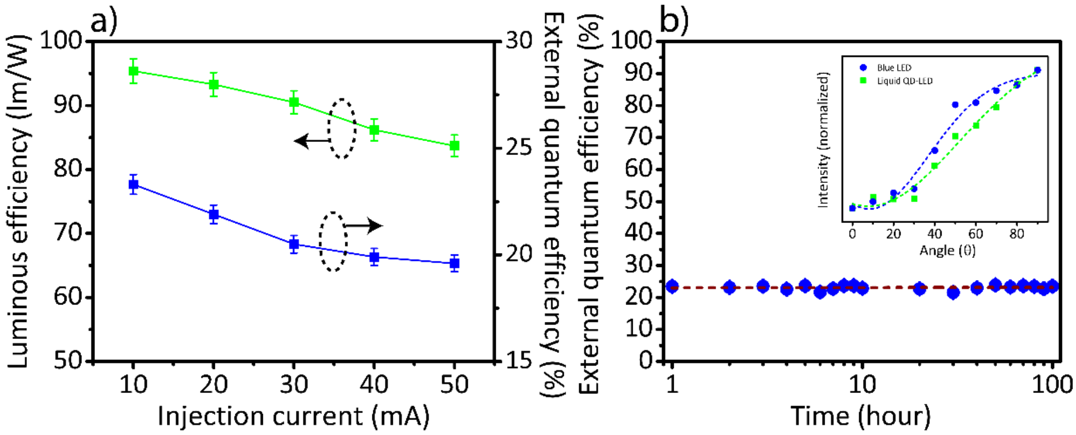

Figure 3.25: (a) Luminous efficiency of the green QD-LED at optical density of 6.6 for different current injection levels from 10 to 50 mA. (b) Photo-stability of the green QD-LED and 10 mA for 100 hours. (n=3). In 100 hours the volume of QD liquid evaporated less than 5%. Inset: Angle-dependent optical density for bare blue LED and QD-LEDs.

3.4.7 The comparison between the efficiency levels of this study and previous studies

The LE of the green QD-LEDs in previous reports [26, 55, 116, 123, 209, 210, 214, 215, 223-235] was summarized in Figure 3.26. In the previous studies, the maximum reported LE was 80 lm/W [236] and in this study we improved the state-of-the-art LE level to 95 lm/W (Figure 3.26). The LE increase in this study is due to the liquid integration of the green-emitting QDs that enables the preservation of the QY of the QDs inside the active device. According to our simulations, there is also significant room for further efficiency improvement. While the EQE of the blue LED was assumed as the highest reported value of 80% [114] with the green QDs having unity QY, our simulation showed that the maximum achievable LE and EQE of the green QD-LED can be improved up to 279 lm/W and 61.6%, respectively (Figure 3.24c and 3.24d).

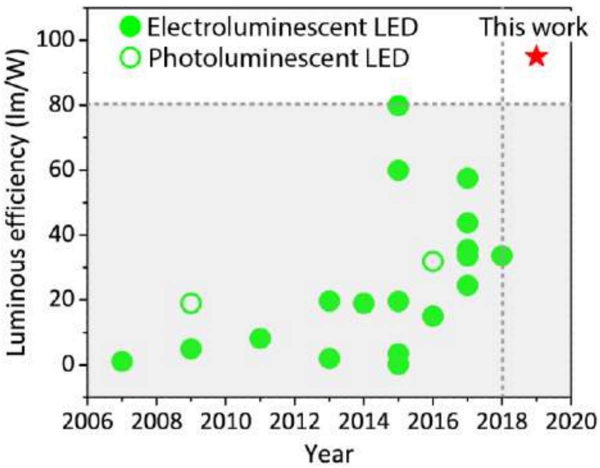

Figure 3.26: The luminous efficiency levels of the green photoluminescent (unfilled circles) and electroluminescent (filled spheres) QD-LEDs reported in previous studies, and the luminous efficiency of the green QD-LED at optical density of 6.6 in this study (red star symbol).

Color conversion QD-LEDs show long lifetimes that are suitable both for display and lighting applications. In addition, the liquid state integration of QDs advantageously facilitates preservation of QY in device architecture. For example, while close-packed films were integrated on blue LEDs at optical density of 6.6, the luminous efficiency significantly dropped to 23 lm/W. However, there exist relevant risks involved with the liquid-state integration such as leakage of the toxic materials, phase change of liquid host material in extreme conditions and the corrosivity of the LED package elements, which can be overcome by using “green” nanomaterials [50] and choosing stable and less-corrosive liquid, respectively.

3.4.8 Conclusion

In this section, green-emitting CdSe@ZnS QDs with a QY of 91% were synthesized and integrated in liquid-state on blue LED die. The fabricated liquid green QD-LEDs showed a maximum LE of 95 lm/W and EQE of 23.3% at an optical density level of 6.6, which is the highest LE reported so far for green-emitting QD-based LEDs. The fabricated green QD-based LEDs also showed the luminous efficacy of 409 lm/W. The performance levels can be further improved by further increasing efficiency of QDs and LEDs. Hence, LEDs using green-emitting QDs in liquid matrix can pave the way towards super-bright green light sources.

3.5 High quality quantum dots polymeric films as color converters for smartphone display technology

This section is based on the publication "*High quality quantum dots polymeric films as color converters for smartphone display technology*" S. Sadeghi, S. E. Mutcu, S. B. Srivastava, G. Aydindogan, S. Caynak, K. Karsli, R. Melikov, and S. Nizamoglu, Materials Research Express 6. 3 (2018) 035015. Reproduced (or "Reproduced in part") with permission from IOP Publishing Group Ltd Copyright 2018.

QDs have high potential to fulfill the ever-increasing demands for high-quality displays due to their outstanding size-tunable optical properties, high quantum yield and reduced costs. The synthesis of efficient materials and their integration in uniform and thin polymeric films are necessary for displays. In this section, we synthesized red- and green-emitting Cd-based QDs with quantum yields of 52% and 74%, respectively. We incorporated the synthesized QDs into the PDMS polymer matrix by using doctor blade technique, which led polymeric films with 123 mm×68 mm dimensions for smart phone displays. We fabricated QD-polymeric films having thickness ranging from 100 to 500 μm to investigate their color conversion and display application performances. By using the large-area QD-polymeric films on blue-emitting backlight unit, the NTSC and sRGB color gamut ratio was measured as 91% and 127%, respectively. Therefore, QD polymeric films show promise for smart phone applications.

3.5.1 Introduction

Display technologies have attracted significant attention both by scientific community and industrial companies. The main motivation in the technological transition is the requirement for brighter, more colorful and high resolution imaging systems for a wide variety of electronic devices (e.g., mobile phones, TVs, smart watches, etc.). Starting from the cathode-ray tube (CRT) display, thin film transistor liquid-crystal display (TFT-LCD) is currently the leading technology. In this technology, the backlight units (BLU) is one of the most important part of display devices, which consist of a light source and light-manipulation components such as light guide plate, diffuser plate, diffuser sheet, prism sheet and reflective polarizer [237, 238]. Today, LEDs are preferred in comparison with traditional sources of lighting such as fluorescent lamps and incandescent light bulbs due to their small-size, high-efficiency, long-lifetime and low-cost [48, 239].

QDs show advantageous properties for display technology due to their size-dependent optical properties, high quantum yield and narrow emission linewidths in comparison with phosphors [201, 225, 230, 240, 241]. Because of that, by varying the synthesis parameters (i.e. reaction time, temperature, precursor ratio, and etc.) it is possible to sensitively tune the emission peak wavelengths that can decrease the yellow and cyan spectral windows, which are not effectively used in the RGB filters in the liquid crystal display module. A QD-based white LED basically consists of a blue LED die, which excites the red- and green-emitting QDs that is integrated on it. The down-converted red and green photoluminescence combine with the extracted blue electroluminescence and generate white light altogether. Although phosphor-based LEDs provide higher luminous efficiency, their color gamut values are relatively low because of their spectrally wide emission in green and red regions [25]. As an alternative, QDs offer higher color gamut levels with their narrower band widths in red- and green-emitting regions (FWHM of around 30 nm for CdSe QDs, whereas ~50-100 nm for inorganic phosphors) [55]. QD-based LEDs have been investigated, however, the previous display applications are generally used QDs in LED structures [25, 55, 160, 224, 225, 230, 242-252].

Previous studies have been performed to investigate the down conversion of the QD-based polymeric films as color conversion layers in LED applications. Lin *et al.* utilized UV LEDs for the excitation of the QDs layers [253], however, the white light color conversion was not investigated. The similar investigation for green LEDs was also performed [254]. However, the green layer dimensions was not sufficiently large for cell phone applications. Different from the previous studies, in this section we demonstrate the design and optimization of large-area and homogenous QD films for the cell phone application. For that, we synthesized efficient red- and green-emitting QDs and embedded them in PDMS polymer matrix as the color conversion films for smart phone application. Tuning the synthesis parameters enabled us to achieve high quantum yield for the synthesized QDs above 50% for red- and green-emitting QDs. Simultaneously, we optimized the photoluminescence peak wavelength of the QDs to achieve an enlarged color gamut with NTSC color space over 90% and with sRGB color space over 120% gamut ratio. We engineered the optimum balance of red (R), green (G) and blue (B) portion of the generated white light by varying the thickness of the red- and green-emitting QDs-polymeric films from 100 to 500 µm. Finally, we demonstrated the whole display architecture by using red- and green-emitting QD-polymeric films on a backlight unit for display.

3.5.2 The synthesis of green- and red-emitting QDs

Synthesis of red-emitting CdSe/CdS QDs

CdSe/CdS quantum dots were synthesized based on the Jang method, partially similar to section 3.1.2 [110]. In a typical synthesis, 0.4 mmol cadmium oxide (0.0515 g, >99.99% Aldrich), 1.6 mmol oleic acid (0.5 ml, 99% Alfa), and 5 ml tri-n-octylamine (>97% TCI) were mixed together in a 100 ml three-neck round bottom flask. The solution was heated to 150 °C under nitrogen inert atmosphere. At this temperature, the solution was evacuated by vacuum and placed under inert atmosphere repeatedly. After degassing process, the solution was heated to 300 °C. Once the temperature was stable, 0.05 ml of 0.792 g selenium (>99.5% Aldrich) in trioctylphosphine (90% Acros) precursor (2M TOPSe) was injected into the solution. After 2 minutes, 1.5 ml of 210 μl 1-octanethiol (>98.5% Aldrich) in 6 ml TOA precursor was injected into the solution incrementally in 90 seconds. The heating continued for 40 minutes until the reaction was complete. Then, the solution was cooled down to room temperature. The obtained red solution consisted of red-emitting CdSe/CdS QDs which was purified with ethanol and re-dispersed in hexane. The methods to improve the FWHM of the red emission QDs can be swift injection of 1-octanethiol ligand, size selective precipitation and surface treatment.

Synthesis of green-emitting CdSe@ZnS QDs

The synthesis procedure for green-emitting CdSe@ZnS alloyed structure is similar to section 3.4.2. Differently, once the synthesis finished, the synthesized QDs will be re-dispersed in hexane solvent in order to facilitate the evaporation and curing of the film.

3.5.3 The optical properties of the QDs

For achieving wide color gamut, it is necessary to have red- and green-emission combined with blue. For this purpose, green-emitting QDs were synthesized based on the synthesis method, which leads to the formation of CdSe core with gradient shell of ZnS [221]. Advantageously, the gradient shell (, in which ZnS concentration increased in the radial direction) provides lower lattice mismatch between CdSe and ZnS at the core and shell interface to yield a better surface passivation and higher quantum yield [200, 255]. The photoluminescence peak wavelength was at 521 nm, which was suitable for a wide color gamut in the final backlight unit application (Figure 3.27a). The synthesized green-emitting CdSe@ZnS QDs was shown in Figure 3.27a under 365 nm UV irradiation. The synthesized green-emitting QDs showed absolute quantum yield of 74% in hexane solution. The reabsorption has an active contribution in the emission spectrum due to the spectral overlap between absorbance and photoluminescence. This reabsorption caused significant red-shift of the in-solution photoluminescence peak wavelength from 521 nm to 547 nm when incorporated into the polymeric film (Figure 3.27a). The green-emitting QDs showed the absolute quantum yield of 29% inside the polymeric film.

Red-emitting CdSe/CdS core/shell QDs were synthesized [110], and the ability to control the CdS shell thickness (by optimization of the reaction time) was resulted in the photoluminescence peak wavelength of the synthesized QDs to be fixed at 645 nm (Figure 3.27b). The absolute quantum yield of the synthesized red-emitting CdSe/CdS QDs was measured as 52% in hexane solution using an integrating sphere. The color of CdSe/CdS QD photoluminescence was shown under 365 nm UV irradiation in Figure 3.27b. Moreover, red-emitting QDs have lower spectral overlap between the emission and absorption. Here, this is due to the quasi-Type-II band alignment of the CdSe-CdS heterojunction, which leads to a separation of the electron and hole wave-functions. The large Stokes-shift between absorbance and photoluminescence of red-emitting CdSe/CdS QDs (Figure 3.27b) caused less peak wavelength shift from 645 nm in solution to 652 nm in polymeric film in comparison with green-emitting QDs. The red-emitting QDs showed the absolute quantum yield of 17% when embedded inside the polymeric film.

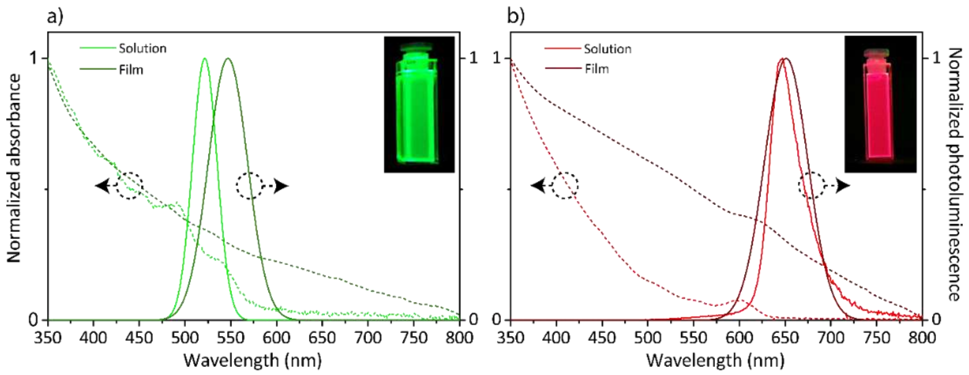

Figure 3.27: The absorbance and photoluminescence spectra of (a) green-emitting CdSe@ZnS quantum dots with gradient shell, and (b) red-emitting CdSe/CdS core/shell quantum dots in solution and embedded in polymeric film. Inset: The synthesized quantum dots under 365 nm UV irradiation.

3.5.4 The fabrication of polymeric films embedded with QDs

To fabricate the QD-polymeric films, we mixed as-synthesized red- and green-emitting QDs with PDMS polymer. As previously mentioned in section 3.5.2, hexane solvent was used to dissolve the QDs due to lower boiling temperature (at 69 ºC) [256], which simultaneously facilitated curing process of PDMS polymer and the evaporation of the QDs solution. To fabricate the polymeric films, an ultra-thin (19 µm thickness) transparent PET polymer film was placed on top of the normal glass substrate (Figure 3.28a). Then, the QD solution and PDMS mixture, which was prepared by mixing 3 g SYLGARD 184 silicon elastomer, 1.5 g curing agent and red- and green-emitting QDs in hexane solution was poured on top of the PET film (Figure 3.28b). To achieve smooth films and control the desired thickness, doctor blade technique was used (Figure 3.28c-schematic). The different thicknesses of the mixture film (both for red- and green-emitting QDs) were generated from 100 to 500 µm. Right after the film coating, the glass substrate was heated at 90 ºC for 12 hours in the oven to complete the curing process (Figure 3.28d). When the film was cured, it can be cut into different proportions based on the different dimensions used in display technology. Here, we cut the cured red- and green-emitting QD-polymeric films into 123 mm×68 mm dimensions, which are suitable for smart phone displays (Figure 3.28e).

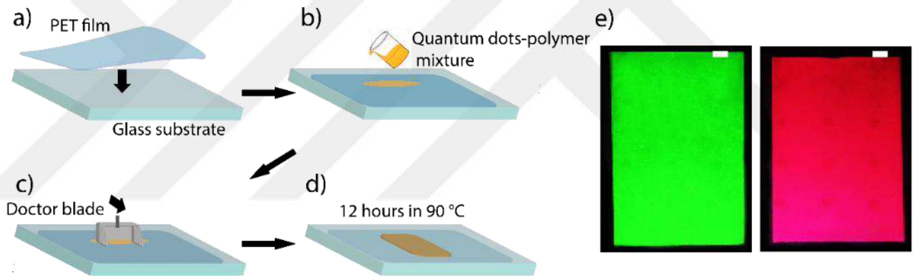

Figure 3.28: The schematic of QD-polymeric film formation. (a) One layer of PET polymer film was placed on top of the normal glass substrate. (b) The QD solution and PDMS polymer mixture was poured on top of the PET film. (c) The film was generated with different dimensions using doctor blade technique. (d) Curing process, which was performed at 90 ºC for 12 hours. (e) The photograph of the fabricated red- and green-emitting QD-polymeric film under 365 nm UV irradiation. (Scale bar=1 cm)

3.5.5 The optical analysis of the QD-based polymeric films

Single-layer architecture

To evaluate the optical performance of the fabricated red- and green-emitting QDs-polymeric film, we fabricated QDs-polymeric films with the same concentration and different thicknesses from 100 µm to 500 µm using doctor blade technique (as shown in Figure 3.29a and 3.29c). For polymeric film formation, 600 µl red-emitting QDs (with the optical density of 0.58 at 605 nm) was mixed with 3 g PDMS and 1.5 g curing agent. Separately, 300 µl of green-emitting QDs solution (with the optical density of 0.93 at 518 nm) was mixed with corresponding amount of PDMS and curing agent. If the concentration of red- and green-emitting QDs solution exceeded the above mentioned ratio, the QD agglomeration in the films was started to be observed, which reduces the color conversion homogeneity [28]. As the thickness of the QDs-polymeric film increased from 100-500 μm, more brightness was observed when irradiated under 365 nm UV light due to the increased absorption and the resultant emission (Figure 3.29a and 3.29c). This was also confirmed with optical output intensity measurement of the QD-polymeric films when excited by the 454 nm blue LED (Figure 3.29b). As the thickness of the red- and green-emitting QDs polymeric films increased, the blue light intensity decreased due to the more color conversion ratio of the red and green emission from the QDs. The increase in green emission of the QDs illuminated by blue pump was higher than red emission due to the higher efficiency of the green-emitting QDs (Figure 3.29b and 3.29d).

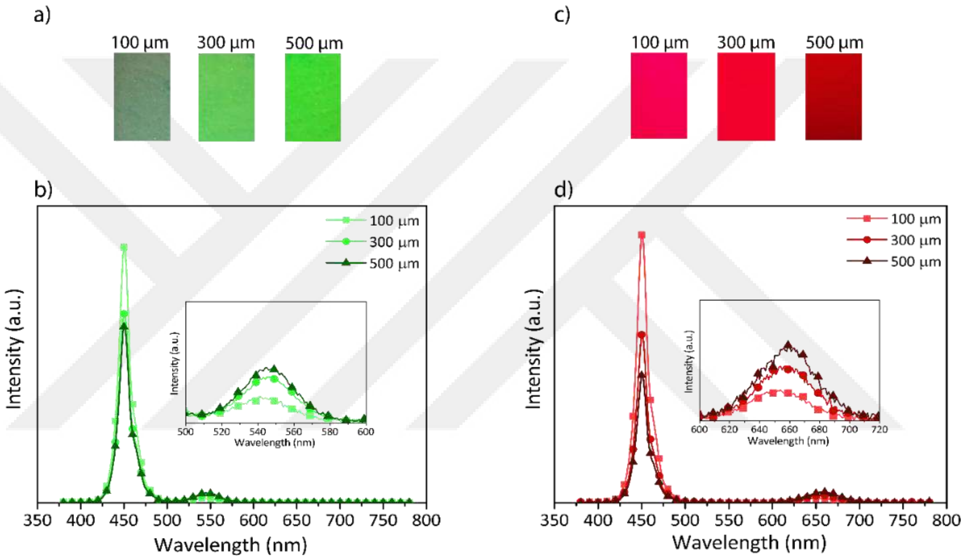

Figure 3.29: (a) Green-emitting QD-polymeric films with different thickness from 100-500 μm under 365 nm UV irradiation. (b) The optical intensity output of the fabricated green-emitting films with different thicknesses when excited by 454 nm blue BLU. (c) Red-emitting QD-polymeric films with different thickness from 100-500 μm under 365 nm UV irradiation. (d) The optical intensity output of the fabricated red-emitting films with different thicknesses when excited by 454 nm blue BLU.

Double-layer architecture

To evaluate the optical performance of the red- and green-emitting QD-polymeric films in a double layer structure, we placed one red-emitting and another subsequent green-emitting QD films on top of the backlight unit, which consists of blue LEDs, diffuser and prism sheets (Figure 3.30a). Prism sheet (or as in the display industry called brightness enhancement films) collimates the light into the on-axis of viewer direction to increase luminance level of BLU. Diffuser sheet decreases the discontinuities of light distribution on the screen. We measured the optical output spectrum from top of the diffuser sheet layer. The reason of the above mentioned ordered structure was that if the green-emitting layer was placed on top of the BLU and the red-emitting layer was placed on top of that, red-emitting QDs absorb the emitted light from green-emitting QDs, which results in higher reabsorption and lower color conversion efficiency. The optical output intensity collected from red- and green-emitting layers were shown in Figure 3.30b-d. As the thickness of the green-emitting QD-layer increased from 100 µm to 500 µm, more blue to green color conversion was observed (Figure 3.30b-d). When QDs are integrated into the polymeric film, reabsorption have an active contribution in the final BLU spectrum due to the cross-sectional area between absorbance and photoluminescence spectra, which results in a red-shift in photoluminescence spectra and lower external quantum efficiency. But, this shift does not hinder the spectral match between the filter in the TFT-LCD and RGB emission. While keeping the thickness of the green-emitting layer constant, more red color conversion was observed by increasing the red-emitting layer thickness, as expected. This was also shown by the ratio of green to blue emission intensity and red to blue emission intensity in different thicknesses of the red- and green-emitting QD polymeric layers (Figure 3.30e and 3.30f). When only green-emitting layers with different thicknesses were illuminated by the BLU, the ratio of green to blue emission intensity was increased as the thickness of the green-emitting layer increased from 100 to 500 µm (from 0.022 to 0.067 in Figure 3.30e). This increase was also observed when both red- and green emitting layers was illuminated with BLU. By increasing the thickness of the green-emitting layer, more red color conversion intensity was also observed when the thickness of both red- and green-emitting layers are 100 µm to 0.1 when the thickness of both red- and green-emitting layers are 500 µm (Figure 3.30f).

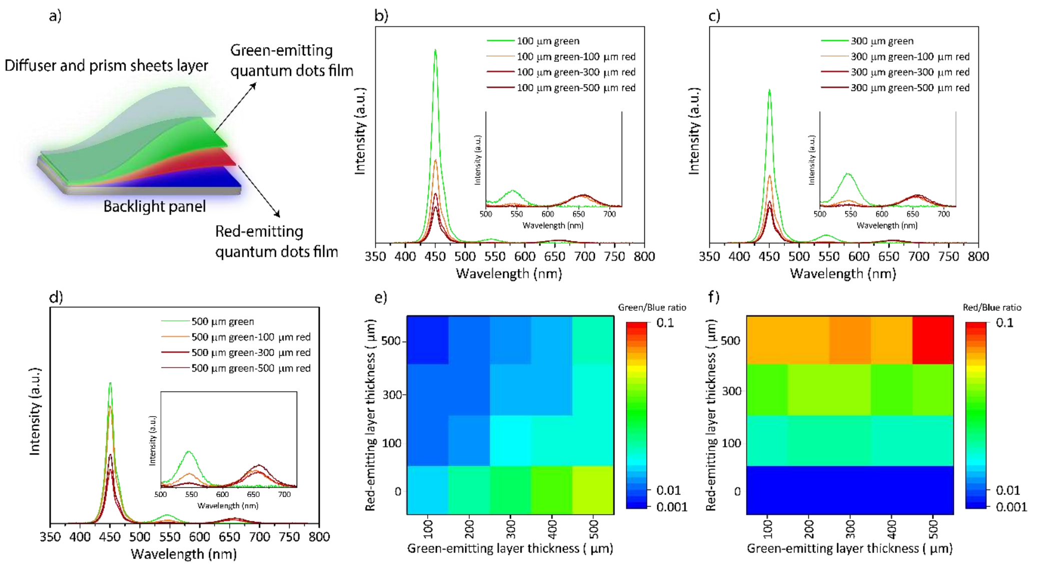

Figure 3.30: (a) The schematic representation of the structure, which was used for double layer color conversion. Double layer color conversion spectra: (b) 100 µm thickness of green-emitting QD-polymeric film with red-emitting QD-polymeric films having thicknesses from 100 to 500 µm, (c) 300 µm thickness of green-emitting QD-polymeric film with red-emitting QD-polymeric films having thicknesses from 100 to 500 µm, (d) 500 µm thickness of green-emitting QD-polymeric film with red-emitting QD-polymeric films having thicknesses from 100 to 500 µm. (e) The green to blue peak and (f) red to blue peak ratio of different combinations of QD-polymeric films on a blue LED.

Color gamut calculations

To assess the color gamut by using QD-polymeric films, we measured the color gamut area change by using red- and green-emitting layers with 500 µm thicknesses as double layer demonstration. For this purpose, we used a blue LED BLU with 454 nm emission wavelength, diffuser and prism sheets to illuminate the 7-inch display (Figure 3.31a). The illuminated photo showed no color difference due to the absence of color conversion layers. After we placed the fabricated red- and green-emitting QD-polymeric films on top of the BLU, the emission from the red- and green-emitting QDs combined with blue LED emission and generated white light, which enabled the appearance of a wide variety of colors in the illuminated photo in the display (Figure 3.31b). The generated white light spectrum with complete cell phone structure was shown in Figure 3.31c. The blue/green and blue/red ratio was calculated as 2.86 and 3.1, respectively. We calculated color gamut of the generated spectra based on the color filters (see Appendix C), and the final color gamut after integration of QD-polymeric films inside the display structure showed color gamut with NTSC color space of 91% and with sRGB color space of 127%, respectively (as shown in Figure 3.31d).

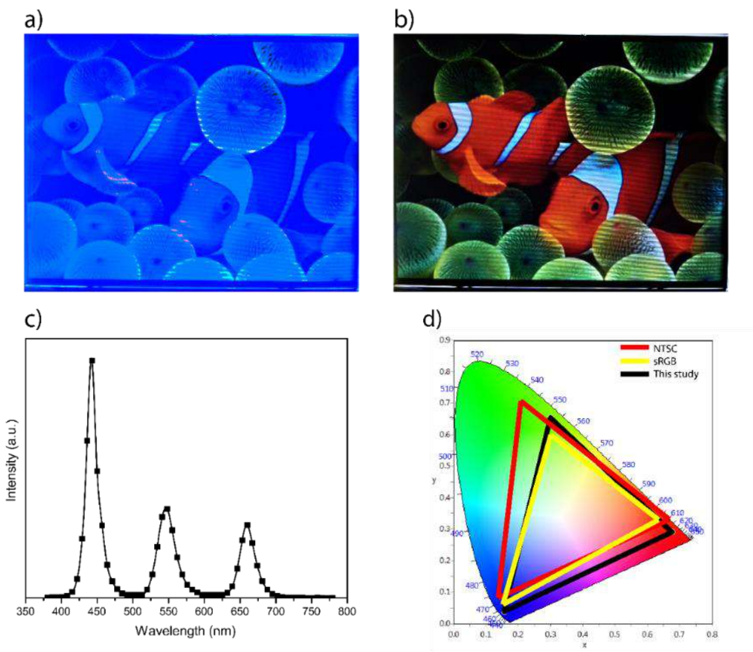

Figure 3.31: The photo of the illuminated display when (a) illuminated only with blue LED BLU (b) illuminated with red- and green-emitting QDs-polymeric films on top of the blue LED BLU. (c) The spectrum of the generated white light with red- and green-emitting polymeric films with diffuser and prism sheets.(d) The CIE 1931 color tristimulus which showed the NTSC (red line), sRGB (yellow line) color gamut and the gamut coverage of the generated white light with QDs-polymeric films (black line).

3.5.6 Conclusion

In conclusion, we synthesized red- CdSe/CdS and green-emitting CdSe@ZnS QDs with 52% and 74% quantum yield, respectively. The synthesized red- and green-emitting QDs were integrated in PDMS polymer matrix and the doctor blade technique enabled to generate large-area QD-polymeric films with various thicknesses and dimensions coated on top of the PET film. The fabricated QD-polymeric films were used as color converter layers using backlight LED panel in display application. By using red- and green-emitting QD-polymeric films, the generated white light color gamut achieved a color space of 91% and 127% for NTSC and sRGB, respectively. QD-polymeric films show promise for future smart phone display applications. The fabricated polymeric films were finally placed in the VESTEL Venus cell phone model for demonstration (Figure 3.32).

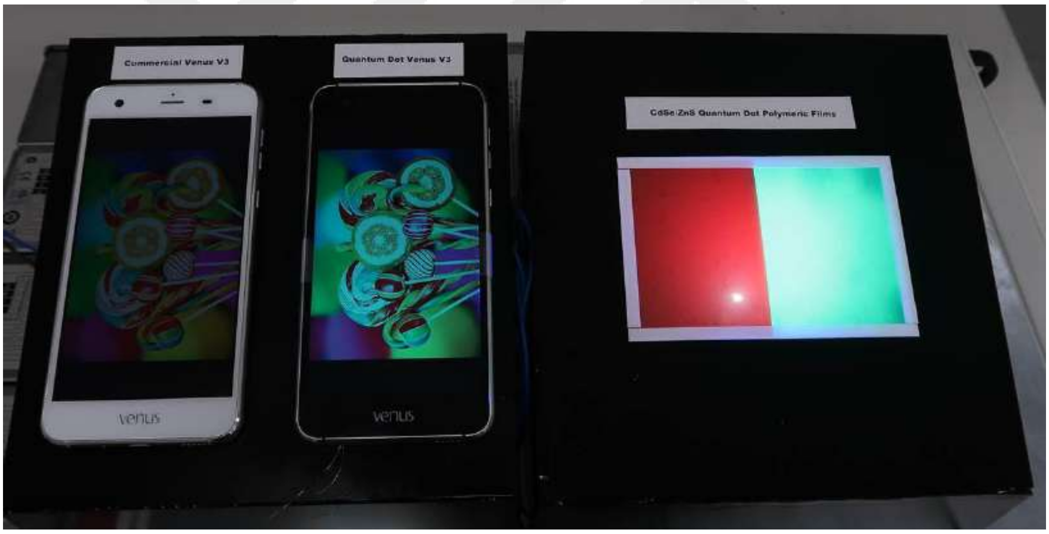

Figure 3.32: The demonstration of red- and green-emitting QD polymeric films under UV illumination and the cellphone structure (left) without and (right) with the QD films. The difference in the visibility of the colors and the brightness is distinctive between the two architectures.

Chapter 4

NOVEL NANOMATERIAL-BASED LUMINESCENT SOLAR CONCENTRATORS

4.1 High-performance, Large-area and Ecofriendly Luminescent Solar Concentrators Using Copper-doped InP Quantum Dots

This section is based on the publication "*High-performance, Large-area and Ecofriendly Luminescent Solar Concentrators Using Copper-doped InP Quantum Dots*" S. Sadeghi, H. B. Jalali, S. B. Srivastava, R. Melikov, I. Baylam, A. Sennaroglu, and S. Nizamoglu, iScience (2020) Reproduced (or "Reproduced in part") with permission from Cell Press Copyright 2020.

Luminescent solar concentrators (LSCs) are energy harvesting devices that can boost electricity production by solar energy via absorbing large-area solar radiation and directing the converted photoluminescence to the solar cells. Colloidal QDs are promising building blocks for LSCs, and to unlock the significant potential for their widespread use they need to simultaneously satisfy non-toxic material content, low reabsorption, high photoluminescence quantum yield (PLQY) and large-scale production. In this section, copper-doping of zinc carboxylate-passivated InP core and nano-engineering of ZnSe shell facilitated high in-device quantum efficiency of QDs over 80%, having well-matched spectral emission profile with the photo-response of silicon solar cells. The optimized QD-LSCs showed an optical quantum efficiency (η_{OQE}) of 37% and an internal concentration factor of 4.7 for a 10 × 10 cm^2 device area under solar illumination, which is comparable with the state-of-the-art LSCs based on cadmium-containing QDs and lead-containing perovskites. Synthesis of the copper-doped InP/ZnSe QDs in gram-scale and large-area deposition (3000 cm^2) onto commercial window glasses via doctor-blade technique further showed the applicability for their wide-spread use. These results position InP-based QDs as a promising alternative for efficient solar energy harvesting and point out a significant step-forward towards their global use in buildings, vehicles and roofs.

4.1.1 Introduction

The global demand for the electrical energy is increasing in each year. According to the International Energy Agency (IEA) report on 2018 [257], the worldwide electrical energy consumption showed significant increase in the last 10 years from 18000 TWh in 2008 to approximately 24000 TWh in 2018. Today the majority of the global electricity production is done by using fossil fuels, which drastically increases the air pollution and greenhouse gas emission with significant side effects (e.g., global warming, extinction of species and public health). Despite its great advancements during the recent years, the contribution of the solar energy is limited to only 1.8% (450 TWh) [258], which remained far below its great potential as being one of the most abundant form of 'green' energy.

Semi-transparent luminescent solar concentrators (LSCs) offer simple and cost-effective solar energy harvesting solutions to boost the solar energy contribution to global electricity production. LSCs are made of fluorescent materials embedded inside transparent optical waveguides. Fluorescent materials absorb the incoming solar radiation impinging on a large area, convert it to longer-wavelength radiation and the down-converted light is then guided to the small-area solar cells placed at the edges of the waveguide. The concentration of light by luminescence leads to a significant increase of energy production for the same area of solar cells [12-15]. Therefore, this approach provides a practical energy harvesting solution that can be broadly used as 'solar windows' in buildings, vehicles and roofs (Figure 4.1).

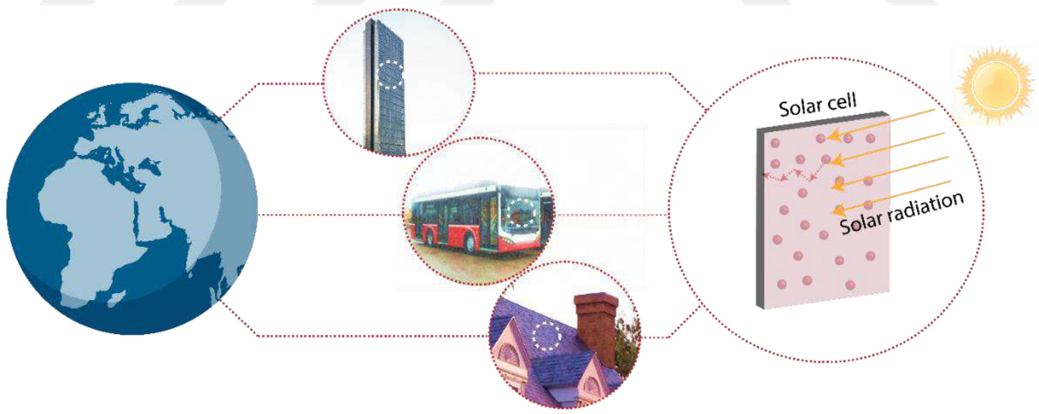

Figure 4.1. The schematic representation of widespread usability of luminescent solar concentrators (LSCs) in buildings, vehicles and roofs as 'solar windows' that can boost the solar energy contribution to global electricity production. The fluorescent particles absorb the sunlight and re-emit photons, which are guided through the glass substrate by total internal reflection (TIR) and collected by the solar cells coupled to the edges.

For its wide-spread use, LSC technology needs to be transformed such that it can simultaneously satisfy efficiency, biocompatibility, and feasibility for large-volume production. More specifically, the following challenges need to be simultaneously addressed: (1) high PLQY of fluorescent material in its synthesis batch, (2) high quantum efficiency (QE) of them in host matrix, (3) low overlap between the absorbance and photoluminescence (i.e., reabsorption) of the fluorophore, (4) well-matched spectral profile between the photoluminescence of the fluorescent material with the photo-response of the solar cells, (5) being free of toxic elements and (6) scalable production for wide-spread use. Optical quantum efficiency of a LSC is a key efficiency-related figure of merit [19] defining the ratio of the output photons, which are extracted from the edges of the LSC to the total number of absorbed photons by the LSC. In order to reach a high optical quantum efficiency level, simultaneous satisfaction of (1)-(3) are required. In addition, (4) allows for efficient conversion of luminescence to electricity, (5) ensures minimum adverse effects of LSCs on environmental sustainability, and (6) shows their ability for large-scale production. Therefore, fulfilling the requirements (1)-(6) can lead to an efficient, ecofriendly and practical LSC technology for safe and effective solar energy harvesting.

Fluorophores inside the transparent medium are the key building-block of the LSCs. To date, different types of fluorophores have been employed in LSC structures such as organic dyes [16], fluorescent proteins [17], lanthanide-based materials [18] and perovskites [19]. However, the use of each type of these fluorophores is accompanied with major challenges. Organic dyes have low stability and PLQY when integrated into host materials [37]. Fluorescent proteins, despite their unique bio-compatibility and even edibility, similarly suffer from the low PLQY in solid-state, which leads to high optical losses [17, 63]. Lanthanides show low absorption coefficient and their compounds are expensive, which are not appropriate for their wide-spread use [18, 64]. Perovskites show limited operational lifetime for LSCs [19, 65].

Alternatively, colloidal QDs offer exceptional optoelectronic properties for LSCs. They allow the control of the optical properties by tuning their size, shape and chemical composition [66-69]. By using different inorganic core/shell structures, high PLQY can be reached to decrease the optical losses [70]. The ability of precisely tailoring the absorbance and emission of the QDs can enable low reabsorption losses, which is important to efficiently deliver the down-converted light to solar cells [13]. Moreover, the photo/chemical stability of the QDs can be optimized for long-term use [71-74]. Therefore, QDs are highly promising candidates for LSC applications.

One compelling material design of QDs is Stokes-shift engineering that can suppress reabsorption losses, which is important to minimize the propagation losses of the down-converted luminescence inside the waveguide. Different synthetic procedures have been performed to enlarge the Stokes-shift of the QDs such as using indirect band-gap materials [75], varying the semiconductor compositions [76], growing giant shells [13] and synthesis of quasi-Type II QDs [13, 77]. However, QDs produced by these approaches have either toxic heavy-metal content (such as cadmium or lead) or low in-device PLQY. An alternative strategy to engineer the Stokes-shift of QDs and enhancing the in-device PLQY can be doping with transition-metal ions [78-80]. Incorporation of small amount of metal impurities (0.1-10 atomic %) as dopants into the host semiconductor QDs introduces new electronic states within the bandgap [80, 81]. The emission from these states are due to the exchange-mediated energy transfer from the photo-excited host semiconductor [82]. Based on the energy level of the metal activator ion, the reabsorption can be effectively suppressed in doped QDs and leads to the Stokes-shift up to hundreds of meV [83, 84]. However, the QE of the doped QDs is typically low due to the slow radiative recombinations, which can be easily outcompeted with the non-radiative processes [13]. Overall, the quest for finding the promising QD candidates, which simultaneously address the above challenges of (1)-(6), is still continuing.

Indium phosphide (InP) QDs, one of the most promising members of QD family for future optoelectronics, showed exceptional efficiency levels for LEDs [40], photo-catalysis [259] and neural interfaces [201], and also hold high potential for LSCs. Due to their large exciton Bohr radius (~10 nm) [260] InP QDs are one of the most studied colloidal semiconductor nanocrystals, and their photoluminescence can be sensitively tuned within the visible spectrum via quantum confinement effect. Advantageously, due to its environmentally-benign nature, they are more favorable in comparison with its counterparts containing cadmium and lead elements [40]. Although the optoelectronic properties of InP QDs have been investigated extensively [260], their use for LSCs have been limited due to their high reabsorption and low efficiency in host materials.

In this section, we report LSCs based on synthetically- and structurally-engineered copper-doped InP QDs that can simultaneously meet the needs of (1)-(6). The synthesized QDs were integrated inside a PDMS polymeric host matrix and deposited on a 10×10 cm^2 commercial glass via doctor blade deposition. Due to efficient excitation transfer from the semiconductor host to the emissive copper ions, photoluminescence in these structures occurs in a nearly reabsorption-free mid-gap region, resulting in an exceptionally high in-film PLQY of 81.2%, which led to an optical quantum efficiency of 37% and internal concentration factor of 4.7 for 10 × 10 cm^2 LSCs under the illumination of AM 1.5G solar spectrum. These efficiency levels are comparable to the best previously reported efficiency levels of cadmium-containing QDs and lead-based perovskite nanostructures (see Appendix D). We further synthesized QDs at gram-scale and fabricated non-toxic, low-loss and large-area QD-based LSCs with an area of 3000 cm^2, which can be directly used in buildings and vehicles as the main source of harnessing the solar power to generate electricity. These results position InP-based QDs as a promising alternative for efficient solar energy harvesting.

4.1.2 The synthesis of copper-doped InP/ZnSe QDs

We aimed at the synthesis of efficient and bio-compatible QDs with large Stokes-shift. For that, firstly, we synthesized surface-passivated InP cores by hot-injection method [261]. Passivation of the InP core was performed by removing the surface dangling bonds using zinc carboxylate [262]. Zinc carboxylates have the advantages of stable valence state, weak reactivity with phosphorous and low affinity for doping of InP lattice structure, low melting point, high thermal stability at reaction temperature and non-toxicity [262]. Moreover, they provide a zinc-rich surface on top of the InP core QDs, which facilitates the growth of additional multi-layer ZnSe shells. Unlike the previous study [81], which employs indium acetate as the indium precursor, we used indium chloride to form an in situ complex with different ligands. Since indium is easily reduced by many Lewis bases, a mixture of hexadecylamine (HDA) and stearic acid (SA) was used to form stable In (III)−ligand complexes. Then, we chemically doped copper ions to the host InP cores by thermal decomposition of copper stearate (Figure 4.2a). Since the reaction temperature is a key parameter in the successful doping of InP nanocrystals, we added the copper precursor to the reaction at the temperature of 180 °C for complete lattice incorporation [81]. Then, for an effective lattice diffusion [81], the reaction was heated up to 220 °C (Figure 4.2b). The Cu:P precursor ratio was optimized and the maximum PLQY of 27.6% was obtained at 1% for copper-doped InP core QDs (see Appendix D). To decrease the surface defects and increase the PLQY, we choose ZnSe as the shell material since it has lower lattice mismatch with InP (3.4%) [263] compared to other commonly-used wide bandgap semiconductors such as ZnS (7.7%) [263]. By this way, InP can be coated with a thick shell without causing large accumulation of strain. We performed multiple ZnSe shelling up to 6 monolayers (MLs) by successive ionic layer adsorption and reaction (SILAR) method. The TEM analysis indicated that the averaged particle size of InP core (2.5 nm ± 0.2) increased slightly after copper doping (2.7 nm ± 0.2) (Figure 4.2c). After ZnSe shelling, the QDs were enlarged to 6.3 nm ± 0.2 (for 3 ML ZnSe) and 8.5 nm ± 0.3 (for 5 ML ZnSe). Since each monolayer of ZnSe shell with cubic crystal structure represents 0.57 nm [264], full monolayer coverage was seen in multiple shelling (Figure 4.2d). For the detailed synthesis procedure and the precursor amounts see Appendix D.

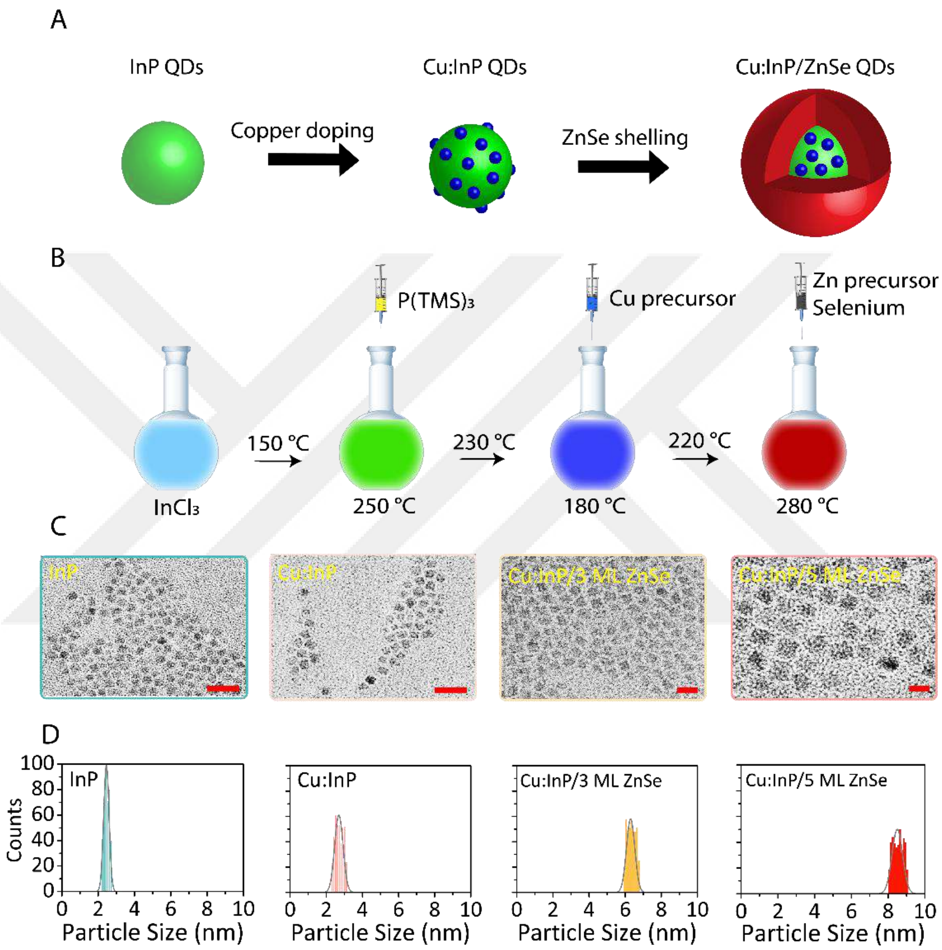

Figure 4.2: (a) After the synthesis of InP core QDs by hot-injection method, core QDs were doped by introducing the copper activator ions. Finally, multiple shelling of ZnSe was performed on the doped InP QDs to increase the PLQY and further suppress the reabsorption. (b) The synthesis of the InP core QDs was performed by hot injection of the phosphorous precursor ($P(TMS)_3$) to indium precursor ($InCl_3$). After the formation of the InP QDs, the copper precursor was introduced to the reaction, which caused the color change of the solution. Finally, the growth of the ZnSe shell was conducted by injection of the zinc and selenium precursors to the reaction batch via SILAR method. (c) TEM and (d) size distribution of the synthesized QDs. By increasing the shell thickness from 0 to 5 ML, the size of the synthesized QDs increased from 2.5 nm for InP QDs to 8.5 nm for copper-doped InP/5 ML ZnSe QDs. Scale bar for InP and Cu:InP QDs is 5 nm, and scale bar for Cu:InP/3 ML and Cu:InP /5 ML ZnSe QDs is 10 nm. The size distribution of the particles was performed for 400 particles in each TEM image.

4.1.3 The optical properties of copper-doped InP/ZnSe QDs

To determine the nanostructure with low reabsorption and high efficiency that is suitable for LSC applications, we investigated the optical properties of the synthesized QDs. We performed time-resolved photoluminescence (TRPL) decay measurements of the InP core and copper-doped InP/5 ML ZnSe. The PL decay of the InP core is described by a biexponential decay due to the insufficient surface passivation. The contribution of the fast decay components was decreased by multiple ZnSe shelling, which supports the decrease of the non-radiative components (Figure 4.3e) [70]. In addition, we observed that after copper-doping, InP QDs experienced a significant PL red-shift of 0.72 eV that leads to a substantial decrease of the reabsorption (Figure 4.3a and 4.3b). Furthermore, the presence of copper dopant centers located in the interior of the copper-doped InP core upon lattice diffusion leads to higher PLQY in comparison with the intrinsic InP cores [81]. Via the growth of ZnSe shell, the emission and absorption bands were further separated, and led to the significant Stokes-shift up to 650 meV (the difference between the PL peak at 1.62 eV and the absorption broad shoulder at 2.27 eV) and suppression of reabsorption (Figure 4.3a). In addition to the decrease of reabsorption, the shell growth isolates the surface traps and effectively confines the electron-hole wave functions inside the nanostructure, which leads to the increase of the PLQY. To select the appropriate nanostructure for LSC, the quenching factor (i.e., reabsorption × ($1-\Phi_{PL}$)) was calculated for different ZnSe shell thicknesses (Figure 4.3c) and the minimum of the quenching factor was observed for 5 MLs. The maximum PLQY of QDs in hexane solution was observed as 87% ± 4 for 5 monolayers of ZnSe shell formation (Figure 4.3d). Hence, considering the quenching factor and PLQY, we selected copper-doped InP/5 ML ZnSe as the optimum sample for LSC fabrication. To investigate the photo-stability of the QDs in-film, their quantum efficiency was measured by accelerated-ageing test under the 365-nm illumination (see Appendix D) and showed only 5.8% decrease (from 81.2% to 76.5%) in 50 days (Figure 4.3f).

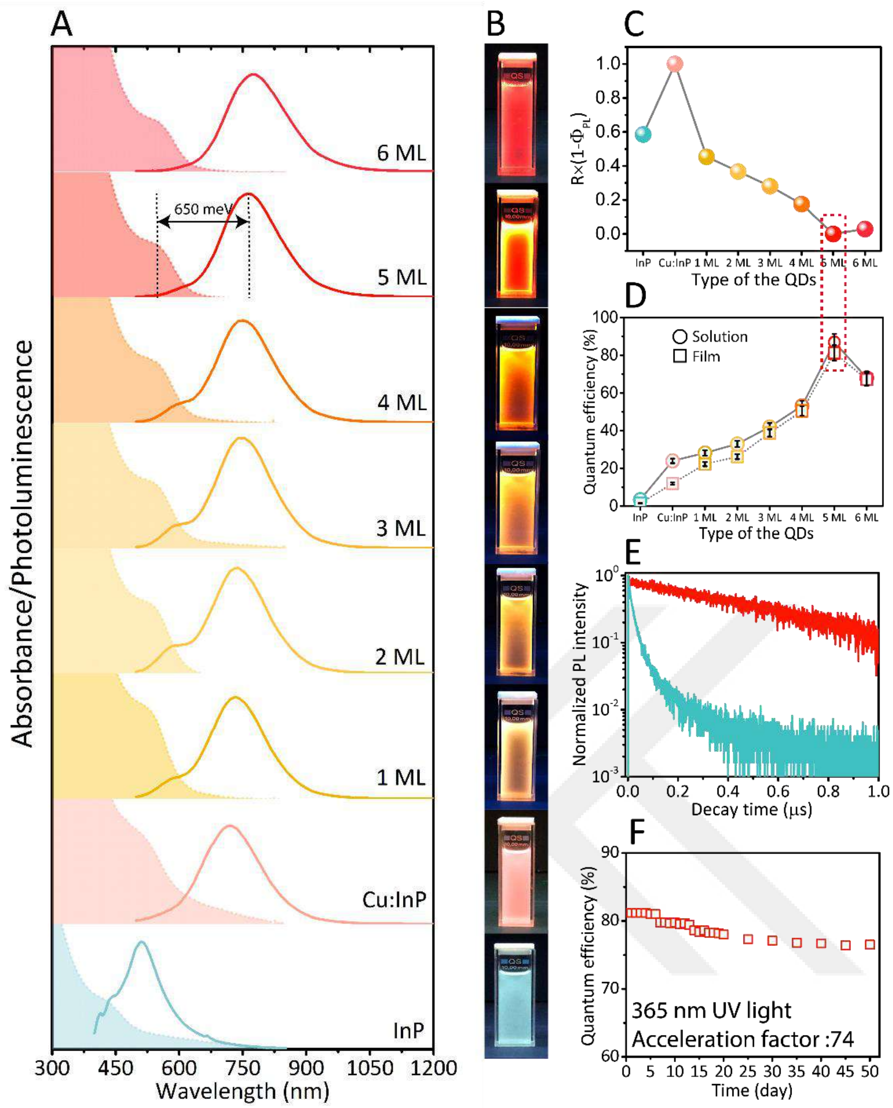

Figure 4.3: (a) The evolution of the absorbance and photoluminescence spectra of the core InP, copper-doped InP and copper-doped InP QDs with different ZnSe shell thicknesses ranging from 1 to 6 ML. The absorbance range for each panel was from 0 to 0.1. (b) The photograph of the synthesized QDs under 365 nm ultraviolet irradiation. (c) Normalized quenching factor of the copper-doped InP QDs calculated by multiplication of reabsorption (R) and (1-Φ_{PL}). (d) The evolution of the PLQY by increasing ZnSe shell thickness from 0 to 6 ML. The average PLQY increased from 3.4% for InP QDs to 87% for copper-doped InP/5 ML ZnSe QDs in hexane (circles). The similar behavior was also observed in the PLQY of the QDs when embedded inside the polymeric matrix of PDMS (squares) as the average QE of the QDs was increased from 1.5% for InP to 81.2% for copper-doped InP/5 ML ZnSe QDs. Due to the low reabsorption and high QE, the copper-doped InP/5 ML ZnSe is an appropriate nanostructure for LSCs (red dashed rectangular in (c) and (d)). (The error bars were calculated by the standard error of mean of three samples) (e) The time-resolved PL measurements of the InP core and copper-doped InP/5 ML ZnSe QDs in hexane. The copper-doping increased the fluorescent lifetime decay significantly from 45 ns for InP to 292 ns for copper-doped InP/5 ML ZnSe due to the introduction of the localized states by the copper ions. (f) The accelerated-aging test performed by the excitation of the copper-doped InP/5 ML ZnSe QD film at 365 nm UV irradiation.

4.1.4 *The non-linear absorbance spectroscopy*

To further investigate the nature of the Stokes-shift in the synthesized copper-doped QDs and understand the emission mechanisms (Figure 4.4a), the non-linear absorption and ultrafast decay properties of the copper-doped and undoped InP/5 ML ZnSe QDs were further investigated by using a femtosecond pump-probe spectrometer [265]. QD solutions were excited at 400 nm at a fluence of 135 $\mu J.cm^{-2}$ and the difference between the absorbance of the pumped and unpumped sample ($\Delta A = A_{pumped} - A_{unpumped}$) was probed by using a femtosecond white light continuum ranging from 450 to 800 nm (Figure 4.4b). The ΔA peak wavelength of the undoped QDs remains almost identical to the absorbance shoulder of the QDs at 556 nm (2.23 eV), showing that the interband transitions are responsible for the transitions in the undoped samples (see Appendix D). The ultrafast transient evolution of the nonlinear absorbance (Figure 4.4c) was analyzed by employing a bi-exponential decay fit consisting of decay times τ_1 and τ_2. Similar to what was reported in earlier investigations [266, 267], the decay times τ_1 and τ_2 describe fast decay due to intermediate trapping states. In addition, as can be seen from Figure 4.4b, ΔA remains non-zero beyond a probe delay of 700 ps, due to inter-band electron-hole recombination that occurs over ns time scales. The latter transition rates are determined from luminescence decay measurements described in Figure 4.3e. The measured ultrafast decay times of copper-doped QDs (τ_1=0.9 ps, τ_2=6.3 ps) at the probe wavelength of 580 nm (Figure 4.4c) are considerably shorter than those for undoped QDs (τ_1=2.4 ps, τ_2=25.5 ps, probe wavelength of 500 nm, see Figure 4.4b) due to copper-induced mid-gap states. In addition, the peak wavelength of the ΔA spectrum of the doped QDs shifted from 566 nm (2.19 eV) to 591 nm (2.09 eV) over a delay of 1.5 ps (Figure 4.4d). The pump fluence was relatively low (the estimated average number of generated electron-hole pairs corresponded to $\langle N \rangle \sim 0.5$) for the observation of a Stark effect induced spectral change and at the same fluence level no spectral variation was observed for the undoped QDs. Hence, we attributed that the copper dopants in InP/5 ML ZnSe QDs play the role as an ‘extra’ hole acceptor level [268].

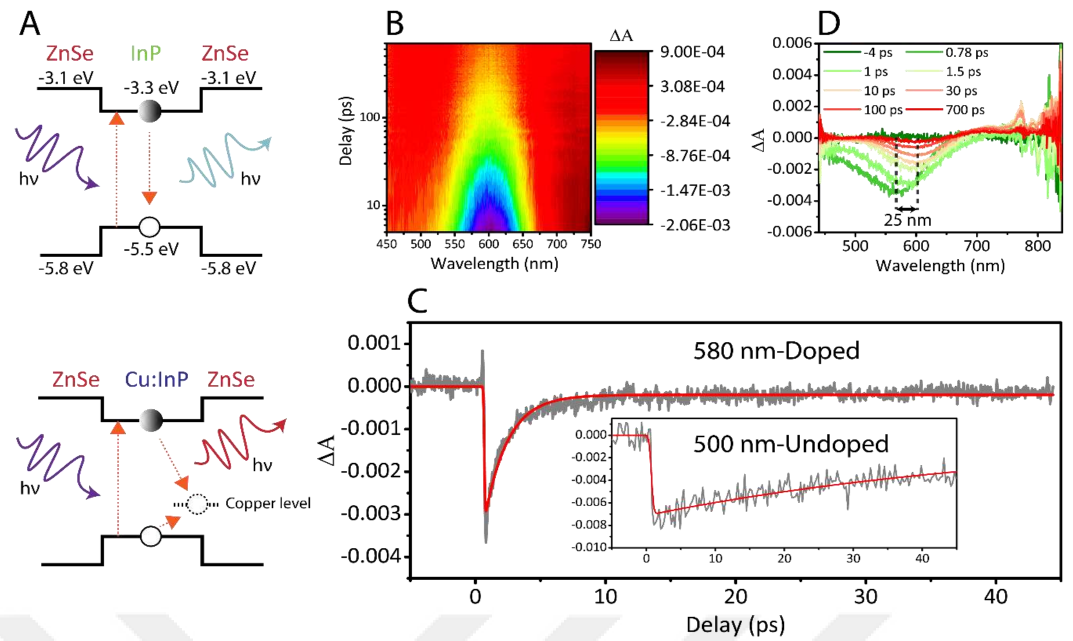

Figure 4.4: (a) The energy band diagram of the undoped (upper panel) and copper-doped (lower panel) InP/ZnSe QDs. In undoped QDs, the photon is absorbed and interband recombination takes place. When QDs are doped with copper, mid-gap states are introduced, which are responsible for the red shift in emission. (b) The contour plot showing the measured ΔA of the copper-doped InP/ZnSe QDs as a function of probe delay and wavelength. (c) Time-resolved ΔA response of the copper-doped InP/ZnSe QDs at the probe wavelength of 580 nm. The decay lifetimes of the copper-doped QDs were determined as 0.9 and 6.3 ps. Inset: Time-resolved ΔA response of the undoped InP/ZnSe QDs at the probe wavelength of 500 nm with the decay lifetimes 2.4 and 25.5 ps. (d) The measured ΔA spectra of the QDs at eight selected probe delays ranging from -4 ps to 700 ps. The excitation wavelength was 400 nm.

4.1.5 Low-loss InP-based QD-LSCs

We fabricated copper-doped InP/ZnSe QD based LSCs by doctor-blade deposition of QD-polymer mixture (d=100 µm) onto the glass substrates (D=2 mm) (Figure 4.5a). We selected PDMS elastomer as the polymeric host matrix that is highly transparent both in the visible and near-IR region [269] and offers inexpensive large-scale production [142, 270, 271]. Despite the favorable properties of PDMS, in fact, the initiator radicals of such polymers can interact with QDs and increase the non-radiative channels [77]. This has the risk to significantly decrease the QE of QDs. For example, in previous reports, a QE decrease of 50% is observed [53], which can be solved by special methods such as cell-casting [13]. Noticeably, without any special treatment of PDMS, we observed strong photoluminescence of QDs in regular PDMS films with only a ~6% QE decrease with respect to the solution due to the strong confinement of photo-generated charge carriers via the sufficiently thick ZnSe shell (Figure 4.3d and 4.5c). The total internal reflection of the photoluminescence was especially visible at the edges of the waveguide (Figure 4.5c). The QD layer in the fabricated QD-LSC showed a small PL peak wavelength change from 767 nm in solution to 772 nm in film, respectively (Figure 4.5d).

Advantageously, the thin film deposition of QD-polymer layer preserves the transparency of the fabricated QD-LSCs, which is critical for indoor and outdoor solar window applications (Figure 4.5b). The absorbance of the QD-LSC at the first excitonic peak was measured as 0.093 (Figure 4.5d), equal to the high transmission level of 81%, which was also observable in the photograph of QD-LSC slab under ambient light (Figure 4.5b). The small offset (0.05) in the absorbance of the device (dashed line in Figure 4.5d) is due to the light reflection from the LSC (equal to ~11% reflectivity).

To evaluate the suitability of the copper-doped InP/5 ML ZnSe QDs in LSC panels, the optical properties of the fabricated QD-based LSC with the dimensions of 10×10 cm^2 were investigated. To simulate the situations, in which the solar window panels are illuminated partially by sunlight irradiation on the different hours of the day, the portion of the illumination area under ultraviolet light was altered (Figure 4.5e). As illumination area increased from 0 to 100 cm^2 (equal to the full length of LSC at 10 cm), the optical output intensity increased with a linear slope due to the effective suppression of the reabsorption by QDs (Figure 4.5e). At the same time, the emission spectra of the QDs at different illumination area showed almost no significant spectral peak position change ($\Delta\lambda$= 4 nm), demonstrating the low reabsorption of the LSC under different areal illumination conditions (Figure 4.5f), and the emission spectrum also matched well with the spectral response of silicon photovoltaic cells for efficient light harvesting. For direct evaluation of the reabsorption in the fabricated QD-LSC, laser light at 365 nm was used to excite the face of QD film and the output intensity was recorded from the edge at different optical distances from the excitation spot (Figure 4.5g). The normalized integrated PL intensity decreased by 21%, by increasing the optical distance up to 10 cm (Figure 4.5g and 4.5h). This trend mainly originates from the reabsorption and scattering losses. To figure out the scattering losses, we investigated experimentally by propagating a laser beam through the edge of the fabricated QD-based LSC at the wavelength of 780 nm, where QDs have negligible absorption (Figure 4.5d). The output light was collected at different optical distances from the illumination edge by using an optical fiber. By increasing the light collection distance up to 10 cm, the output intensity corresponds to a scattering loss of 0.016 cm^{-1}. By including the scattering term in the PL decay (Figure 4.5g), the effective reabsorption coefficient corresponds to 0.004 cm^{-1}, showing that the reabsorption was significantly suppressed.

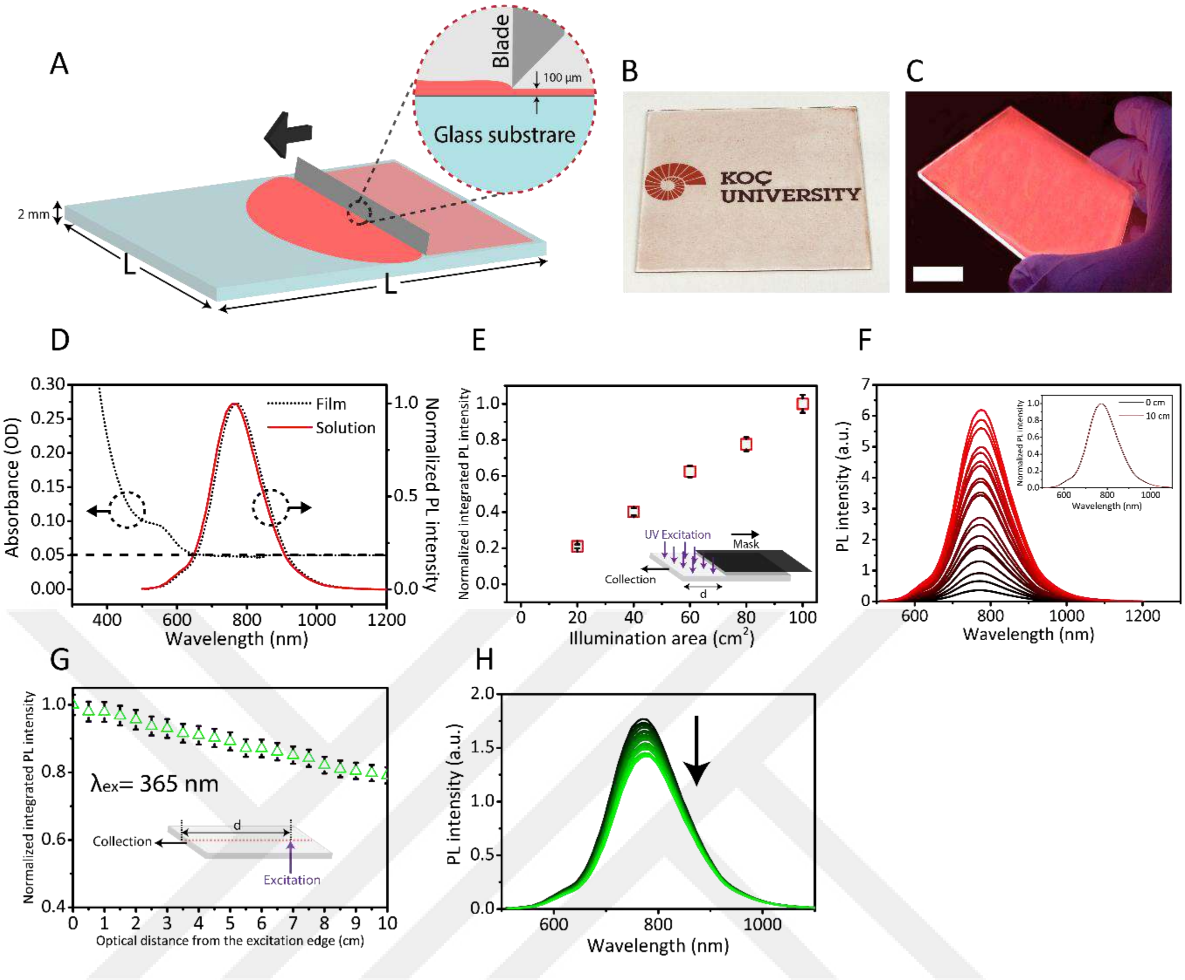

Figure 4.5: (a) The schematic representation of the fabrication process. After mixing the QD solution with PDMS elastomer and degassing, the mixture was poured onto a glass substrate. Then, by using the doctor-blade, a thin film with the thickness of 100 µm was formed on the glass. (b) The transparency of the fabricated LSC with the loading concentration of 26 mg.ml^{-1} was shown under ambient light. (c) The photograph of the QD-based LSC under 365 nm ultraviolet irradiation. The total internal reflection is visible on the edges as they seemed brighter. (Scale bar =1 cm) (d) The absorbance and PL of the QDs in the film (black dashed line) with the loading concentration of 26 mg.ml^{-1} and in solution (red line). (e) The optical output intensity of the 10 × 10 cm^2 QD-based LSC by changing the illumination area from 0 to 100 cm^2. Inset: Schematic of the setup to change the portion of the illuminated area of LSC under ultraviolet radiation. (f) The output emission spectra of the LSC, when illumination area increased as in (e). Inset: Normalized output spectra at the optical distances of 0 and 10 cm from the collection edge. (g) The spectrally integrated output of QD-based LSC under the illumination by an ultraviolet laser beam at 365 nm wavelength. Inset: Laser beam excitation was perpendicular to the surface with different optical distances and the light was collected at the slab edge. (h) The output emission spectra of the LSC, when the optical distance from the excitation point and the collection edge was increased as in (g). (The error bars were calculated by the standard error of mean for three measurements.)

4.1.6 The efficiency parameters

We characterized and analyzed the efficiency of the copper-doped QD-based LSCs. To investigate the effect of LSC size, we fabricated QD-LSCs with the dimensions of 5 × 5 cm^2, 10 × 10 cm^2 and 20 × 20 cm^2 having loading concentration of 26 mg.ml^{-1}. At the same time, we fabricated two separate LSCs with the same dimension of 10 × 10 cm^2 having different loading concentrations of 13 and 52 mg.ml^{-1}. QD-LSCs were illuminated orthogonal to its front surface by a calibrated AM 1.5G solar spectrum, and the photoluminescence generated by the QDs was coupled to the silicon solar cell positioned on the collection edge.

In order to measure the optical quantum efficiency of the fabricated LSCs, Equation (4.1) was used [19]:

$$\eta_{OQE} = (J_{LSC}A_{PV})/(J_{PV}A_{LSC}\eta_{abs}q_{LSC}\eta_{coupling}) \tag{4.1}$$

was used, where J_{LSC} is the short-circuit current of the solar cell coupled to the LSC when LSC is illuminated by the solar simulator, J_{PV} is the short-circuit current of the solar cell when the solar cell is directly illuminated by the solar simulator without LSC, q_{LSC} is the reshaping factor equal to 1.73, η_{abs} is the absorption efficiency dependent on the loading concentration of the QDs (Figure 4.6b) and $\eta_{coupling}$ is the PL coupling efficiency from the LSC to the solar cell, which is calculated as 75.2% (see Appendix D) [15]. Based on the electro-optical characterizations, J_{LSC}/J_{PV} values measured as 0.24, 0.44 and 0.74 for the loading concentration of 13, 26 and 52 mg.ml^{-1}, respectively (Figure 4.6a), which resulted in the optical quantum efficiency of QD-LSCs of 40.7% to 39.9% and 37.2% for a 10 × 10 cm^2 area, respectively (Figure 4.6c). When the side length of LSC changed to 5 and 20 cm at 26 mg.ml^{-1}, J_{LSC}/J_{PV} values of the QD-LSCs were shifted 0.24 and 0.73, respectively (see Appendix D). But, at the same time since the G factor increased from 6.25 to 25, the optical quantum efficiency of the QD-LSC with different LSC lengths led to 44.3% and 32.7%, respectively (Figure 4.6d). The observed optical quantum efficiency levels are as a result of high in-film QE of the QDs, suppressed reabsorption due to the separation of absorption and emission centers (Stokes-shift > 600 meV), and the high optical quality of the fabricated films mitigating the propagation-loss problem. To the best of our knowledge, the optical quantum efficiencies of the more environmentally benign InP-based LSCs have comparable efficiency levels with the best Cd- and Pb-based LSCs.

Besides, the optical quantum efficiency of the InP QD-LSC having 52 mg.ml^{-1} led to a high internal concentration factor calculated by Equation (4.2) [19]:

$$CF_{int} = G \times \eta_{OQE} \tag{4.2}$$

,which corresponds to 4.7 for the LSC panels with the dimensions of 10 × 10 cm^2. The external quantum efficiency of the LSC is defined as the ratio of the number of the photons reaching to the coupled solar cell to the total number of the input photons. As a result of electro-optical measurement, the concentration of 52 mg.ml^{-1} achieved the highest external quantum efficiency of 5.9% due to high absorption efficiency in comparison with the other LSCs having different concentration levels (Figure 4.6c and 4.6d). These external quantum efficiency are also in agreement with the simulations based on Equation (4.3):

$$\eta_{EQE} = \eta_{abs}\eta_{OQE}q_{LSC}\eta_{coupling} \tag{4.3}$$

Moreover, the solar-to-electrical power conversion efficiency (i.e., PCE_{LSC}) corresponds to 0.9% by using a stand-alone solar cell that has an efficiency of 14.5%, respectively.

To understand the ultimate efficiency levels achievable by the QD-LSCs, we performed the simulation of the optical quantum efficiency by considering QEs of 10%, 50%, 81.2% (this study) and 100%, while LSC length and loading concentration ranging from 1 to 100 cm and from 2.6 to 520 mg.ml^{-1}, respectively (Figure 4.6e). By increasing the QE of the QDs to unity, the ultimate optical quantum efficiency levels of QD-LSCs can reach up to 70% for an area of 10 × 10 cm^2, while keeping sufficient level of transmittance more than 50% in the eye sensitivity peak (λ=555 nm). Thus, the optical quantum efficiency of 70% can push up the external quantum efficiency to the maximum value of ~14% while a refractive index-matching polymer between LSC and PV module is used and a moderate absorption efficiency of 20% is assumed. If a more efficient solar cell module (having 23.7%) [15] would be used for optical quantum efficiency of 70%, the power conversion efficiency could be further increased up to ~3.3% under the standard AM 1.5G solar illumination. In addition, integration of lower-band gap QDs emitting at 900-1000 nm matching with the responsivity of the silicon solar cells can significantly boost the power conversion efficiency levels. Furthermore, the use of reflectors on the bottom of the LSC can increase the power conversion efficiency though decreasing the transparency.

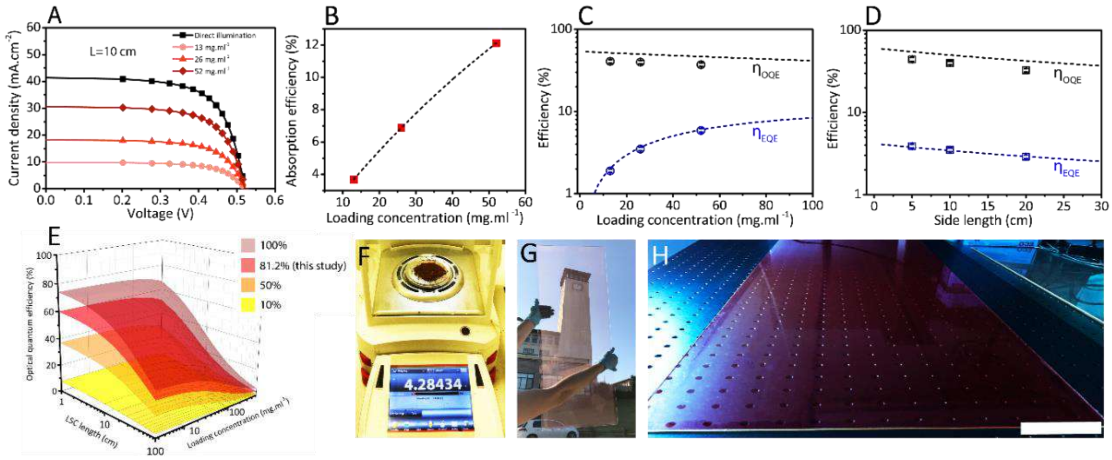

Figure 4.6: (a) The J-V curves of the silicon solar cells coupled to the QD-LSCs with the LSC length of 10 cm at different loading concentrations of 13, 26 and 52 mg.ml^{-1} under the illumination of AM 1.5G solar simulator. The J-V curve of the silicon solar cell under direct illumination of the solar simulator was also shown (black line). (b) The absorption efficiency values for different loading concentration of the QDs. The dashed line and the points represent the simulated and experimental results, respectively. (c) The simulated (dashed line) and experimental (symbols) values of optical and external quantum efficiency for the QD-LSCs with different loading concentration of the QDs ranging from 13, 26 and 52 mg.ml^{-1} and (d) different side lengths of 5, 10 and 20 cm. (e) The simulation of the optical quantum efficiency of QD-LSCs having different QE of QDs ranging from 10%, 50%, 81.2% (QE of this study) and unity at different LSC lengths ranging from 1 to 100 cm and different loading concentration between 2.6 and 520 mg.ml^{-1}. (f) Up-scaled amount of copper-doped InP/ZnSe core/shell QDs after single synthesis. (g) The fabricated large-area QD-based LSC under sunlight irradiation with the dimensions of 100 × 30 cm^2. (h) The large-area LSC under weak ultraviolet illumination. (Scale bar=5 cm)

4.1.7 Scalability of copper-doped InP QDs for large-area and wide-spread-usable LSCs

In order to fabricate large-area QD-based LSCs, the amount of QDs needs to be scaled up to a sufficient level. For that, we increased the reaction yield up to 4.28 g of the copper-doped InP/5 ML ZnSe QDs in one reaction batch (Figure 4.6f) (see Appendix D for detailed amounts of precursors and synthetic procedure). To assess the applicability of the fabricated LSCs to large-area solar window applications, the synthesized copper-doped QDs with the concentration of 26 mg.ml^{-1} were mixed with the polymer and deposited on 100 × 30 cm^2 glass substrate by using doctor-blade technique (Figure 4.6g). Regardless of the size and the high loading concentration of the QDs in the large-area device (26 mg.ml^{-1}), the fabricated devices are highly transparent under sunlight irradiation (Figure 4.6g). At the same time, the ultraviolet illumination of the large area QD-based LSC led to strong emission from all parts of the fabricated device, indicating the feasibility for large-area LSC operation and fabrication (Figure 4.6h).

4.1.8 Conclusion

In this section, we showed that InP-based QDs are a promising candidate for future LSC technology that can simultaneously fulfill the requirements of the efficiency, eco-compatibility and large-scale production. The Stokes-shift of the InP QDs was realized by copper-doping (650 meV) and the PLQY of the synthesized QDs was boosted up to 87% in the 'near-infrared window' by passivation of surface traps via zinc carboxylation and strong confinement of electron-hole pairs inside the nanostructure via growing lattice-matched ZnSe shell. Moreover, the high PLQY over 80% is also maintained in solid-state form due to the thick ZnSe shell. The high PLQY and low reabsorption facilitated high optical quantum efficiencies over 30%, comparable to the best reported Cd and Pb containing LSCs. By using the doctor-blade technique, a large-area QD-based LSC (3000 cm^2) was fabricated, which indicates the applicability for 'solar window' applications. Moreover, incorporation of QDs having QE of 100% into LSCs can lead to power conversion efficiency levels above 3%. Collectively, this work demonstrates a significant step forward towards the realization of ecofriendly, efficient and large-area LSCs, which show remarkable potential to be widely used for solar powered buildings and vehicles in the near future.

4.2 Stokes-shift-engineered indium phosphide quantum dots for efficient luminescent solar concentrators

This section is based on the publication *"Stokes-shift-engineered indium phosphide quantum dots for efficient luminescent solar concentrators*" S. Sadeghi, H. B. Jalali, R. Melikov, B. G. Kumar, C. W. Ow-Yang, and S. Nizamoglu, ACS Applied Materials and Interfaces 10.15 (2018) 12975-12982. Reproduced (or "Reproduced in part") with permission from American Chemical Society Copyright 2018.

LSCs show promise due to their potential for low-cost, large-area and high-efficiency energy harvesting. Stokes-shift engineering of luminescent QDs is a favorable approach to suppress reabsorption losses in LSCs; however, the use of highly-toxic heavy metals in QDs constitutes a serious concern for environmental sustainability. In this section, we report LSCs based on cadmium-free InP/ZnO core/shell QDs with Type-II band alignment that allow for suppression of reabsorption by Stokes-shift engineering. The spectral emission and absorption overlap was controlled by the growth of a ZnO shell on an InP core. At the same time, the ZnO layer also facilitates the photostability of QDs within the host matrix. We analyzed the optical performance of indium-based LSCs and identified the optical efficiency as 1.45%. The transparency, flexibility, and cadmium-free content of the LSCs hold promise for solar window applications.

4.2.1 Introduction

Today there exists an intense worldwide effort toward the use of green energy production technologies due to the concerns about environmental sustainability and global warming. Among eco-friendly power technologies (wind, wave, etc.), solar radiation provides a clean and abundant form of energy. To harvest solar energy, silicon-based photovoltaic (Si-PV) cells have received significant attention in the last three decades [272-275], and recently the cost of Si-based PV modules has lowered down to 70%, which substantially shortened the economic payback period [276]. The improvement in energy efficiency of these PV systems can further enhance their potential for the widespread use. To fulfill this demand, conventional solar concentrators that use mobile mirrors and lenses have been developed to track the sun and improve the sunlight energy harvesting [277]. However, they have some drawbacks, which are costly opto-mechanical equipment to track the sun, cooling focal point of the mirrors, and inadequacy to concentrate diffused sunlight [278].

LSCs have been started to be explored as a versatile platform to improve the energy production capability of Si-PVs and consequently to reduce the energy production cost per unit watt [273, 279-282]. A typical LSC consists of an optical waveguide that includes photoluminescent materials, which absorb direct and diffused sunlight radiation and re-emit at higher wavelengths [283-286]. The down-converted luminescence is then guided by total internal reflection (TIR) and absorbed by the PV cells placed at the edges of the waveguide [287]. Since the lateral area of LSC is significantly larger than its edge area, the generated photon density is considerably increased because of the "concentrator effect", which results in improved energy harvesting [286]. By coordinating the wavelength of the PV responsivity maxima with the photoluminescence peak wavelength of the fluorescent emitters, the output power can be exceptionally enhanced [105]. Moreover, the transparency of these concentrators makes them suitable to utilize as ″solar windows″ [105, 274, 288].

Among the wide variety of fluorescent materials, colloidal quantum dots show advantageous properties such as high photoluminescence quantum efficiency, spectral tunability via quantum confinement effect, and high photostability [80, 213, 272, 289-295]. Even though QDs show high QE after synthesis, their performance in LSC applications is limited due to the reabsorption [296, 297]. Reabsorption losses can be decreased by increasing Stokes-shift, which is the energy separation between the emission and absorption spectra. Stokes-shift can be controlled by using indirect-bandgap materials [75], varying semiconductor compositions,[76] and doping with transition metal ions [78, 79, 105, 278, 298].

Alternatively, heterojunction formation in QDs provides an effective approach to engineer the Stokes-shift. The transition from a Type-I to a quasi-Type-II carrier localization can decrease the spectral emission and absorption overlap [105]. So far, this is typically achieved by the growth of a thick shell on CdSe core QDs [105]. This thick shell also allows for the minimization of the host material effect, which significantly decrease the efficiency drop of the QDs when transferred from solution into polymer matrix. Even though this approach is advantageous to simultaneously suppress the reabsorption losses and host material effect, there are major concerns about the use of highly-toxic cadmium content in various applications [299, 300]. Indium phosphide QD is a strong alternative to cadmium-based QD because of its non-toxic material content [301-303]. Indium have been started to be used in commercial applications in TVs (e.g., InGaN light-emitting diodes), which shows the mass production potential and its safe use [304, 305]. Therefore, the development of indium-based QDs with low reabsorption losses and low host-material sensitivity is essential.

In this section, we demonstrated InP/ZnO core/shell QD-based LSCs that show significant suppression of reabsorption over a long optical path. We did colloidal synthesis and nano-engineered InP/ZnO core/shell QDs for efficient solar concentration. The ZnO shell growth on InP core QDs facilitated a Type-II band alignment (Figure 4.7a) [306], which leads to increasing the Stokes-shift and decreasing the reabsorption losses. For LSC fabrication, we incorporated QDs into PDMS waveguide and the QE and time-resolved measurements confirmed that the host material effect is also simultaneously reduced.

4.2.2 The synthesis of InP/ZnO core/shell QDs

ZnO was grown on an InP core by thermal decomposition of zinc acetylacetonate ($Zn(acac)_2$). Previously, zinc acetate ($Zn(OAc)_2$) and zinc acetylacetonate ($Zn(acac)_2$) have been used as precursor for synthesizing ZnO QDs [307-311], but $Zn(acac)_2$ resulted in smaller and more mono-disperse ZnO QDs with weaker trap emission [311]. Moreover, using oleylamine as stabilizing agent can help to prevent ZnO grain from aggregating [309]. To synthesize highly luminescent InP cores, we used zinc undecylenate as the surface passivator [262], and oleylamine and oleic acid as the stabilizing ligands. In short, InP cores were synthesized by hot injection of tris(trimethylsilyl)phosphine ($P(TMS)_3$) on indium chloride ($InCl_3$) in the presence of oleylamine and oleic acid ligands with 1-octadecene solvent. Once the InP core was formed, the ZnO stock solution consisting of $Zn(acac)_2$, oleylamine, oleic acid and octadecene was added to the InP core solution and heated to 280 °C (see Appendix E for the detailed synthesis procedure). Even though the lattice mismatch between InP and ZnO is 11%, which is higher than the well-known InP/ZnS lattice mismatch (~ 8%) [312], the synthesized InP/ZnO QDs exhibit excellent optical and electronic properties similar to the previously reported Type-II heterostructure of CdTe/ZnSe with a higher lattice mismatch of up to 14% [313]. The ZnO crystal growth on InP was observed with the increase of the QD diameter from 1.95 nm for InP only core to 3.01 nm for InP/2ZnO (with two times shelling) and 4.31 nm for InP/5ZnO (for five times shelling), respectively, where each shelling corresponds to a thickness of ~0.27 nm (see Appendix E). In addition, we carried out SEM-EDAX measurement (Appendix E), and InP/ZnO structures showed progressive enhancement of zinc content from 10.70 wt%

for InP core structure to 23.33 wt% for InP/5ZnO core/shell structures. Moreover, the crystal structure of the synthesized QDs studied by XRD, and InP and ZnO showed a cubic and hexagonal structure, respectively. (Appendix E). Additionally, TEM and XRD measurements confirmed the presence of InP/ZnO core/shell structure, which caused the significant red-shift in photoluminescence peak position.

4.2.3 The optical properties of InP/ZnO QDs

Absorbance and PL spectra of the synthesized QDs were characterized to investigate the effect of shell thickness on their optical properties (as shown in Figure 4.7b). The emission peak wavelength of QDs was red-shifted from 576 to 627 nm by growing ZnO shell on the InP core because the electron had a tendency to delocalize toward the ZnO shell, while the hole was strongly confined inside the core (as shown in Figure 4.7a). Thus, the delocalization of the exciton led to less confinement energy and red-shift in the emission. As the shell thickness increased, the electron and hole recombination lifetime also increased from an average value of 11 ns for InP to 31 ns for InP/5ZnO (Figure 4.8a and 4.8b), owing to the smaller cross-section of electron and hole wave function overlap. Noticeably, in Figure 4.7b the indium-based Type-II heterostructures enabled the control on the Stokes-shift, and while the shell thickness increased, the spectral overlap between the emission and absorption significantly decreased. Because in InP/5ZnO QDs the shell volume was nearly 10 times higher than InP core QDs (~300 nm^3 for InP/5ZnO versus only ~30 nm^3 for InP core), the absorption spectrum was significantly affected by ZnO shell. This was also observable in cadmium-based counterparts [105].

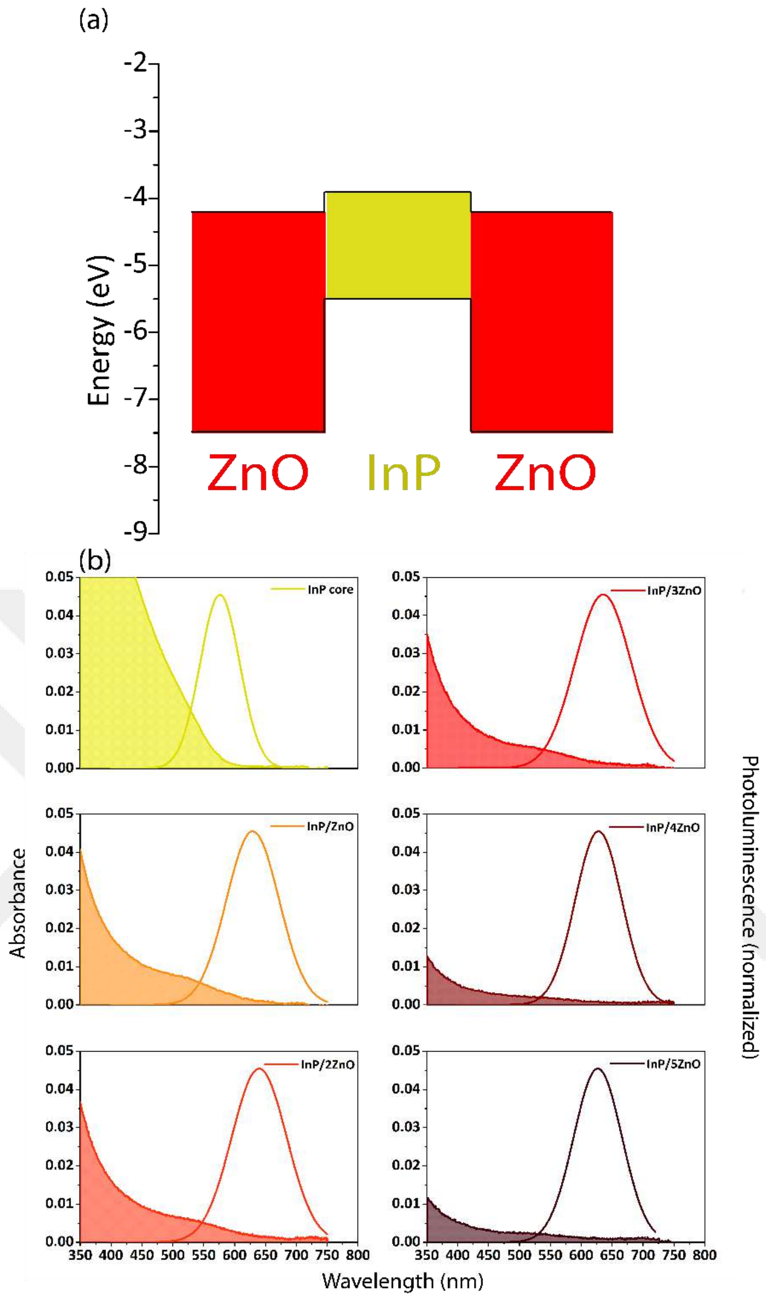

Figure 4.7: (a) The band-alignment of InP/ZnO core/shell QDs. (b) The absorption (shading) and photoluminescence (no shading) spectra of InP/ZnO QDs with increasing shell layers (from 0 to 5) in hexane. Each shell layer corresponded to a shell thickness of 0.27 nm.

QE measurement of QDs in hexane and in the PDMS polymer matrix was performed, as shown in Figure 4.8c. Increasing the shell thickness up to InP/2ZnO results in a 3-fold enhancement in QE (35.9%), which was due to better surface passivation by shell formation [314]. Further increase of the ZnO shell thickness caused the QE to decrease (i.e., 17.6% for InP/5ZnO) presumably due to the higher interfacial strain, which was generated by incomplete monolayer coverage (for detailed monolayer coverage calculation see Appendix E) [21]. In addition, while ZnO shell is grown on top of the InP core, the heterostructure shifts from a Type-I to a Type-II carrier localization meaning that while the hole is confined in the InP core, the electron starts to be localized in the shell. Up to 2 MLs of ZnO, the QD also possibly shows a quasi-type-II carrier localization, in which both the electron and hole mainly recombine in the core region. While the shell thickness is further increased, the recombination starts to occur with an electron that significantly localized in the shell and a hole in the core, which also leads a decrease in the oscillator strength and QY.

The QE of the QD slabs (Figure 4.8c) showed a decrease in comparison with in-solution QDs due to the host material effect, which introduced the additional non-radiative channels. The QE of the films followed a similar trend with the QE of the solutions, which was increased up to InP/2ZnO and then decreased as the shell growth continues up to InP/5ZnO. Notably, as the shell thickness increased from 2 to 5 layers, the difference between the QE of films and solutions showed less change in efficiency. While the QE change was 9.3% for InP/2ZnO, it decreased to 1.4% for InP/5ZnO. This enhanced photostability against host material effect was also visible in time-resolved decay spectra for the QDs (Figures 4.8a and 4.8b). In both hexane and PDMS, the absorbance of InP/5ZnO QDs was similar due to the low scattering loss and the QDs additionally showed a stable photoluminescence peak wavelength at 627 nm (Figure 4.8d). Moreover, we investigated the relative change of the reabsorption loss [272] and the relative reabsorption decreased while the shell grows (see Appendix E).

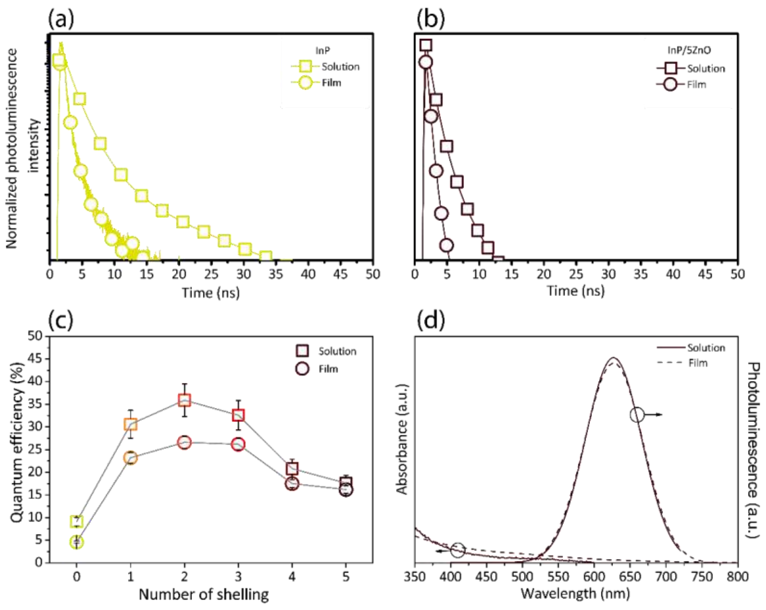

Figure 4.8: (a-b) Time-resolved fluorescence measurement of InP and InP/5ZnO QDs in hexane (square) and PDMS film (circle). (c) QE of the corresponding QDs in hexane solution (square) and PDMS film (circle) (N=3). (d) Absorption and photoluminescence spectra of InP/5ZnO QDs in hexane solution (solid line) and in PDMS film (dashed line).

4.2.4 The LSCs based on InP/ZnO QDs

LSCs should absorb sufficient incident radiation and direct the down-converted luminescence toward edges for light concentration. For that, 0.05 wt% of QDs was integrated into PDMS slabs (Figure 4.9a) and at this loading concentration level the transparency of LSCs promotes the appropriate reduction of incident sun light quality that can transmit to the inside of homes and offices (Figure 4.9a). In terms of light harvesting, LSC absorbs ~24% of the incoming radiation (at 525 nm) (Figure 4.9b). Moreover, the surfaces of the LSC were sufficiently smooth for total internal reflection and light guiding. Hence, under UV light exposure, the luminescence of the fabricated slab was especially visible in the edges comparing to faces due to the waveguiding effect (Figure 4.9c). Furthermore, the flexibility of the QD-polymer slabs was shown in Figure 4.9c and this property can be useful to integrate LSCs on curved surfaces and to keep the light intensity fixed while the sun is changing its position during a day.

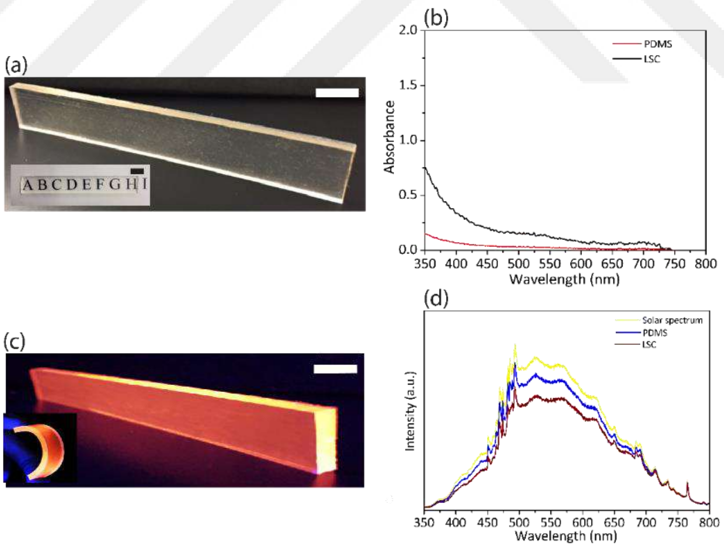

Figure 4.9: (a) The photograph of InP/5ZnO QD-LSC under ambient light. Inset: Frontal view of InP/5ZnO QD-LSC. (b) The absorbance spectra of PDMS and LSC with 0.05 wt% concentration of InP/5ZnO QDs. (c) InP/5ZnO QD-LSC under UV irradiation. The edges seem brighter due to the total internal reflection in LSC. Inset: The flexibility of the QD-LSC. (d) The solar spectrum before and after PDMS slab and QD-LSC incorporated with 0.05 wt% InP/5ZnO QDs. The scale bar was 1 cm in all figures.

4.2.5 The evaluation of optical performance

To evaluate the change in the photometric quality of the light that passes through the LSCs, it was illuminated by a collimated solar spectrum (solar simulator AM 1.5 G) and the transmitted light was coupled to a spectrometer. CRI is an important measure that shows the ability to render true colors of the illuminated objects, and the transparent PDMS polymer matrix was a suitable material to be used for windows due to keeping the CRI of the transmitted light fixed in comparison with the incoming light generated by solar simulator (Figure 4.9d). Remarkably, InP/5ZnO QD-based LSC also exhibited no change of CRI with respect to the solar simulator as well, demonstrating its potential for solar windows (see Appendix E).

To investigate the effect of Stokes-shift engineering on the LSC performance, InP/2ZnO QDs with highest QE and InP/5ZnO QDs with lowest reabsorption were integrated inside PDMS waveguide (with 9 cm×1.5 cm× 0.3 cm dimensions) at the same level of weight percentage (0.05 wt%). We analyzed the dependence of the optical output power versus the illuminated area. For that, we covered a specific part of LSCs, excited the remaining area with UV light (at 365 nm) and measured optical output at the edge (Figure 4.10a). While InP/2ZnO-based LSC had a near exponential behavior, InP/5ZnO-based LSC showed a linear response for output optical power as the coverage area increased (Figure 4.10a). The linearity in InP/5ZnO LSC was due to the negligible reabsorption loss, whereas reabsorption loss in InP/2ZnO LSC led to an exponential response while the illuminated area increased.

The emission spectra of InP/2ZnO and InP/5ZnO QD-LSCs were analyzed with the same configuration shown in Figure 4.10a under UV excitation. Even though the photoluminescence peak wavelength in InP/2ZnO-polymer slab experienced a significant spectral peak shift (of $\Delta\lambda$=28.4 nm) in the end of the optical waveguide (Figure 4.10b), for InP/5ZnO-polymer slab the peak wavelength stayed almost at the same value with a slight change (of $\Delta\lambda$=3.2 nm) due to the less overlap of absorbance and photoluminescence spectra. Moreover, the spectral linewidth of the output intensity spectra was shown in Figure 4.10c, and FWHM of InP/5ZnO QD-LSC was decreasing with a lower slope (1.80 nm/cm) through the optical distance of 9 cm in comparison with the slope of FWHM in InP/2ZnO QD-LSC (3.29 nm/cm) due to lower reabsorption. Figure 4.10d showed the photoluminescence decay through the LSC structure. However, since the reabsorption loss was low in InP/5ZnO QD-LSC, the scattering needed to have an effect on the observed decay. To evaluate the difference between scattering and reabsorption of QD-PDMS LSCs, a beam was propagated through PDMS and InP/5ZnO QD-LSC at the wavelength of 665 nm (Figure 4.10d) [105]. The scattered light was collected from the upper face at different optical distances ranging from 1 to 8 cm from the excitation edge. As illustrated in Figure 4.10d, the scattering corrected intensity which was the subtraction of InP/5ZnO QD-LSC photoluminescence from the scattering, keeps nearly its intensity and this demonstrated that the optical output decay was mainly due to scattering.

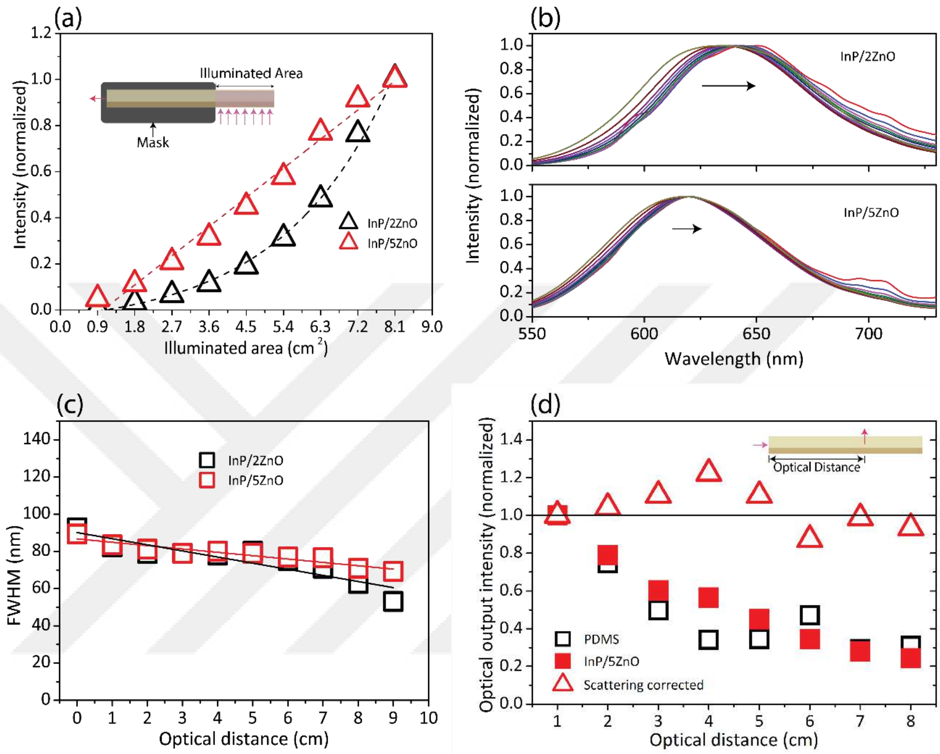

Figure 4.10: (a) The dependence of the optical output intensity by varying the illuminated area. Both InP/2ZnO (black triangle) and InP/5ZnO (red triangle) QD-LSCs excited at 365 nm UV radiation. Inset: The optical setup configuration in which the illumination was from the bottom and the output light extraction was from the edge. The mask blocks the light and allows for partial illumination. (b) Spectrum of InP/2ZnO (upper panel) and InP/5ZnO (lower panel) QD-LSCs for different optical distances (up to 9 cm). (c) The full-width-at-half-maximum (FWHM) of the optical output spectra for InP/2ZnO (black square) and InP/5ZnO (red square) QD-LSCs at different optical distances. (The measurements in (b) and (c) were done as shown in the inset of (a). (d) The optical output intensity of PDMS (blank square) and InP/5ZnO (red filled square) QD-LSC. The scattering corrected intensity (red triangle) was done by subtracting optical output intensity of PDMS from InP/5ZnO QD-LSC. Inset: The light at 665 nm was coupled from the edge and collected from the top.

The optical efficiency is an important measure to evaluate the power conversion performance of LSCs. In order to measure the efficiency, we illuminated the surface of a LSC with a solar simulator and black-painted (blocked) all edges except one, which was coupled to the solar cell. We calculated the optical efficiency by using Equation (4.4), where I_{LSC} is the short-circuit current of a solar cell coupled to the LSC when LSC is illuminated by a solar simulator, A_{PV} is the area of the light collection edge, I_{PV} is the short-circuit current of a solar cell when the solar cell is directly illuminated by a solar simulator without LSC, and A_{LSC} is the illumination area of LSC surface [286]. The efficiency of InP/5ZnO QD-LSC with a geometrical factor of 5 corresponded to 1.45% at an optical transmission level of 73%.

$$\eta_{opt} = \frac{I_{LSC} \times A_{PV}}{I_{PV} \times A_{LSC}} \quad (4.4)$$

Moreover, we performed the analytical simulations to explore the highest possible optical efficiency by using Equation (4.5) [277], in which $< \alpha_1>$ is the averaged absorption coefficient of the QDs, d and L are the thickness and length of the LSC (Figure 4.11a), η_{PL} is the measured QE of QDs in PDMS, η_{TIR} is the total internal reflection efficiency for PDMS polymer matrix, β is a numerical value fixed to 1.4 based on [315], and α_2 is the absorbance at the emission peak wavelength. The results in Figure 4.11b showed that the optical efficiency of the LSCs can be controlled by varying the geometrical factor (G factor). We measured the optical efficiency of a LSC with a G factor of 30 as 0.24%, which was in agreement with the simulation in Figure 4.11b. Moreover, the efficiency levels can be improved over 20% by increasing the QE of the QDs over 60%. Additional improvement in optical efficiency can be obtained by employing back-reflector in PV cells.

$$\eta_{opt} = \frac{1.05 \times (1-R) \times (1-e^{-<\alpha_1>d})\eta_{PL}\eta_{TIR}}{1+\beta\alpha_2 L(1-\eta_{PL}\eta_{TIR})} \quad (4.5)$$

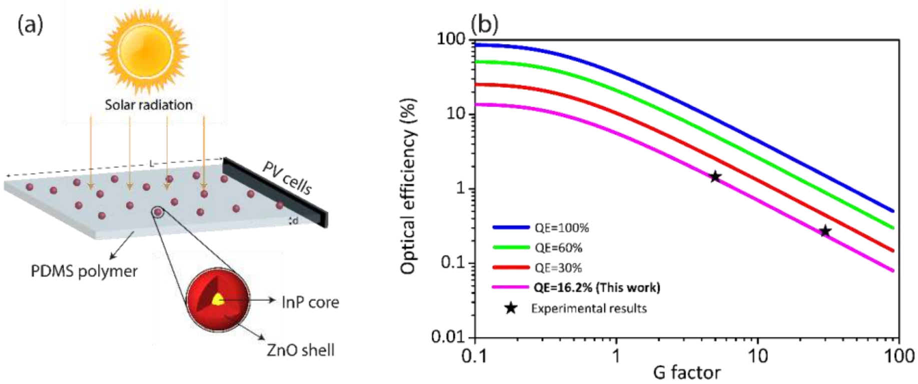

Figure 4.11: (a) Schematic of a LSC that consists of InP/ZnO core/shell QDs inside the PDMS polymer matrix. The light at the edge will be absorbed by the photovoltaic cells and converted into electrical power. The geometry of the LSC (L and d) affects the optical efficiency by changing the geometrical factor. (b) The simulations were done for QE levels of QDs as 16.2%, 30%, 60% and 100%. Star symbol indicated the experimental measurements of LSCs with a loading concentration of 0.05wt% for G=5 and G=30.

The effect of loading concentration on the optical efficiency was also investigated. Four different LSCs with different loading concentrations of 0.01 wt%, 0.05 wt%, 0.1 wt% and 0.5 wt% of InP/5ZnO QDs were fabricated and illuminated with solar spectrum. While quantum efficiency slightly decrease from 19.1% for 0.01 wt% to 16.4 % for 0.5 wt%, the optical efficiency also increase from 0.28% to 3.22% (Table 4.1). Here, the optical efficiency is enhanced by increasing the loading concentration due to strong absorption (e.g., 0.5 wt%), but the transmission of the LSC significantly drops (e.g., to 13% at 525 nm) (see Appendix E), which is not suitable for solar window application. Therefore, it is important to optimize the light harvesting and transmission properties of LSCs for solar window application.

Table 4.1: Quantum efficiency and optical efficiency of the fabricated LSCs with different loading concentration of InP/5ZnO QDs.

	0.01 wt%	**0.05 wt%**	**0.1 wt%**	**0.5 wt%**
Quantum efficiency (%)	19.1	17.5	17.1	16.4
Optical efficiency (%) G=30	0.049	0.225	0.195	0.43
Optical efficiency (%) G=5	0.28	1.4	1.27	3.22

4.2.6 *Conclusion*

We demonstrated efficient luminescent solar concentrators based on cadmium-free QDs. The Type-II band alignment of InP/ZnO core/shell QDs enabled the Stokes-shift engineering, which led to suppression of the reabsorption losses. At the same time, the shell advantageously protected the recombination dynamics and QE against host material effect. Indium-based optoelectronic materials and devices are already used in displays at homes and offices. Therefore, these indium phosphide nanomaterials may also find wide-spread use as luminescent solar concentrators in the windows.

4.3 *Ecofriendly and efficient luminescent solar concentrators based on fluorescent proteins*

This section is based on the publication "*Ecofriendly and efficient luminescent solar concentrators based on fluorescent proteins*" S. Sadeghi, R. Melikov, H. B. Jalali, O. Karatum, S. B. Srivastava, D. Conkar, E. N. Firat-Karalar, and S. Nizamoglu, ACS Applied Materials and Interfaces 11.9 (2019) 8710-8716. Reproduced (or "Reproduced in part") with permission from American Chemical Society Copyright 2019.

In recent years, LSCs have received renewed attention as a versatile platform for large-area, high-efficiency and low-cost solar energy harvesting. So far, artificial or engineered optical materials, such as rare-earth ions, organic dyes and colloidal QDs have been incorporated into LSCs. Incorporation of non-toxic materials into efficient device architectures is critical for environmental sustainability and clean energy production. In this section, we demonstrated LSCs based on fluorescent proteins, which are biologically-produced, ecofriendly and edible luminescent biomaterials along with exceptional optical properties. We synthesized mScarlet fluorescent proteins in Escherichia coli expression system, which is the brightest protein with a quantum yield of 61% in red spectral region that matches well with the spectral response of silicon solar cells. Moreover, we integrated fluorescent proteins in an aqueous medium into solar concentrators, which preserved their quantum efficiency in LSCs and separated luminescence and wave-guiding regions due to refractive index contrast for efficient energy harvesting. Solar concentrators based on mScarlet fluorescent proteins achieved an external LSC efficiency of 2.58%, and the integration at high concentrations increased their efficiency approaching to 5%, which may facilitate their use as "luminescent solar curtains" for in-house applications. The liquid-state integration of proteins paves a way towards efficient and "green" solar energy harvesting.

4.3.1 Introduction

LSCs have attracted significant attention as a versatile platform to harvest solar radiation [272]. They are optical waveguides, which consist of fluorophores that are incorporated into a solid host matrix. The optical efficiency of the LSC depends on the quantum efficiency, absorption-emission overlap and scattering of fluorophore [13, 77]. For efficient LSCs, organic dyes [316] and rare-earth ions [273] have been used as fluorophores. In addition, recently a wide variety of colloidal QDs have also been investigated for LSCs [294, 317-320]. Unfortunately, there are concerns related to the utilization of QDs. European Union [145] pointed out that QDs represent a significantly diverse group of substances with different toxic potentials based on their physical and chemical properties, size, shape, crystalline structures, surface electric charge, chemical compositions of the core and shell, and also purity, which lead to unique toxicokinetics. All of these characteristics governing the toxicity behavior need to be investigated to assure the safe usage conditions of the QDs [145].

Fluorescent proteins can be an alternative for eco-friendly and efficient solar energy harvesting. They have been naturally produced by the jellyfish Aequorea Victoria and have been present for millions of years in our ecosystem [4]. Since the green fluorescent proteins were discovered in 1960s, they have been widely used for functional imaging of cellular activities in biology [321, 322]. Recently, due to bridging the worlds of biology and optics and the need for transition toward waste-free technologies, they have started to be explored for different areas such as lasers and LEDs [33, 323]. The significant interest in fluorescent proteins in recent years is due to their bio-compatibility and ecofriendly nature along with mass production capability and advantageous photoluminescence features including high quantum yield, narrow emission and photo-stability [4]. Furthermore, this material can be produced in genetically encoded organisms [30], and it is also edible and digestible in the mammalian stomach [150]. Among a wide variety of fluorescent proteins, mScarlet is a new type of fluorescent protein with a high quantum yield of around 70% [324]. At the same time, the photoluminescence peak in the red spectral region matches with the spectral responsivity of silicon solar cells and makes it a suitable alternative for solar energy harvesting.

The incorporation of luminescent materials at high efficiency levels into device architectures is critical. In general, the optical efficiency of the LSCs have been significantly deteriorated by the quantum efficiency drop of fluorophores when they are transferred from liquid- to solid-state into polymeric matrix [13]. The liquid- to solid-state transition introduces additional non-radiative channels, which reduces the quantum efficiency of luminescent materials. Different approaches have been investigated to suppress the efficiency drop of fluorophores during the liquid to solid transition. One strategy is the growth of a thick shell surrounding the core QDs that reduces the interaction of the core with the surrounding medium [13]. Another strategy is the encapsulation of the fluorescent material within a silica shell [28]. Alternatively, strategies that can combine simplicity and efficiency with "green" materials can be beneficial to further widen the spread of LSC technology.

In this section, for the first time we propose and incorporate an entirely new biomaterial class, fluorescent proteins, for efficient LSCs. For that, we synthesized and incorporated mScarlet fluorescent proteins in aqueous medium, which was free of toxic elements (Figure 4.12a). Liquid-state integration enabled the preservation of the quantum yield compared to solid-state. At the same time, the liquid-state integration enabled the separation of luminescent and wave-guiding regions due to the refractive index difference between aqueous medium as the natural host material of the fluorescent proteins and the surrounding polymer (Figure 4.12a). The LSC based on mScarlet fluorescent proteins at a concentration of 5 wt% showed an external efficiency over 2%. In addition, the incorporation of the proteins at high concentration levels (10 wt%) leads to an efficiency over 4% with partial solar light transmission (26%) that opens up the application as "luminescent solar curtain" inside buildings due to their biocompatible nature (Figure 4.12b).

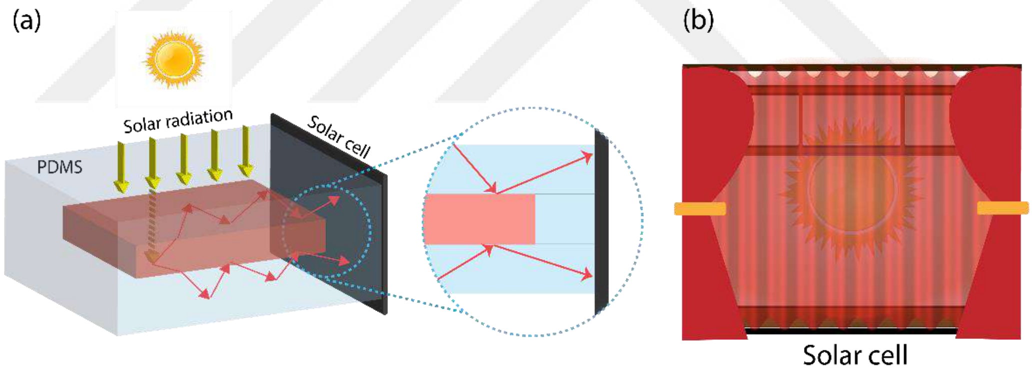

Figure 4.12: (a) The light interaction in luminescent solar concentrator structure that is composed of PDMS sheets at the top and the bottom and mScarlet fluorescent protein dispersed in aqueous medium (red central area). The total internal reflection of the emitted light takes place inside the PDMS polymer sheets due to the higher refractive index of PDMS (n=1.40) in comparison with water (n=1.33). (b) The concept of the "luminescent solar curtain". The "luminescent solar curtain" is illuminated with solar radiation and generates photoluminescence (as shown in (a) or fluorophores integrated inside a solid polymeric film) that is coupled to solar cell in the edge.

4.3.2 The synthesis of mScarlet fluorescent proteins

Like other fluorescent proteins, mScarlet is a molecule, which confines a chromophore surrounded by a nano-cylinder structure with 8.6 nm and 3.5 nm dimensions (Figure 4.13a). The protective shell acts as a natural "bumper", which prevents aggregation with the neighboring fluorescent protein molecules. For the synthesis, mScarlet coding sequence [324] was amplified by PCR from mScarlet cDNA (85042, Addgene) using the forward primer (GGG GAC AAC TTT GTA CAA AAA AGT TGA T ATG GTG AGC AAG GGC GAG GCA) and the reverse primer (GGG GAC AAC TTT GTA CAA GAA AGT TGT TTA CTT GTA CAG CTC GTC CAT GCC G) and cloned into pDONR221. To generate GST (glutathione *S*-transferase) expression vector, gateway cloning between pDONR221-mScarlet and pDEST-GST was performed (Thermo-Fisher), and DNA sequences of all plasmids were verified by Sanger sequencing. For the protein expression and purification, GST-mScarlet expression was induced in *E. coli* BL21(DE3.1) cells grown to OD_{600}=0.6 with 1 mM isopropyl-1-thio-beta-D-galactopyronoside (IPGT) for 3 days at 30 °C. The lysogeny broth (LB) culture medium was supplemented with 50 µg/ml ampicillin every other day. Following expression, the culture was clarified by centrifugation at 4000 rpm for 20 minutes at 4 °C. The pellet was re-suspended in GST−binding lysis buffer (137 mM NaCl, 2.7 mM KCl, 10 mM Na_2HPO_4, 1.8 mM KH_2PO_4, 0.25 M KCl, protease inhibitors (10 µg/ml each of aprotinin, leupeptin, pepstatin, and 1 mM phenylmethylsulfonyl fluoride)). Bacterial cell wall was lysed with 1 mg/ml lysozyme by incubation on ice for 1 hour, followed by sonication 7X for 20 seconds each. The lysate was clarified by centrifugation and GST-Scarlet was purified by affinity chromatography on glutathione−Sepharose (GE Healthcare). Purified protein was concentrated using 10.000 NMWL centrifugal filters (Amicon® Ultra-4), followed by dialysis first into PBS and then ddH_2O using Slide-A-Lyzer™ dialysis cassettes (Thermo-Fisher). The purified protein solution emits orange color under UV excitation (Figure 4.13a).

4.3.3 The optical properties of mScarlet proteins

We investigated the optical properties of mScarlet fluorescent proteins. The fluorescent proteins in aqueous environment showed an absorption wavelength peak at 569 nm and emission wavelength peak at 595 nm, which has good spectral overlap with the silicon solar cell responsivity spectrum (Figure 4.13b). Furthermore, by using an integrating sphere we measured the absolute quantum yield, and it showed a quantum yield of 61.2%. The fluorescent proteins can be used in their solid-state form for photonic applications [325]. Hence, we investigated the effect of liquid- to solid-state transition on the optical properties of the mScarlet fluorescent protein. For that, we generated a close-packed form of proteins by removing the solvent and the solid showed absorbance and photoluminescence peaks at 575 nm and 620 nm, respectively (Figure 4.13b and Appendix F). Since they are positioned in nearby to each other, the transition dipole moments start to “feel” each other that can lead to Förster-type resonance energy transfer [153]. To analyze this interaction, we carried out time-resolved photoluminescence (TRPL) spectroscopy using a time-correlated single-photon counting (TCSPC) method [200] (Figure 4.13c). The photoluminescence decay of mScarlet in solid-state showed shorter lifetime (5.9 ns ± 0.12) than aqueous medium (7.8 ns ± 0.71) because of the energy transfer. This cannot be originated from a Dexter-type energy transfer due to the shield surrounding the emissive center that behaves as a quantum mechanical barrier for the photo-generated charge carriers. In principle, while the proteins are assembled in film, the photoluminescence shows a red-shift that can lead to a higher energy harvesting efficiency due to the higher responsivity of silicon detectors at deep red spectral region (Figure 4.13b). However, the quantum efficiency of the solid-state proteins drastically decreased to 4.3%, which was around 15-fold lower than the proteins in liquid-state (Figure 4.13d). Since the quantum efficiency of the fluorophore directly affects the performance of LSCs, the integration of mScarlet in liquid-state appears as the most convenient approach for efficient luminescent solar concentration.

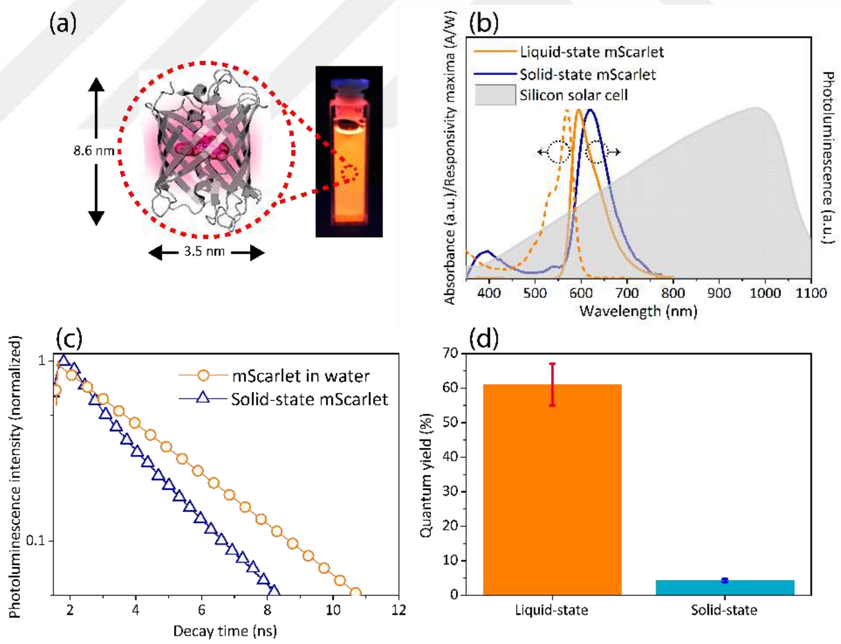

Figure 4.13: (a) The schematic of mScarlet fluorescent protein molecule consisting of a helix structure surrounding the chromophore. The cuvette showed mScarlet fluorescent protein dispersed in water under UV irradiation. (b) The normalized absorbance (orange dashed line) and photoluminescence (orange solid line) spectra of liquid-state mScarlet. The normalized photoluminescence (blue solid line) spectra of solid-state mScarlet. The gray shaded area shows the silicon solar cell responsivity spectrum. (c) The time-resolved photoluminescence of liquid-state (orange line) and solid-state mScarlet (blue line). (d) The absolute quantum yield of liquid-state (orange bar) and solid-state (blue bar) mScarlet fluorescent proteins (n=3).

4.3.4 The LSCs based on mScarlet proteins

For the fabrication, we developed an architecture that can hold the fluorescent liquid material inside a solid-state PDMS slab. For that, a sheet of PDMS polymer (with the dimensions of 2.5 cm × 2.5 cm × 0.2 cm) was prepared by using a pre-fabricated aluminum mold (Figure 4.14a). Then, UV curable polymer was plastered at the edges of the PDMS polymeric sheet to ensure leakage proof. PDMS polymer spacer, which was cut in the desired dimensions to specify the liquid area, was placed on top of the sheet. Then, the structure was illuminated with UV irradiation to complete the curing process of the resin. As the next step, another PDMS sheet with the same dimensions was adhered on top of the PDMS spacer by addition of UV curable polymer and subsequent photo-curing. The final structure included a central hollow space, which was supported by PDMS spacer. Finally, mScarlet fluorescent protein solution with the concentration of 5 wt% (with optical density of 0.0588 at 500 nm) was injected inside the central area by using a micro-syringe (Figure 4.14a).

For solar window applications, the transparency of an LSC needs to be at a sufficient level that will simultaneously allow the transmission of sunlight for interior illumination and guidance of the photoluminescence for energy harvesting. The LSC was illuminated with UV irradiation, and the total internal reflection of the orange emitted light by the mScarlet molecules was visible at the edges of the LSC (Figure 4.14b). To assess the transparency of the LSC, the structure was illuminated with the AM 1.5G solar simulator and the transmittance corresponded to 45% at 525 nm (Figure 4.14c).

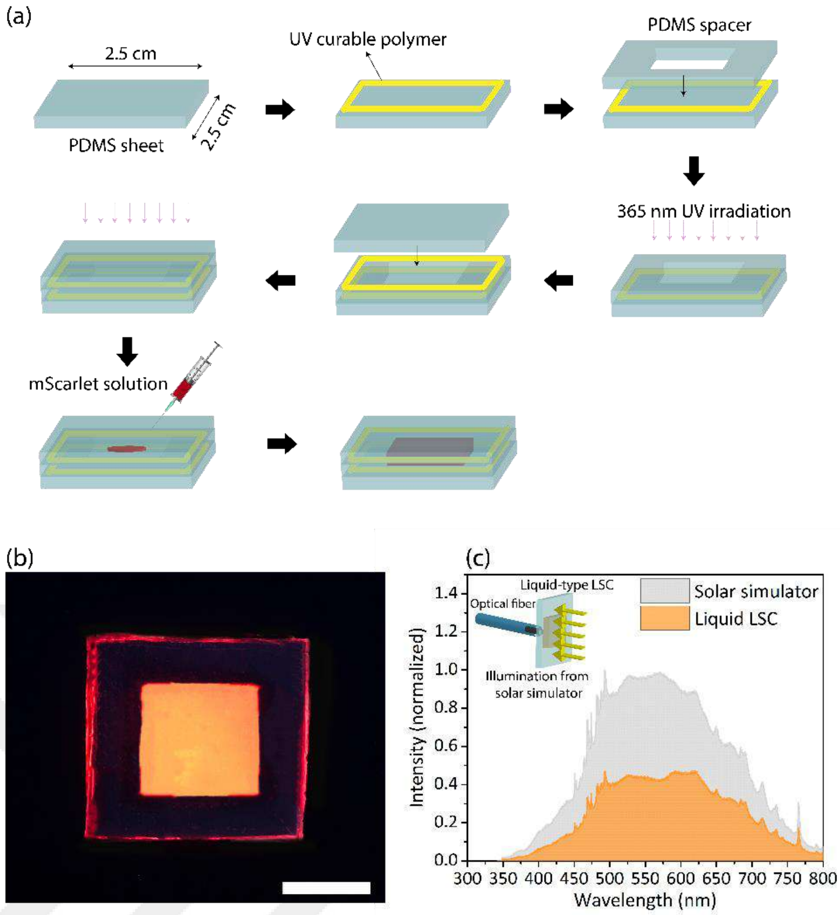

Figure 4.14: (a) The schematic of fabrication process for liquid-type luminescent solar concentrator. (b) The LSC composed of aqueous mScarlet (central orange area) under UV irradiation (Scale bar=1 cm). (c) The optical output intensity of LSC and solar simulator. Inset: The schematic of setup, in which one face of the LSC was illuminated by solar simulator and the optical fiber was placed on the other face to measure the transmission of the fabricated LSC.

4.3.5 The evaluation of optical efficiency

To experimentally quantify the optical performance, the edge of the fabricated LSC (2.5 cm×0.6 cm) was coupled to a calibrated solar cell and LSC was illuminated by the solar simulator orthogonal to its surface (with an active area of 1.5 cm×1.5 cm). The output light was collected on its edge by the calibrated silicon solar cell. To calculate the external LSC efficiency (η_{ext}), Equation (4.6) was used [15]:

$$\eta_{ext} = \frac{I_{LSC} \times A_{PV}}{q_{LSC} I_{PV} \times A_{LSC}} \tag{4.6}$$

q_{LSC} was calculated as 1.0248 and consequently we obtained an external LSC efficiency of 2.58%. The experimentally achieved external efficiency can be further improved by coupling luminescence to the solar cells positioned on all the edges of the LSC. Integration of back-reflectors can also increase the efficiency of the device, while decreasing the transparency.

The external efficiency of an LSC is directly proportional with the internal efficiency (η_{int}), which measures the reabsorption effect inside the LSC by considering quantum efficiency of fluorophore. To understand the quantum efficiency at different concentrations, we performed a simulation that calculates all the possible combinations of radiative energy transfer processes in the mScarlet medium [113]. According to our simulation, as the concentration increased from 3 wt% toward 10 wt%, the quantum efficiency decreased from 66.9% to 53.1% (Figure 4.15a). Here, the decrease was due to the reabsorption, which was originated by the spectral overlap of photoluminescence and absorption. Experimentally, as the concentration of the fluorophore increased from 3 wt% to 7 wt% and 10 wt%, the quantum yield decreased from 64.1% to 56.0% and 51.0%, respectively, which agreed with the simulation results (Figure 4.15a). In principle, the decrease of quantum yield lowers the external efficiency of the device, but the effect of decrease in quantum yield outcompetes with the higher absorption in higher concentrations (based on Equation (4.7)). As a result, while the fluorophore loading concentration increased from 3 wt% to 7 wt% and 10 wt%, the external efficiencies of the LSCs were measured as 1.72%, 3.16% and 4.42%, respectively (Figure 4.15b). Increasing fluorophore concentration strengthens absorption and this leads to higher number of photo-generated excitons that simultaneously results in brighter luminescence and higher external efficiency, though higher reabsorption losses. Furthermore, we also measured the transmittance of the LSCs having different concentrations. The measured transmittance from the LSCs with 3 wt%, 7 wt% and 10 wt% showed the transmittance level of 63%, 38% and 26%, respectively (Figure 4.15c). Even though the transmittance at 10 wt% is around a quarter, it may be useful as a partially-transmitting “luminescent solar curtain” for geographical locations having strong daylight illumination.

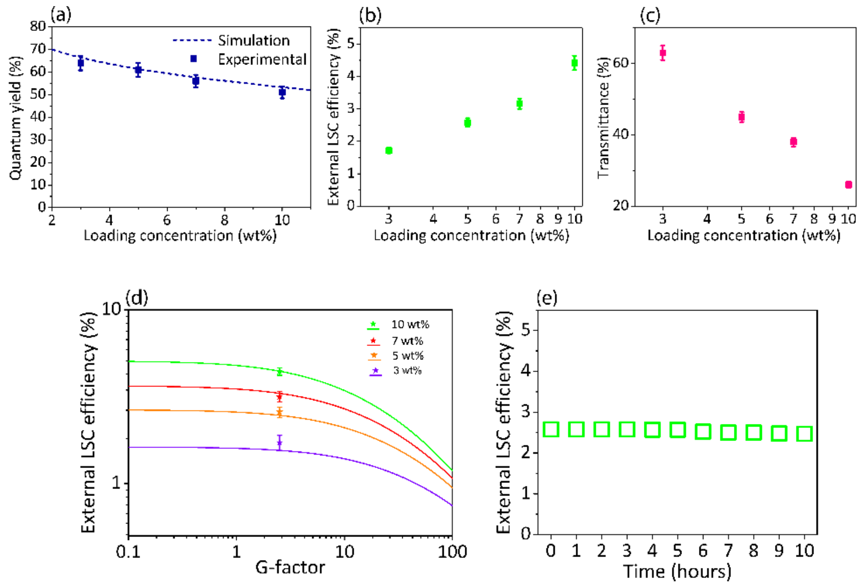

Figure 4.15: (a) The quantum yield, (b) the external efficiency and (c) the transmittance of LSCs with different fluorophore loading concentrations ranging from 3 wt%, 5 wt%, 7 wt% and 10 wt% (n=3). (d) The external efficiency simulation (line) and experimental results (stars) of LSCs with different loading concentrations. (e) The photostability measurement of the fabricated protein-based LSC during 10 hours of illumination time.

To estimate the ultimate optical performance of the fabricated fluorescent protein-based LSCs, we also simulated external LSC efficiency levels having different gain factors (G-factors) in different loading concentrations ranging from 3 wt% to 10 wt% (Figure 4.15d). The G-factor is defined as the ratio of the illumination area to the light collection edge area. For the fluorescent protein-based LSC, the entire edge area was considered as the light collection area due to the total internal reflection by the PDMS layers (1.5 cm × 0.6 cm). As a result, G-factor was calculated as 2.5. Equation (4.7) was used for the calculation of internal efficiency as follows [15]:

$$\eta_{int} = \frac{\int 1.05 \frac{\eta_{TIR}\eta_{PL}}{1+\beta\alpha_{eff}(\lambda)L(1-\eta_{TIR}\eta_{PL})}\phi_{PL}(\lambda)d\lambda}{\int \phi_{PL}(\lambda)d\lambda} \tag{4.7}$$

,where η_{TIR} and η_{PL} are the total internal reflection efficiency and quantum efficiency of mScarlet fluorescent protein in aqueous medium as 0.88 and 61.2%, respectively, L is the length of the LSC panel, β was considered as 1.4 based on [86] and α_{eff} was calculated based on Equation (4.8) as follows [15]:

$$\alpha_{eff}(\lambda) = \alpha(\lambda)\frac{d_{protein}}{d_{protein}+d_{PDMS}} \tag{4.8}$$

, in which $d_{protein}$ and d_{PDMS} are the thicknesses of liquid-state fluorescent protein (0.2 cm) and PDMS areas (0.6 cm) and $\alpha(\lambda)$ is the absorption coefficient of the fluorescent protein calculated based on Figure 4.13b. Based on Equation (4.7), the internal efficiency was calculated as 0.5118 for the protein-based LSC at the G-factor of 2.5 with 5 wt% concentration. Moreover, the absorption efficiency (η_{abs}) of the LSC device was calculated based on Equation (4.9) [15], which quantifies the ratio of the absorbed number of photons overall solar spectrum.

$$\eta_{abs} = \frac{\int \phi_{sol}(1-R)\left(1-e^{-\alpha(\lambda)d}\right)d\lambda}{\int \phi_{sol}(\lambda)d\lambda} \tag{4.9}$$

, where $\phi_{sol}(\lambda)$ is the spectral profile of the solar spectrum, R is reflectivity, which was calculated based on Equation (4.10) as 0.0278 by considering n_{PDMS}=1.40 [326] and n_{air}=1. d was considered as the fluorescent protein area thickness, which was 0.2 cm.

$$R = \frac{(n_2-n_1)^2}{(n_2+n_1)^2} \tag{4.10}$$

The absorption efficiency was yielded as 0.0470 for the concentration of 5 wt%. As a result, the external LSC efficiency was calculated as 2.40% at the G-factor of 2.5 based on Equation (4.11) as follows [15]:

$$\eta_{ext} = \eta_{abs}\eta_{int} \tag{4.11}$$

The simulation results have strong correlation with the experimental results (Figure 4.15d). One of the main reasons of the deviation between the experimental and simulation results was due to the separation of the luminescence and light guiding regions [315]. The scattering of the light by the polymeric host matrix and fluorescent protein molecules may also cause the deviation between the simulation and experimental results of the external LSC efficiency. To assess the photostability of the protein-based LSCs, we constantly illuminated a fabricated LSC with concentration 5 wt% for 10 hours with solar simulator and measured the external efficiency of the device (Figure 4.15e). The external efficiency was relatively decreased ~3% after 10-hours illumination (from 2.58% at 0 hour to 2.47% at 10 hours).

Moreover, the external efficiency of the fluorescent protein-based LSC (2.58%) is comparable with the state-of-the-art efficiency levels of the QD-based LSCs [13, 85] The liquid-state integration of mScarlet fluorescent protein with high QY enabled to achieve a comparable external efficiency with state-of-the-art QD-based LSCs. At the same time, the separation of waveguiding regions decreased the reabsorption losses, which also resulted in the higher external LSC efficiency levels. Ecofriendly nature, bio-production capability, large volume synthesis and edibility while having high quantum yield and emission in the red spectral region makes mScarlet unique and advantageous for their widespread use, even, for direct internal use as “luminescent solar curtain” applications.

4.3.6 Conclusion

This study demonstrated the incorporation of a biocompatible, edible and efficient fluorescent material for LSCs for the first time. The feasibility of the “green” and efficient LSCs was demonstrated by using mScarlet fluorescent proteins as the luminescent emitter. A new strategy incorporating fluorophores in their aqueous environment was applied that preserved the high-quantum yield of mScarlet in the device architecture. The structure can be converted to an all-biodegradable platform by replacing the PDMS with biodegradable polymers such as polylactic acid, polylactic-co-glycolic acid, etc. Advantageously, the liquid-state integration also separated the luminescence and waveguiding regions. Since the materials in the LSC is biocompatible, it can be safely used for in-house applications. Hence, beside the solar window applications, the integration using high concentration and lower transparency may open up a new paradigm of “luminescent solar curtains”.

4.4 Single Integrated Unit of Bulk Heterojunction Solar Cell Array and Luminescent Solar Concentrator for Internet of Things

Internet of Things (IoT) inter-connecting objects such as buildings, vehicles and cities has attracted significant attention in the last decade. Unplugged and battery-free energy-harvesting approaches can enable self-standing and independent operation for IoT devices. In this section, we report a single integrated unit of a bulk heterojunction solar cell array and luminescent solar concentrator for energy harvesting at low light intensity levels. For that, alloyed CdSe@ZnS QDs, which were incorporated into a PDMS waveguide, were synthetically engineered to match their photoluminescence spectra with the photo-response of P3HT:$PC_{61}BM$ solar cells. QDs maintained high in-film photoluminescence quantum yield of 64% that led to an optical quantum efficiency of 44.7%. LSCs can generate sufficient power for the active radio frequency identification (RFID) tags to send signals in the communication distance of 35 meters at low power levels of 0.1-sun and ~0.1 km under 1-sun conditions, respectively, which is sufficient for indoor and outdoor communications. This study paves the way toward using luminescent solar concentrators for transparent, efficient, and configurable energy harvesting solution for IoT applications.

4.4.1 Introduction

Internet of Things, which refers to inter-related computing devices or objects with the ability to transfer data over a network, has attracted significant attention both by industry and academia in the last decade [327-329]. Nowadays, IoT is further extended toward smart cities via connected industries, buildings and cars, which constitute more than 60% of the in-progress IoT-related technologies worldwide [330]. Tens of billions of IoT-connected devices already exist all around the world and this number will continue to grow as the internet connectivity has become a standard platform for electronic devices. The projection of the expanding global market size of the IoT (from 200 billion dollars in 2019 to 1600 billion dollars in 2025) reveals the significance of the investment on IoT technologies in the near future [331]. Unplugged and battery-free energy-harvesting approaches can enable self-standing and independent operation of IoT devices. The quest for finding alternative energy solutions for the IoT devices is continuing.

LSCs offer a cost-effective photon-energy harvesting solution [13, 28, 85, 292]. They consist of a transparent optical waveguide (polymer or glass), which is incorporated or coated with fluorescent particles. Under illumination, fluorescent particles can absorb large-area radiation and re-emit at longer wavelengths reaching the photovoltaic cells placed at the edges of the waveguide by total internal reflection (Figure 4.16). Beside their contribution for zero-energy buildings [14, 332], LSCs possess potential to power-up independent IoT devices for data transmission, processing and reception due to their scalable size, transparency and configurable operation (Figure 4.16).

So far, the efforts to harvest solar energy via LSCs are mostly focused on the coupling of conventional silicon solar cells placed at the edges of the waveguide [333-335]. Silicon solar cells were commonly used for LSC applications due to their high-power conversion efficiency in the visible to near IR solar spectrum (E_g = 1.1 eV) and mass production ability [336]. Even though silicon photovoltaics is the premier choice for LSCs, its utilization under solid-state lighting that have emission in the visible spectrum with dominant blue light was limited due to its responsivity maximum at near-IR [337, 338]. Alternatively, organic photovoltaics are promising candidates for the next-generation renewable energy harnessing technologies due to low-cost and large-scale production, flexibility, and strong absorption in the visible spectrum [339-341]. The high-performance operation at low light intensity levels is another advantage of organic solar cells, which have not been studied for LSCs and IoT operating under a wide range of lighting levels [342-344].

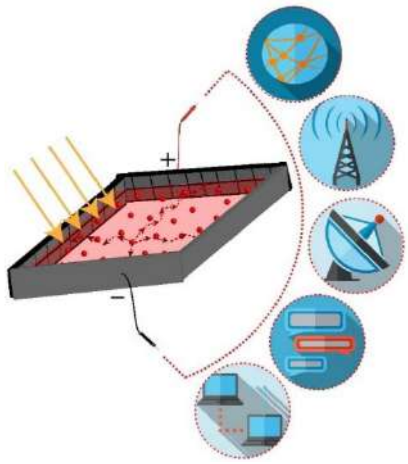

Figure 4.16: The schematic of the luminescent solar concentrator embedded with quantum dots. When illuminated by solar radiation, quantum dots will absorb the sunlight and re-emit at higher wavelengths. The generated photoluminescence from the quantum dots will be absorbed by the organic solar cells placed at the edges of the waveguide. The quantum dot-based LSCs can be used to empower a wide variety of IoT applications such as telecommunication, radar signal transmission and network.

In this section, we report a novel LSC architecture that is directly integrated with an array of bulk heterojunction organic photovoltaics during the LSC fabrication process. Among a wide variety of available fluorophores used for LSC applications as down-conversion materials such as organic dyes [16], lanthanide-based materials [18], and fluorescent proteins [17], we used QDs due to high PLQY and fine spectral photoluminescence tuning ability. The photoluminescence of alloyed CdSe@ZnS QDs was synthetically engineered to match with the photovoltaic responsivity of P3HT:PC_{61}BM solar cells. Moreover, high PLQY of 64% in polymeric waveguide facilitated an optical quantum efficiency of 44.7%. The fabricated organic solar cell-LSC architecture can generate sufficient power for the RFID tags to send signals in the high communication distance of 35 meters and ~0.1 km under 0.1-sun condition and 1-sun conditions, respectively, which is sufficient for indoor and outdoor communications.

4.4.2 Organic solar cells based on P3HT:PC_{61}BM

For light to electricity conversion, bulk heterojunction organic solar cells using P3HT as a donor and the fullerene derivative of PC_{61}BM as an acceptor were fabricated in an inverted geometry of ITO/ZnO/P3HT:PC_{61}BM/MoO_x/Ag in the ambient condition. The P3HT:PC_{61}BM blend was used as photoactive layer for LSC application because it is one of the most widely studied and successful organic semiconductor blend with proven record of efficiency and stability [345, 346]. The energy band diagram was shown in Figure 4.17a, which confirms the suitability of the band alignment for charge transport and collection. The scanning electron microscopy (SEM) was used to confirm the thicknesses of various layers of the organic solar cell (Figure 4.17b). The current-voltage (*J-V*) characteristics was studied under 1-sun AM 1.5G illumination (Figure 4.17c). The solar cells achieved a power conversion efficiency (PCE) of 3.8% with an open circuit voltage (V_{oc}) of 0.59 V, a short-circuit current density (J_{sc}) of 11.9 mA.cm^{-2} and a fill factor (FF) of 0.55. The achieved electrical parameters are well in the range of the state-of-the-art reports for the P3HT:PC_{61}BM-based organic solar cells [347].

To understand the effect of light intensity over the performance of the organic solar cells, the current-voltage (*J-V*) characteristics of the fabricated organic solar cells were investigated (Figure 4.17d). The systematic variation of J_{sc} and V_{oc} with respect to the illumination intensity were shown in Figures 4.17e and 4.17f. Both the J_{sc} and V_{oc} values were increased by increasing the light intensity from 0.1- to 1-sun [348-350] and the slope of the J_{sc} with respect to the light intensity in the log-log plot is linear, which reveals the single photon-induced processes [350, 351]. At the same time, the slope of the V_{oc} with respect to light intensity in semi-log plot showed a linear variation for P3HT:PC_{61}BM solar cells. Hence, the PCE of the organic solar cells are 2.8% for 0.1-sun and 3.8% under 1-sun illumination showing efficient operation within the intensity range.

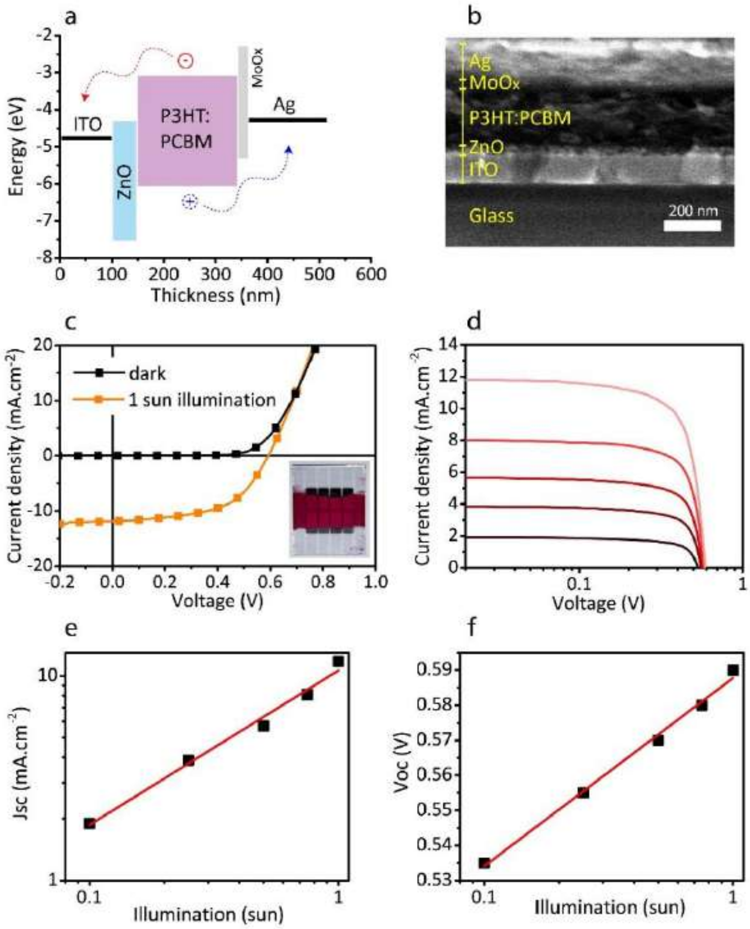

Figure 4.17: (a) Energy level diagram of inverted organic solar cell (ITO/ZnO/P3HT:$PC_{61}BM/MoO_x$/Ag) accompanied with charge transport mechanism. (b) Corresponding cross-sectional SEM image of the active area. (c) The *J-V* characteristics of the optimized organic solar cell device under AM 1.5G illumination with 100 mW.cm^{-2}. Inset: Image of the fabricated device consisting of an array of 8 solar cell pixels. (d) The *J-V* characteristics of the organic solar cell at different light intensities ranging from 0.1- to 1-sun. (e) The measured values of Jsc and (f) Voc under different illumination intensities ranging from 0.1- to 1-sun.

4.4.3 The synthesis of green-emitting CdSe@ZnS QDs

To maximize the energy harvesting efficiency by the LSC, the photoluminescence of the fluorophore inside the waveguide needs to have good spectral overlap with the absorption of the solar cells. For that, the photoluminescence of the synthesized alloyed CdSe@ZnS QDs was tuned by varying the reaction time during the synthesis procedure and the photoluminescence was recorded at each reaction time. As the reaction time increased from 5 to 20 minutes, the peak wavelengths changed from 498 nm to 574 nm, respectively (Figure 4.18a). The green-emitting QDs with photoluminescence peak position at 521 nm, which has a size of 8.6 nm ± 0.97 nm (Figure 4.18b), was selected for the integration inside the polymer matrix that match with the absorbance peak wavelength of the active layer located at 515 nm (Figure 4.18a). At the same time, the green-emitting CdSe@ZnS QDs showed high PLQY of 91% and 64% in solution- and solid-state, respectively, which makes them suitable for LSC applications.

4.4.4 The fabrication of QD-based LSCs

Different from the previous studies combining waveguides and solar cells in the post-LSC-fabrication phase [342-344], we directly integrated the photovoltaics inside the QD-doped polymeric waveguide during the LSC formation. First, the synthesized QDs were mixed with PDMS elastomer and curing agent and degassed under vacuum to remove bubbles. The fabricated organic solar cells were fixed at the edges of the pre-fabricated aluminum mold (Figure 4.18c). Then, the mixture was poured in the mold covering the organic solar cells (Figure 4.18d). The mold was placed in the oven and heated at the temperature of 70 °C for 6 hours to complete the curing process (Figure 4.18e). Upon completion of the curing process, the organic solar cells were attached to the QD-polymer composite. The QD-polymer composite integrated with the organic solar cells were removed from the mold (Figure 4.18f). The photograph of the device showed the sufficient level of transparency under ambient light (Figure 4.18g) and strong luminescence under UV radiation (Figure 4.18h). The direct integration of the waveguide and photovoltaic units advantageously enables the coupling of light from the low refractive index (n_{PDMS}=1.42) [352] to the high refractive index solar cells (n_{opv}=1.95) [353] without any reflection losses due to an air gap.

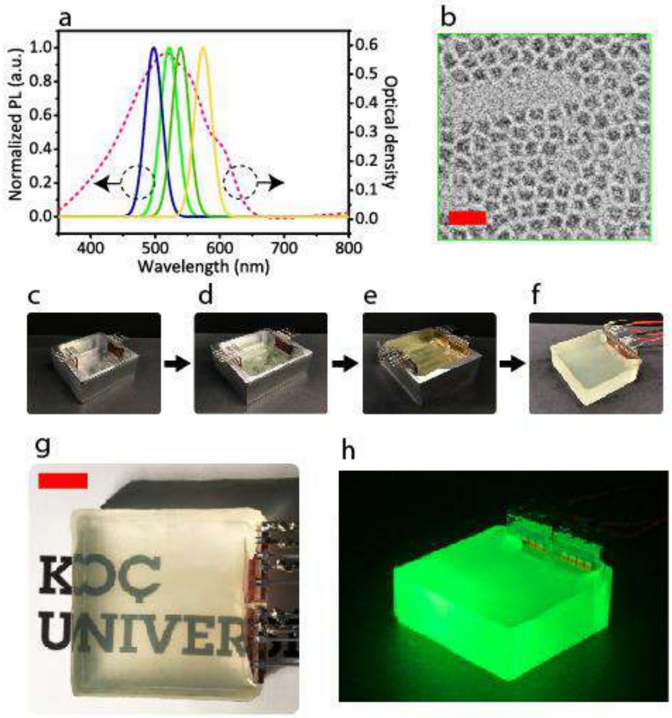

Figure 4.18: (a) The absorbance (dashed red line) of the organic active layer of the bulk heterojunction solar cell and the photoluminescence (solid lines) of the quantum dots synthesized in different reaction time ranging from 5 to 20 minutes. As the time elapses, the photoluminescence shows red shift. (b) The TEM

image of the synthesized quantum dots (scale bar=20 nm). (c) The fabricated solar cells were placed to the edges of the 5×5×1 cm^3 aluminum mold. (d) The green-emitting quantum dots and PDMS elastomer mixture was degassed and poured in the aluminum mold. (e) The mold was heated in the oven for 6 hours at 70°C. (f) After the curing process was finished, the mold was taken out form the oven and the LSC was evacuated from the mold. (g) The photograph of the fabricated device under ambient light (scale bar = 1 cm). (h) The quantum dot-based luminescent solar concentrator integrated with organic solar cells under UV illumination.

4.4.5 The optical analysis of the integrated LSCs

We analyzed the optical performance of the integrated LSC under the standard AM 1.5G solar radiation. We adjusted the QD loading concentration as 0.8 wt%, which leads to the sufficient transmission level of more than 40% in the visible wavelength region (Figure 4.19a). Due to the high PLQY of the synthesized QDs inside the polymeric matrix (64%), the optical quantum efficiency of the LSC was calculated as high as 44.7%. The high value of optical quantum efficiency of the fabricated devices (44.7%) results in the concentration factor of 2.2 based on C.F = $\eta_{OQE} \times G$ [354], which indicates the effective light concentration inside the QD-LSC architecture. In order to determine the optical efficiency of the fabricated QD-LSC, Equation (4.12) was used as follows:

$$\eta_{opt} = \frac{I_{LSC}}{I_{OPV} \times G} \tag{4.12}$$

In Equation (4.12), I_{LSC} is the short circuit current level of organic solar cells when the top surface of the LSC is being illuminated by the light, I_{OPV} is the short circuit current level of organic solar cell arrays when being directly illuminated by the light and G is the optical gain factor of the LSC calculated based on G = $A_{top\ surface}/A_{collection\ edge}$ equal to 5. When being illuminated by a calibrated AM 1.5G solar spectrum, the short circuit current of the QD-LSC was measured as 2.9 $mA.cm^{-2}$ (Figure 4.19b), which yielded to the optical efficiency of 4.9%.

Today, solid-state lighting sources that are used in internal lighting and in the mobile phones have strong blue spectral content [25, 51, 53, 142], and we investigated the performance of the LSC under blue LED with the emission peak position at 445 nm and the power density of 100 $mW.cm^{-2}$ (see Appendix G). When being illuminated by the blue LED, a current density of 3.5 $mA.cm^{-2}$ was observed (Figure 4.19c), which corresponded to the optical efficiency of 5%. To investigate the effect of emission from QDs on the enhancement of the output short-circuit current in the fabricated QD-LSCs, another device integrated with organic solar cells were fabricated by using only PDMS polymer without integration of the green-emitting QDs. Under the same light intensity level, a 2.2-fold lower short-circuit current level of 1.6 $mA.cm^{-2}$ was obtained (Figure

4.19c). Here, the significant level of current by the pure PDMS is induced due to the large divergence angle of LEDs that are guided to the solar cells.

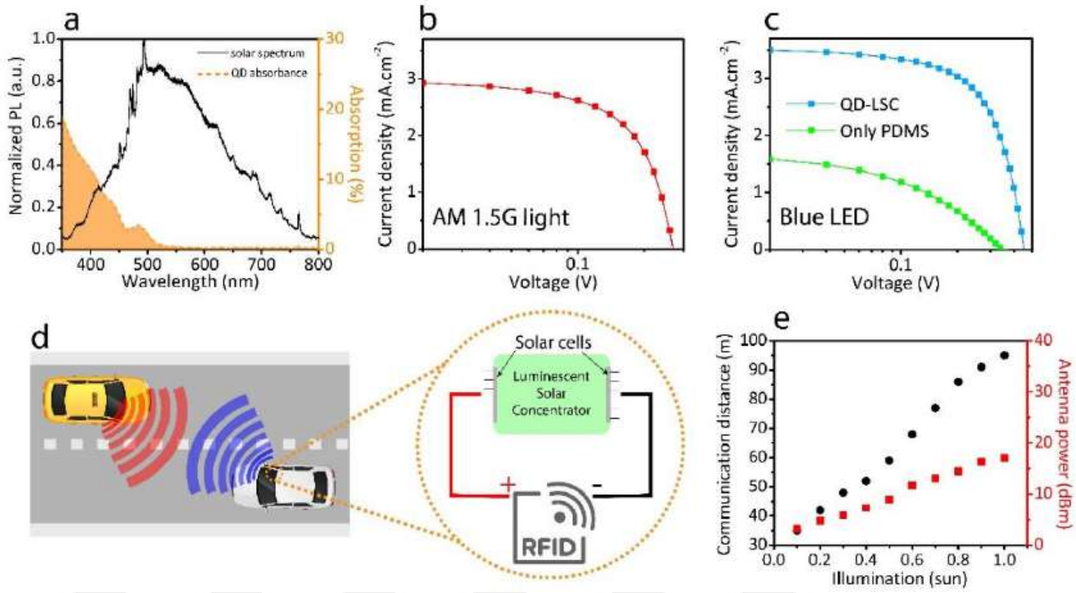

Figure 4.19: (a) The absorption percentage of the QDs (orange) and the solar spectrum (black) at visible wavelength region. The *J-V* curves of the solar cell-integrated LSCs under (b) AM 1.5G light with the output power of 100 mW.cm^{-2} and (c) blue light with the output power of 100 mW.cm^{-2}. (d) The schematic represents the organic solar cell-LSC architecture, which empowers a RFID chips to be used for connected cars applications. (e) The effect of illumination power on the maximum communication distance (black dots) and the antenna power (red dots) of the RFID chip.

4.4.6 Integration of RFID chips

Five main IoT technologies including radio frequency identification (RFID), wireless sensor networks (WSN), middleware, cloud computing and IoT application software are widely applied for the implementation of IoT products and services [328]. Among them, we selected RFID, which is an automatic technology that aids machines or computers to identify objects, record metadata and control individual target through radio waves [355, 356]. A typical RFID system consists of a transmitter/receiver microchip connected to an antenna, which can be attached to an object as the identifier. Active RFID tags have already started to be used for vehicle positioning (Figure 4.19d), automobile connections, manufacturing, hospital laboratories, and remote-sensing (e.g., temperature, pressure and chemical) [328, 357]. Active RFID tags have their own battery supply and we replaced this unit with our fabricated LSC (Figure 4.19d). We tested transmitter performance by changing illumination intensity from 0.1- to 1-sun condition to evaluate the RFID functionality. The experiment was carried out without any additional antenna. For RFID part, a commercial 433 MHz DRA888TX ASK RF transmitter module with optimal operating voltage of 1.5 V and injection current of 2.1 mA was used.

The maximum communication distance, which corresponds to the maximum distance to communicate with 8 Kbps rate without any information loss, was measured for different sun intensities. The transmitter power was measured with a spectrum analyzer. The results indicated that output antenna power varies between 3-17 dBm, which corresponds to maximum communication distances between approximately 35 to 95 meters for 0.1- and 1-sun illumination, respectively (Figure 4.19e). The communication distance results revealed that fabricated device can be used for RFID applications for connected cars even with a RF transceiver chip that has a built-in low power antenna. Although up to 95 meters communication distance can be used for short range vehicle-to-vehicle communication, the communication distance can be improved by utilizing additional transmitter and receiver antennas, which only requires additional solar cell pixels to be powered. Moreover, the high current levels under blue light (Figure 4.19b) is also sufficient for supplying enough energy by solid-state lighting sources. Our demonstration can be directly applied for vehicle-to-vehicle communications that prevents car crashes in short range traffic or smart parking lot purposes, and it showed the potential of LSCs integrated with organic solar cells for future IoT applications. A broad range of low power communication modules can be directly integrated to our system [358]. Moreover, utilizing low power GSM modules with 5G technology may bring the opportunity to create vehicle-to-cloud or even vehicle-to-everything communication and our design idea can be utilized efficiently in large area vehicles like trains or ferries as well.

4.4.7 Conclusion

In this section, a single integrated unit of bulk heterojunction solar cell array and quantum dot luminescent solar concentrator was designed, fabricated, and used for data transmission for IoT. The optical properties of the synthesized CdSe@ZnS QDs was tailored to match with the absorbance peak of the P3HT: $PC_{61}BM$ as the active layer of the organic photovoltaics. The synthesized QDs showed high PLQY of 64% inside the polymer that led to an optical quantum efficiency of 44.7%. The tailoring of optical properties and the direct integration of the organic solar cells inside the QD-LSC architecture further led to the optical efficiency of 4.9% and 5% under AM 1.5G and blue LED illumination, respectively. The fabricated QD-LSC integrated with organic photovoltaics was used to empower the RFID chips for connecting cars in IoT applications. The generated power by 0.1-sun illumination led to the communication distance of up to 35 meters. By increasing the illumination intensity up to 1-sun illumination, the communication distance can reach up to ~0.1 km, which is suitable for all types of vehicle-to-vehicle communication, traffic and parking lots to avoid crashes and optimized navigation. Due to the transparency and flexibility of LSC polymer, LSCs can be further integrated on the windows and other surfaces on the cars for vehicle-to-vehicle, vehicle-to-cloud and vehicle-to-everything communication [359]. The results reveal the potential of the luminescent solar concentrators for future IoT applications.

Chapter 5

CONCLUSIONS

With the rapidly increasing demand to optoelectronic devices, interest in alternative nanomaterials with superior optoelectronic properties also increases. QDs and fluorescent proteins are considered among such materials, which have attracted significant attention in lighting, display and energy harvesting applications due to their outstanding optical properties. However, there are the main concerns of efficiency and biocompatibility, which limits the widespread use of nanomaterial-based optoelectronic devices. In this thesis, we demonstrated novel architecture of liquid-state integration, which can preserve the efficiency of the nanomaterials in optoelectronic devices. The liquid-integration have been performed for different class of nanomaterials inside the light-emitting diodes and luminescent solar concentrator architectures, and showed great promise for eliminating the efficiency barriers in near future. Moreover, we proposed, developed and demonstrated the new class of highly efficient QD-based luminescent solar concentrators based on InP QDs.

To summarize, in this thesis work:

- We suppress the host material effect in QD-based light-emitting diodes by simple liquid-state integration that lead to a luminous efficiency of 64 lm/W for RGB-based (Red, Green, Blue) and 105 lm/W for GB-based (Green, Blue) white light generation. For that, we maximized the PLQY of red-emitting CdSe/CdS/ZnS and green-emitting CdSe//ZnS/CdSZnS QDs by optimizing the synthesis parameters and integrated efficient QDs with PLQY up to 84% on blue LED dies in liquid form at appropriate injection amounts for high-efficiency white lighting. Liquid-state integration showed two-fold and six-fold enhancement of efficiency in comparison with incorporation of QDs in PDMS film and close-packed formation, respectively. The luminous efficiency level of 105 lm/W is the highest efficiency of white QD-LEDs reported to date. This study was highlighted by OSA, AAAS, APS and etc. (Figure 5.1) that resulted in an altmetric score of 159.

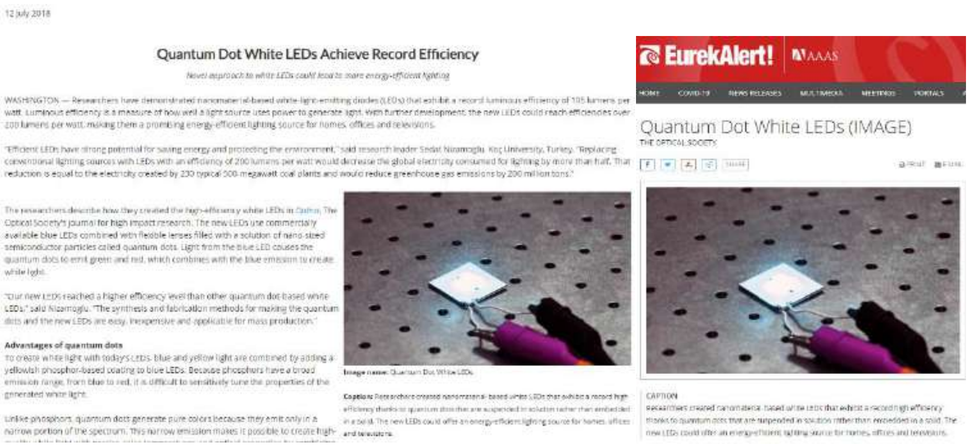

Figure 5.1: The part of the news in OSA and AAAS newsroom covering our study published in *Optica*.

- We used the red-emitting mScarlet and green-emitting eGFP fluorescent proteins for the fabrication of high-performance white LEDs. The green- and red-emitting proteins were expressed in living Escherichia coli and integrated in their natural aqueous environment onto blue LED chips. The aqueous integration preserved PLQY levels of the proteins above 70% in the device architecture and facilitated a high luminous efficiency of 81 lm/W with a color rendering index of 83, which is the most efficient eco-friendly white LED reported to date. Due to the high efficiency and color quality, the fabricated protein-based LEDs can be used both for illumination and display purposes. This study was highlighted as the frontispiece in the June 2020 issue of *Advanced Materials Technologies*.

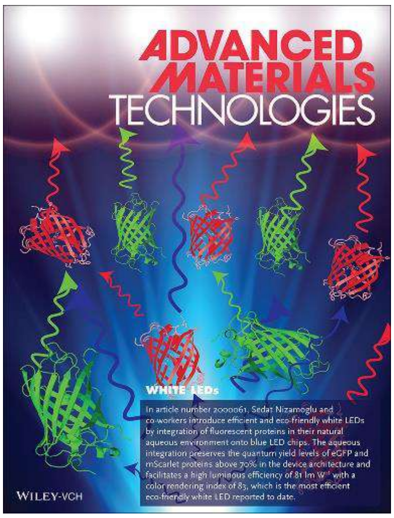

Figure 5.2: The frontispiece of the Advanced Materials Technologies (June 2020), which highlights the fluorescent protein-based liquid LEDs.

- We demonstrated QD-based LEDs that operate at a luminous efficiency level of 95 lumens per electrical watt, luminous efficacy of optical radiation of 395 lumens per optical watt, and external quantum efficiency (EQE) of 23.3% in the green spectral region, which has the highest luminous efficiency among the green QD-LEDs reported to date.. For that, we synthesized 1-octanethiol-capped CdSe@ZnS QDs with an absolute PLQY of 91% and integrated them in liquid matrix that allows conservation of the QD efficiency in device architecture.

- We maximized the PLQY of trap-assisted CdSe QDs by controlling the synthesis parameters of reaction time and temperature, and their PLQY reached up to 22% without shell formation or post treatment process for white LEDs. To prevent a possible decay of the QD efficiency in device architecture due to host material effect, we hybridized QDs in liquid-state on blue LED die that led to a white LED with a color rendering index up to 89 and a luminous efficiency of ~10 lm/W at a high current injection level of 0.1 A, which was higher than the previous studies.

- We synthesized red-emitting CdSe/CdS and green-emitting CdSe@ZnS QDs with PLQY levels of 52% and 74%, respectively. The synthesized red- and green-emitting QDs were integrated in PDMS polymer matrix and the doctor blade technique enabled to generate large-area QD-polymeric films with various thicknesses and dimensions coated on top of the PET film. The fabricated QD-polymeric films were used as color converter layers using backlight LED panel in display application. By using red- and green-emitting QD-polymeric films, the generated white light color gamut achieved a color space of 91% and 127% for NTSC and sRGB, respectively, which show great promise for future smart phone display applications.

- We showed that InP-based QDs are a promising candidate for future LSC technology that can simultaneously fulfill the requirements of the efficiency, eco-compatibility and large-scale production. The Stokes-shift of the InP QDs was realized by copper-doping (650 meV) and the PLQY of the synthesized QDs was boosted up to 87% in the 'near-infrared window' by passivation of surface traps via zinc carboxylation and strong confinement of electron-hole pairs inside the nanostructure via growing lattice-matched ZnSe shell. Moreover, the high PLQY over 80% is also maintained in solid-state form due to the thick ZnSe shell. The high PLQY and low reabsorption facilitated high optical quantum efficiencies over 30%, comparable to the best reported Cd and Pb containing

LSCs. By using the doctor-blade technique, a large-area QD-based LSC (3000 cm^2) was fabricated, which indicates the applicability for 'solar window' applications.

- For the first time, we demonstrated LSCs based on cadmium-free InP/ZnO core/shell QDs with type-II band alignment that allow the suppression of reabsorption by Stokes-shift engineering. We analyzed the optical performance of indium-based LSCs and identified the optical efficiency as 1.45%.

- For the first time, we propose and incorporate an entirely new biomaterial class, fluorescent proteins, for efficient LSCs. The liquid-state integration preserved the quantum efficiency level of protein and enabled the separation of luminescent and wave-guiding regions due to the refractive index difference between aqueous medium as the natural host material of the fluorescent proteins and the surrounding polymer. The LSC based on mScarlet fluorescent proteins at a concentration of 5 wt% showed an optical efficiency over 2%.

Overall, our studies holds several contributions to the scientific community. First, our focus to improve the optical performance of the light-emitting devices achieved the state-of-the-art LEDs positioning the quantum dot-based LEDs in the near level of efficiency, which are currently being used in TV market such as phosphorous-based LEDs. Second, our highly-efficient fluorescent protein-based white LEDs bridged the gap to the wide-spread use of eco-friendly and efficient nanomaterial-based light-emitting devices. Third, our quantum dot-based polymeric films (in collaboration with VESTEL) was directly used in VENUS cellphones in order to increase the color quality and opened a new paradigm for wide-spread use of quantum dots in cellphone technology. Fourth, our efforts to improve the optical performance of the luminescent solar concentrators led to the quantum dot-based devices, which can be directly used in buildings, offices and homes as sunlight energy harvesting devices.

As a result of our studies, I published ten articles as first-author in high-impact journals including *Optica*, *iScience*, *ACS Applied Materials and Interfaces* (2 papers), *Chemistry of Materials*, *Advanced Materials Technologies*, *Nanotechnology*, *IEEE Transitions on Electron Devices*, *Scientific Reports* and *Materials Research Express*, and co-authored eight more journal papers published in *ACS Nano*, *Nano Letters*, *ACS Photonics*, *Scientific Reports*, *Advanced Materials Interfaces*, *ACS Biomaterials Science and Engineering*, *Journal of Applied Physics* and *Journal of Physical Chemistry C.*

I received the Best Poster Presentation award from 21st conference on Optics, Electro-optics and Photonics of Turkey (Fotonik 2019), the Outstanding Teaching Award-Fall 2017 from Koç University graduate school of sciences and engineering, and the Scientific and Technological Research Council of Turkey (TUBITAK) prize for the project number 115E115 entitled "Ekran Teknolojisi Için Yüksek Kaliteli Ve Verimli Nanokristal Tabanlı Led'Ler".

APPENDIX A

A.1 Quantum yield optimization

A.1.1 Photoluminescence peak wavelengths of efficient red-emitting CdSe QDs

In section 3.1, we mentioned that during the QY optimization for red-emitting CdSe QDs, there were other points with different reaction times and temperatures, which have similar QYs with the selected point of 2 minutes reaction time at 300 °C. The photoluminescence peak wavelength of the synthesized CdSe QDs at 240 °C of reaction temperature and 60 minutes of reaction time was 657 nm with QY of 37%. The photoluminescence peak wavelength of the synthesized CdSe QDs at 260 °C of reaction temperature and 7 minutes of reaction time was 612 nm with QY of 35.5%, and the photoluminescence peak wavelength of the synthesized CdSe QDs at 300 °C of reaction temperature and 2 minutes of reaction time (our selected point) was 640 nm with QY of 38%. Moreover, the photoluminescence spectra of these points were shown in Figure A.1.

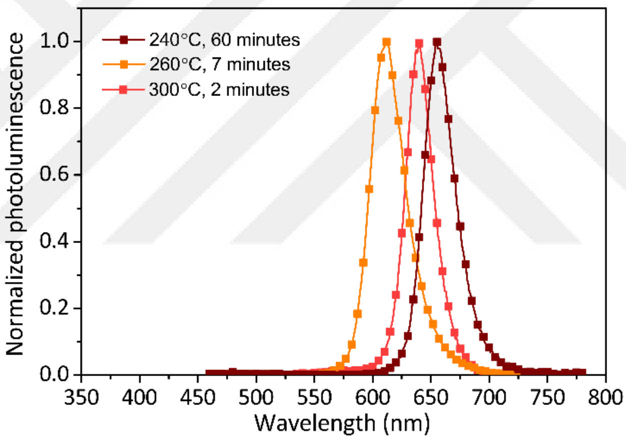

Figure A.1: The photoluminescence spectra of the synthesized red-emitting CdSe QDs with different reaction times and temperatures, which have similar QY with the selected point of 2 minutes reaction time at 300 °C.

A.1.2 Quantum yield and FWHM of the synthesized QDs at each shelling step

The FWHM and QY of red-emitting CdSe, CdSe/CdS and CdSe/CdS/ZnS QDs were shown in Figure A.2. The FWHM of the QDs remained almost constant during the shelling process, which indicated the homogenous dispersion and growth of the synthesized QDs. For green-emitting QDs, the FWHM of CdSe core was significantly high, which was due to the initial surface state trap formation. The surface traps broadened the photoluminescence spectra of green-emitting CdSe QDs. Continuation of shelling process led to narrow FWHM, which passivated the surface traps. Moreover, the change in QY of the synthesized QDs in each step of shelling process was shown in Figure A.2.

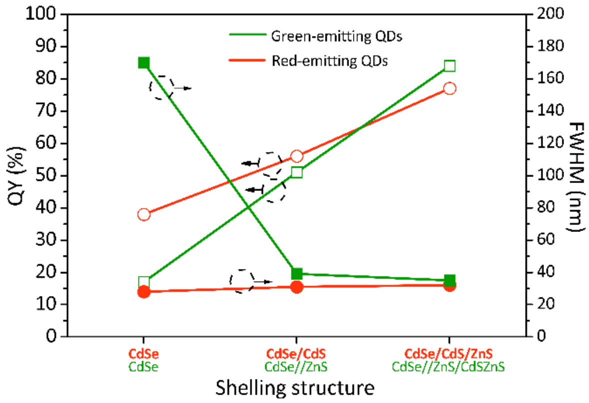

Figure A.2: Quantum yield and FWHM of red- and green-emitting QD structures.

A.1.3 The effect of CdS multiple shelling

We investigated the effect of different CdS and ZnS shelling and measured QY for each sample. Figure A.3 showed the QY results for CdS and ZnS shelling (from 1 to 3 times) of red-emitting QDs. Our optimization confirmed that the red-emitting QD structure with only one shelling of CdS and ZnS showed the highest QY of 77%.

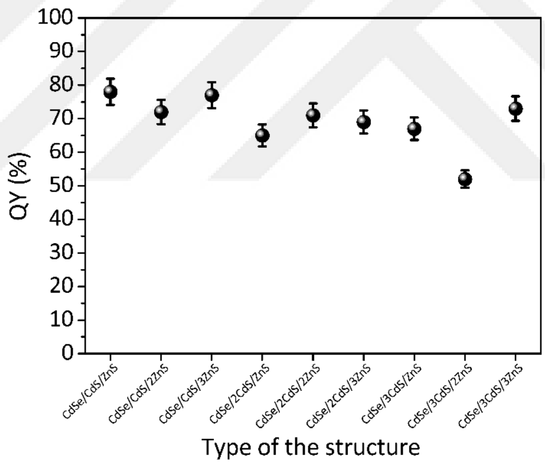

Figure A.3: The quantum yield of red-emitting CdSe/CdS/ZnS QDs with different shell combinations.

A.2 Structural characterization

A.2.1 SEM-EDAX

As mentioned in section 3.1, elemental analysis was performed on the red- and green-emitting QDs to investigate the presence of cadmium, selenium, zinc and sulfur in QD structures. The results showed that cadmium, selenium, zinc and sulfur elements are present in both red- and green-emitting QDs, respectively (Figure A.4).

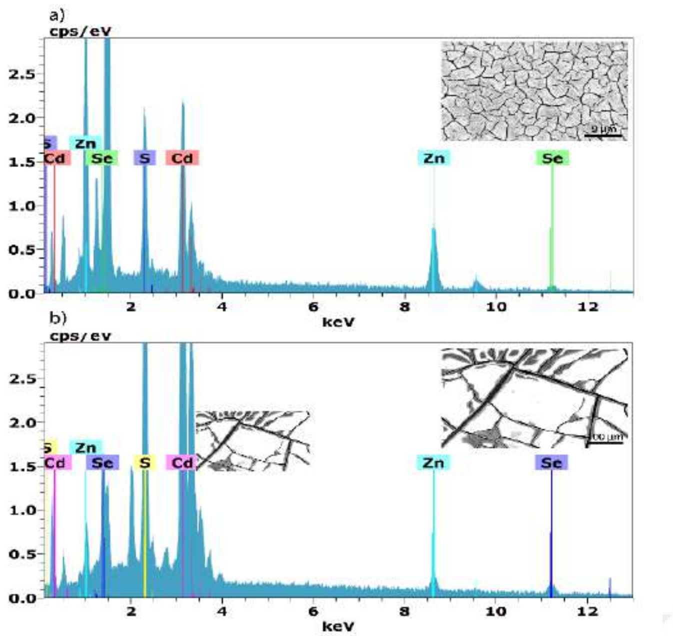

Figure A.4: The elemental composition for (a) red- and (b) for green-emitting QDs. Inset: The SEM image of the QDs sample dried on a glass substrate.

A.2.2 XRD

The XRD measurement was performed to investigate the structural analysis of the synthesized red- and green-emitting QDs. The diffraction pattern of CdSe, CdS and ZnS structures were shown in Figure A.5 (lower panel). As mentioned in section 3.1, the peaks at 25°, 28°, 42°, and 57° confirmed the CdSe, CdS and ZnS cubic structures in A.5 (upper panel). The shift in some diffraction peaks (e.g. at 26°) was due to the lattice mismatch between core and shell [311].

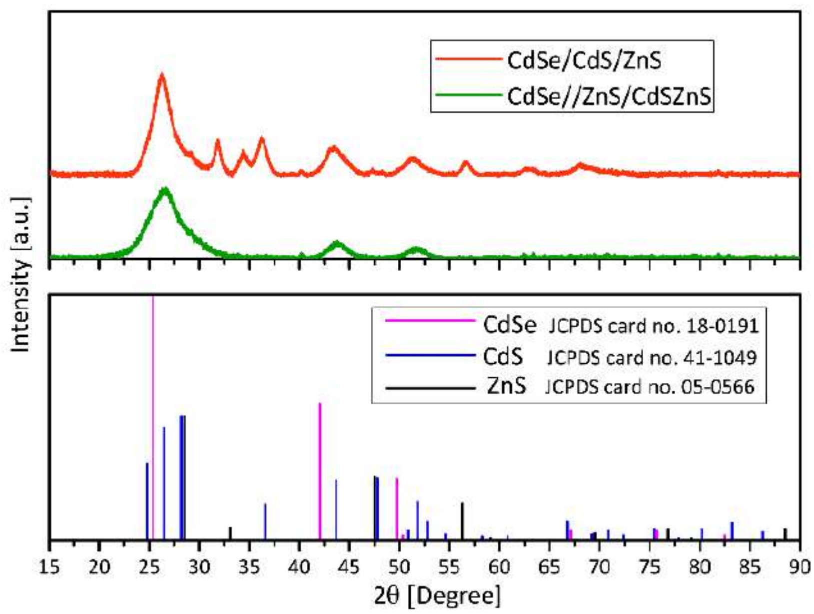

Figure A.5: XRD measurement of red- and green-emitting QDs. Upper panel showed the XRD pattern of red- and green-emitting QDs, and lower panel showed the diffraction patterns of the CdSe, CdS and ZnS cubic structures.

A.2.3 XPS

The XPS measurement was used to confirm the core/shell formation in both red- and green-emitting QDs. The change in binding energy of cadmium, zinc, selenium and sulfur indicated formation of new bonding between elements, which was due to the core and shell structure formation (Figure A.6). At the same time, XPS measurement also confirmed the presence of cadmium, zinc, selenium and sulfur elements in red- and green-emitting QDs.

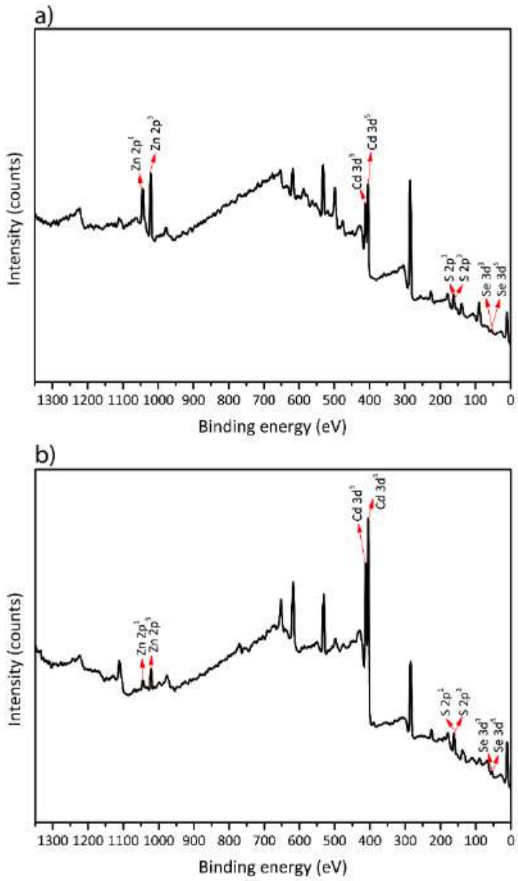

Figure A.6: The XPS spectrum of (a) red- and (b) green-emitting QDs.

A.3 The simulation of optical parameters

The calculation is based on our previous study [113]. Shortly, the spectral overlap between the absorbance of the fluorophore and electroluminescence intensity of the pump results in photoluminescence of the fluorophore, where photons are absorbed and spontaneous emission occurs. In this process, incoming photon flux with power spectral density $(\overrightarrow{S_{in}(\lambda)})$ is absorbed by the fluorophore with absorption coefficient $(\alpha_i(\lambda))$. Total output power spectral density ($\overrightarrow{S_{out}(\lambda)}$) generated by combination of photoluminescence of the fluorophore and transmitted incoming photon flux. The matrix formulation presented in Equation (A.1) takes into account reabsorption and inter-absorption processes where $\kappa_i(\lambda)$ corresponded to absorption ratio of electroluminescent pump by i_{th} fluorophore. W_i corresponded to the emission strength, which showed the absorption of each fluorophore by electroluminescent pump scaled by QY meaning that only emission (radiative recombination) is considered. $M_{i,i}$ corresponded to the reabsorption of the i_{th} fluorophore and $M_{i,j}$ corresponded to inter-absorption between i_{th} and j_{th} fluorophore. $P_{j,n}$ corresponded to normalized spectral emission strength at n_{th} wavelength of the j_{th} fluorophore. $\bar{\bar{C}}$ was the spectral multiplication factor to the overall emission due to reabsorption and inter-absorption, which was the simplified form of the sum of infinitely many reabsorption and inter-absorption cycles.

$$\overrightarrow{S_{out}(\lambda)} = \overrightarrow{S_{in}(\lambda)} \exp\left[-\sum_j \alpha_j(\lambda) D_j\right] + \vec{W}^T \times \bar{\bar{C}} \times \bar{\bar{P}} \tag{A.1}$$

$$\kappa_i(\lambda) = \frac{\alpha_i(\lambda) D_i}{\sum_j \alpha_j(\lambda) D_j} \tag{A.2}$$

$$W_i = Q_i \int S_{in}(\lambda) \kappa_i(\lambda) \left\{1 - \exp\left[-\sum_j \alpha_j(\lambda) D_j\right]\right\} d\lambda \tag{A.3}$$

$$M_{i,j} = Q_j \int P_i(\lambda) \kappa_j(\lambda) \left\{1 - \exp\left[-\sum_j \alpha_j(\lambda) D_j\right]\right\} d\lambda \tag{A.4}$$

$$\bar{\bar{C}} = (I - \bar{\bar{M}})^{-1} \exp\left[-\sum_j \alpha_j(\lambda) D_j\right] \tag{A.5}$$

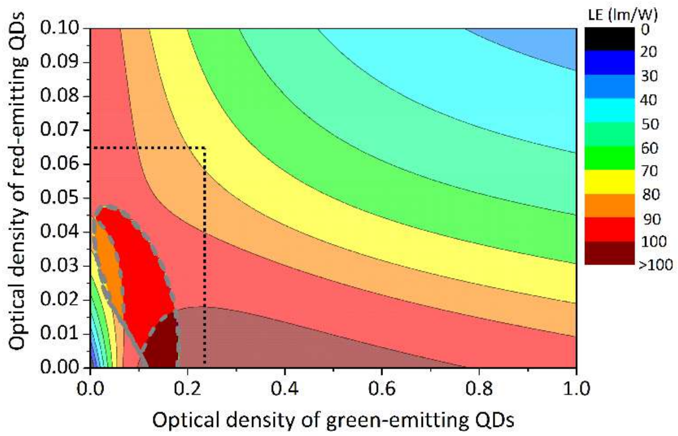

Figure A.7: The bright-dashed region showed the combination of red- and green-emitting QDs, which led to white light generation. The black-dashed rectangle indicated the specific area shown in Figure 3.7.

A.4 The optical properties of the blue LED die

The optical properties of the blue LEDs, which were used in section 3.1, were characterized (Figure A.8).

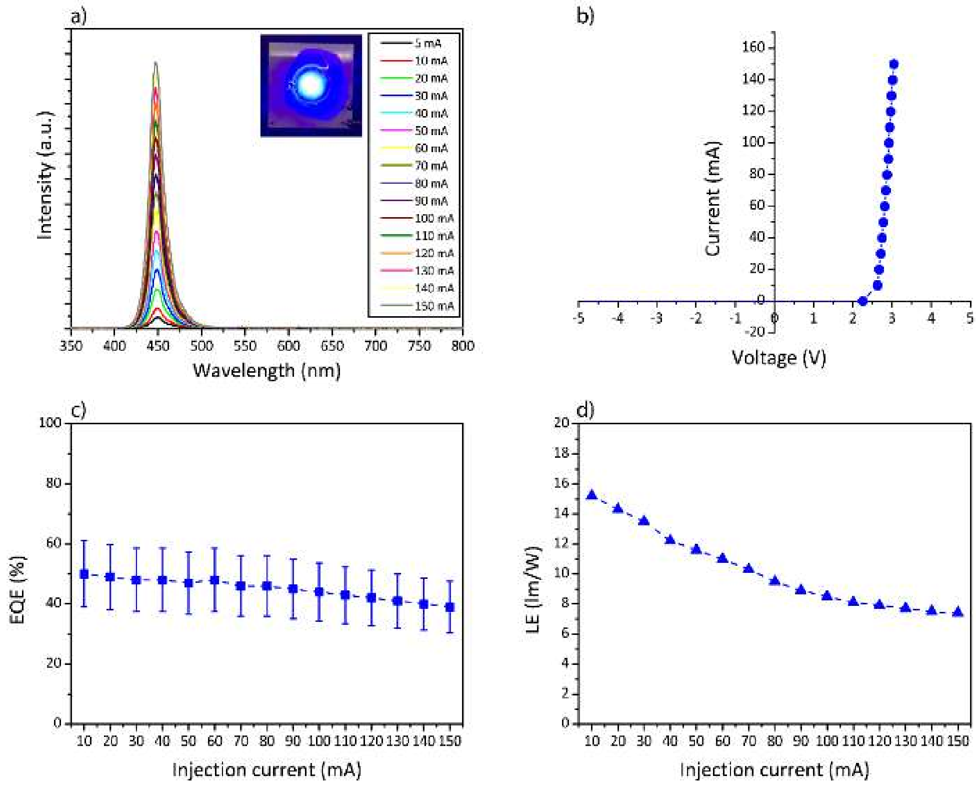

Figure A.8: (a) Intensity spectra of an exemplary blue LED chip at different injection currents from 5 to 150 mA. Inset: the photograph of the blue chip when the LED was turned on. (b) I-V curve of the blue LED. (c) The EQE of the blue LED chips at different injection currents from 10 to 150 mA. (n=4) (d) The luminous efficiency of a blue LED at different injection currents from 10 to 150 mA.

A.5 GB-based LQD-LED

The green-emitting QDs with the optical density of 0.13 was injected onto a blue LED. The combination of green emission and blue light generated a point with (x, y) coordinates of (0.31, 0.39) in CIE 1931 color tristimulus, which was inside the white region (Figure A.9).

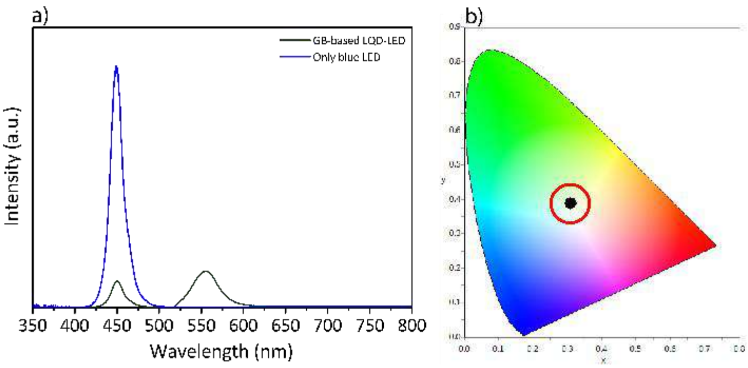

Figure A.9: (a) The spectrum of GB-based LQD-LED (b) The (x, y) tristimulus coordinates of GB-based LQD-LED in CIE 1931 chromaticity diagram.

A.6 The simulation results of color gamut, LE and CRI

As mentioned in section 3.1, we performed a simulation in order to investigate the effect of PL peak wavelengths of the red- and green-emitting QDs on the NTSC color gamut ratio. We selected a range of 510-580 nm and 580-660 nm for green- and red-emitting QDs, respectively. The step size was selected as 5 nm. Our simulation results showed that the NTSC gamut ratio of 104% was achievable with the PL peak wavelength of 515 nm for green-emitting QDs and the PL peak wavelength of 635-660 nm for red-emitting QDs. These results were shown in Figure A.10-color map.

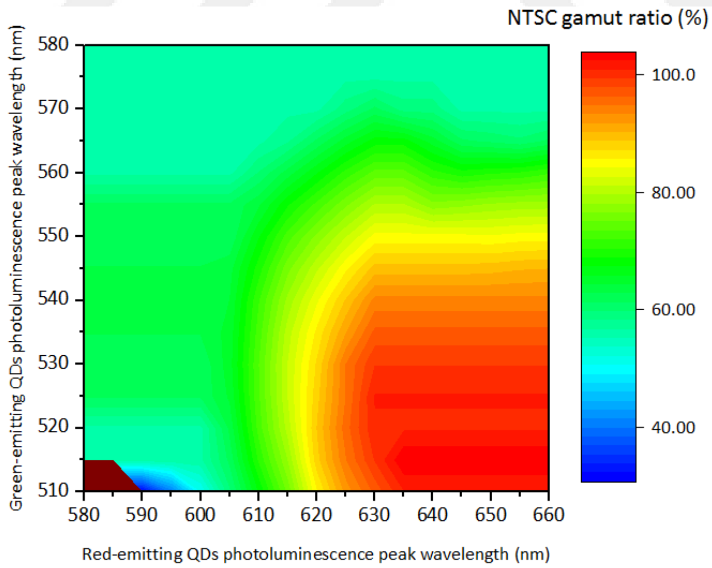

Figure A.10: The simulation results that investigated the maximum NTSC gamut ratio by varying the photoluminescence peak positions of red- and green-emitting QDs.

We performed the similar simulation to investigate the effect of PL peak wavelength of red- and green-emitting QDs on LE of the generated white light. Our simulation results showed that by the PL peak wavelength of 555-560 nm for green-emitting QDs for all PL peak wavelengths of red-emitting QDs from 580 nm to 660 nm, maximum LE of 120 lm/W was achievable. These results were shown in Figure A.11-color map.

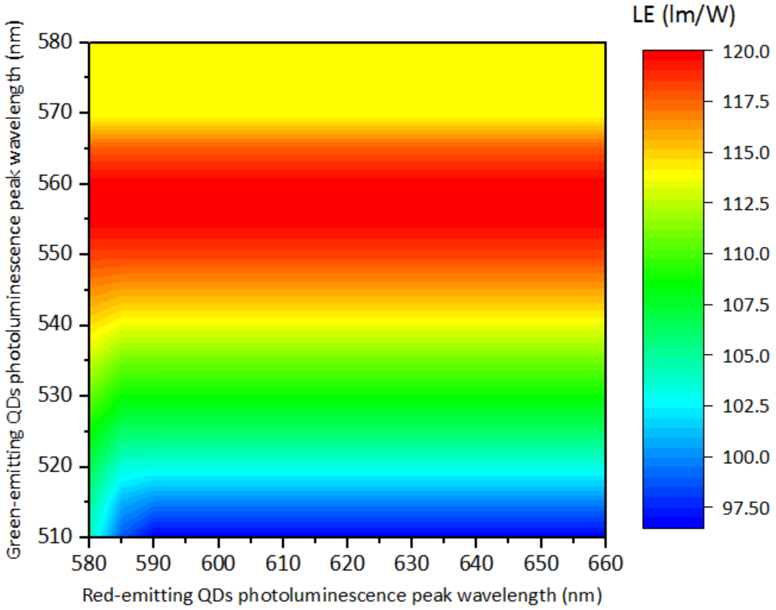

Figure A.11: The simulation results that investigated the maximum luminous efficiency by varying the photoluminescence peak positions of red- and green-emitting QDs.

We also simulated the dependence of CRI values with LE using the optical parameters of the optimized red- and green-emitting QDs. The results indicated that maximum LE of 80 lm/W with CRI of 84 was achievable using the optimized red- and green-emitting QDs (Figure A.12).

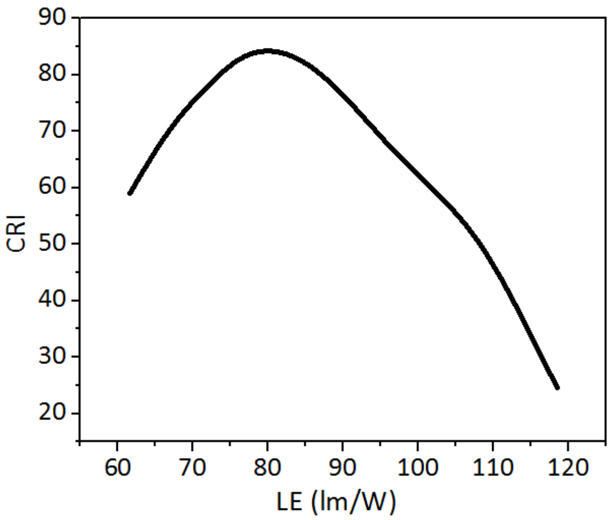

Figure A.12: The simulation of CRI-LE based on the photoluminescence and absorbance of the synthesized red- and green-emitting QDs

A.7 The optical properties of the LEDs with different architectures

The EQE, LE, and LER of the liquid-state, solid-state and close-packed QD-LED at different injection currents were shown in Figure A.13.

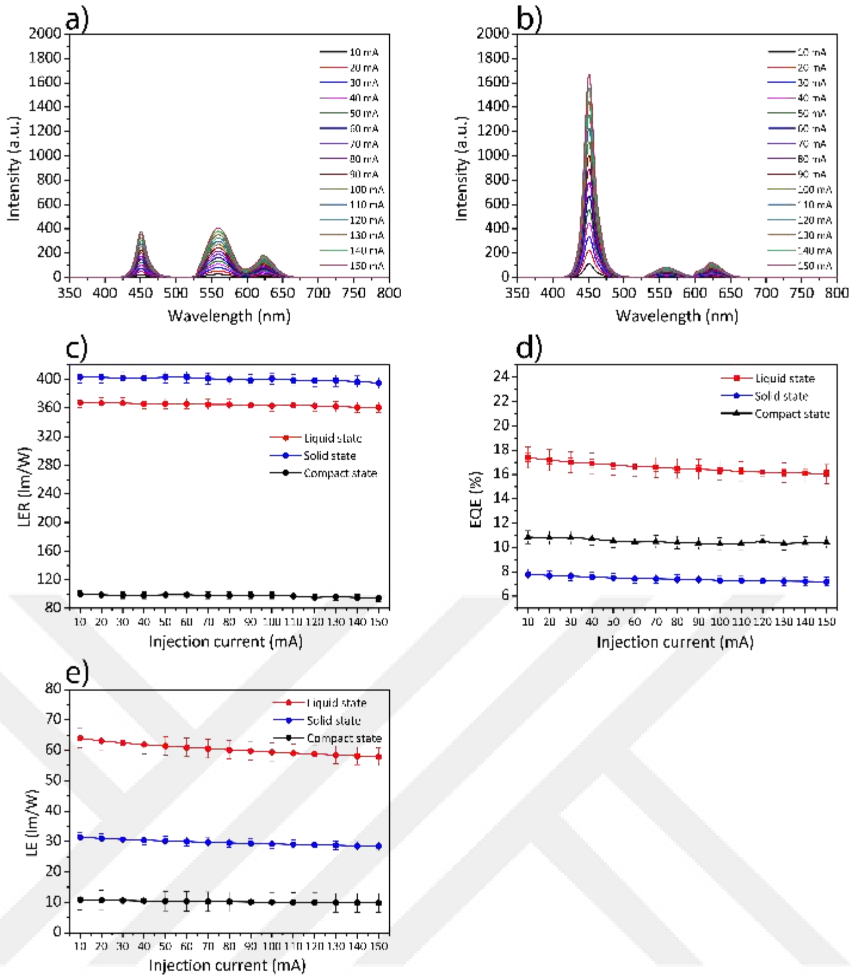

Figure A.13: The intensity spectra of (a) solid-state and (b) close-packed QD-LED at different injection current from 10 to 150 mA. (c) The luminous efficiency of radiation (LER) (d) The EQE, and (e) the luminous efficiency of different structures of QD-LEDs at different injection currents from 10 to 150 mA.

APPENDIX B

B.1 Simulation of the different combinations of green- and red-emitting fluorescent proteins

Fluorescent proteins provide a large emission-color palette via genetic modifications. Among them, we choose four green-emitting of Sapphire, eGFP, mHoneydew and Citrine and four red-emitting fluorescent proteins of mScarlet, mPlum, dTomato and mCherry, which cover the entire green and red spectral regions. Green-emitting proteins have FWHM ranging from 23 nm to 81 nm and PLQY ranging from 12% to 78%. Red-emitting proteins have FWHM ranging from 52 nm to 83 nm and PLQY ranging from 10% to 71%. We used EL blue LED pump with emission peak at 460 nm with FWHM of 20 nm and the EQE of 42.5%. The LE of the blue LED was measured as 30 lm/W at the injection current of 10 mA. The simulation algorithm for color conversion and photometric analysis is shown in Figure B.1.

For the simulation, first, the optical properties of EL blue LED pump and green and red-emitting proteins and the standard CIE (1931) constants and functions are imported into simulation tool, which was based on the built-in MATLAB code. Then, all combinations of green- and red-emitting proteins were generated. For each protein, the path length, which corresponded to the effective length that light interacts with the fluorescent proteins with unity absorption coefficient at maximum absorption strength, are varied from 0.01 to 20 mm. The step size for the generated spectra was constant as 5 nm. Color conversion spectra were generated using matrix formulation and stored for all the combinations of proteins. Finally, the photometric parameters such as (x, y) chromaticity coordinates, correlated color temperature (CCT), CRI, LE and LER of the generated white spectra were calculated by using the mathematical formulations described in reference [7]. In total, more than 7 million spectra were generated and analyzed, and among them more than 0.1 million spectra were in the white region, which were defined in Equations (B.1)-(B.3) [151].

$$x' = \frac{y+1.67x-0.885}{1.9495} \tag{B.1}$$

$$y' = \frac{y-0.607x-0.109}{1.1648} \tag{B.2}$$

$$\frac{x'^2}{0.1339^2} + \frac{y'^2}{0.0944^2} \leq 1 \tag{B.3}$$

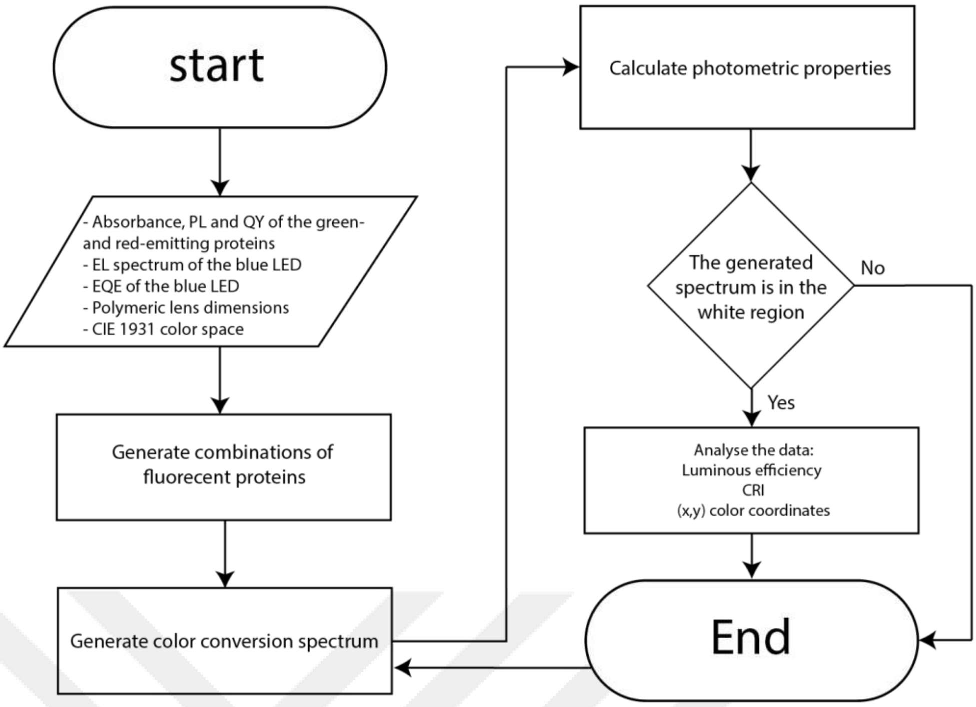

Figure B.1: The simulation algorithm for color conversion and photometric analysis in this study.

B.2 Photonics processes for white light generation

The responsible photonics processes for white light generation at each cycle are illustrated in Figure B.2.

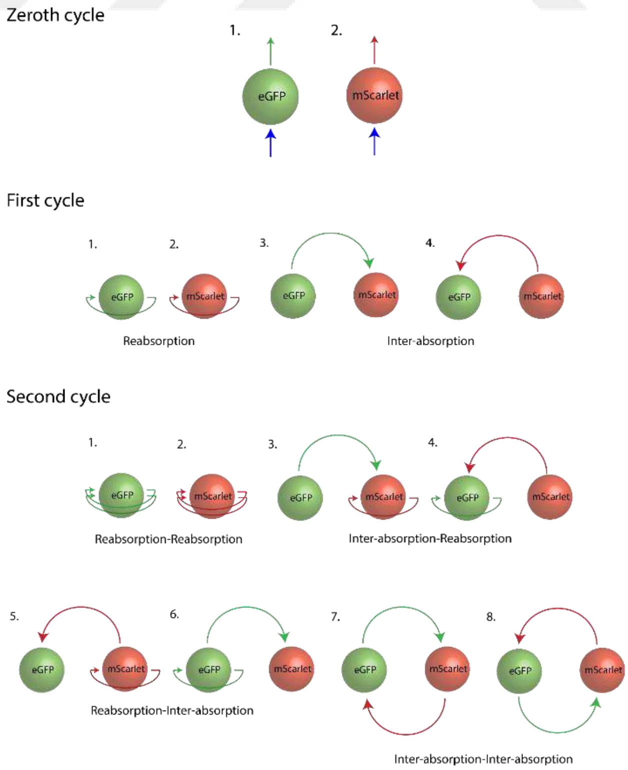

Figure B.2: The contribution of absorption, reabsorption and interabsorption in each cycle of the photonic processes for white light generation.

B.3 Thermal stability of eGFP and mScarlet proteins

We measured the thermal stability of the green- and red-emitting fluorescent proteins. For that, we drop casted 50 µl of proteins in aqueous medium onto the glass substrate and excited the solutions with blue LEDs with similar emission profile (emission peak at 460 nm), which was used in this study. The glass substrates were heated from 25 °C to 80 °C, and the output intensity was collected by using an optical fiber (Figure B.3). By increasing the temperature up to 80 °C, the photoluminescence peak wavelength was shifted from 510 nm to 513 nm for eGFP and from 600 to 608 nm for mScarlet, respectively (Figure B.3a and B.3b). At the same time, by increasing temperature up to 80 °C, the intensity drop of 48% and 51% was observed in eGFP and mScarlet proteins, respectively (Figure B.3c and B.3d). By considering that the liquid type QD LED can keep the surface temperature below 50 °C even at high current injection levels (around 200 mA), liquid fluorescent proteins can show both high performance and reliability at moderate current injection levels [155]. For high power applications, two compartmentalization of liquid can be used to save the proteins against thermal quenching; the liquid just above the blue LED (i.e., first compartment) can be used for proper thermal management and above it (i.e., second compartment) the proteins that operate at low temperatures can be placed.

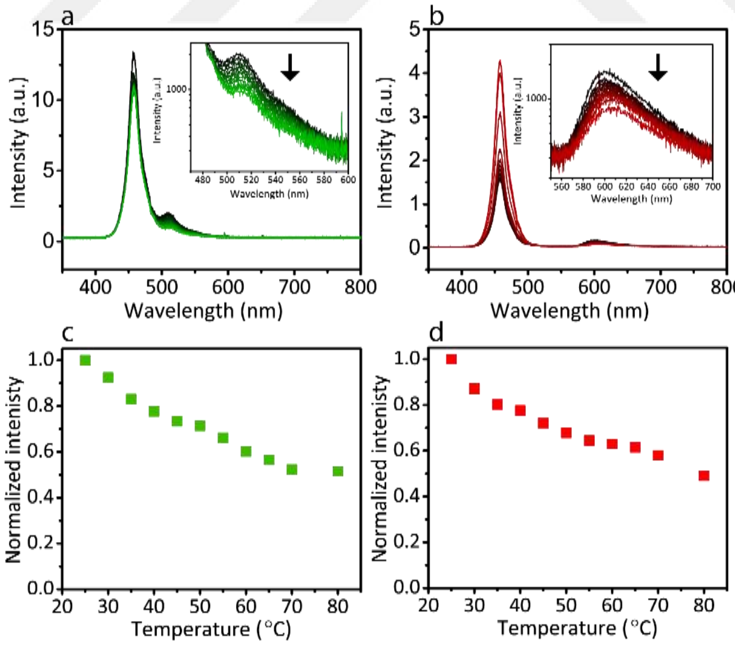

Figure B.3: The thermal stability of the green- and red-emitting fluorescent proteins. The output intensity of (a) green-emitting eGFP and (b) red-emitting mScarlet by increasing the temperature from 25 °C to 80 °C. Inset: the photoluminescence of the proteins were zoomed for better comparison. The arrows indicate the direction of increasing the temperature. The normalized output intensity of (c) eGFP and (d) mScarlet proteins by increasing the temperature from 25 °C to 80 °C.

B.4 The optical stability of the white PLED under constant illumination

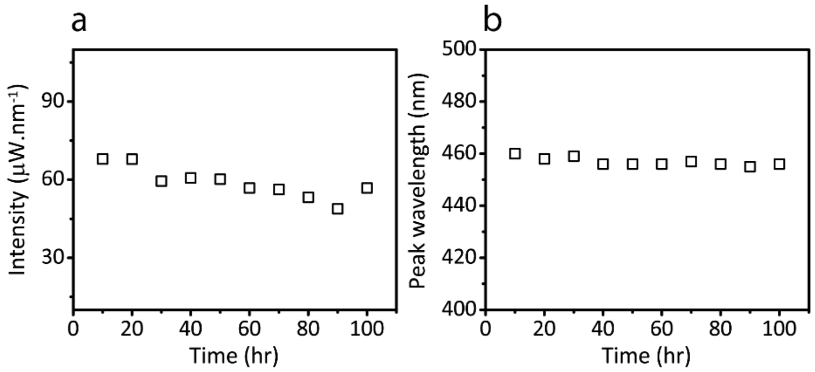

Figure B.4: (a) The intensity level and (b) the peak wavelength of the blue LED under constant illumination during 100 hours.

B.5 Calculation of the color quality scale (CQS) and extended CRI

R9-R15 values for the generated white light from the liquid PLED with the highest CRI of 92 was shown in Figure B.5. We also used the formulation in the previous study [360] for the calculation of the color quality scale (CQS). A MATLAB code was written for CQS calculations and the spectra of the white PLEDs were used as the input data. Our calculations showed that the CQS for the spectrum of the white PLED having CRI of 92 corresponds to 74. At the same time, the calculations also showed the CQS of 85 for the spectrum of the white PLED with the highest luminous efficiency of 81 lm/W.

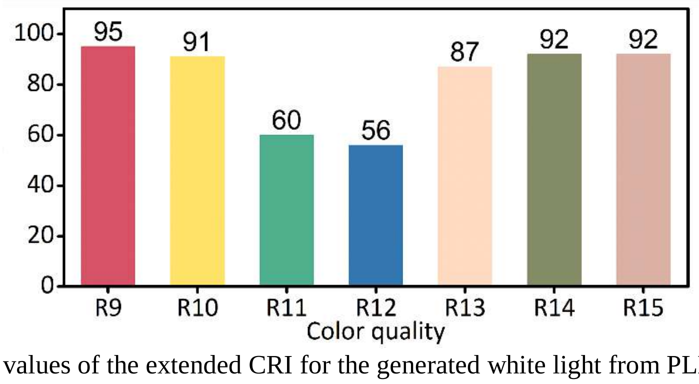

Figure B.5: R9-R15 values of the extended CRI for the generated white light from PLED with CRI of 92.

APPENDIX C

C.1 The injection procedure for the fabrication of liquid QD-LED

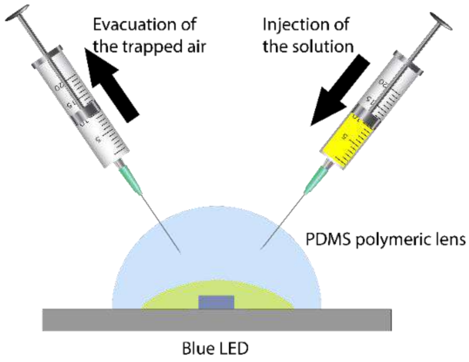

Figure C.1: The schematic of the injection procedure, in which one micro-syringe was used for the injection of the solution, while the other micro-syringe was used to evacuate the trapped air.

C.2 Comparison between luminous efficiency of liquid and close-packed white-emitting QDs-based LEDs

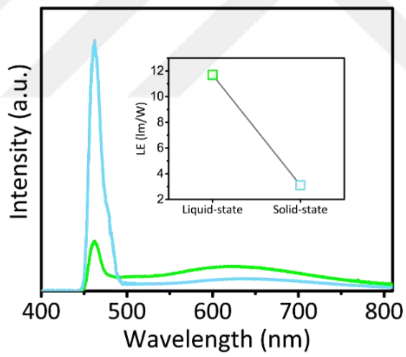

Figure C.2: The intensity spectra of the (green) liquid and close-packed (blue) white-emitting QD-based LED. Inset: the luminous efficiency of the liquid-state and close-packed solid-state QD-LEDs.

C.3 The optical properties of the blue LED

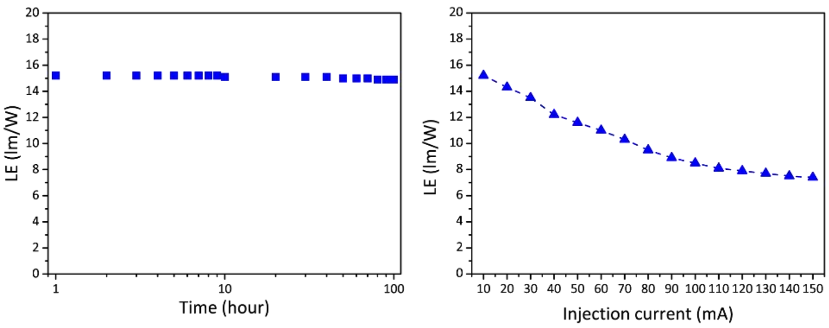

Figure C.3: The optical properties of the blue LED, which was used in this study. (a) The luminous efficiency of the fabricated liquid LED, which was filled only with solvent during the constant illumination time from 1 to 100 hours. (b) The luminous efficiency of the blue LED with different injection currents ranging from 10 mA to 150 mA.

C.4 Color filters for the color gamut calculations

The color filters which were used to calculate the color gamut ratio were shown in Figure C.4.

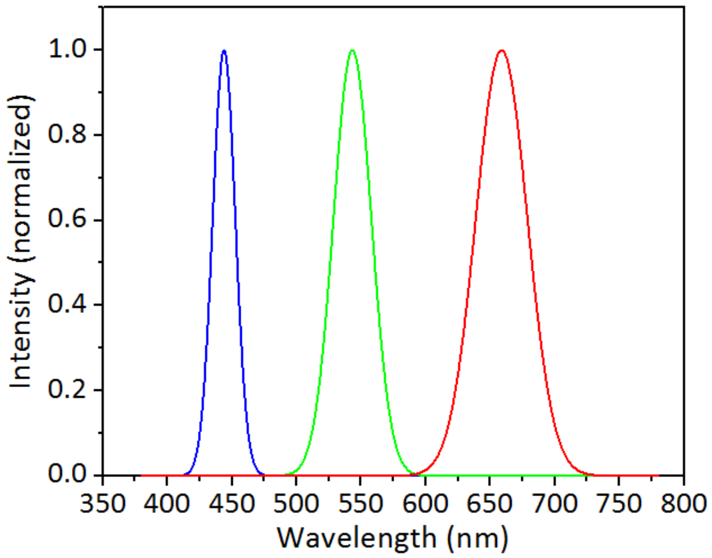

Figure C.4: The red, green and blue color filters which was used to calculate the color gamut of the generated white light.

APPENDIX D

D.1 The synthesis procedure of copper-doped QDs

D.1.1 The preparation of precursor stock solution

A solution of $P(TMS)_3$ in ODE was prepared with the concentration of 0.2 $mmol.ml^{-1}$ and stored in inert atmosphere at -40 °C. 0.5 mmol $Cu(Ac)_2$ and 1 mmol SA were stirred in 5 ml ODE at 150 °C for 1 h. The solution was kept in inert atmosphere. 0.1 M solution of zinc stearate in ODE was prepared and stored in inert atmosphere. 0.1 M solution of selenium in TOP was prepared and stored in inert atmosphere.

D.1.2 Small-scale synthesis

The colloidal synthesis was performed in a nitrogen filled Schlenk line. For InP core synthesis, 0.1 mmol $InCl_3$, 0.2 mmol HDA, 0.1 mmol zinc undecylenate and 0.1 mmol SA were mixed in 3 ml ODE in a three-neck 50 ml round bottom reaction flask. The solution was firstly degassed at 150 °C for 1 h, then heated up to 250 °C under nitrogen atmosphere. 0.5 ml of the $P(TMS)_3$ stock solution was injected to the solution at this temperature. The solution was kept at 230 °C for 20 min and then cooled down to 180 °C. At this temperature, 1 µmol copper stearate was introduced to the solution and then heated up to the 220 °C. For the first ZnSe shelling, 600 µl of the zinc stearate stock solution was added to the reaction flask. After 10 minutes keeping at 220 °C, 600 µl of the selenium stock solution introduced to the reaction. For a successful shelling, the solution was heated up to 280 °C, kept at that temperature for 20 min and finally cooled down to room temperature. For second, third, fourth, fifth and sixth shelling, 825 µl, 1050 µl, 1400 µl, 1750 µl and 2275 µl of stock solution were used, respectively. For purification, ethanol was added to the solutions and then centrifuged at 9000 rpm for 15 min for two times. The precipitated QDs were dispersed in hexane and kept at 5 ºC in inert atmosphere.

D.1.3 Large-scale synthesis

For the large-scale synthesis, the amounts used in the above small-scale section were multiplied by 10. The large-scale synthesis was performed in a 100 ml round-bottom reaction flask. Phosphine solution is extremely air sensitive and needs to be handled very carefully for injection.

D.2 Accelerated-ageing test

In the accelerated-ageing test (Figure 4.3f), firstly the acceleration factor was calculated by considering the absorbance of the QDs inside the film (0.35) at the illumination wavelength (365 nm). This absorbance value is corresponding to 55.3% absorbance. The absorbance of the film (55.3%) was multiplied with the calculated power density of the UV lamp at 365 nm (~8 $mW.cm^{-2}$) and resulted in 4.43 $mW.cm^{-2}$ of the absorbed power at the excitation wavelength. By dividing the value of absorbed power with the ratio of the absorbed photons by the film under 1 sun condition (~6%), the acceleration factor of ~74 was achieved. The quantum efficiency measurement of the QD film was performed under 16 hours and multiplied to the acceleration factor, which result in ~50 days.

D.3 The fabrication of the QD-based LSC

The synthesized QD solutions dissolved in hexane were mixed with the silicon elastomer (SYLGARD 184) and curing agent with the concentrations of 13 $mg.ml^{-1}$, 26 $mg.ml^{-1}$ and 52 $mg.ml^{-1}$. The ratio of the curing agent to the elastomer was adjusted to 1/10. Then, the mixture was stirred for 5-10 minutes until the bubbles appeared. The mixture was degassed at the vacuum desiccator for 1 hour to remove the bubbles and form a homogenous mixture. After the degassing process, the QD-polymer composite was poured on the glass substrate with different dimensions to form a strip in front of the doctor-blade device. The doctor-blade was translated over the LSC length to from a thin QD-polymer composite layer. The substrate was cured at the oven at 70 °C to remove hexane solvent and form a high-quality film. The thickness of the glass substrate in all QD-LSC structures was 2 mm. The curing of the large-area QD-based LSC after the deposition of the QD-polymer mixture was performed over the hot plates.

D.4 The TEM images of the synthesized QDs

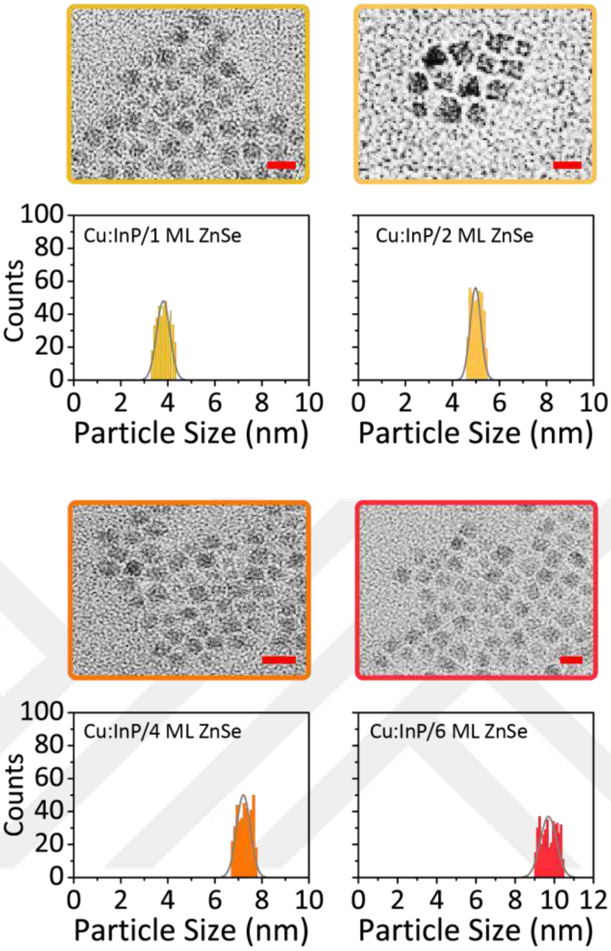

Figure D.1: The TEM images and size distribution of copper-doped InP QDs with 1, 2, 4 and 6 ML of ZnSe shell. The scale bar in two upper panel images = 5 nm and in two lower panel images = 10 nm.

Table D.1: The mean size of the synthesized QDs in each step of the synthesis procedure.

Type	InP	Cu:InP	1 ML ZnSe	2 ML ZnSe	3 ML ZnSe	4 ML ZnSe	5 ML ZnSe	6 ML ZnSe
Size (nm)	2.5 ± 0.2	2.7 ± 0.2	3.8 ± 0.3	5.0 ± 0.3	6.3 ± 0.2	7.2 ± 0.3	8.5 ± 0.3	9.7 ± 0.4

D.5 The high-resolution TEM (HRTEM) images of synthesized QDs

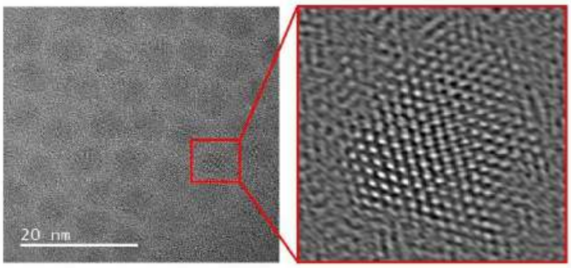

Figure D.2: The high-resolution TEM (HRTEM) image of the synthesized copper-doped InP/5ML ZnSe QDs.

D.6 The XRD pattern of the synthesized QDs

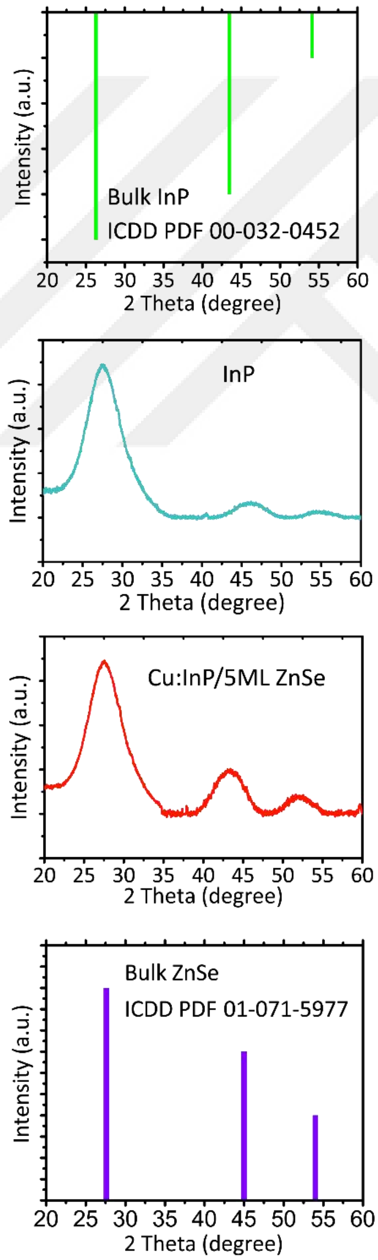

Figure D.3: The XRD patterns of InP and copper-doped InP/5ML ZnSe QDs. The top and bottom panels show the XRD peaks of the bulk InP and ZnSe, respectively.

D.7 The optimization of the Cu:P ratio

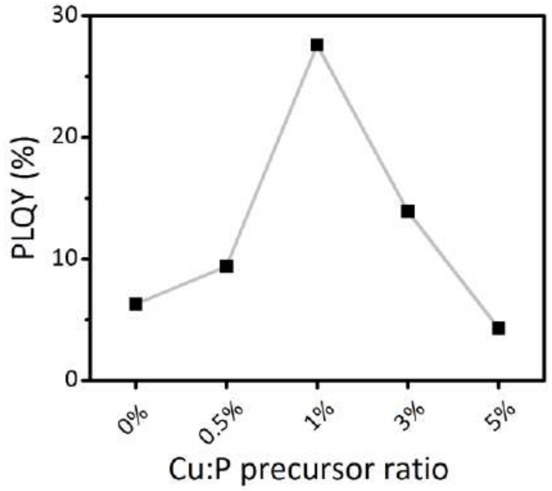

Figure D.4: The evolution of the PLQY by increasing Cu:P precursor ratio. At the Cu:P ratio of 1%, the highest PLQY of 27.6% was achieved.

D.8 The measurement data for PLQY of the synthesized QDs

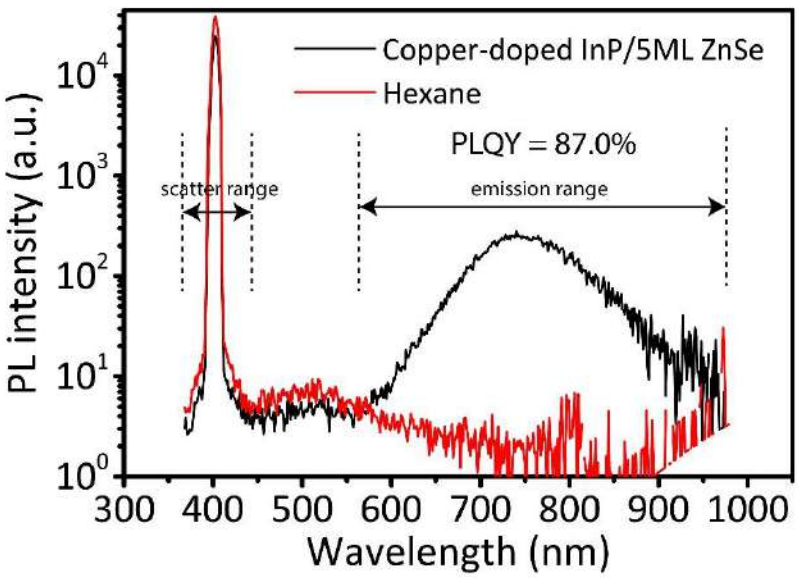

Figure D.5: The PL intensity spectra of the synthesized copper-doped InP/5ML ZnSe QDs and hexane solvent as the reference for the PLQY measurement.

D.9 The comparison of the PLQY between the synthesized copper-doped InP/ZnSe in this study and the previous studies

The PLQY of the synthesized copper-doped InP/ZnSe QDs was compared with the previously synthesized QDs in the literature with the QDs having PL peak position in the near infrared wavelength region (Table D.2).

Table D.2: The comparison between the PLQY of the QDs in this study and the previous studies synthesized in the near infrared wavelength region.

	Type of the QDs	Photoluminescence peak wavelength range (nm)	FWHM (nm)	PLQY (%)	Stokes-shift (meV)	Ref
1	Copper-doped CdSe	650-700	~115	97	~1400	[70]
2	Ag-doped InP	900	~250	40	~520	[361]
3	InAs/InP/ZnSe	940	60-75	76	~140	[362]
4	GSH-coated PbS	950-1200	~250	16	---	[363]
5	PbS	900-1050	250	17	~120	[364]
6	Ag_2Te/ZnS	1000-1100	200	5.6	---	[365]
7	PEGylated-DHLA-Ag_2S	1150-1220	43	15.5	---	[366]
8	$CuInS_2/ZnS$	862	250	91	550	[258]
9	$CuInSe_2/ZnS$	805	150	72	160	[15]
10	Manganese-doped $Cd_xZn_{1-x}S/ZnS$	600	200	78	750	[15]
11	Copper-doped InP	630-1100	100-175	23	~1630	[81]
12	$CuInS_2/CdS$	750	150	75	500	[367]
13	$CuInSe_xS_{2-x}/ZnS$	965	260	40	530	[368]
14	Si	830	240	50	400	[369]
15	CdSe/CdS/CdZnS/ZnS	630	100	45	~50	[333]
16	$CdSe/Cd_{1-x}Zn_xS$	628	60	70	720	[28]
17	$CdSe/Cd_xPb_{1-x}S$	560-620	23-26	40	300	[294]
18	PbS/CdS	850-1550	---	40-50	250	[335]
19	CdSe/CdS	640	65	45	400	[13]
20	Copper-doped InP/5ML ZnSe (This study)	720-775	165	87	650	---

D.10 The large-area QD-LSC under ambient light

Figure D.6: (a) The large-area QD-LSC with the dimensions of 100 cm× 30 cm under ambient light. (b) The zoomed view of the scale for better visualization.

D.11 The LSCs with different loading concentration of QDs

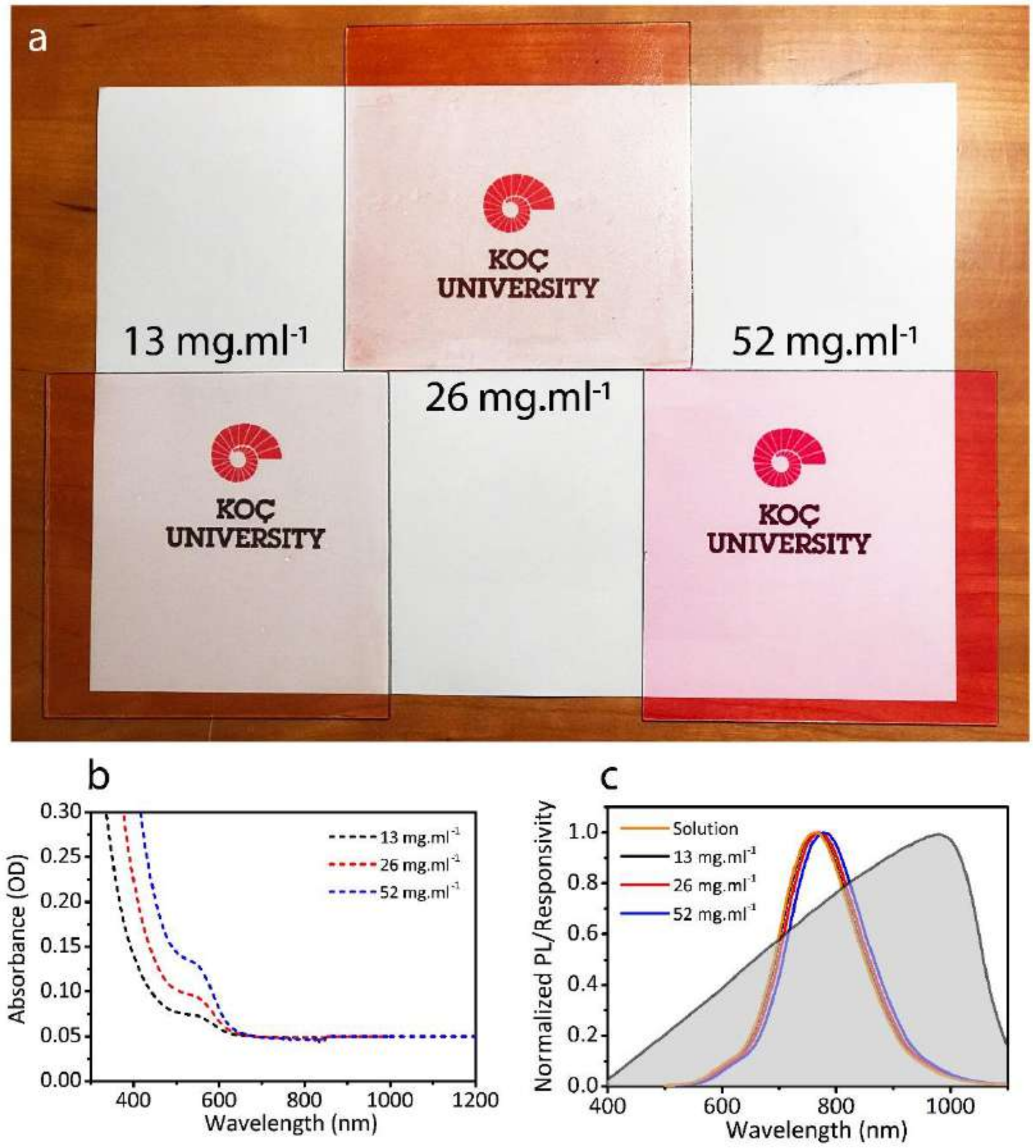

Figure D.7: (a) The photograph, (b) the absorbance and (c) the normalized PL output of the fabricated QD-based LSCs with different QD loading concentrations of 13, 26, and 52 mg.ml^{-1}. The grey shaded spectrum in (c) is the responsivity of silicon PV.

D.12 The calculation of reabsorption coefficient in the fabricated QD-LSCs

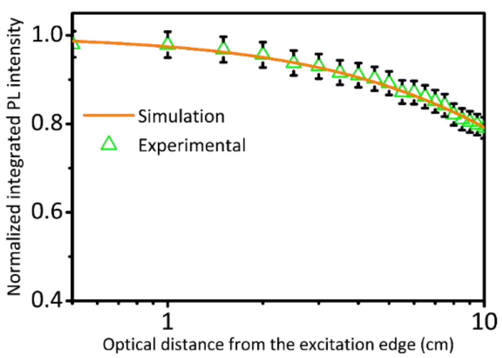

Figure D.8: The optical output decay in the fabricated QD-LSC. The spectrally integrated output of QD-based LSC under the illumination by an ultraviolet laser beam at 365 nm wavelength. Orange line shows the simulation results. The reabsorption coefficient was done by the calculation of α in the fitted waveguiding efficiency by using the equation of $\eta_{\text{waveguiding}} = 1/(1 + \beta(\alpha_{2,\text{eff}} + s_2)L[1 - ((\alpha_{2eff}\eta_{PL} + s_2)/(\alpha_2 eff + s_2))\eta_{TIR}]$. The QD concentration is 26 mg.ml^{-1}.

D.13 The scattering measurement in the fabricated QD-LSCs

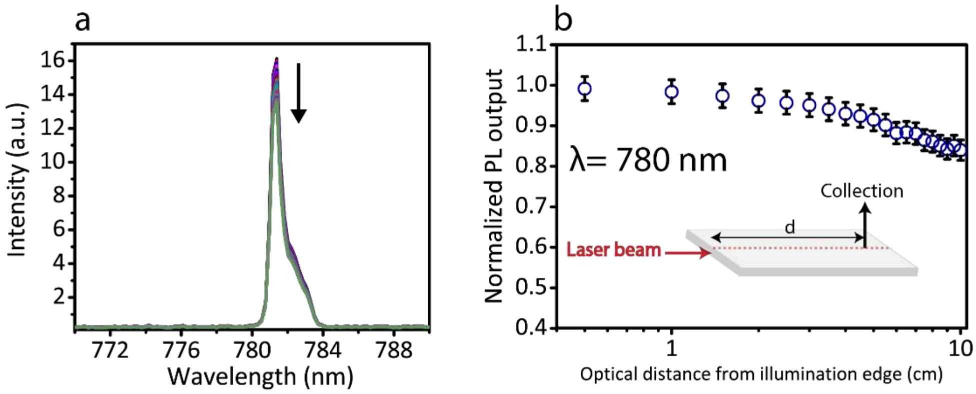

Figure D.9: (a) The PL output was shown at different optical distances ranging from 0 to 10 cm in the arrow direction when the laser beam with the wavelength of 780 nm was propagated inside the slab based on the setup schematic demonstrated at (b)-inset. (b) The normalized PL output was shown at different optical distances ranging from 0 to 10 cm when the laser beam with the wavelength of 780 nm was propagated inside the slab. Inset: The schematic demonstrates the setup, in which the QD-based LSC illuminated by the laser beam at the edge and the optical output was collected from the face by using an optical fiber.

D.14 The EQE of the silicon solar cell and the intensity profile of the solar simulator

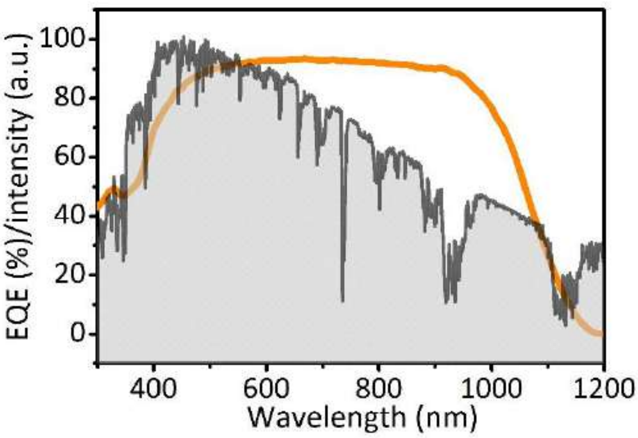

Figure D.10: The EQE of the silicon solar cell and the intensity profile of the solar simulator. The orange line shows the EQE graph of the silicon solar cell and the grey shaded area shows the intensity profile of the solar simulator used in this study.

D.15 The simulation of the optical and external quantum efficiency of QD-based LSCs

The optical quantum efficiency of the LSC (Equation (D.1)) [15] is directly proportional with QE of the QDs embedded inside the polymeric matrix (η_{PL}) and light trapping efficiency inside the waveguide (η_{TIR}). η_{PL} is already measured in an integrating sphere and it is 81.2%. $\eta_{\text{TIR}} = \cos(\arcsin 1/n)$ [86] is 74.5% for glass with a refractive index (n) of 1.51 in the visible wavelength region. By using the measured scattering (s_2) and absorption coefficient ($\alpha_{2\text{eff}}$) of the LSC, the calculated optical quantum efficiency corresponded to 49.9% for LSC with the loading concentration of 26 mg.ml^{-1} and side length of 10 cm. The optical quantum efficiency values of the QD-LSC with the side length of 10 cm at the loading concentrations of 13 and 52 mg.ml^{-1} were also corresponding to 51.8% and 46.7%, respectively. Moreover, by changing the side length to 5 and 20 cm, the optical quantum efficiency of LSC with the loading concentration of 26 mg.ml^{-1} corresponded to 54.8% and 42.7%, respectively.

$$\eta_{OQE} = \frac{\int \frac{\eta_{TIR}\eta_{PL}}{1+\beta(\alpha_{2eff}+s_2)L(1-(\frac{\alpha_{2eff}\eta_{PL}+s_2}{\alpha_2 eff+s_2})\eta_{TIR})}\phi_{PL}(\lambda)d\lambda}{\int \phi_{PL}(\lambda)d\lambda} \quad (D.1)$$

Absorption efficiency, which quantifies the number of the absorbed photons over solar spectrum was calculated based on Equation (D.2) [86] as follows:

$$\eta_{abs} = \frac{\int \phi_{sol}(1-R)(1-e^{-\alpha(\lambda)d})d\lambda}{\int \phi_{sol}(\lambda)d\lambda} \quad (D.2)$$

$\phi_{sol}(\lambda)$ is the spectral profile of the solar spectrum. R is reflectivity, which was calculated based on Equation (D.3). d was considered as the LSC thickness and α(λ) is the absorption coefficient of the copper-doped InP/5 ML ZnSe QDs calculated from absorbance spectrum.

$$R = \frac{(n_2-n_1)^2}{(n_2+n_1)^2} \quad (D.3)$$

The simulated values of external quantum efficiency was calculated based on Equation (D.4).

$$\eta_{EQE} = \eta_{OQE}\eta_{abs} \quad (D.4)$$

The external quantum efficiency of the LSCs with different side lengths and loading concentration of the QDs was shown in Figure D.11 and Table D.3.

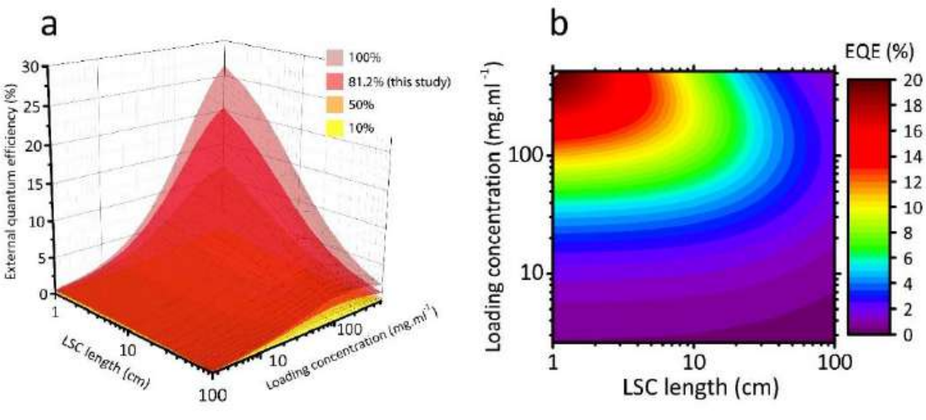

Figure D.11: (a) The simulation of the external quantum efficiency of QD-LSCs having different QE of QDs ranging from 10%, 50%, 81.2% (QE of this study) and unity at different LSC lengths ranging from 1 to 100 cm and different loading concentration between 2.6 and 520 mg.ml-1. (b) The contour plot of the external quantum efficiency of the QD-LSC having QE of QDs of 81.2%.

Table D.3: The summary of the calculation results for the fabricated LSCs with different loading concentrations and side lengths.

Device number	Side length (cm)	Loading concentration ($mg.ml^{-1}$)	Absorption efficiency (η_{abs})	Optical quantum efficiency (η_{OQE})	External quantum efficiency (η_{EQE})
1	5	26	6.9%	54.8%	3.8%
2	10	13	3.6%	51.8%	1.9%
3	10	26	6.9%	49.9%	3.5%
4	10	52	12.1%	46.7%	5.7%
5	20	26	6.9%	42.7%	3.0%

D.16 Reshaping factor (q_{LSC})

q_{LSC} is the reshaping factor, which was calculated based on Equation (D.5) [15].

$$q_{LSC} = \frac{<Q_{PL}>}{<Q_s>} = \frac{\int \phi_{PL}(\lambda)\mathrm{EQE}(\lambda)\mathrm{d}\lambda}{\int \phi_{sol}(\lambda)\mathrm{EQE}(\lambda)\mathrm{d}\lambda} \tag{D.5}$$

In Equation (D.5), $\phi_{PL}(\lambda)$, EQE(λ), and $\phi_{sol}(\lambda)$ are the photoluminescence spectral profile of the copper-doped QDs, external quantum efficiency of the silicon solar cell and the spectral profile of the solar spectrum that obtained from the solar simulator, respectively. Based on Equation (D.5), $<Q_{PL}>$ and $<Q_s>$ were calculated as 0.9098 and 0.5253, respectively, which resulted in the q_{LSC} as 1.73. In order to compare the calculated reshaping factor in this study with the previous studies, we used the similar integration method and wavelength range and calculated the reshaping factor of the standard PV cell. Our calculations also resulted with the reshaping factor of 2 for a standard PV cell similar to previous study [28].

D.17 Calculation of coupling efficiency ($\eta_{coupling}$)

In the electro-optical measurements, the solar cells were attached to the LSC edges in order to absorb the incoming photons. In the experimental setup, no refractive-index-matching adhesive was used between LSCs and solar cells. As a result, there will be a photon-loss due to the thin air gap between the LSC edge and coupled solar cells. Based on the refractive index difference between the LSC, air and the solar cell, we calculated the ratio of the number of photons reaching into the cell with respect to the number of photons reaching to the LSC edge. We introduced it as the coupling efficiency ($\eta_{coupling}$). For the calculation of the coupling efficiency, Fresnel equations (Equations (D.6) and (D.7)) were used as follows [284]:

$$R_s = \left| \frac{n_1 \cos(\theta_i) - n_2 \sqrt{1 - (\frac{n_1}{n_2}\sin(\theta_i))^2}}{n_1 \cos(\theta_i) + n_2 \sqrt{1 - (\frac{n_1}{n_2}\sin(\theta_i))^2}} \right|^2 \quad \text{(D.6)}$$

$$R_p = \left| \frac{n_2 \cos(\theta_i) - n_1 \sqrt{1 - (\frac{n_1}{n_2}\sin(\theta_i))^2}}{n_2 \cos(\theta_i) + n_1 \sqrt{1 - (\frac{n_1}{n_2}\sin(\theta_i))^2}} \right|^2 \quad \text{(D.7)}$$

$$R_{eff} = \frac{R_s + R_p}{2} \quad \text{(D.8)}$$

Photoluminescence of QDs is un-polarized. Hence, effective reflectance can be calculated by averaging s and p polarization equations (see Equation (D.8)). Generated light travels from glass to air (R_{s1}, R_{p1}) and then from air to solar cell (R_{s1}, R_{p1}), hence the coupling efficiency can be calculated based on Equation (D.9) as follows:

$$\eta_{coupling} = \sum_0^{90-\theta_c} \left(1 - R_{eff1}(\theta)\right)\left(1 - R_{eff2}(\theta)\right)/(90 - \theta_c) \quad \text{(D.9)}$$

It should be noted that only guided light can reach to edge of the luminescent solar concentrator, hence reflectance are averaged from 0 to $90 - \theta_c$, all other light confined in the luminescent solar concentrator. Here, $\theta_c = 41.5^0$ and s and p polarization reflectance were shown in Figure D.12 and D.13. Using Equation (D.8), effective reflectance of un-polarized PL from glass to air under solar cell is 4.39% when integrated from 0^0 to 48.5^0. Similarly, when the light moves from air to solar cell, effective reflectance is 21.26%. Using Equation (D.9), the coupling efficiency was yielded as $\eta_{coupling} = 75.2\%$.

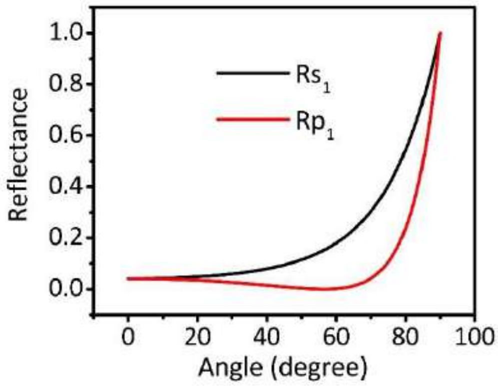

Figure D.12: s and p polarization reflectance values from air to PV.

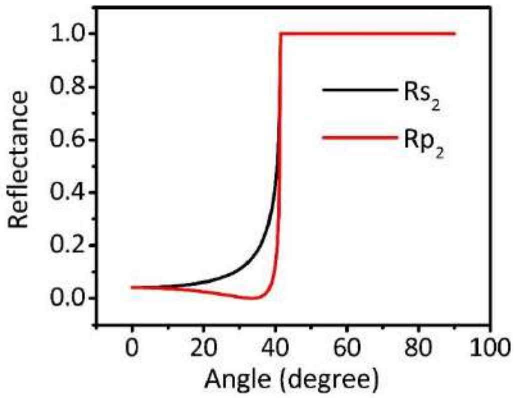

Figure D.13: s and p polarization reflectance values from glass to air.

D.18 The J-V curve of the used silicon solar cell

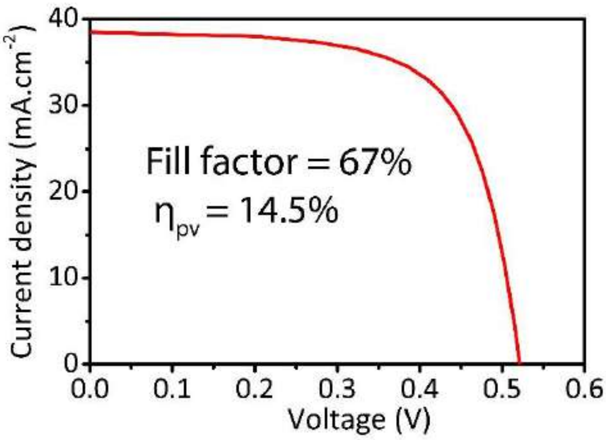

Figure D.14: The J-V curve of the silicon solar cell used for the electro-optical measurements under the solar illumination with the power of 100 mW.cm^{-2}.

D.19 The electro-optical measurements for the fabricated QD-LSC devices

As mentioned in section 4.1, the fabricated LSCs with different LSC lengths and loading concentrations were coupled to the silicon solar cell with the measured external quantum efficiency (η_{pv}) of 14.5%. The devices were illuminated by the calibrated AM 1.5G solar simulator with the power density of 100 mW.cm^{-2} and the short-circuit current from the illumination of the solar cell (J_{PV}) and with the LSC (J_{LSC}) was measured and used in order to calculate the optical and external quantum efficiency of the QD-LSCs. The J-V curves for the fabricated devices with the same loading concentration of 26 mg.ml^{-1} and different LSC lengths of 5 and 20 cm were shown in Figure D.15.

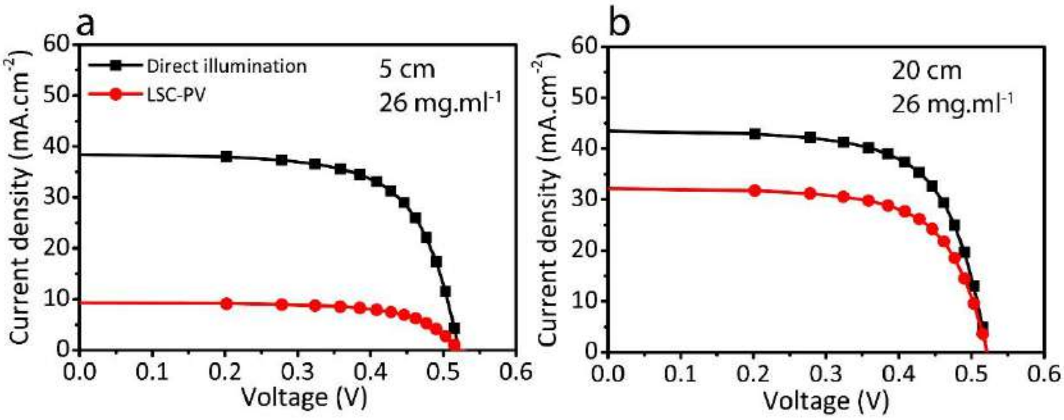

Figure D.15: The J-V curves of the silicon solar cells coupled to the QD-LSCs with the loading concentration of 26 $mg.ml^{-1}$ and the LSC length of (a) 5 cm and (b) 20 cm.

The measurement results extracted from Figure 4.6 and Figure D.15 were shown in Table D.4. In order to measure the optical quantum efficiency values for the fabricated devices, Equation (D.10) was used as follows [354]:

$$\eta_{OQE}\ (\%) = \frac{J_{LSC}}{J_{PV}\ \times G \times q_{LSC} \times \eta_{abs} \times \eta_{coupling}} \tag{D.10}$$

For the measurement of optical quantum efficiency, it should be mentioned that the short circuit current values represent the number of photons reached to the solar cells. However, the optical quantum efficiency considers the number of photons exiting from the LSC edge. As a result, the values obtained from the electro-optical measurements need to be divided by the coupling efficiency in order to obtain the optical quantum efficiency values for different QD-LSCs.

Table D.4: The summary of the electro-optical measurement results for the fabricated LSCs with different loading concentrations and side lengths.

Device number	**Side length (cm)**	**Loading concentration ($mg.ml^{-1}$)**	**Geometrical factor (G)**	**J_{LSC}/J_{PV}**	**EQE**	**Optical quantum efficiency**	**External optical efficiency (EQE/q_{LSC})**	**PCE**
1	5	26	6.25	0.24	3.9%	44.3%	2.3%	0.6%
2	10	13	12.5	0.24	1.9%	40.7%	1.1%	0.3%
3	10	26	12.5	0.44	3.5%	39.9%	2.0%	0.5%
4	10	52	12.5	0.74	5.9%	37.2%	3.4%	0.9%
5	20	26	25	0.73	2.9%	32.7%	1.7%	0.4%

The optical gain factor was measured based on G = L / (4D), in which the L is the side length of LSC and D is the thickness of the QD-LSC equal to approximately 0.2 cm. As a result, the G factor for the devices with the LSC lengths of 5, 10 and 20 cm yielded to

6.25, 12.5 and 25, respectively.

The power conversion efficiency of the QD-LSCs were calculated by using Equation (D.11) [15].

$$\text{PCE}\ (\%) = \eta_{EQE-LSC}\eta_{EQE-PV} \tag{D.11}$$

, in which the $\eta_{EQE\text{-}LSC}$ is the measured external quantum efficiency of the device based on the electro-optical measurements (Table D.4) and $\eta_{EQE\text{-}PV}$ is the external quantum efficiency of the PV cells equal to 14.5% based on Figure D.14.

D.20 The comparison between the external quantum efficiency of this study and previous studies

Based on Table D.5, the measured optical quantum efficiency of the fabricated QD-LSCs with the dimensions of 10 cm × 10 cm under the illumination of AM 1.5G solar simulator in this study is comparable with the highest values reported in the literature.

In reference [354], the authors reported the optical quantum efficiency level of 26% with the same dimensions of this study and higher thickness of the film (0.2 cm).

In reference [369], for the calculation of the optical quantum efficiency, the reshaping factor has not been considered in the calculations, which may lower the reported value of 30%. We used the emission profile of the QDs in reference [369] in order to calculate the reshaping factor (PL wavelength range from 560-1040 nm centered at 830 nm). Our calculations yielded to the values of 0.9126 and 0.4592 for $\langle Q_{PL} \rangle$ and $\langle Q_s \rangle$, respectively. As a result, the q_{LSC} was calculated as 1.9874. By dividing the reported value of η_{OQE} (~30%) by the calculated reshaping factor (~2), the η_{OQE} was decreased nearly two-fold to a new value of 15%, almost half of the reported value in this study (28%). The significant deference in the optical quantum efficiencies is due to the difference in the QE of the QDs, which was almost two times higher in this study (81.2%) in comparison with the reported value for silicon QDs (46%) in the previous study.

Table D.5: The comparison between this study and the previous studies in the literature.

Fluorophore		**Type**	**LSC active area (cm×cm)**	**Light source**	**η_{OQE} (%)**	**EQE (%)**	**Ref**
Quantum dots	1	$CdSe/Cd_{1-x}Zn_xS$	10.2 × 10.2	405 nm light solar simulator	24 21	1.9	[28]
	2	CdSe/CdS	21.5 × 1.35	solar simulator	10	0.6	[13]

	3	$(PEA)_2MAPb_2Br_7$ Layered perovskite	10 × 10	solar simulator	26	0.9	[354]
	4	$CsPb(I_xBr_{1-x})_3$	1.3 × 9	solar simulator	5	2	[320]
	5	Si	12 × 12	solar simulator	30	---	[369]
	6	Carbon dots	1.5 × 9	solar simulator	2.6	0.2	[370]
	7	$CuInS_2/ZnS$	10 × 10	solar simulator	23	8.1	[258]
	8	$CuInSe_xS_{2-x}/ZnS$	12 × 12	solar simulator	17	3.3	[368]
	9	$CuInS_2$	30 × 30	Solar simulator	29.2	6.8	[371]
	10	Copper-doped InP/ZnSe (This study)	10 × 10	solar simulator	37.2	5.9	---
	11	Manganese-doped $Cd_xZn_{1-x}S/ZnS$	12 × 12	385 nm light	58	3.4	[15]
	12	$CuInSe_2/ZnS$	12 × 12	385 nm light	19	5.1	[15]
	13	Manganese-doped ZnSe	2.5 × 7.5	400 nm light	37	---	[80]
	14	CdSe/CdS	2 × 2	400 nm light	59	---	[272]
	15	Copper-doped CdSe	10 × 10	---	---	1.65	[70]
	16	Tandem structure from No. (1) and (2)	15.2 × 15.2	---	---	6.4	[15]
	17	$CuInS_2/CdS$	7.5 × 7.5	---	---	5.7	[367]
	18	CdSe/CdS/CdZnS/ZnS	4.95 × 3.1	---	---	---	[333]
	19	$CdSe/Cd_xPb_{1-x}S$	7 × 1.5	---	---	1.4	[294]
	20	PbS/CdS	2 × 1.5	---	---	6.1	[335]
	21	InP/ZnO	9 × 1.5	---	---	3.22	[77]

	22	Carbon dots- tandem	10 × 10	---	---	1.1	[370]
Organic Dyes	23	Lumogen F Red305 Fluorescence Yellow CRS 040	5 × 5	---	---	---	[334]
	24	DCJTB	3 cm^2	---	---	3.84	[372]
	25	Pyrromethene 567	10 × 10	---	---	---	[373]
	26	TPFE-Rho	1.8 × 1.8	---	---	3.55	[374]
Fluorescent proteins	27	mScarlet fluorescent protein	1.5 × 1.5	---	---	4.42	[17]

D.21 The non-linear absorption spectroscopy

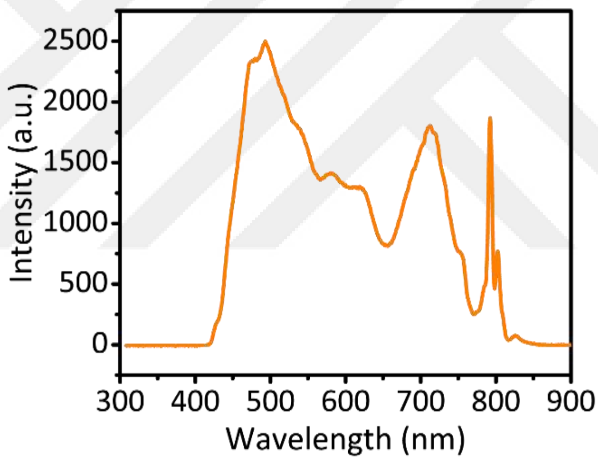

Figure D.16: The measured white light continuum spectrum, which was used as the probe beam during the experiments.

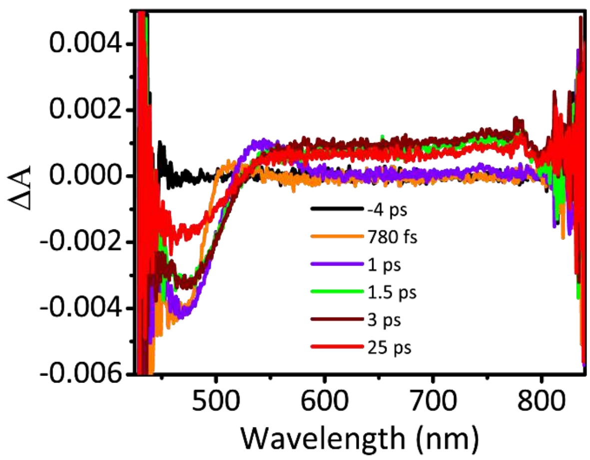

Figure D.17: The non-linear absorbance spectroscopy of undoped InP/5 ML ZnSe QDs with the same delays with the doped sample.

D.22 The calculation of the visible light transmittance (VLT)

Equation (D.12) was used in order to calculate the weighted average visible light transmittance (VLT) of the LSC windows according to reference [258] as follows:

$$\text{visible light trasmittance (VLT)} = \frac{\int \mathrm{T}(\lambda)\mathrm{P}(\lambda)\mathrm{S}(\lambda)\mathrm{d}\lambda}{\int \mathrm{P}(\lambda)\mathrm{S}(\lambda)\mathrm{d}\lambda} \quad \text{(D.12)}$$

, where T (λ) is the transmittance of the window, P (λ) is the eye-sensitivity function and S (λ) is the solar spectrum. The wavelength range was adjusted to 300-750 nm (i.e., visible wavelength region). Our calculations showed that the fabricated QD-LSCs with the loading concentration of 52 $mg.ml^{-1}$ has the VLT value of 41%. As a result, the VLT of the fabricated LSCs with lower concentration will be >41%, which can be used as tinted architectural windows.

D.23 The consistency check for the calculation of external quantum efficiency values

As the final consistency check for the calculated values of the EQE of the LSC devices, we used the formulation in the recent study [88]. In the reference, the authors used Equation (D.13) for the calculation of the external quantum efficiency of the LSC as follows:

$$\eta_{LSC} = \eta^*_{opt}\eta^*_{PV} \quad \text{(D.13)}$$

, in which η^*_{opt} and η^*_{PV} was calculated based on Equations (D.14) and (D.16), respectively.

$$\eta^*_{opt} = \frac{\int \mathrm{AM\ 1.5G}\ (\lambda)\ \eta_{opt}(\lambda)\mathrm{d}\lambda}{\int \mathrm{AM\ 1.5G}\ (\lambda)\mathrm{d}\lambda} \quad \text{(D.14)}$$

In Equation (D.14), $\eta_{opt}(\lambda)$ is the optical efficiency of the LSC at different wavelengths. For the calculation of the optical efficiency, Equation (D.15) was used.

$$\eta_{opt} = \left(1 - R_f(\lambda)\right) A(\lambda)\ \eta_{PL}\eta_{TIR}\eta_{wg} \quad \text{(D.15)}$$

In Equation (D.15), R_f (λ) is the reflection spectrum of the incident light at the front surface. A(λ) is the absolute absorption spectrum, η_{PL} is the quantum efficiency of the QDs in-film as 81.2%, η_{TIR} and η_{wg} are 74.5% and 73.6% based on the calculations in the main text, respectively. As a result, η^*_{opt} yielded to 35.2%. η^*_{PV} was calculated based on Equation (D.16) as follows:

$$\eta^*_{PV} = \left[\frac{\eta_{PV}\ (AM\ 1.5G)}{\eta^{PV}_{abs}(AM\ 1.5G)}\right]\frac{\int \mathrm{EQE}_{PV}\ (\lambda')\ PL(\lambda')\mathrm{d}\lambda'}{\int PL(\lambda')\mathrm{d}\lambda'} \quad \text{(D.16)}$$

In Equation (D.16), $\eta_{PV}(AM\ 1.5G)$ is the power conversion efficiency of the edge-mounted PV cell under the AM 1.5G solar illumination, $PL(\lambda')$ is the emission profile of the synthesized QDs in the device architecture, and $\eta_{abs}^{PV}(AM\ 1.5G)$ is the absorption efficiency of the silicon photovoltaics. Based on our calculations, η_{PV}^{*} corresponded to 16.2%. As a result, the external quantum efficiency η_{LSC} of the LSC corresponded to 5.7%, which is in close approximation of our measured external quantum efficiency based on the electro-optical measurements (5.9% as shown in Table D.4).

APPENDIX E

E.1 Synthesis of InP/ZnO QDs

E.1.1 Indium phosphide core synthesis

0.3 mmol zinc undecylenate, 98 µl oleic acid and 204 µl oleylamine were mixed in 9 ml ODE in a 100 ml three-neck round bottom flask. The solution was heated to 100ºC, evacuated and refilled with nitrogen repeatedly to provide oxygen and water-free reaction atmosphere. 0.3 mmol $InCl_3$ was then added to the solution in the glove-box. The flask was heated to 240ºC with strong agitation under nitrogen flow. At this temperature, 1.5 ml of phosphine stock solution ($P(TMS)_3$-ODE 0.2 mmol.ml^{-1}) was injected to the solution swiftly. The color of the solution became dark right after injection. The dark solution was kept at 210 ºC for 20 min and then cooled down to room temperature.

E.1.2 Preparation of 0.015 M zinc oxide stock solution for shelling process

0.1 mmol $Zn(acac)_2$, 32 µl oleic acid, and 1 ml oleylamine were mixed in 6 ml of ODE at 60 °C.

E.1.3 Shelling procedure

The solution containing indium phosphide QDs was heated to 60 ºC. Once the temperature was stable, 530 µl of the prepared zinc oxide stock solution was added to the indium phosphide solution. Then, the solution was heated up to 280 ºC and stirred for 20 minutes.

Multiple Shelling procedure

For preparation of InP/2ZnO, InP/3ZnO, InP/4ZnO and InP/5ZnO quantum dots, 670 µl, 835 µl, 1170 µl, and 1835 µl of the prepared zinc oxide stock solution was added, respectively. The rest of the shelling process was the same as InP/ZnO procedure.

E.1.4 Purification and storage

4 ml toluene was added to the QDs solution and the precipitate was centrifuged at 9000 rpm for 15 minutes and removed. Ethanol was added to the solution until it became turbid, then the solution was centrifuged at 9000 rpm for 5 min three times. The precipitated QDs were dispersed in hexane. The purified QDs solutions were kept at 5 ºC.

E.2 Device fabrication

6 mg of purified QDs was dissolved in 1 ml hexane solvent as stock solution. For preparation of each slab, 355 µl of QDs stock solution, 4.5 ml PDMS SYLGARD 184

and 0.45 ml of SYLGARD 184 curing agent were used. The mixture was degassed repeatedly and kept under vacuum for 20 minutes. The degassed mixture was transferred to the mold and cured at 70 °C for 6 hours. The cured LSC was peeled off from the aluminum mold after completion of heating process.

E.3 TEM images of InP core, InP/2ZnO and InP/5ZnO QDs

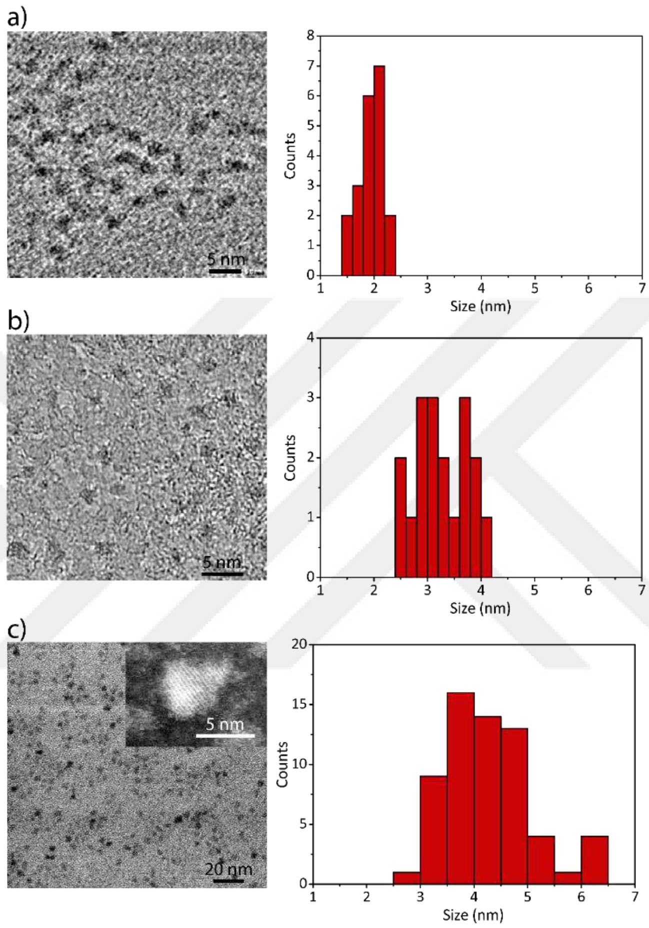

Figure E.1: The TEM images and size distribution of (a) InP core, (b) InP/2ZnO, and (c) InP/5ZnO QDs. Inset: the Z-contrast image of InP/5ZnO QDs.

Based on TEM images, we performed monolayer calculation and the results were showed in Table E.1. The definition of the monolayer here is the ZnO shell which measures 5.2 Å (along [002] plane due to the wurtzite structure). Hence, the number of monolayers based on the amount of zinc precursor which was used for each number of shelling can be calculated from the TEM images.

Table E.1: Calculations of monolayer coverage based on TEM images.

	size (nm)	**monolayer coverage**	**Zinc precursor volume (µl) (layer-by-layer)**
InP core	1.95 ± 0.24	----	----
InP/2ZnO	3.01 ± 0.64	1.01	670
InP/5ZnO	4.31 ± 0.86	2.26	1835

E.4 SEM-EDAX measurement of InP core, InP/2ZnO and InP/5ZnO QDs

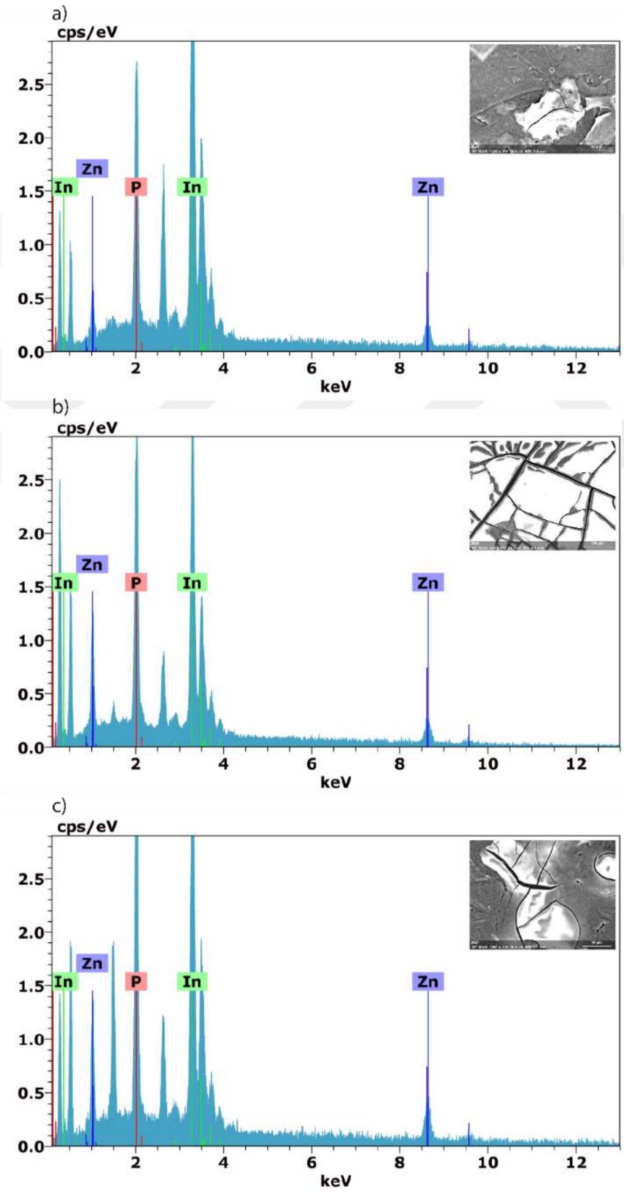

Figure E.2: SEM-EDAX measurement of (a) InP core, (b) InP/2ZnO and (c) InP/5ZnO QDs.

Table E.2: The quantitative analysis of SEM-EDAX measurement from InP, InP/2ZnO and InP/5ZnO.

	InP	InP/2ZnO	InP/5ZnO
Phosphorus	13.55 wt% ± 2.53%	16.22 wt% ± 3.57%	16.26 wt% ± 4.53%
Indium	75.75 wt% ± 11.51%	66.82 wt% ± 10.43%	60.41 wt% ± 8.21%
Zinc	10.70 wt% ± 3.48%	16.97 wt% ± 4.08%	23.33 wt% ± 4.96%

E.5 XRD measurement of InP/ZnO QDs

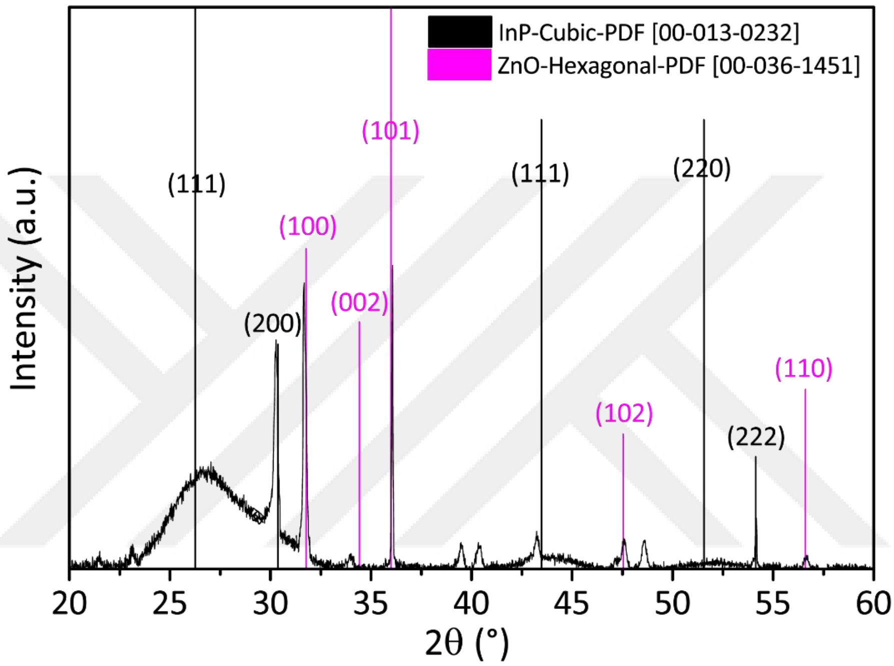

Figure E.3: The XRD measurement of InP/2ZnO QDs.

E.6 Calculation of absorbance and photoluminescence spectral overlap

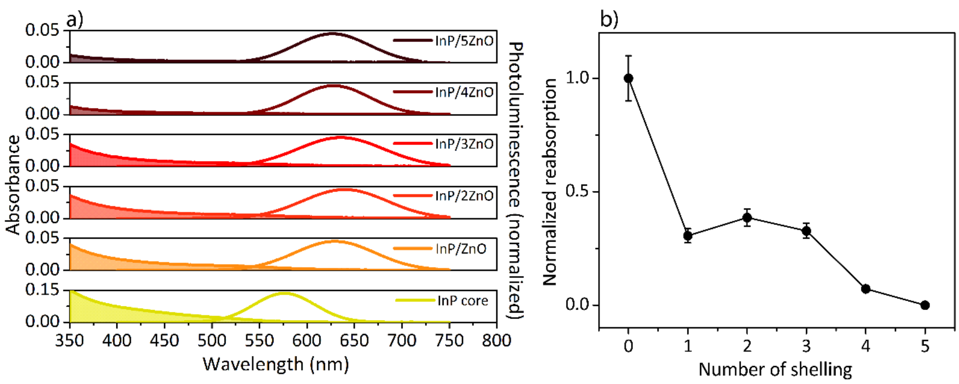

Figure E.4: (a) The cross-sectional area of absorbance and photoluminescence spectra of synthesized QDs decreased with increasing the amount of shell volume. (b) The change of normalized reabsorption with respect to increasing the shell volume.

E.7 Device fabrication

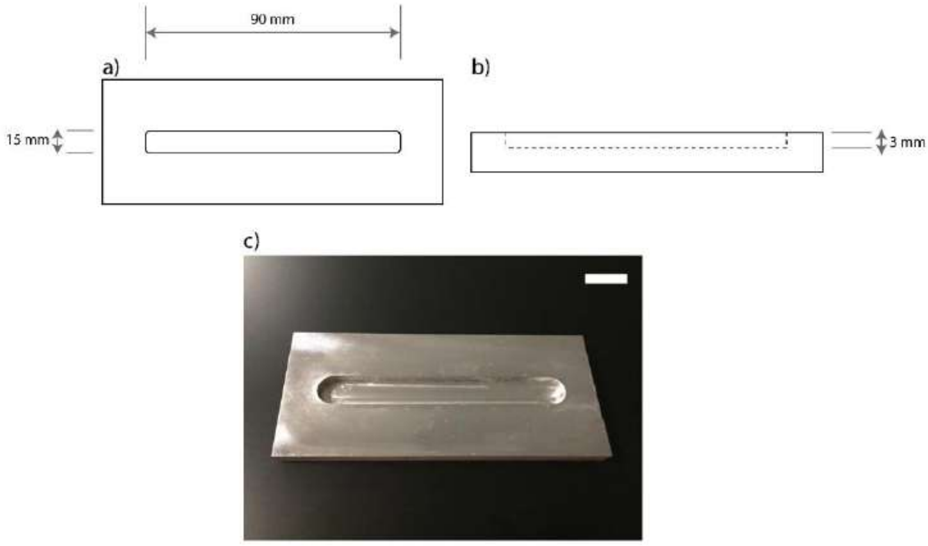

Figure E.5: CAD drawing of the mold design from (a) top and (b) side view, respectively. (c) The fabricated aluminum mold after machining. The scale bar represents 2 cm.

E.8 The FTIR spectra of the samples

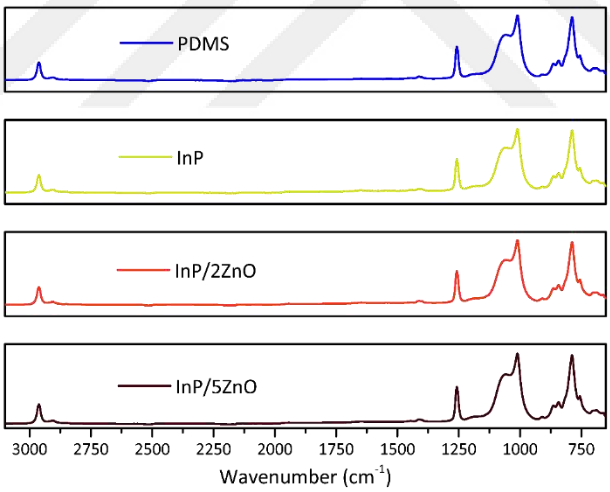

Figure E.6: The FT-IR measurement of PDMS, InP, InP/2ZnO and InP/5ZnO. The FT-IR spectra proved the fact that when QDs were incorporated into the PDMS polymer, the chemical properties of the PDMS were not changed. It shows both the PDMS capability to contain QDs and QDs perfect integration into the PDMS host.

E.9 The optical parameters of the output intensity spectra from LSCs excited by solar spectrum

Table E.3: Calculated optical parameters of LSC under solar simulator spectrum

	CRI	CCT (K)	(x, y) coordinates
Solar spectrum	82	5595	(0.33,0.40)
PDMS	82	5496	(0.33,0.40)
InP/2ZnO	82	4829	(0.36,0.42)
InP/5ZnO	82	5221	(0.34,0.41)

E.10 The effect of concentration on the optical efficiency of QD-LSC

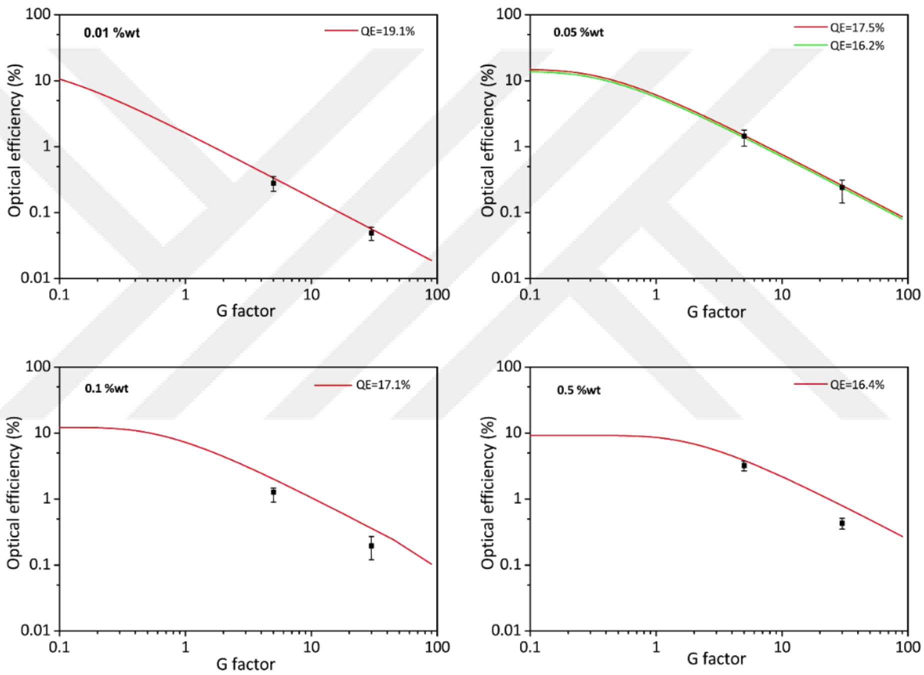

Figure E.7: The simulation and experimental results of optical efficiencies for LSCs with different loading concentrations of InP/5ZnO QDs.

E.11 The effect of concentration on the output intensity spectra from LSCs excited by solar spectrum

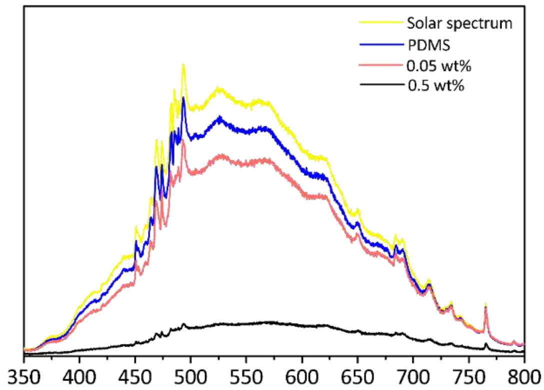

Figure E.8: The intensity spectra of illuminated LSCs with different loading concentrations of QDs.

APPENDIX F

F.1 The optical properties of the solid-state mScarlet fluorescent protein

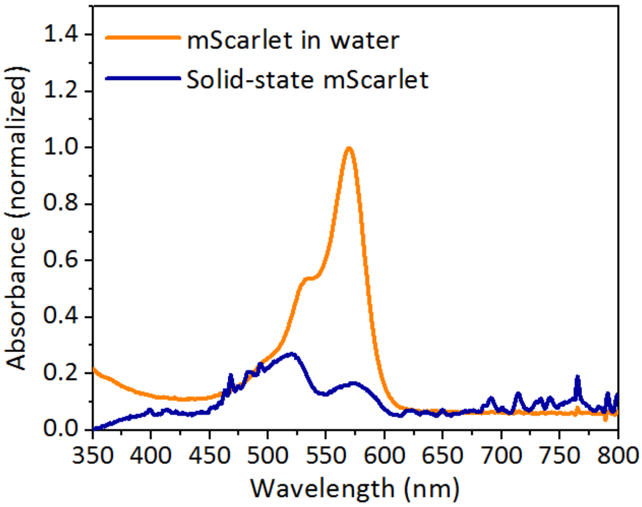

Figure F.1: The absorbance spectra of the solid-state mScarlet (blue line) and the liquid-state mScarlet (orange line).

F.2 The external quantum efficiency of the silicon solar cell

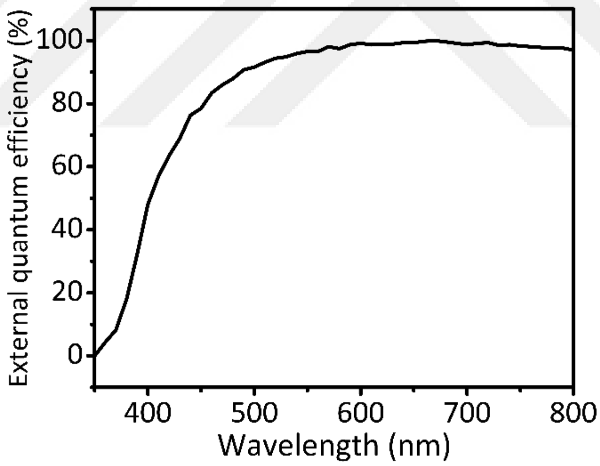

Figure F.2: The external quantum efficiency graph of a typical silicon solar cell.

APPENDIX G

G.1 Organic solar cell fabrication and characterization

Inverted bulk heterojunction photovoltaic devices were fabricated on patterned indium tin oxide (ITO) substrates with the configurations of ITO/ZnO/P3HT:PCBM/MoO_3/Ag. Firstly, ITO coated glass substrates were sonicated in 10% of Hellmanex liquid alkaline concentrate in de-ionized (DI) water for 15 minutes at 50 °C. The substrates were then rinsed with hot and cold DI water, respectively, and then sonicated in acetone for 15 minutes and isopropanol for 15 minutes, one after other. Next, the substrates were dried in the oven at 100 °C and treated with UV-ozone for 15 minutes. A sol-gel of ZnO (0.45 M) was prepared using zinc acetate dehydrate in 2-methoxyethanol and ethanolamine. The prepared solution was spin coated at 2000 rpm for 60 seconds to deposit ZnO thin film (~50 nm) on the substrate. A drying process was performed on a hot plate at 250 °C for 15 minutes at room temperature. The P3HT and $PC_{61}BM$ were used as it was received from Sigma Aldrich. The P3HT:$PC_{61}BM$ blend was deposited by spin-coating a solution (20 mg.ml^{-1}) of P3HT:$PC_{61}BM$ (1:0.6 ratio) in o-dichlorobenzene at 400 rpm for 150 seconds on top of ZnO layer. The P3HT:$PC_{61}BM$ layer was dried at 150 °C at hot plate for 15 minutes to remove the excess solvent. The thickness of the active layer used in these devices is ~ 210 nm. 10 nm of Molybdenum trioxide (MoO_3), an electron blocking layer, was deposited on top of the active layer by thermal evaporation. A silver cathode (100 nm) was deposited by thermal evaporation through a shadow mask under a pressure of ~ 2×10^{-6} mbar to complete the device, resulting a device area of approximately 0.0256 cm^2.

G.2 Current-voltage measurements

Current-voltage (*J-V*) characteristics of organic solar cells were measured under an AM 1.5G illumination source with intensity of 100 mW.cm^{-2} in an ambient condition. The light intensity was adjusted with a NREL calibrated silicon solar cell. The Keithley 2400 source meter was used for the measurement of *J-V* characteristics of the organic photovoltaic devices.

G.3 RFID Chip Integration and Antenna Power Measurements

For RFID transmitter and receiver chips, we used a 433 MHz WL101-341 RF receiver and DRA888TX ASK transmitter modules. We used 6 solar cell pixels to achieve the minimum operating voltage for these chips, ~1.5 V, even under light intensities as low as

0.1-sun. Moreover, to utilize voltage and current supply of each pixel, these 6 individual pixels connected in series for the circuitry supplying the chips. An Arduino Uno R3 with an ATmega328P processor was utilized to code the transmitter and receiver modules to work at 8 Kbps data rate. The data transmission and received message were constantly monitored to ensure proper communication without data loss in the transmitted message. Moreover, the antenna power for transmitter module, which was powered by our solar cell integrated LSC, was measured using a Rigol DSA815-TG spectrum analyzer that works within 9 kHz-1.5 GHz frequency range. During the experiments, the sun illumination intensity was changed from 0.1- to 1-sun and transmitted message and antenna power levels were recorded for each sun intensity.

G.4 The current-voltage (J-V) curve of the organic solar cells under blue LED spectrum

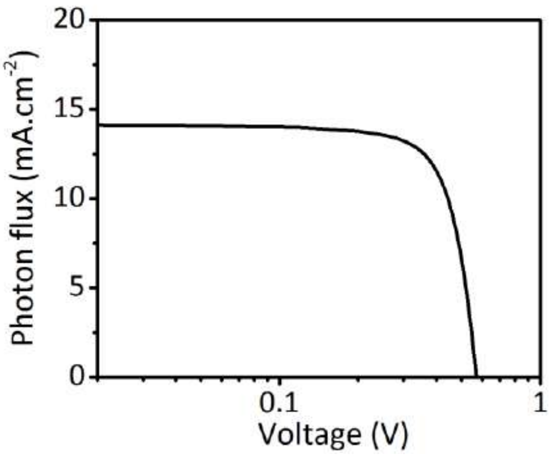

Figure G.1: The J-V curve of the organic solar cells under the direct illumination from blue LED with the output power of 100 mW.cm^{-2}.

G.5 The blue LED spectrum used for optical efficiency experiments

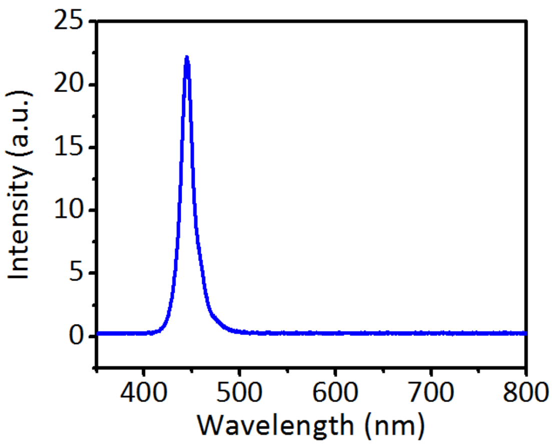

Figure G.2: The emission spectrum of the blue LED.

BIBLIOGRAPHY

[1] S. Pimputkar, J. S. Speck, S. P. DenBaars, and S. Nakamura, "Prospects for LED lighting," *Nature photonics,* vol. 3, pp. 180-182, 2009.

[2] M. R. Krames, O. B. Shchekin, R. Mueller-Mach, G. O. Mueller, L. Zhou, G. Harbers*, et al.*, "Status and future of high-power light-emitting diodes for solid-state lighting," *Journal of display technology,* vol. 3, pp. 160-175, 2007.

[3] J. Cho, J. H. Park, J. K. Kim, and E. F. Schubert, "White light-emitting diodes: History, progress, and future," *Laser & Photonics Reviews,* vol. 11, p. 1600147, 2017.

[4] V. Fernández-Luna, P. B. Coto, and R. D. Costa, "When Fluorescent Proteins Meet White Light-Emitting Diodes," *Angewandte Chemie International Edition,* vol. 57, pp. 8826-8836, 2018.

[5] M. M. Krause, J. Mooney, and P. Kambhampati, "Chemical and thermodynamic control of the surface of semiconductor nanocrystals for designer white light emitters," *ACS nano,* vol. 7, pp. 5922-5929, 2013.

[6] Y. Huang, G. Tan, F. Gou, M. C. Li, S. L. Lee, and S. T. Wu, "Prospects and challenges of mini-LED and micro-LED displays," *Journal of the Society for Information Display,* 2019.

[7] E. F. Schubert, *Light-emitting diodes*: E. Fred Schubert, 2018.

[8] Y. Narukawa, M. Sano, T. Sakamoto, T. Yamada, and T. Mukai, "Successful fabrication of white light emitting diodes by using extremely high external quantum efficiency blue chips," *physica status solidi (a),* vol. 205, pp. 1081-1085, 2008.

[9] C.-H. Liang, Y.-C. Chang, and Y.-S. Chang, "Synthesis and photoluminescence characteristics of color-tunable BaY 2 ZnO 5: Eu 3+ phosphors," *Applied Physics Letters,* vol. 93, p. 211902, 2008.

[10] K. Bando, K. Sakano, Y. Noguchi, and Y. Shimizu, "Development of high-bright and pure-white LED lamps," *Journal of Light & Visual Environment,* vol. 22, pp. 1_2-1_5, 1998.

[11] O. Graydon, "The new oil," *Nat. Photonics,* vol. 5, p. 1, 2011.

[12] F. Meinardi, F. Bruni, and S. Brovelli, "Luminescent solar concentrators for building-integrated photovoltaics," *Nature Reviews Materials,* vol. 2, p. 17072, 2017.

[13] F. Meinardi, A. Colombo, K. A. Velizhanin, R. Simonutti, M. Lorenzon, L. Beverina*, et al.*, "Large-area luminescent solar concentrators based on 'Stokes-shift-engineered'nanocrystals in a mass-polymerized PMMA matrix," *Nature Photonics,* vol. 8, p. 392, 2014.

[14] F. Meinardi, S. Ehrenberg, L. Dhamo, F. Carulli, M. Mauri, F. Bruni*, et al.*, "Highly efficient luminescent solar concentrators based on earth-abundant indirect-bandgap silicon quantum dots," *Nature Photonics,* vol. 11, p. nphoton. 2017.5, 2017.

[15] K. Wu, H. Li, and V. I. Klimov, "Tandem luminescent solar concentrators based on engineered quantum dots," *Nature Photonics,* vol. 12, p. 105, 2018.

[16] H. Liang, Z. Zheng, Z. Li, J. Xu, B. Chen, H. Zhao*, et al.*, "Fabrication and amplification of Rhodamine B-doped step-index polymer optical fiber," *Journal of applied polymer science,* vol. 93, pp. 681-685, 2004.

[17] S. Sadeghi, R. Melikov, H. Bahmani Jalali, O. Karatum, S. Srivastava, D. Conkar*, et al.*, "Ecofriendly and Efficient Luminescent Solar Concentrators Based on Fluorescent Proteins," *ACS applied materials & interfaces,* 2019.

[18] J. Graffion, X. Cattoën, M. Wong Chi Man, V. R. Fernandes, P. S. André, R. A. Ferreira*, et al.*, "Modulating the photoluminescence of bridged silsesquioxanes incorporating Eu3+-complexed n, n′-diureido-2, 2′-bipyridine isomers: application for luminescent solar concentrators," *Chemistry of Materials,* vol. 23, pp. 4773-4782, 2011.

[19] M. Wei, F. P. G. de Arquer, G. Walters, Z. Yang, L. N. Quan, Y. Kim*, et al.*, "Ultrafast narrowband exciton routing within layered perovskite nanoplatelets enables low-loss luminescent solar concentrators," *Nature Energy,* vol. 4, pp. 197-205, 2019.

[20] M. A. Hines and P. Guyot-Sionnest, "Synthesis and characterization of strongly luminescing ZnS-capped CdSe nanocrystals," *The Journal of Physical Chemistry,* vol. 100, pp. 468-471, 1996.

[21] B. O. Dabbousi, J. Rodriguez-Viejo, F. V. Mikulec, J. R. Heine, H. Mattoussi, R. Ober*, et al.*, "(CdSe) ZnS core– shell quantum dots: synthesis and characterization of a size series of highly luminescent nanocrystallites," *The Journal of Physical Chemistry B,* vol. 101, pp. 9463-9475, 1997.

[22] X. Peng, M. C. Schlamp, A. V. Kadavanich, and A. P. Alivisatos, "Epitaxial growth of highly luminescent CdSe/CdS core/shell nanocrystals with photostability and electronic accessibility," *Journal of the American Chemical Society,* vol. 119, pp. 7019-7029, 1997.

[23] J. S. Steckel, J. P. Zimmer, S. Coe-Sullivan, N. E. Stott, V. Bulović, and M. G. Bawendi, "Blue luminescence from (CdS) ZnS core–shell nanocrystals," *Angewandte Chemie International Edition,* vol. 43, pp. 2154-2158, 2004.

[24] J. S. Steckel, P. Snee, S. Coe-Sullivan, J. P. Zimmer, J. E. Halpert, P. Anikeeva*, et al.*, "Color-Saturated Green-Emitting QD-LEDs," *Angewandte Chemie International Edition,* vol. 45, pp. 5796-5799, 2006.

[25] E. Jang, S. Jun, H. Jang, J. Lim, B. Kim, and Y. Kim, "White-light-emitting diodes with quantum dot color converters for display backlights," *Advanced materials,* vol. 22, pp. 3076-3080, 2010.

[26] H. Zhang, S. Chen, and X. W. Sun, "Efficient Red/Green/Blue Tandem Quantum-Dot Light-Emitting Diodes with External Quantum Efficiency Exceeding 21%," *ACS nano,* 2017.

[27] R. Rossetti, S. Nakahara, and L. E. Brus, "Quantum size effects in the redox potentials, resonance Raman spectra, and electronic spectra of CdS crystallites in aqueous solution," *The Journal of Chemical Physics,* vol. 79, pp. 1086-1088, 1983.

[28] H. Li, K. Wu, J. Lim, H.-J. Song, and V. I. Klimov, "Doctor-blade deposition of quantum dots onto standard window glass for low-loss large-area luminescent solar concentrators," *Nature Energy,* vol. 1, p. 16157, 2016.

[29] S. Sadeghi, H. Bahmani Jalali, R. Melikov, B. Ganesh Kumar, M. Mohammadi Aria, C. W. Ow-Yang*, et al.*, "Stokes-shift-engineered Indium Phosphide Quantum Dots for Efficient Luminescent Solar Concentrators," *ACS applied materials & interfaces,* 2018.

[30] L. Zhuo, B. Sun, C.-L. Zhang, A. Fine, S.-Y. Chiu, and A. Messing, "Live astrocytes visualized by green fluorescent protein in transgenic mice," *Developmental biology,* vol. 187, pp. 36-42, 1997.

[31] M. C. Gather and S. H. Yun, "Lasing from Escherichia coli bacteria genetically programmed to express green fluorescent protein," *Optics letters,* vol. 36, pp. 3299-3301, 2011.

[32] M. D. Weber, L. Niklaus, M. Pröschel, P. B. Coto, U. Sonnewald, and R. D. Costa, "Bioinspired Hybrid White Light-Emitting Diodes," *Advanced Materials,* vol. 27, pp. 5493-5498, 2015.

[33] D. A. Press, R. Melikov, D. Conkar, E. N. Firat-Karalar, and S. Nizamoglu, "Fluorescent protein integrated white LEDs for displays," *Nanotechnology,* vol. 27, p. 45LT01, 2016.

[34] A. C. Berends and C. de Mello Donega, "Ultrathin one-and two-dimensional colloidal semiconductor nanocrystals: Pushing quantum confinement to the limit," *The Journal of Physical Chemistry Letters,* vol. 8, pp. 4077-4090, 2017.

[35] C.-Y. Han, H. Yang, C.-Y. Han, and H. Yang, "Development of colloidal quantum dots for electrically driven light-emitting devices," *Journal of the Korean*

Ceramic Society, vol. 54, pp. 449-469, 2017.
[36] J. Chang and E. R. Waclawik, "Colloidal semiconductor nanocrystals: controlled synthesis and surface chemistry in organic media," *RSC Advances,* vol. 4, pp. 23505-23527, 2014.
[37] Y. Zhou, H. Zhao, D. Ma, and F. Rosei, "Harnessing the properties of colloidal quantum dots in luminescent solar concentrators," *Chemical Society Reviews,* vol. 47, pp. 5866-5890, 2018.
[38] A. Chilvery, S. Das, P. Guggilla, C. Brantley, and A. Sunda-Meya, "A perspective on the recent progress in solution-processed methods for highly efficient perovskite solar cells," *Science and Technology of advanced MaTerialS,* vol. 17, pp. 650-658, 2016.
[39] B. P. Singh, S.-Y. Lin, H.-C. Wang, A.-C. Tang, H.-C. Tong, C.-Y. Chen*, et al.*, "Inorganic red perovskite quantum dot integrated blue chip: a promising candidate for high color-rendering in w-LEDs," *RSC advances,* vol. 6, pp. 79410-79414, 2016.
[40] Y.-H. Won, O. Cho, T. Kim, D.-Y. Chung, T. Kim, H. Chung*, et al.*, "Highly efficient and stable InP/ZnSe/ZnS quantum dot light-emitting diodes," *Nature,* vol. 575, pp. 634-638, 2019.
[41] C. J. Murphy, T. K. Sau, A. M. Gole, C. J. Orendorff, J. Gao, L. Gou*, et al.*, "Anisotropic metal nanoparticles: synthesis, assembly, and optical applications," ed: ACS Publications, 2005.
[42] R. Helmes, M. Sindel, L. Borda, and J. Von Delft, "Absorption and emission in quantum dots: Fermi surface effects of Anderson excitons," *Physical Review B,* vol. 72, p. 125301, 2005.
[43] Y. Zhang and A. Clapp, "Overview of stabilizing ligands for biocompatible quantum dot nanocrystals," *Sensors,* vol. 11, pp. 11036-11055, 2011.
[44] D. A. Hanifi, N. D. Bronstein, B. A. Koscher, Z. Nett, J. K. Swabeck, K. Takano*, et al.*, "Redefining near-unity luminescence in quantum dots with photothermal threshold quantum yield," *Science,* vol. 363, pp. 1199-1202, 2019.
[45] Y. Shirasaki, G. J. Supran, M. G. Bawendi, and V. Bulović, "Emergence of colloidal quantum-dot light-emitting technologies," *Nature Photonics,* vol. 7, p. 13, 12/27/online 2012.
[46] W. G. van Sark, P. L. Frederix, A. A. Bol, H. C. Gerritsen, and A. Meijerink, "Blueing, bleaching, and blinking of single CdSe/ZnS quantum dots," *ChemPhysChem,* vol. 3, pp. 871-879, 2002.
[47] W. M. Girma, M. Z. Fahmi, A. Permadi, M. A. Abate, and J.-Y. Chang, "Synthetic strategies and biomedical applications of I–III–VI ternary quantum dots," *Journal of Materials Chemistry B,* vol. 5, pp. 6193-6216, 2017.
[48] S. Pimputkar, J. S. Speck, S. P. DenBaars, and S. Nakamura, "Prospects for LED lighting," *Nature photonics,* vol. 3, p. 180, 2009.
[49] "http://www.nobelprize.org/nobel_prizes/physics/laureates/2014/."
[50] E. F. Schubert, T. Gessmann, and J. K. Kim, *Light emitting diodes*: Wiley Online Library, 2005.
[51] S. Sadeghi, R. Melikov, H. B. Jalali, and S. Nizamoglu, "Ultraefficient Green LEDs Using Quantum Dots in Liquid Matrix," *IEEE Transactions on Electron Devices,* vol. 66, pp. 4784-4789, 2019.
[52] Y. Shirasaki, G. J. Supran, M. G. Bawendi, and V. Bulović, "Emergence of colloidal quantum-dot light-emitting technologies," *Nature Photonics,* vol. 7, pp. 13-23, 2013.
[53] S. Sadeghi, B. G. Kumar, R. Melikov, M. M. Aria, H. B. Jalali, and S. Nizamoglu, "Quantum dot white LEDs with high luminous efficiency," *Optica,* vol. 5, pp. 793-802, 2018.
[54] V. L. Colvin, M. C. Schlamp, and A. P. Alivisatos, "Light-emitting diodes made from cadmium selenide nanocrystals and a semiconducting polymer," *Nature,* vol. 370, pp. 354-357, 1994.
[55] Y. Shirasaki, G. J. Supran, M. G. Bawendi, and V. Bulović, "Emergence of colloidal

quantum-dot light-emitting technologies," *Nature photonics,* vol. 7, p. 13, 2013.
[56] J. Látal, P. Koudelka, V. Vašinek, F. Dostál, and K. Sokanský, "Possible use of power LEDs for lighting and communication," 2011.
[57] J. Y. Tsao, "Light emitting diodes (LEDs) for general illumination," *Optoelectronics Industry Development Association, Washington DC,* pp. 289-290, 2002.
[58] A. Kshirsagar, S. Pickering, J. Xu, and J. Ruzyllo, "Light emitting diodes formed using mist deposition of colloidal solution of CdSe nanocrystalline quantum dots," *ECS Transactions,* vol. 35, pp. 71-77, 2011.
[59] O. Shimomura, "Discovery of green fluorescent protein (GFP)(Nobel Lecture)," *Angewandte Chemie International Edition,* vol. 48, pp. 5590-5602, 2009.
[60] O. Shimomura, F. H. Johnson, and Y. Saiga, "Extraction, purification and properties of aequorin, a bioluminescent protein from the luminous hydromedusan, Aequorea," *Journal of cellular and comparative physiology,* vol. 59, pp. 223-239, 1962.
[61] V. Sample, R. H. Newman, and J. Zhang, "The structure and function of fluorescent proteins," *Chemical Society Reviews,* vol. 38, pp. 2852-2864, 2009.
[62] C. F. Aguiño, M. Lang, V. n. Fernández-Luna, M. Pröschel, U. Sonnewald, P. B. Coto*, et al.*, "Single-Component Biohybrid Light-Emitting Diodes Using a White-Emitting Fused Protein," *ACS Omega,* vol. 3, pp. 15829-15836, 2018.
[63] S. Sadeghi, R. Melikov, D. Conkar, E. N. Firat-Karalar, and S. Nizamoglu, "Ultra-Efficient and High-Quality White Light-Emitting Devices using Fluorescent Proteins in Aqueous Medium," *Advanced Materials Technologies,* p. 2000061, 2020.
[64] M. M. Nolasco, P. M. Vaz, V. T. Freitas, P. P. Lima, P. S. André, R. A. Ferreira*, et al.*, "Engineering highly efficient Eu (III)-based tri-ureasil hybrids toward luminescent solar concentrators," *Journal of Materials Chemistry A,* vol. 1, pp. 7339-7350, 2013.
[65] Z. Li, A. Johnston, M. Wei, M. I. Saidaminov, J. M. de Pina, X. Zheng*, et al.*, "Solvent-Solute Coordination Engineering for Efficient Perovskite Luminescent Solar Concentrators," *Joule,* 2020.
[66] C. R. Kagan, E. Lifshitz, E. H. Sargent, and D. V. Talapin, "Building devices from colloidal quantum dots," *Science,* vol. 353, p. aac5523, 2016.
[67] H. Huang, A. S. Susha, S. V. Kershaw, T. F. Hung, and A. L. Rogach, "Control of emission color of high quantum yield CH3NH3PbBr3 perovskite quantum dots by precipitation temperature," *Advanced science,* vol. 2, p. 1500194, 2015.
[68] M. Grabolle, M. Spieles, V. Lesnyak, N. Gaponik, A. Eychmüller, and U. Resch-Genger, "Determination of the fluorescence quantum yield of quantum dots: suitable procedures and achievable uncertainties," *Analytical chemistry,* vol. 81, pp. 6285-6294, 2009.
[69] H. Bahmani Jalali, S. Sadeghi, M. Sahin, H. Ozturk, C. W. Ow-Yang, and S. Nizamoglu, "Colloidal aluminum antimonide quantum dots," *Chemistry of Materials,* vol. 31, pp. 4743-4747, 2019.
[70] M. Sharma, K. Gungor, A. Yeltik, M. Olutas, B. Guzelturk, Y. Kelestemur*, et al.*, "Near-Unity Emitting Copper-Doped Colloidal Semiconductor Quantum Wells for Luminescent Solar Concentrators," *Advanced Materials,* vol. 29, p. 1700821, 2017.
[71] M. D. Regulacio and M.-Y. Han, "Composition-tunable alloyed semiconductor nanocrystals," *Accounts of chemical research,* vol. 43, pp. 621-630, 2010.
[72] H. Zhao, H. Liang, F. o. Vidal, F. Rosei, A. Vomiero, and D. Ma, "Size dependence of temperature-related optical properties of PbS and PbS/CdS core/shell quantum dots," *The Journal of Physical Chemistry C,* vol. 118, pp. 20585-20593, 2014.
[73] X. Zheng, J. Troughton, N. Gasparini, Y. Lin, M. Wei, Y. Hou*, et al.*, "Quantum Dots Supply Bulk-and Surface-Passivation Agents for Efficient and Stable

Perovskite Solar Cells," *Joule,* vol. 3, pp. 1963-1976, 2019.
[74] B. H. Kim, S. Nam, N. Oh, S.-Y. Cho, K. J. Yu, C. H. Lee*, et al.*, "Multilayer transfer printing for pixelated, multicolor quantum dot light-emitting diodes," *ACS nano,* vol. 10, pp. 4920-4925, 2016.
[75] Z. Wang, W. Yang, and Y. Wang, "Self-Trapped Exciton and Large Stokes Shift in Pristine and Carbon-Coated Silicon Carbide Quantum Dots," *The Journal of Physical Chemistry C,* vol. 121, pp. 20031-20038, 2017.
[76] R. E. Bailey and S. Nie, "Alloyed semiconductor quantum dots: tuning the optical properties without changing the particle size," *Journal of the American Chemical Society,* vol. 125, pp. 7100-7106, 2003.
[77] S. Sadeghi, H. Bahmani Jalali, R. Melikov, B. Ganesh Kumar, M. Mohammadi Aria, C. W. Ow-Yang*, et al.*, "Stokes-shift-engineered indium phosphide quantum dots for efficient luminescent solar concentrators," *ACS applied materials & interfaces,* vol. 10, pp. 12975-12982, 2018.
[78] R. Viswanatha, S. Brovelli, A. Pandey, S. A. Crooker, and V. I. Klimov, "Copper-doped inverted core/shell nanocrystals with “permanent” optically active holes," *Nano letters,* vol. 11, pp. 4753-4758, 2011.
[79] A. Sahu, M. S. Kang, A. Kompch, C. Notthoff, A. W. Wills, D. Deng*, et al.*, "Electronic impurity doping in CdSe nanocrystals," *Nano letters,* vol. 12, pp. 2587-2594, 2012.
[80] C. S. Erickson, L. R. Bradshaw, S. McDowall, J. D. Gilbertson, D. R. Gamelin, and D. L. Patrick, "Zero-reabsorption doped-nanocrystal luminescent solar concentrators," *ACS nano,* vol. 8, pp. 3461-3467, 2014.
[81] R. Xie and X. Peng, "Synthesis of Cu-doped InP nanocrystals (d-dots) with ZnSe diffusion barrier as efficient and color-tunable NIR emitters," *Journal of the American Chemical Society,* vol. 131, pp. 10645-10651, 2009.
[82] R. Beaulac, P. I. Archer, and D. R. Gamelin, "Luminescence in colloidal Mn2+-doped semiconductor nanocrystals," *Journal of solid state chemistry,* vol. 181, pp. 1582-1589, 2008.
[83] C. R. Ronda, *Luminescence: from theory to applications*: John Wiley & Sons, 2007.
[84] J. D. Bryan and D. R. Gamelin, "Doped semiconductor nanocrystals: synthesis, characterization, physical properties, and applications," *Progress in inorganic chemistry,* vol. 54, pp. 47-126, 2005.
[85] Y. Zhou, H. Zhao, D. Ma, and F. Rosei, "Harnessing the properties of colloidal quantum dots in luminescent solar concentrators," *Chemical Society Reviews,* 2018.
[86] V. I. Klimov, T. A. Baker, J. Lim, K. A. Velizhanin, and H. McDaniel, "Quality factor of luminescent solar concentrators and practical concentration limits attainable with semiconductor quantum dots," *ACS Photonics,* vol. 3, pp. 1138-1148, 2016.
[87] A. Sennaroglu, U. Demirbas, S. Ozharar, and F. Yaman, "Accurate determination of saturation parameters for Cr 4+-doped solid-state saturable absorbers," *JOSA B,* vol. 23, pp. 241-249, 2006.
[88] C. Yang, D. Liu, and R. R. Lunt, "How to Accurately Report Transparent Luminescent Solar Concentrators," *Joule,* vol. 3, pp. 2871-2876, 2019.
[89] Q. Sun, Y. A. Wang, L. S. Li, D. Wang, T. Zhu, J. Xu*, et al.*, "Bright, multicoloured light-emitting diodes based on quantum dots," *Nature photonics,* vol. 1, pp. 717-722, 2007.
[90] D. Psaltis, S. R. Quake, and C. Yang, "Developing optofluidic technology through the fusion of microfluidics and optics," *Nature,* vol. 442, pp. 381-386, 2006.
[91] H. Schmidt and A. R. Hawkins, "The photonic integration of non-solid media using optofluidics," *Nature photonics,* vol. 5, pp. 598-604, 2011.
[92] Y. Yang, A. Liu, L. Lei, L. Chin, C. Ohl, Q. Wang*, et al.*, "A tunable 3D optofluidic waveguide dye laser via two centrifugal Dean flow streams," *Lab on a Chip,* vol. 11, pp. 3182-3187, 2011.

[93] Y. Yang, A. Liu, L. Chin, X. Zhang, D. Tsai, C. Lin, *et al.*, "Optofluidic waveguide as a transformation optics device for lightwave bending and manipulation," *Nature communications,* vol. 3, p. 651, 2012.

[94] R. M. Vazquez, G. Nava, M. Veglione, T. Yang, F. Bragheri, P. Minzioni, *et al.*, "An optofluidic constriction chip for monitoring metastatic potential and drug response of cancer cells," *Integrative Biology,* vol. 7, pp. 477-484, 2015.

[95] M. Schadt, H. Seiberle, and A. Schuster, "Optical patterning of multi-domain liquid-crystal displays with wide viewing angles," *Nature,* vol. 381, pp. 212-215, 1996.

[96] F. P. Schäfer, *Dye lasers* vol. 1: Springer Science & Business Media, 2013.

[97] C. K. Chan, H. Peng, G. Liu, K. McIlwrath, X. F. Zhang, R. A. Huggins, *et al.*, "High-performance lithium battery anodes using silicon nanowires," *Nature nanotechnology,* vol. 3, pp. 31-35, 2008.

[98] D. B. Wolfe, R. S. Conroy, P. Garstecki, B. T. Mayers, M. A. Fischbach, K. E. Paul, *et al.*, "Dynamic control of liquid-core/liquid-cladding optical waveguides," *Proceedings of the National Academy of Sciences of the United States of America,* vol. 101, pp. 12434-12438, August 24, 2004 2004.

[99] R. Melikov, D. A. Press, B. G. Kumar, I. B. Dogru, S. Sadeghi, M. Chirea, *et al.*, "Silk-hydrogel Lenses for Light-emitting Diodes," *Scientific Reports,* vol. 7, p. 7258, 2017/08/03 2017.

[100] C.-W. Sher, C.-H. Lin, H.-Y. Lin, C.-C. Lin, C.-H. Huang, K.-J. Chen, *et al.*, "A high quality liquid-type quantum dot white light-emitting diode," *Nanoscale,* vol. 8, pp. 1117-1122, 2016.

[101] S. Y. Lee, K.-I. Park, C. Huh, M. Koo, H. G. Yoo, S. Kim, *et al.*, "Water-resistant flexible GaN LED on a liquid crystal polymer substrate for implantable biomedical applications," *Nano Energy,* vol. 1, pp. 145-151, 2012.

[102] M. Lu, X. Bai, Y. Lin, C. Ji, H. Wu, C. Ruan, *et al.*, "Liquid-type AgInS 2/ZnS quantum dot-based warm white light-emitting diodes," *Chemical Physics Letters,* vol. 661, pp. 228-233, 2016.

[103] Y. Wang, X. Bai, T. Wang, L. Yan, T. Zhang, Y. Zhang, *et al.*, "Efficient near-infrared light-emitting diodes based on liquid PbSe quantum dots," *Nanotechnology,* vol. 28, p. 215703, 2017.

[104] B. N. Pal, Y. Ghosh, S. Brovelli, R. Laocharoensuk, V. I. Klimov, J. A. Hollingsworth, *et al.*, "'Giant'CdSe/CdS core/shell nanocrystal quantum dots as efficient electroluminescent materials: strong influence of shell thickness on light-emitting diode performance," *Nano letters,* vol. 12, pp. 331-336, 2011.

[105] F. Meinardi, A. Colombo, K. A. Velizhanin, R. Simonutti, M. Lorenzon, L. Beverina, *et al.*, "Large-area luminescent solar concentrators based on/Stokes-shift-engineered/'nanocrystals in a mass-polymerized PMMA matrix," *Nature Photonics,* vol. 8, pp. 392-399, 2014.

[106] Y. Chen, J. Vela, H. Htoon, J. L. Casson, D. J. Werder, D. A. Bussian, *et al.*, "“Giant” multishell CdSe nanocrystal quantum dots with suppressed blinking," *Journal of the American Chemical Society,* vol. 130, pp. 5026-5027, 2008.

[107] T. A. Klar, T. Franzl, A. L. Rogach, and J. Feldmann, "Super-efficient exciton funneling in layer-by-layer semiconductor nanocrystal structures," *Advanced Materials,* vol. 17, pp. 769-773, 2005.

[108] S. Nizamoglu and H. V. Demir, "Resonant nonradiative energy transfer in CdSe/ZnS core/shell nanocrystal solids enhances hybrid white light emitting diodes," *Optics express,* vol. 16, pp. 13961-13968, 2008.

[109] H. M. Haverinen, R. A. Myllylä, and G. E. Jabbour, "Inkjet printing of light emitting quantum dots," *Applied Physics Letters,* vol. 94, p. 073108, 2009.

[110] J. Lim, S. Jun, E. Jang, H. Baik, H. Kim, and J. Cho, "Preparation of Highly Luminescent Nanocrystals and Their Application to Light-Emitting Diodes," *Advanced Materials,* vol. 19, pp. 1927-1932, 2007.

[111] S. Jun and E. Jang, "Interfused semiconductor nanocrystals: brilliant blue

photoluminescence and electroluminescence," *Chemical Communications,* pp. 4616-4618, 2005.

[112] C. Pu and X. Peng, "To battle surface traps on CdSe/CdS core/shell nanocrystals: shell isolation versus surface treatment," *Journal of the American Chemical Society,* vol. 138, pp. 8134-8142, 2016.

[113] R. Melikov, D. A. Press, B. Ganesh Kumar, S. Sadeghi, and S. Nizamoglu, "Unravelling radiative energy transfer in solid-state lighting," *Journal of Applied Physics,* vol. 123, p. 023103, 2018.

[114] Y. Narukawa, M. Ichikawa, D. Sanga, M. Sano, and T. Mukai, "White light emitting diodes with super-high luminous efficacy," *Journal of physics D: Applied physics,* vol. 43, p. 354002, 2010.

[115] J. C. McDonald and G. M. Whitesides, "Poly (dimethylsiloxane) as a material for fabricating microfluidic devices," *Accounts of chemical research,* vol. 35, pp. 491-499, 2002.

[116] L. Qian, Y. Zheng, J. Xue, and P. H. Holloway, "Stable and efficient quantum-dot light-emitting diodes based on solution-processed multilayer structures," *Nature photonics,* vol. 5, p. 543, 2011.

[117] C. Luk, L. Tang, W. Zhang, S. Yu, K. Teng, and S. Lau, "An efficient and stable fluorescent graphene quantum dot–agar composite as a converting material in white light emitting diodes," *Journal of Materials Chemistry,* vol. 22, pp. 22378-22381, 2012.

[118] H. Wang, K.-S. Lee, J.-H. Ryu, C.-H. Hong, and Y.-H. Cho, "White light emitting diodes realized by using an active packaging method with CdSe/ZnS quantum dots dispersed in photosensitive epoxy resins," *Nanotechnology,* vol. 19, p. 145202, 2008.

[119] V. Wood, M. J. Panzer, J. Chen, M. S. Bradley, J. E. Halpert, M. G. Bawendi, *et al.*, "Inkjet-printed quantum dot–polymer composites for full-color ac-driven displays," *Advanced Materials,* vol. 21, pp. 2151-2155, 2009.

[120] Y.-S. Su, C.-C. Hsiao, and S.-R. Chung, "CdSe white quantum dots-based white light-emitting diodes with high color rendering index," in *Fifteenth International Conference on Solid State Lighting and LED-based Illumination Systems*, 2016, p. 99540B.

[121] S. J. Yang, J. H. Oh, S. Kim, H. Yang, and Y. R. Do, "Realization of InP/ZnS quantum dots for green, amber and red down-converted LEDs and their color-tunable, four-package white LEDs," *Journal of Materials Chemistry C,* vol. 3, pp. 3582-3591, 2015.

[122] H.-Y. Lin, S.-W. Wang, C.-C. Lin, K.-J. Chen, H.-V. Han, Z.-Y. Tu*, et al.*, "Excellent color quality of white-light-emitting diodes by embedding quantum dots in polymers material," *IEEE Journal of Selected Topics in Quantum Electronics,* vol. 22, pp. 35-41, 2016.

[123] H. Shen, Q. Lin, H. Wang, L. Qian, Y. Yang, A. Titov*, et al.*, "Efficient and bright colloidal quantum dot light-emitting diodes via controlling the shell thickness of quantum dots," *ACS applied materials & interfaces,* vol. 5, pp. 12011-12016, 2013.

[124] K.-J. Chen, C.-C. Lin, H.-V. Han, C.-Y. Lee, S.-H. Chien, K.-Y. Wang*, et al.*, "Wide-range correlated color temperature light generation from resonant cavity hybrid quantum dot light-emitting diodes," *IEEE Journal of Selected Topics in Quantum Electronics,* vol. 21, pp. 23-29, 2015.

[125] Y.-K. Kim, K.-C. Choi, Y.-K. Baek, and P.-W. Shin, "Enhanced luminescence stability of quantum dot-based inorganic nanocomposite particles for white-light-emitting diodes," *Materials Letters,* vol. 124, pp. 129-132, 2014.

[126] P.-H. Chuang, C. C. Lin, and R.-S. Liu, "Emission-tunable CuInS2/ZnS quantum dots: structure, optical properties, and application in white light-emitting diodes with high color rendering index," *ACS applied materials & interfaces,* vol. 6, pp. 15379-15387, 2014.

[127] X. Yuan, R. Ma, W. Zhang, J. Hua, X. Meng, X. Zhong, *et al.*, "Dual emissive manganese and copper co-doped Zn–In–S quantum dots as a single color-converter for high color rendering white-light-emitting diodes," *ACS applied materials & interfaces,* vol. 7, pp. 8659-8666, 2015.

[128] S. H. Park, A. Hong, J.-H. Kim, H. Yang, K. Lee, and H. S. Jang, "Highly bright yellow-green-emitting CuInS2 colloidal quantum dots with core/shell/shell architecture for white light-emitting diodes," *ACS applied materials & interfaces,* vol. 7, pp. 6764-6771, 2015.

[129] B. Chen, H. Zhong, M. Wang, R. Liu, and B. Zou, "Integration of CuInS 2-based nanocrystals for high efficiency and high colour rendering white light-emitting diodes," *Nanoscale,* vol. 5, pp. 3514-3519, 2013.

[130] X. Yuan, J. Hua, R. Zeng, D. Zhu, W. Ji, P. Jing, *et al.*, "Efficient white light emitting diodes based on Cu-doped ZnInS/ZnS core/shell quantum dots," *Nanotechnology,* vol. 25, p. 435202, 2014.

[131] J. Ryckaert, A. Correia, M. D. Tessier, D. Dupont, Z. Hens, P. Hanselaer, *et al.*, "Selecting the optimal synthesis parameters of InP/CdxZn 1– x Se quantum dots for a hybrid remote phosphor white LED for general lighting applications," *Optics express,* vol. 25, pp. A1009-A1022, 2017.

[132] H. C. Yoon, H. Kang, S. Lee, J. H. Oh, H. Yang, and Y. R. Do, "Study of perovskite QD down-converted LEDs and six-color white LEDs for future displays with excellent color performance," *ACS applied materials & interfaces,* vol. 8, pp. 18189-18200, 2016.

[133] D. Shindell, G. Faluvegi, K. Seltzer, and C. Shindell, "Quantified, localized health benefits of accelerated carbon dioxide emissions reductions," *Nature climate change,* vol. 8, p. 291, 2018.

[134] K. K. Rigaud, A. de Sherbinin, B. Jones, J. Bergmann, V. Clement, K. Ober, *et al.*, *Groundswell: Preparing for internal climate migration*: World Bank, 2018.

[135] B. C. Zoeteman, H. R. Krikke, and J. Venselaar, "Handling WEEE waste flows: on the effectiveness of producer responsibility in a globalizing world," *The International Journal of Advanced Manufacturing Technology,* vol. 47, pp. 415-436, 2010.

[136] Y. Shimizu, K. Sakano, Y. Noguchi, and T. Moriguchi, "Light emitting device having a nitride compound semiconductor and a phosphor containing a garnet fluorescent material," ed: Google Patents, 1999.

[137] Z. Luo, Y. Chen, and S.-T. Wu, "Wide color gamut LCD with a quantum dot backlight," *Optics express,* vol. 21, pp. 26269-26284, 2013.

[138] T. G. Mack, L. Jethi, and P. Kambhampati, "Strategy for Exploiting Self-Trapped Excitons in Semiconductor Nanocrystals for White Light Generation," *ACS Photonics,* vol. 6, pp. 1118-1124, 2019.

[139] B. Guzelturk, P. L. H. Martinez, Q. Zhang, Q. Xiong, H. Sun, X. W. Sun, *et al.*, "Excitonics of semiconductor quantum dots and wires for lighting and displays," *Laser & Photonics Reviews,* vol. 8, pp. 73-93, 2014.

[140] B. Guzelturk, P. L. Hernandez-Martinez, V. K. Sharma, Y. Coskun, V. Ibrahimova, X. W. Sun, *et al.*, "Excitonically driven quantum dot light-emitting diodes: exLEDs," in *CLEO: 2013,* 2013, pp. 1-2.

[141] S. Sadeghi, S. K. Abkenar, C. W. Ow-Yang, and S. Nizamoglu, "Efficient White LEDs Using Liquid-state Magic-sized CdSe Quantum Dots," *Scientific reports,* vol. 9, p. 10061, 2019.

[142] S. Sadeghi, S. E. Mutcu, S. B. Srivastava, G. Aydindogan, S. Caynak, K. Karslı, *et al.*, "High quality quantum dots polymeric films as color converters for smart phone display technology," *Materials Research Express,* vol. 6, p. 035015, 2018.

[143] W.-S. Song and H. Yang, "Fabrication of white light-emitting diodes based on solvothermally synthesized copper indium sulfide quantum dots as color converters," *Applied Physics Letters,* vol. 100, p. 183104, 2012.

[144] Z. Zhang, D. Liu, D. Li, K. Huang, Y. Zhang, Z. Shi, *et al.*, "Dual emissive Cu: InP/ZnS/InP/ZnS nanocrystals: single-source “greener” emitters with flexibly

tunable emission from visible to near-infrared and their application in white light-emitting diodes," *Chemistry of Materials,* vol. 27, pp. 1405-1411, 2015.
[145] E. C. Agency, "Literature study on the uses and risks of nanomaterials as pigments in the European Union," *European Chemicals Agency,* September 2018 2018.
[146] Y. Cui, T. Song, J. Yu, Y. Yang, Z. Wang, and G. Qian, "Dye Encapsulated Metal-Organic Framework for Warm-White LED with High Color-Rendering Index," *Advanced Functional Materials,* vol. 25, pp. 4796-4802, 2015.
[147] Z. He, C. Zhang, Y. Dong, and S.-T. Wu, "Emerging Perovskite Nanocrystals-Enhanced Solid-State Lighting and Liquid-Crystal Displays," *Crystals,* vol. 9, p. 59, 2019.
[148] Z. He, C. Zhang, H. Chen, Y. Dong, and S.-T. Wu, "Perovskite Downconverters for Efficient, Excellent Color-Rendering, and Circadian Solid-State Lighting," *Nanomaterials,* vol. 9, p. 176, 2019.
[149] H. Huang, M. I. Bodnarchuk, S. V. Kershaw, M. V. Kovalenko, and A. L. Rogach, "Lead halide perovskite nanocrystals in the research spotlight: stability and defect tolerance," *ACS energy letters,* vol. 2, pp. 2071-2083, 2017.
[150] H. A. Richards, C.-T. Han, R. G. Hopkins, M. L. Failla, W. W. Ward, and C. N. Stewart Jr, "Safety assessment of recombinant green fluorescent protein orally administered to weaned rats," *The Journal of nutrition,* vol. 133, pp. 1909-1912, 2003.
[151] T. Erdem, S. Nizamoglu, X. W. Sun, and H. V. Demir, "A photometric investigation of ultra-efficient LEDs with high color rendering index and high luminous efficacy employing nanocrystal quantum dot luminophores," *Optics Express,* vol. 18, pp. 340-347, 2010.
[152] M. M. Bradford, "A rapid and sensitive method for the quantitation of microgram quantities of protein utilizing the principle of protein-dye binding," *Analytical biochemistry,* vol. 72, pp. 248-254, 1976.
[153] M. C. Gather and S. H. Yun, "Bio-optimized energy transfer in densely packed fluorescent protein enables near-maximal luminescence and solid-state lasers," *Nature Communications,* vol. 5, p. 5722, 12/08/online 2014.
[154] B. G. Kumar, S. Sadeghi, R. Melikov, M. M. Aria, H. B. Jalali, C. Ow-Yang, *et al.*, "Structural Control of InP/ZnS Core/Shell Quantum Dots Enables High-quality White LEDs," *Nanotechnology,* 2018.
[155] C.-W. Sher, C.-H. Lin, H.-Y. Lin, C.-C. Lin, C.-H. Huang, K.-J. Chen, *et al.*, "A high quality liquid-type quantum dot white light-emitting diode," *Nanoscale,* vol. 8, pp. 1117-1122, 2015.
[156] Z. Bai, W. Ji, D. Han, L. Chen, B. Chen, H. Shen, *et al.*, "Hydroxyl-terminated CuInS2 based quantum dots: toward efficient and bright light emitting diodes," *Chemistry of Materials,* vol. 28, pp. 1085-1091, 2016.
[157] C. Sun, Y. Zhang, K. Sun, C. Reckmeier, T. Zhang, X. Zhang, *et al.*, "Combination of carbon dot and polymer dot phosphors for white light-emitting diodes," *Nanoscale,* vol. 7, pp. 12045-12050, 2015.
[158] T. Xuan, X. Yang, S. Lou, J. Huang, Y. Liu, J. Yu, *et al.*, "Highly stable CsPbBr 3 quantum dots coated with alkyl phosphate for white light-emitting diodes," *Nanoscale,* vol. 9, pp. 15286-15290, 2017.
[159] W. Chen, X. Tang, Z. Zang, Y. Shi, Z. Yang, and J. Du, "Tunable dual emission in Mn2+-doped CsPbX3 (X= Cl, Br) quantum dots for high efficiency white light-emitting diodes," *Nanotechnology,* vol. 30, p. 075704, 2018.
[160] W.-S. Song and H. Yang, "Efficient white-light-emitting diodes fabricated from highly fluorescent copper indium sulfide core/shell quantum dots," *Chemistry of Materials,* vol. 24, pp. 1961-1967, 2012.
[161] C. Sun, Y. Zhang, C. Ruan, C. Yin, X. Wang, Y. Wang, *et al.*, "Efficient and stable white LEDs with silica-coated inorganic perovskite quantum dots," *Advanced Materials,* vol. 28, pp. 10088-10094, 2016.

[162] X. Wang, X. Yan, W. Li, and K. Sun, "Doped quantum dots for white-light-emitting diodes without reabsorption of multiphase phosphors," *Advanced Materials,* vol. 24, pp. 2742-2747, 2012.

[163] P. B. Tchounwou, C. G. Yedjou, A. K. Patlolla, and D. J. Sutton, "Heavy metal toxicity and the environment," in *Molecular, clinical and environmental toxicology,* ed: Springer, 2012, pp. 133-164.

[164] P. Pattison, J. Tsao, G. Brainard, and B. Bugbee, "LEDs for photons, physiology and food," *Nature,* vol. 563, pp. 493-500, 2018.

[165] Z. He, H. Chen, Y.-H. Lee, and S.-T. Wu, "Tuning the correlated color temperature of white light-emitting diodes resembling Planckian locus," *Optics express,* vol. 26, pp. A136-A143, 2018.

[166] J. Lee, J. Yang, S. G. Kwon, and T. Hyeon, "Nonclassical nucleation and growth of inorganic nanoparticles," *Nature Reviews Materials,* vol. 1, p. 16034, 2016.

[167] C. M. Evans, L. Guo, J. J. Peterson, S. Maccagnano-Zacher, and T. D. Krauss, "Ultrabright PbSe magic-sized clusters," *Nano letters,* vol. 8, pp. 2896-2899, 2008.

[168] A. Kasuya, R. Sivamohan, Y. A. Barnakov, I. M. Dmitruk, T. Nirasawa, V. R. Romanyuk, *et al.*, "Ultra-stable nanoparticles of CdSe revealed from mass spectrometry," *Nature materials,* vol. 3, p. 99, 2004.

[169] S. M. Harrell, J. R. McBride, and S. J. Rosenthal, "Synthesis of ultrasmall and magic-sized CdSe nanocrystals," *Chemistry of Materials,* vol. 25, pp. 1199-1210, 2013.

[170] Z. A. Peng and X. Peng, "Nearly monodisperse and shape-controlled CdSe nanocrystals via alternative routes: nucleation and growth," *Journal of the American Chemical Society,* vol. 124, pp. 3343-3353, 2002.

[171] Y.-H. Liu, F. Wang, Y. Wang, P. C. Gibbons, and W. E. Buhro, "Lamellar assembly of cadmium selenide nanoclusters into quantum belts," *Journal of the American Chemical Society,* vol. 133, pp. 17005-17013, 2011.

[172] Z. Li and X. Peng, "Size/shape-controlled synthesis of colloidal CdSe quantum disks: ligand and temperature effects," *Journal of the American Chemical Society,* vol. 133, pp. 6578-6586, 2011.

[173] S. Ithurria, G. Bousquet, and B. Dubertret, "Continuous transition from 3D to 1D confinement observed during the formation of CdSe nanoplatelets," *Journal of the American Chemical Society,* vol. 133, pp. 3070-3077, 2011.

[174] B. M. Cossairt and J. S. Owen, "CdSe clusters: At the interface of small molecules and quantum dots," *Chemistry of Materials,* vol. 23, pp. 3114-3119, 2011.

[175] Y. Wang, Y. Zhang, F. Wang, D. E. Giblin, J. Hoy, H. W. Rohrs*, et al.*, "The magic-size nanocluster (CdSe) 34 as a low-temperature nucleant for cadmium selenide nanocrystals; Room-temperature growth of crystalline quantum platelets," *Chemistry of Materials,* vol. 26, pp. 2233-2243, 2014.

[176] C. Giansante and I. Infante, "Surface Traps in Colloidal Quantum Dots: A Combined Experimental and Theoretical Perspective," *The journal of physical chemistry letters,* vol. 8, pp. 5209-5215, 2017.

[177] M. Yuan, M. Liu, and E. H. Sargent, "Colloidal quantum dot solids for solution-processed solar cells," *Nature Energy,* vol. 1, p. 16016, 02/29/online 2016.

[178] A. H. Ip, S. M. Thon, S. Hoogland, O. Voznyy, D. Zhitomirsky, R. Debnath*, et al.*, "Hybrid passivated colloidal quantum dot solids," *Nature nanotechnology,* vol. 7, pp. 577-582, 2012.

[179] E. Lifshitz, M. Brumer, A. Kigel, A. Sashchiuk, M. Bashouti, M. Sirota*, et al.*, "Air-Stable PbSe/PbS and PbSe/PbSe x S1-x Core– Shell Nanocrystal Quantum Dots and Their Applications," *The Journal of physical chemistry B,* vol. 110, pp. 25356-25365, 2006.

[180] M. J. Bowers, J. R. McBride, and S. J. Rosenthal, "White-light emission from magic-sized cadmium selenide nanocrystals," *Journal of the American Chemical Society,* vol. 127, pp. 15378-15379, 2005.

[181] L. Su, X. Zhang, Y. Zhang, and A. L. Rogach, "Recent progress in quantum dot based white light-emitting devices," *Topics in Current Chemistry,* vol. 374, p. 42, 2016.

[182] S. Nizamoglu, E. Mutlugun, O. Akyuz, N. K. Perkgoz, H. V. Demir, L. Liebscher*, et al.*, "White emitting CdS quantum dot nanoluminophores hybridized on near-ultraviolet LEDs for high-quality white light generation and tuning," *New Journal of Physics,* vol. 10, p. 023026, 2008.

[183] S. Nizamoglu, T. Ozel, E. Sari, and H. Demir, "White light generation using CdSe/ZnS core–shell nanocrystals hybridized with InGaN/GaN light emitting diodes," *Nanotechnology,* vol. 18, p. 065709, 2007.

[184] J. C. Newton, K. Ramasamy, M. Mandal, G. K. Joshi, A. Kumbhar, and R. Sardar, "Low-temperature synthesis of magic-sized CdSe nanoclusters: influence of ligands on nanocluster growth and photophysical properties," *The Journal of Physical Chemistry C,* vol. 116, pp. 4380-4389, 2012.

[185] M. A. Schreuder, K. Xiao, I. N. Ivanov, S. M. Weiss, and S. J. Rosenthal, "White light-emitting diodes based on ultrasmall CdSe nanocrystal electroluminescence," *Nano letters,* vol. 10, pp. 573-576, 2010.

[186] T. E. Rosson, S. M. Claiborne, J. R. McBride, B. S. Stratton, and S. J. Rosenthal, "Bright white light emission from ultrasmall cadmium selenide nanocrystals," *Journal of the American Chemical Society,* vol. 134, pp. 8006-8009, 2012.

[187] S. Sapra, S. Mayilo, T. A. Klar, A. L. Rogach, and J. Feldmann, "Bright White-Light Emission from Semiconductor Nanocrystals: by Chance and by Design," *Advanced Materials,* vol. 19, pp. 569-572, 2007.

[188] H. S. Chen, S. J. J. Wang, C. J. Lo, and J. Y. Chi, "White-light emission from organics-capped ZnSe quantum dots and application in white-light-emitting diodes," *Applied Physics Letters,* vol. 86, p. 131905, 2005.

[189] V. K. Sharma, B. Guzelturk, T. Erdem, Y. Kelestemur, and H. V. Demir, "Tunable white-light-emitting Mn-doped ZnSe nanocrystals," *ACS applied materials & interfaces,* vol. 6, pp. 3654-3660, 2014.

[190] E. R. Dohner, A. Jaffe, L. R. Bradshaw, and H. I. Karunadasa, "Intrinsic white-light emission from layered hybrid perovskites," *Journal of the American Chemical Society,* vol. 136, pp. 13154-13157, 2014.

[191] J. Yang, F. Muckel, W. Baek, R. Fainblat, H. Chang, G. Bacher*, et al.*, "Chemical Synthesis, Doping, and Transformation of Magic-Sized Semiconductor Alloy Nanoclusters," *Journal of the American Chemical Society,* vol. 139, pp. 6761-6770, 2017.

[192] D.-Y. Jo, D. Kim, J.-H. Kim, H. Chae, H. J. Seo, Y. R. Do*, et al.*, "Tunable white fluorescent copper gallium sulfide quantum dots enabled by Mn doping," *ACS applied materials & interfaces,* vol. 8, pp. 12291-12297, 2016.

[193] M. C. Gather, A. Köhnen, and K. Meerholz, "White organic light-emitting diodes," *Advanced Materials,* vol. 23, pp. 233-248, 2011.

[194] M. K. Choi, J. Yang, D. C. Kim, Z. Dai, J. Kim, H. Seung*, et al.*, "Extremely Vivid, Highly Transparent, and Ultrathin Quantum Dot Light-Emitting Diodes," *Advanced Materials,* vol. 30, 2018.

[195] S. Dai, C.-B. Siao, S.-R. Chung, K.-W. Wang, and X.-Q. Pan, "Developed One-pot Synthesis of Dual-color CdSe Quantum Dots for White Light-emitting Diode Application," *Journal of Materials Chemistry C,* 2018.

[196] Y. Jiang, S.-Y. Cho, and M. Shim, "Light-Emitting Diodes of Colloidal Quantum Dots and Nanorod Heterostructures for Future Emissive Displays," *Journal of Materials Chemistry C,* 2018.

[197] P. Rastogi, F. Palazon, M. Prato, F. Di Stasio, and R. Krahne, "Enhancing the Performance of CdSe/CdS Dot-in-Rod Light Emitting Diodes via Surface Ligand Modification," *ACS Applied Materials & Interfaces,* 2018.

[198] B. Xie, Y. Cheng, J. Hao, X. Yu, W. Shu, K. Wang*, et al.*, "White Light-Emitting Diodes With Enhanced Efficiency and Thermal Stability Optimized by Quantum

Dots-Silica Nanoparticles," *IEEE Transactions on Electron Devices,* vol. 65, pp. 605-609, 2018.

[199] L. Qu and X. Peng, "Control of photoluminescence properties of CdSe nanocrystals in growth," *Journal of the American Chemical Society,* vol. 124, pp. 2049-2055, 2002.

[200] H. Bahmani Jalali, R. Melikov, S. Sadeghi, and S. Nizamoglu, "Excitonic Energy Transfer within InP/ZnS Quantum Dot Langmuir–Blodgett Assemblies," *The Journal of Physical Chemistry C,* vol. 122, pp. 11616-11622, 2018.

[201] H. Bahmani Jalali, M. Mohammadi Aria, U. M. Dikbas, S. Sadeghi, B. Ganesh Kumar, M. Sahin*, et al.*, "Effective Neural Photostimulation Using Indium-Based Type-II Quantum Dots," *ACS nano,* vol. 12, pp. 8104-8114, 2018.

[202] M. Abdellah, K. J. Karki, N. Lenngren, K. Zheng, T. r. Pascher, A. Yartsev*, et al.*, "Ultra long-lived radiative trap states in CdSe quantum dots," *The Journal of Physical Chemistry C,* vol. 118, pp. 21682-21686, 2014.

[203] W. G. Van Sark, P. L. Frederix, D. J. Van den Heuvel, H. C. Gerritsen, A. A. Bol, J. N. Van Lingen*, et al.*, "Photooxidation and photobleaching of single CdSe/ZnS quantum dots probed by room-temperature time-resolved spectroscopy," *The Journal of Physical Chemistry B,* vol. 105, pp. 8281-8284, 2001.

[204] J. Owen and L. Brus, "Chemical synthesis and luminescence applications of colloidal semiconductor quantum dots," *Journal of the American Chemical Society,* vol. 139, pp. 10939-10943, 2017.

[205] Y. Yin and D. Talapin, "The chemistry of functional nanomaterials," *Chemical Society Reviews,* vol. 42, pp. 2484-2487, 2013.

[206] X. Dai, Z. Zhang, Y. Jin, Y. Niu, H. Cao, X. Liang*, et al.*, "Solution-processed, high-performance light-emitting diodes based on quantum dots," *Nature,* vol. 515, pp. 96-99, 2014.

[207] H. Zhang, X. Sun, and S. Chen, "Over 100 cd A− 1 Efficient Quantum Dot Light-Emitting Diodes with Inverted Tandem Structure," *Advanced Functional Materials,* vol. 27, p. 1700610, 2017.

[208] B. S. Mashford, M. Stevenson, Z. Popovic, C. Hamilton, Z. Zhou, C. Breen*, et al.*, "High-efficiency quantum-dot light-emitting devices with enhanced charge injection," *Nature photonics,* vol. 7, p. 407, 2013.

[209] H. Peng, Y. Jiang, and S. Chen, "Efficient vacuum-free-processed quantum dot light-emitting diodes with printable liquid metal cathodes," *Nanoscale,* vol. 8, pp. 17765-17773, 2016.

[210] H. Zhang, S. Chen, and X. W. Sun, "Efficient red/green/blue tandem quantum-dot light-emitting diodes with external quantum efficiency exceeding 21%," *ACS nano,* vol. 12, pp. 697-704, 2017.

[211] Y. Yang, Y. Zheng, W. Cao, A. Titov, J. Hyvonen, J. R. Manders*, et al.*, "High-efficiency light-emitting devices based on quantum dots with tailored nanostructures," *Nature Photonics,* vol. 9, p. 259, 2015.

[212] M. Olutas, B. Guzelturk, Y. Kelestemur, A. Yeltik, S. Delikanli, and H. V. Demir, "Lateral size-dependent spontaneous and stimulated emission properties in colloidal CdSe nanoplatelets," *Acs Nano,* vol. 9, pp. 5041-5050, 2015.

[213] S. Nizamoglu, E. Mutlugun, T. Özel, H. V. Demir, S. Sapra, N. Gaponik*, et al.*, "Dual-color emitting quantum-dot-quantum-well CdSe-ZnS heteronanocrystals hybridized on In Ga N∕ Ga N light emitting diodes for high-quality white light generation," *Applied Physics Letters,* vol. 92, p. 113110, 2008.

[214] S. Nizamoglu, E. Sari, J.-H. Baek, I.-H. Lee, and H. V. Demir, "Green/yellow solid-state lighting via radiative and nonradiative energy transfer involving colloidal semiconductor nanocrystals," *IEEE Journal of Selected Topics in Quantum Electronics,* vol. 15, pp. 1163-1170, 2009.

[215] C. Li, Z. Zang, W. Chen, Z. Hu, X. Tang, W. Hu*, et al.*, "Highly pure green light emission of perovskite CsPbBr 3 quantum dots and their application for green light-emitting diodes," *Optics express,* vol. 24, pp. 15071-15078, 2016.

[216] Y. Kang, Z. Song, X. Jiang, X. Yin, L. Fang, J. Gao, *et al.*, "Quantum dots for wide color gamut displays from photoluminescence to electroluminescence," *Nanoscale research letters,* vol. 12, p. 154, 2017.
[217] C.-H. Lin, Y.-M. Pai, C.-F. Lee, A. Verma, H.-Y. Lin, C.-C. Tu, *et al.*, "Liquid Type Nontoxic Photoluminescent Nanomaterials for High Color Quality White-Light-Emitting Diode," *Nanoscale research letters,* vol. 13, p. 411, 2018.
[218] H. Wang, Y. Mou, Y. Peng, J. Liu, R. Liang, M. Chen, *et al.*, "White Light-Emitting Diodes with High Color Quality Fabricated Using Phosphor-in-Glass Integrated with Liquid-Type Quantum Dot," *IEEE Electron Device Letters,* 2019.
[219] J.-S. Li, Y. Tang, Z.-T. Li, L.-S. Rao, X.-R. Ding, and B.-H. Yu, "High efficiency solid–liquid hybrid-state quantum dot light-emitting diodes," *Photonics Research,* vol. 6, pp. 1107-1115, 2018.
[220] C.-C. LIN, Y.-C. WU, S. SHARMA, T. WU, S. CHUNG, and H.-C. KUO, "Hybrid-typed white LEDs based on inorganic halide perovskite QDs–a candidate for wide color gamut display backlights," 2018.
[221] W. K. Bae, J. Kwak, J. W. Park, K. Char, C. Lee, and S. Lee, "Highly Efficient Green-Light-Emitting Diodes Based on CdSe@ ZnS Quantum Dots with a Chemical-Composition Gradient," *Advanced Materials,* vol. 21, pp. 1690-1694, 2009.
[222] S. Tolbert and A. Alivisatos, "Size dependence of a first order solid-solid phase transition: the wurtzite to rock salt transformation in CdSe nanocrystals," *Science,* vol. 265, pp. 373-376, 1994.
[223] Y. Jiang, Y. Li, Y. Li, Z. Deng, T. Lu, Z. Ma, *et al.*, "Realization of high-luminous-efficiency InGaN light-emitting diodes in the “green gap” range," *Scientific reports,* vol. 5, p. 10883, 2015.
[224] P. O. Anikeeva, J. E. Halpert, M. G. Bawendi, and V. Bulovic, "Quantum dot light-emitting devices with electroluminescence tunable over the entire visible spectrum," *Nano letters,* vol. 9, pp. 2532-2536, 2009.
[225] Q. Sun, Y. A. Wang, L. S. Li, D. Wang, T. Zhu, J. Xu, *et al.*, "Bright, multicoloured light-emitting diodes based on quantum dots," *Nature photonics,* vol. 1, p. 717, 2007.
[226] J. Lim, M. Park, W. K. Bae, D. Lee, S. Lee, C. Lee, *et al.*, "Highly efficient cadmium-free quantum dot light-emitting diodes enabled by the direct formation of excitons within InP@ ZnSeS quantum dots," *ACS nano,* vol. 7, pp. 9019-9026, 2013.
[227] J. Song, J. Li, X. Li, L. Xu, Y. Dong, and H. Zeng, "Quantum dot light-emitting diodes based on inorganic perovskite cesium lead halides (CsPbX3)," *Advanced Materials,* vol. 27, pp. 7162-7167, 2015.
[228] H. Huang, F. Zhao, L. Liu, F. Zhang, X.-g. Wu, L. Shi, *et al.*, "Emulsion synthesis of size-tunable CH3NH3PbBr3 quantum dots: an alternative route toward efficient light-emitting diodes," *ACS applied materials & interfaces,* vol. 7, pp. 28128-28133, 2015.
[229] J. Pan, L. N. Quan, Y. Zhao, W. Peng, B. Murali, S. P. Sarmah, *et al.*, "Highly Efficient Perovskite-Quantum-Dot Light-Emitting Diodes by Surface Engineering," *Advanced Materials,* vol. 28, pp. 8718-8725, 2016.
[230] Y. Yang, Y. Zheng, W. Cao, A. Titov, J. Hyvonen, J. R. Manders, *et al.*, "High-efficiency light-emitting devices based on quantum dots with tailored nanostructures," *Nature Photonics,* vol. 9, p. nphoton. 2015.36, 2015.
[231] H. Shen, Q. Lin, W. Cao, C. Yang, N. T. Shewmon, H. Wang, *et al.*, "Efficient and long-lifetime full-color light-emitting diodes using high luminescence quantum yield thick-shell quantum dots," *Nanoscale,* vol. 9, pp. 13583-13591, 2017.
[232] H.-M. Kim, J. Kim, S.-Y. Cho, and J. Jang, "Solution-Processed Metal-Oxide p–n Charge Generation Junction for High-Performance Inverted Quantum-Dot Light-Emitting Diodes," *ACS applied materials & interfaces,* vol. 9, pp. 38678-38686, 2017.

[233] K.-H. Lee, J.-H. Lee, H.-D. Kang, B. Park, Y. Kwon, H. Ko, *et al.*, "Over 40 cd/A efficient green quantum dot electroluminescent device comprising uniquely large-sized quantum dots," *ACS nano,* vol. 8, pp. 4893-4901, 2014.
[234] Y. Zou, M. Ban, W. Cui, Q. Huang, C. Wu, J. Liu, *et al.*, "A General Solvent Selection Strategy for Solution Processed Quantum Dots Targeting High Performance Light-Emitting Diode," *Advanced Functional Materials,* vol. 27, p. 1603325, 2017.
[235] Z. Li, Y. Hu, H. Shen, Q. Lin, L. Wang, H. Wang, *et al.*, "Efficient and long-life green light-emitting diodes comprising tridentate thiol capped quantum dots," *Laser & Photonics Reviews,* vol. 11, p. 1600227, 2017.
[236] J. R. Manders, L. Qian, A. Titov, J. Hyvonen, J. Tokarz-Scott, K. P. Acharya, *et al.*, "High efficiency and ultra-wide color gamut quantum dot LEDs for next generation displays," *Journal of the Society for Information Display,* vol. 23, pp. 523-528, 2015.
[237] H.-W. Chen, J.-H. Lee, B.-Y. Lin, S. Chen, and S.-T. Wu, "Liquid crystal display and organic light-emitting diode display: present status and future perspectives," *Light: Science & Applications,* vol. 7, p. 17168, 2018.
[238] M. H. Balci, F. Chen, A. B. Cunbul, Ø. Svensen, M. N. Akram, and X. Chen, "Comparative study of blue laser diode driven cerium-doped single crystal phosphors in application of high-power lighting and display technologies," *Optical Review,* vol. 25, pp. 166-174, 2018.
[239] P. Schlotter, R. Schmidt, and J. Schneider, "Luminescence conversion of blue light emitting diodes," *Applied Physics A: Materials Science & Processing,* vol. 64, pp. 417-418, 1997.
[240] X. Dai, Z. Zhang, Y. Jin, Y. Niu, H. Cao, X. Liang, *et al.*, "Solution-processed, high-performance light-emitting diodes based on quantum dots," *Nature,* vol. 515, p. 96, 2014.
[241] D. I. Son, B. W. Kwon, D. H. Park, W.-S. Seo, Y. Yi, B. Angadi, *et al.*, "Emissive ZnO–graphene quantum dots for white-light-emitting diodes," *Nature nanotechnology,* vol. 7, p. 465, 2012.
[242] K. Bourzac, "Quantum dots go on display: adoption by TV makers could expand the market for light-emitting nanocrystals," *Nature,* vol. 493, pp. 283-284, 2013.
[243] S. Coe-Sullivan, W. Liu, P. Allen, and J. S. Steckel, "Quantum dots for LED downconversion in display applications," *ECS Journal of Solid State Science and Technology,* vol. 2, pp. R3026-R3030, 2013.
[244] S. Kim, S. H. Im, and S.-W. Kim, "Performance of light-emitting-diode based on quantum dots," *Nanoscale,* vol. 5, pp. 5205-5214, 2013.
[245] T.-H. Kim, K.-S. Cho, E. K. Lee, S. J. Lee, J. Chae, J. W. Kim, *et al.*, "Full-colour quantum dot displays fabricated by transfer printing," *Nature photonics,* vol. 5, p. 176, 2011.
[246] T.-H. Kim, S. Jun, K.-S. Cho, B. L. Choi, and E. Jang, "Bright and stable quantum dots and their applications in full-color displays," *MRS bulletin,* vol. 38, pp. 712-720, 2013.
[247] X. Li, Y. Wu, S. Zhang, B. Cai, Y. Gu, J. Song, *et al.*, "CsPbX3 Quantum Dots for Lighting and Displays: Room-Temperature Synthesis, Photoluminescence Superiorities, Underlying Origins and White Light-Emitting Diodes," *Advanced Functional Materials,* vol. 26, pp. 2435-2445, 2016.
[248] R. Liang, D. Yan, R. Tian, X. Yu, W. Shi, C. Li, *et al.*, "Quantum dots-based flexible films and their application as the phosphor in white light-emitting diodes," *Chemistry of Materials,* vol. 26, pp. 2595-2600, 2014.
[249] Z. Luo, D. Xu, and S.-T. Wu, "Emerging quantum-dots-enhanced LCDs," *Journal of display technology,* vol. 10, pp. 526-539, 2014.
[250] J. S. Steckel, J. Ho, C. Hamilton, J. Xi, C. Breen, W. Liu, *et al.*, "Quantum dots: The ultimate down-conversion material for LCD displays," *Journal of the Society for Information Display,* vol. 23, pp. 294-305, 2015.

[251] S. T. Tan, X. Sun, H. V. Demir, and S. DenBaars, "Advances in the LED materials and architectures for energy-saving solid-state lighting toward “lighting revolution”," *IEEE Photonics Journal,* vol. 4, pp. 613-619, 2012.
[252] F. Zhang, H. Zhong, C. Chen, X.-g. Wu, X. Hu, H. Huang*, et al.*, "Brightly luminescent and color-tunable colloidal CH3NH3PbX3 (X= Br, I, Cl) quantum dots: potential alternatives for display technology," *ACS nano,* vol. 9, pp. 4533-4542, 2015.
[253] S. W. Dai, B. W. Hsu, C. Y. Chen, C. A. Lee, H. Y. Liu, H. F. Wang*, et al.*, "Perovskite Quantum Dots with Near Unity Solution and Neat-Film Photoluminescent Quantum Yield by Novel Spray Synthesis," *Advanced Materials,* vol. 30, p. 1705532, 2018.
[254] J. Jagielski, S. Kumar, M. Wang, D. Scullion, R. Lawrence, Y.-T. Li*, et al.*, "Aggregation-induced emission in lamellar solids of colloidal perovskite quantum wells," *Science advances,* vol. 3, p. eaaq0208, 2017.
[255] Y. Fu, D. Kim, W. Jiang, W. Yin, T. K. Ahn, and H. Chae, "Excellent stability of thicker shell CdSe@ ZnS/ZnS quantum dots," *RSC Advances,* vol. 7, pp. 40866-40872, 2017.
[256] H. Wiener, "Structural determination of paraffin boiling points," *Journal of the American Chemical Society,* vol. 69, pp. 17-20, 1947.
[257] "Interantional Energy Agency (IEA) report " 2018.
[258] M. R. Bergren, N. S. Makarov, K. Ramasamy, A. Jackson, R. Guglielmetti, and H. McDaniel, "High-performance CuInS2 quantum dot laminated glass luminescent solar concentrators for windows," *ACS Energy Letters,* vol. 3, pp. 520-525, 2018.
[259] S. Yu, X.-B. Fan, X. Wang, J. Li, Q. Zhang, A. Xia*, et al.*, "Efficient photocatalytic hydrogen evolution with ligand engineered all-inorganic InP and InP/ZnS colloidal quantum dots," *Nature communications,* vol. 9, pp. 1-10, 2018.
[260] S. Tamang, C. Lincheneau, Y. Hermans, S. Jeong, and P. Reiss, "Chemistry of InP nanocrystal syntheses," *Chemistry of Materials,* vol. 28, pp. 2491-2506, 2016.
[261] H. Bahmani Jalali, O. Karatum, R. Melikov, U. M. Dikbas, S. Sadeghi, E. Yildiz*, et al.*, "Biocompatible Quantum Funnels for Neural Photostimulation," *Nano letters,* vol. 19, pp. 5975-5981, 2019.
[262] S. Xu, J. Ziegler, and T. Nann, "Rapid synthesis of highly luminescent InP and InP/ZnS nanocrystals," *Journal of Materials Chemistry,* vol. 18, pp. 2653-2656, 2008.
[263] J. Lim, W. K. Bae, D. Lee, M. K. Nam, J. Jung, C. Lee*, et al.*, "InP@ ZnSeS, core@ composition gradient shell quantum dots with enhanced stability," *Chemistry of Materials,* vol. 23, pp. 4459-4463, 2011.
[264] C. Ippen, T. Greco, and A. Wedel, "InP/ZnSe/ZnS: A novel multishell system for InP quantum dots for improved luminescence efficiency and its application in a light-emitting device," *Journal of Information Display,* vol. 13, pp. 91-95, 2012.
[265] I. Baylam, M. Cizmeciyan, N. Kakenov, C. Kocabas, and A. Sennaroglu, "Ultrafast spectroscopy of voltage reconfigurable graphene saturable absorbers in the visible and near infrared," *2D Materials,* vol. 6, p. 035013, 2019.
[266] A. Dutta, R. Bera, A. Ghosh, and A. Patra, "Ultrafast Carrier Dynamics of Photo-Induced Cu-Doped CdSe Nanocrystals," *The Journal of Physical Chemistry C,* vol. 122, pp. 16992-17000, 2018.
[267] P. Peng, B. Sadtler, A. P. Alivisatos, and R. J. Saykally, "Exciton Dynamics in CdS– Ag2S Nanorods with Tunable Composition Probed by Ultrafast Transient Absorption Spectroscopy," *The Journal of Physical Chemistry C,* vol. 114, pp. 5879-5885, 2010.
[268] K. E. Knowles, K. H. Hartstein, T. B. Kilburn, A. Marchioro, H. D. Nelson, P. J. Whitham*, et al.*, "Luminescent colloidal semiconductor nanocrystals containing copper: Synthesis, photophysics, and applications," *Chemical reviews,* vol. 116, pp. 10820-10851, 2016.
[269] B. Wang, H. Liu, B. Zhang, Y. Han, C. Shen, Q. Lin*, et al.*, "Development of

antibacterial and high light transmittance bulk materials: Incorporation and sustained release of hydrophobic or hydrophilic antibiotics," *Colloids and Surfaces B: Biointerfaces,* vol. 141, pp. 483-490, 2016.

[270] E. K. Sackmann, A. L. Fulton, and D. J. Beebe, "The present and future role of microfluidics in biomedical research," *Nature,* vol. 507, p. 181, 2014.

[271] S. Sadeghi, S. K. Abkenar, C. W. Ow-Yang, and S. Nizamoglu, "Efficient White LEDs Using Liquid-state Magic-sized CdSe Quantum Dots," *Scientific reports,* vol. 9, pp. 1-9, 2019.

[272] I. Coropceanu and M. G. Bawendi, "Core/shell quantum dot based luminescent solar concentrators with reduced reabsorption and enhanced efficiency," *Nano letters,* vol. 14, pp. 4097-4101, 2014.

[273] M. G. Debije and P. P. Verbunt, "Thirty years of luminescent solar concentrator research: solar energy for the built environment," *Advanced Energy Materials,* vol. 2, pp. 12-35, 2012.

[274] W. G. Van Sark, K. W. Barnham, L. H. Slooff, A. J. Chatten, A. Büchtemann, A. Meyer*, et al.*, "Luminescent Solar Concentrators-A review of recent results," *Optics Express,* vol. 16, pp. 21773-21792, 2008.

[275] J. Yoon, L. Li, A. V. Semichaevsky, J. H. Ryu, H. T. Johnson, R. G. Nuzzo*, et al.*, "Flexible concentrator photovoltaics based on microscale silicon solar cells embedded in luminescent waveguides," *Nature communications,* vol. 2, p. 343, 2011.

[276] I. Fraunhofer and A. Energiewende, "Current and future cost of photovoltaics; Long-term scenarios for market development, system prices and LCOE of utilityscale pv-systems," *Agora Energiewende,* p. 82, 2015.

[277] H. Zhao, Y. Zhou, D. Benetti, D. Ma, and F. Rosei, "Perovskite quantum dots integrated in large-area luminescent solar concentrators," *Nano Energy,* pp. 214-223, 2017.

[278] M. Sharma, K. Gungor, A. Yeltik, M. Olutas, B. Guzelturk, Y. Kelestemur*, et al.*, "Near-Unity Emitting Copper-Doped Colloidal Semiconductor Quantum Wells for Luminescent Solar Concentrators," *Advanced Materials,* 2017.

[279] A. J. Chatten, K. W. J. Barnham, B. F. Buxton, N. J. Ekins-Daukes, and M. A. Malik, "Quantum dot solar concentrators," *Semiconductors,* vol. 38, pp. 909-917, August 01 2004.

[280] M. J. Currie, J. K. Mapel, T. D. Heidel, S. Goffri, and M. A. Baldo, "High-efficiency organic solar concentrators for photovoltaics," *Science,* vol. 321, pp. 226-228, 2008.

[281] F. Bellina, C. Manzini, G. Marianetti, C. Pezzetta, E. Fanizza, M. Lessi*, et al.*, "Colourless p-phenylene-spaced bis-azoles for luminescent concentrators," *Dyes and Pigments,* vol. 134, pp. 118-128, 2016.

[282] H. Li, K. Wu, J. Lim, H.-J. Song, and V. I. Klimov, "Doctor-blade deposition of quantum dots onto standard window glass for low-loss large-area luminescent solar concentrators," *Nature Energy,* vol. 1, p. 16157, 2016.

[283] U. Aeberhard, R. Vaxenburg, E. Lifshitz, and S. Tomić, "Fluorescence of colloidal PbSe/PbS QDs in NIR luminescent solar concentrators," *Physical Chemistry Chemical Physics,* vol. 14, pp. 16223-16228, 2012.

[284] W. Weber and J. Lambe, "Luminescent greenhouse collector for solar radiation," *Applied optics,* vol. 15, pp. 2299-2300, 1976.

[285] A. Goetzberger and W. Greube, "Solar energy conversion with fluorescent collectors," *Applied Physics A: Materials Science & Processing,* vol. 14, pp. 123-139, 1977.

[286] K. Nikolaidou, S. Sarang, C. Hoffman, B. Mendewala, H. Ishihara, J. Q. Lu*, et al.*, "Hybrid perovskite thin films as highly efficient luminescent solar concentrators," *Advanced Optical Materials,* vol. 4, pp. 2126-2132, 2016.

[287] L. Jin, G. Sirigu, X. Tong, A. Camellini, A. Parisini, G. Nicotra*, et al.*, "Engineering interfacial structure in “Giant” PbS/CdS quantum dots for photoelectrochemical

solar energy conversion," *Nano Energy,* vol. 30, pp. 531-541, 2016.
[288] D. Chemisana, "Building integrated concentrating photovoltaics: a review," *Renewable and sustainable energy reviews,* vol. 15, pp. 603-611, 2011.
[289] S. V. Gaponenko, *Optical properties of semiconductor nanocrystals* vol. 23: Cambridge university press, 1998.
[290] A. Chatten, K. Barnham, B. Buxton, N. Ekins-Daukes, and M. Malik, "Quantum dot solar concentrators," *Semiconductors,* vol. 38, pp. 909-917, 2004.
[291] Z. Krumer, S. J. Pera, R. J. van Dijk-Moes, Y. Zhao, A. F. de Brouwer, E. Groeneveld*, et al.*, "Tackling self-absorption in luminescent solar concentrators with type-II colloidal quantum dots," *Solar Energy Materials and Solar Cells,* vol. 111, pp. 57-65, 2013.
[292] F. Meinardi, H. McDaniel, F. Carulli, A. Colombo, K. A. Velizhanin, N. S. Makarov*, et al.*, "Highly efficient large-area colourless luminescent solar concentrators using heavy-metal-free colloidal quantum dots," *Nature nanotechnology,* vol. 10, pp. 878-885, 2015.
[293] H. Zhao, A. Vomiero, and F. Rosei, "Ultrasensitive, Biocompatible, Self-Calibrating, Multiparametric Temperature Sensors," *Small,* vol. 11, pp. 5741-5746, 2015.
[294] H. Zhao, D. Benetti, L. Jin, Y. Zhou, F. Rosei, and A. Vomiero, "Absorption Enhancement in "Giant" Core/Alloyed-Shell Quantum Dots for Luminescent Solar Concentrator," *Small,* vol. 12, pp. 5354-5365, 2016.
[295] H. Zhao, G. Sirigu, A. Parisini, A. Camellini, G. Nicotra, F. Rosei*, et al.*, "Dual emission in asymmetric "giant" PbS/CdS/CdS core/shell/shell quantum dots," *Nanoscale,* vol. 8, pp. 4217-4226, 2016.
[296] M. G. Debije, "Solar energy collectors with tunable transmission," *Advanced Functional Materials,* vol. 20, pp. 1498-1502, 2010.
[297] L. Desmet, A. Ras, D. De Boer, and M. Debije, "Monocrystalline silicon photovoltaic luminescent solar concentrator with 4.2% power conversion efficiency," *Optics letters,* vol. 37, pp. 3087-3089, 2012.
[298] J. D. Bryan and D. R. Gamelin, "Doped semiconductor nanocrystals: synthesis, characterization, physical properties, and applications," *Prog. Inorg. Chem,* vol. 54, pp. 47-126, 2005.
[299] M. Hutton, "Human health concerns of lead, mercury, cadmium and arsenic," *Lead, mercury, cadmium and arsenic in the environment,* vol. 31, pp. 53-68, 1987.
[300] J. Baker, "New technology and possible advances in energy storage," *Energy Policy,* vol. 36, pp. 4368-4373, 2008.
[301] W. C. Chan and S. Nie, "Quantum dot bioconjugates for ultrasensitive nonisotopic detection," *Science,* vol. 281, pp. 2016-2018, 1998.
[302] A. R. Clapp, I. L. Medintz, J. M. Mauro, B. R. Fisher, M. G. Bawendi, and H. Mattoussi, "Fluorescence resonance energy transfer between quantum dot donors and dye-labeled protein acceptors," *Journal of the American Chemical Society,* vol. 126, pp. 301-310, 2004.
[303] X. Michalet, F. Pinaud, L. Bentolila, J. Tsay, S. Doose, J. Li*, et al.*, "Quantum dots for live cells, in vivo imaging, and diagnostics," *science,* vol. 307, pp. 538-544, 2005.
[304] E. Mutlugun, P. L. Hernandez Martinez, C. Eroglu, Y. Coskun, T. Erdem, V. K. Sharma*, et al.*, "Large-area (over 50 cm× 50 cm) freestanding films of colloidal InP/ZnS quantum dots," *Nano letters,* vol. 12, pp. 3986-3993, 2012.
[305] P. Pust, P. J. Schmidt, and W. Schnick, "A revolution in lighting," *Nature materials,* vol. 14, pp. 454-458, 2015.
[306] C. G. Van de Walle and J. Neugebauer, "Universal alignment of hydrogen levels in semiconductors, insulators and solutions," *Nature,* vol. 423, pp. 626-628, 2003.
[307] Y.-P. Du, Y.-W. Zhang, L.-D. Sun, and C.-H. Yan, "Efficient energy transfer in

monodisperse Eu-doped ZnO nanocrystals synthesized from metal acetylacetonates in high-boiling solvents," *The Journal of Physical Chemistry C,* vol. 112, pp. 12234-12241, 2008.

[308] M. Salavati-Niasari, F. Davar, and M. Mazaheri, "Preparation of ZnO nanoparticles from [bis (acetylacetonato) zinc (II)]–oleylamine complex by thermal decomposition," *Materials Letters,* vol. 62, pp. 1890-1892, 2008.

[309] J. Liu, Y. Bei, H. Wu, D. Shen, J. Gong, X. Li*, et al.*, "Synthesis of relatively monodisperse ZnO nanocrystals from a precursor zinc 2, 4-pentanedionate," *Materials Letters,* vol. 61, pp. 2837-2840, 2007.

[310] S. Musić, A. Šarić, and S. Popović, "Formation of nanosize ZnO particles by thermal decomposition of zinc acetylacetonate monohydrate," *Ceramics International,* vol. 36, pp. 1117-1123, 2010.

[311] T.-L. Nguyen, M. Michael, and P. Mulvaney, "Synthesis of highly crystalline CdSe@ ZnO nanocrystals via monolayer-by-monolayer epitaxial shell deposition," *Chemistry of Materials,* vol. 26, pp. 4274-4279, 2014.

[312] P. Ramasamy, B. Kim, M.-S. Lee, and J.-S. Lee, "Beneficial effects of water in the colloidal synthesis of InP/ZnS core–shell quantum dots for optoelectronic applications," *Nanoscale,* vol. 8, pp. 17159-17168, 2016.

[313] A. M. Smith, A. M. Mohs, and S. Nie, "Tuning the optical and electronic properties of colloidal nanocrystals by lattice strain," *Nature nanotechnology,* vol. 4, pp. 56-63, 2009.

[314] A. Manjceevan and J. Bandara, "Robust surface passivation of trap sites in PbS q-dots by controlling the thickness of CdS layers in PbS/CdS quantum dot solar cells," *Solar Energy Materials and Solar Cells,* vol. 147, pp. 157-163, 2016.

[315] V. I. Klimov, T. A. Baker, J. Lim, K. A. Velizhanin, and H. McDaniel, "Quality factor of luminescent solar concentrators and practical concentration limits attainable with semiconductor quantum dots," *ACS Photonics,* vol. 3, 2016.

[316] L. Wilson and B. Richards, "Measurement method for photoluminescent quantum yields of fluorescent organic dyes in polymethyl methacrylate for luminescent solar concentrators," *Applied optics,* vol. 48, pp. 212-220, 2009.

[317] Y. Li, P. Miao, W. Zhou, X. Gong, and X. Zhao, "N-doped carbon-dots for luminescent solar concentrators," *Journal of Materials Chemistry A,* vol. 5, pp. 21452-21459, 2017.

[318] Z. Wang, X. Zhao, Z. Guo, P. Miao, and X. Gong, "Carbon dots based nanocomposite thin film for highly efficient luminescent solar concentrators," *Organic Electronics,* vol. 62, pp. 284-289, 2018.

[319] M. Zhu, Y. Li, S. Tian, Y. Xie, X. Zhao, and X. Gong, "Deep-red emitting zinc and aluminium co-doped copper indium sulfide quantum dots for luminescent solar concentrators," *Journal of colloid and interface science,* vol. 534, pp. 509-517, 2019.

[320] H. Zhao, Y. Zhou, D. Benetti, D. Ma, and F. Rosei, "Perovskite quantum dots integrated in large-area luminescent solar concentrators," *Nano energy,* vol. 37, pp. 214-223, 2017.

[321] J. Zhang, R. E. Campbell, A. Y. Ting, and R. Y. Tsien, "Creating new fluorescent probes for cell biology," *Nature reviews Molecular cell biology,* vol. 3, p. 906, 2002.

[322] A.-K. Hadjantonakis and V. E. Papaioannou, "Dynamic in vivo imaging and cell tracking using a histone fluorescent protein fusion in mice," *BMC biotechnology,* vol. 4, p. 33, 2004.

[323] I. B. Dogru, K. Min, M. Umar, H. Bahmani Jalali, E. Begar, D. Conkar*, et al.*, "Single transverse mode protein laser," *Applied Physics Letters,* vol. 111, p. 231103, 2017.

[324] D. S. Bindels, L. Haarbosch, L. Van Weeren, M. Postma, K. E. Wiese, M. Mastop*, et al.*, "mScarlet: a bright monomeric red fluorescent protein for cellular imaging," *nature methods,* vol. 14, p. 53, 2017.

[325] H. J. Oh, M. C. Gather, J.-J. Song, and S. H. Yun, "Lasing from fluorescent protein

crystals," *Optics express,* vol. 22, pp. 31411-31416, 2014.
[326] D. A. Chang-Yen, R. K. Eich, and B. K. Gale, "A monolithic PDMS waveguide system fabricated using soft-lithography techniques," *Journal of lightwave technology,* vol. 23, p. 2088, 2005.
[327] K. Ashton, "That 'internet of things' thing," *RFID journal,* vol. 22, pp. 97-114, 2009.
[328] I. Lee and K. Lee, "The Internet of Things (IoT): Applications, investments, and challenges for enterprises," *Business Horizons,* vol. 58, pp. 431-440, 2015.
[329] I. C. Ng and S. Y. Wakenshaw, "The Internet-of-Things: Review and research directions," *International Journal of Research in Marketing,* vol. 34, pp. 3-21, 2017.
[330] "IOT Analytics," 2018.
[331] "Global IoT Market Size," 2020.
[332] F. Meinardi, F. Bruni, and S. Brovelli, "Luminescent solar concentrators for building-integrated photovoltaics," *Nature Reviews Materials,* vol. 2, pp. 1-9, 2017.
[333] J. Bomm, A. Büchtemann, A. J. Chatten, R. Bose, D. J. Farrell, N. L. Chan*, et al.*, "Fabrication and full characterization of state-of-the-art quantum dot luminescent solar concentrators," *Solar Energy Materials and Solar Cells,* vol. 95, pp. 2087-2094, 2011.
[334] L. H. Slooff, E. E. Bende, A. R. Burgers, T. Budel, M. Pravettoni, R. P. Kenny*, et al.*, "A luminescent solar concentrator with 7.1% power conversion efficiency," *physica status solidi (RRL)–Rapid Research Letters,* vol. 2, pp. 257-259, 2008.
[335] Y. Zhou, D. Benetti, Z. Fan, H. Zhao, D. Ma, A. O. Govorov*, et al.*, "Near infrared, highly efficient luminescent solar concentrators," *Advanced Energy Materials,* vol. 6, p. 1501913, 2016.
[336] K. Yoshikawa, H. Kawasaki, W. Yoshida, T. Irie, K. Konishi, K. Nakano*, et al.*, "Silicon heterojunction solar cell with interdigitated back contacts for a photoconversion efficiency over 26%," *Nature Energy,* vol. 2, p. 17032, 2017/03/20 2017.
[337] V. Bahrami-Yekta and T. Tiedje, "Limiting efficiency of indoor silicon photovoltaic devices," *Optics express,* vol. 26, pp. 28238-28248, 2018.
[338] L. C. Andreani, A. Bozzola, P. Kowalczewski, M. Liscidini, and L. Redorici, "Silicon solar cells: toward the efficiency limits," *Advances in Physics: X,* vol. 4, p. 1548305, 2019.
[339] L. Meng, Y. Zhang, X. Wan, C. Li, X. Zhang, Y. Wang*, et al.*, "Organic and solution-processed tandem solar cells with 17.3% efficiency," *Science,* vol. 361, pp. 1094-1098, 2018.
[340] A. Polman, M. Knight, E. C. Garnett, B. Ehrler, and W. C. Sinke, "Photovoltaic materials: Present efficiencies and future challenges," *Science,* vol. 352, p. aad4424, 2016.
[341] J. Hou, O. Inganäs, R. H. Friend, and F. Gao, "Organic solar cells based on non-fullerene acceptors," *Nature materials,* vol. 17, pp. 119-128, 2018.
[342] M. Peng, S. Hou, H. Wu, Q. Yang, X. Cai, X. Yu*, et al.*, "Integration of fiber dye-sensitized solar cells with luminescent solar concentrators for high power output," *Journal of Materials Chemistry A,* vol. 2, pp. 926-932, 2014.
[343] L. J. Brennan, F. Purcell-Milton, B. McKenna, T. M. Watson, Y. K. Gun'ko, and R. C. Evans, "Large area quantum dot luminescent solar concentrators for use with dye-sensitised solar cells," *Journal of Materials Chemistry A,* vol. 6, pp. 2671-2680, 2018.
[344] S.-J. Ha, J.-H. Kang, D. H. Choi, S. K. Nam, E. Reichmanis, and J. H. Moon, "Upconversion-assisted dual-band luminescent solar concentrator coupled for high power conversion efficiency photovoltaic systems," *ACS Photonics,* vol. 5, pp. 3621-3627, 2018.
[345] G. Li, R. Zhu, and Y. Yang, "Polymer solar cells," *Nature Photonics,* vol. 6, pp. 153-161, 2012/03/01 2012.

[346] G. Li, V. Shrotriya, J. Huang, Y. Yao, T. Moriarty, K. Emery, *et al.*, "High-efficiency solution processable polymer photovoltaic cells by self-organization of polymer blends," *Nature Materials,* vol. 4, pp. 864-868, 2005/11/01 2005.

[347] S. K. Hau, H.-L. Yip, and A. K. Y. Jen, "A Review on the Development of the Inverted Polymer Solar Cell Architecture," *Polymer Reviews,* vol. 50, pp. 474-510, 2010/10/28 2010.

[348] S. Ryu, D. C. Nguyen, N. Y. Ha, H. J. Park, Y. H. Ahn, J.-Y. Park, *et al.*, "Light Intensity-dependent Variation in Defect Contributions to Charge Transport and Recombination in a Planar MAPbI3 Perovskite Solar Cell," *Scientific Reports,* vol. 9, p. 19846, 2019/12/27 2019.

[349] L. Cojocaru, S. Uchida, K. Tamaki, P. V. V. Jayaweera, S. Kaneko, J. Nakazaki, *et al.*, "Determination of unique power conversion efficiency of solar cell showing hysteresis in the I-V curve under various light intensities," *Scientific Reports,* vol. 7, p. 11790, 2017/09/18 2017.

[350] A. K. K. Kyaw, D. H. Wang, V. Gupta, W. L. Leong, L. Ke, G. C. Bazan, *et al.*, "Intensity Dependence of Current–Voltage Characteristics and Recombination in High-Efficiency Solution-Processed Small-Molecule Solar Cells," *ACS Nano,* vol. 7, pp. 4569-4577, 2013/05/28 2013.

[351] Z. Li, F. Gao, N. C. Greenham, and C. R. McNeill, "Comparison of the Operation of Polymer/Fullerene, Polymer/Polymer, and Polymer/Nanocrystal Solar Cells: A Transient Photocurrent and Photovoltage Study," *Advanced Functional Materials,* vol. 21, pp. 1419-1431, 2011/04/22 2011.

[352] C. Meichner, A. E. Schedl, C. Neuber, K. Kreger, H.-W. Schmidt, and L. Kador, "Refractive-index determination of solids from first-and second-order critical diffraction angles of periodic surface patterns," *AIP Advances,* vol. 5, p. 087135, 2015.

[353] A. Ng, C. H. Li, M. K. Fung, A. B. Djurisic, J. A. Zapien, W. K. Chan, *et al.*, "Accurate determination of the index of refraction of polymer blend films by spectroscopic ellipsometry," *The Journal of Physical Chemistry C,* vol. 114, pp. 15094-15101, 2010.

[354] M. Wei, F. P. G. de Arquer, G. Walters, Z. Yang, L. N. Quan, Y. Kim, *et al.*, "Ultrafast narrowband exciton routing within layered perovskite nanoplatelets enables low-loss luminescent solar concentrators," *Nature Energy,* p. 1, 2019.

[355] X. Jia, Q. Feng, and C. Ma, "An efficient anti-collision protocol for RFID tag identification," *IEEE Communications Letters,* vol. 14, pp. 1014-1016, 2010.

[356] X. Jia, Q. Feng, T. Fan, and Q. Lei, "RFID technology and its applications in Internet of Things (IoT)," in *2012 2nd international conference on consumer electronics, communications and networks (CECNet)*, 2012, pp. 1282-1285.

[357] J. Wang, D. Ni, and K. Li, "RFID-based vehicle positioning and its applications in connected vehicles," *Sensors,* vol. 14, pp. 4225-4238, 2014.

[358] N. Akhtar, S. C. Ergen, and O. Ozkasap, "Vehicle mobility and communication channel models for realistic and efficient highway VANET simulation," *IEEE Transactions on Vehicular Technology,* vol. 64, pp. 248-262, 2014.

[359] C. Ding, H. Li, W. Zheng, Y. Wang, N. Chang, and X. Lin, "Luminescent solar concentrator-based photovoltaic reconfiguration for hybrid and plug-in electric vehicles," in *2016 IEEE 34th International Conference on Computer Design (ICCD)*, 2016, pp. 281-288.

[360] W. Davis and Y. Ohno, "Color quality scale," *Optical engineering,* vol. 49, p. 033602, 2010.

[361] A. Vinokurov, G. Chernysheva, N. Mordvinova, and S. Dorofeev, "Optical properties and structure of Ag-doped InP quantum dots prepared by a phosphine synthetic route," *Dalton Transactions,* vol. 47, pp. 12414-12419, 2018.

[362] R. Xie, K. Chen, X. Chen, and X. Peng, "InAs/InP/ZnSe core/shell/shell quantum dots as near-infrared emitters: bright, narrow-band, non-cadmium containing, and biocompatible," *Nano research,* vol. 1, pp. 457-464, 2008.

[363] Y. Nakane, Y. Tsukasaki, T. Sakata, H. Yasuda, and T. Jin, "Aqueous synthesis of

glutathione-coated PbS quantum dots with tunable emission for non-invasive fluorescence imaging in the second near-infrared biological window (1000–1400 nm)," *Chemical Communications,* vol. 49, pp. 7584-7586, 2013.

[364] L. Bakueva, I. Gorelikov, S. Musikhin, X. S. Zhao, E. H. Sargent, and E. Kumacheva, "PbS quantum dots with stable efficient luminescence in the near-IR spectral range," *Advanced Materials,* vol. 16, pp. 926-929, 2004.

[365] C. Chen, X. He, L. Gao, and N. Ma, "Cation exchange-based facile aqueous synthesis of small, stable, and nontoxic near-infrared Ag2Te/ZnS core/shell quantum dots emitting in the second biological window," *ACS applied materials & interfaces,* vol. 5, pp. 1149-1155, 2013.

[366] Y. Zhang, G. Hong, Y. Zhang, G. Chen, F. Li, H. Dai*, et al.*, "Ag2S quantum dot: a bright and biocompatible fluorescent nanoprobe in the second near-infrared window," *ACS nano,* vol. 6, pp. 3695-3702, 2012.

[367] R. Sumner, S. Eiselt, T. B. Kilburn, C. Erickson, B. Carlson, D. R. Gamelin*, et al.*, "Analysis of optical losses in high-efficiency CuInS2-based nanocrystal luminescent solar concentrators: balancing absorption versus scattering," *The Journal of Physical Chemistry C,* vol. 121, pp. 3252-3260, 2017.

[368] F. Meinardi, H. McDaniel, F. Carulli, A. Colombo, K. A. Velizhanin, N. S. Makarov*, et al.*, "Highly efficient large-area colourless luminescent solar concentrators using heavy-metal-free colloidal quantum dots," *Nature nanotechnology,* vol. 10, p. 878, 2015.

[369] F. Meinardi, S. Ehrenberg, L. Dhamo, F. Carulli, M. Mauri, F. Bruni*, et al.*, "Highly efficient luminescent solar concentrators based on earth-abundant indirect-bandgap silicon quantum dots," *Nature Photonics,* vol. 11, p. 177, 2017.

[370] Y. Zhou, D. Benetti, X. Tong, L. Jin, Z. M. Wang, D. Ma*, et al.*, "Colloidal carbon dots based highly stable luminescent solar concentrators," *Nano Energy,* vol. 44, pp. 378-387, 2018.

[371] A. Anand, M. L. Zaffalon, G. Gariano, A. Camellini, M. Gandini, R. Brescia*, et al.*, "Evidence for the Band‐Edge Exciton of CuInS2 Nanocrystals Enables Record Efficient Large‐Area Luminescent Solar Concentrators," *Advanced Functional Materials,* 2019.

[372] W. Zhou, M.-C. Wang, and X. Zhao, "The properties of PMMA/DCJTB thin-film luminescent solar concentrator with various thicknesses," *Solar Energy,* vol. 120, pp. 419-427, 2015.

[373] C. Tummeltshammer, A. Taylor, A. J. Kenyon, and I. Papakonstantinou, "Flexible and fluorophore-doped luminescent solar concentrators based on polydimethylsiloxane," *Optics letters,* vol. 41, pp. 713-716, 2016.

[374] W. Ma, W. Li, M. Cao, R. Liu, X. Zhao, and X. Gong, "Large Stokes-shift AIE fluorescent materials for high-performance luminescent solar concentrators," *Organic Electronics,* 2019.